Inaugural dissertation

for

obtaining the doctoral degree

of the

Combined Faculty of Mathematics, Engineering and Natural Sciences

of the

Ruprecht - Karls - University

Heidelberg

Presented by

M.Sc. Jana Koch

born in: Backnang, Germany

Oral examination: 27.07.2023

The zoonotic viruses Toscana virus and SARS-CoV-2 make a differential use of endosomal acidification for infectious entry

Referees: Prof. Dr. Hans-Georg Kräusslich

Dr. Pierre-Yves Lozach

Table of content

I. Abbreviations

µ	micro
A549*	A549 cells engineered to express ACE2
ACE2	angiotensin-converting enzyme 2
ADAM	a disintegrin and metalloproteinase
AF	Alexa Fluor
Arbovirus	arthropod-borne virus
ASGR1	asialoglycoprotein receptor 1
ASLV	avian sarcoma leukosis virus
AT1	angiotensin II type 1
ATP	adenosine triphosphate
AVPR1B	arginine vasopressin receptor 1B
b	base
BHK	baby hamster kidney
BMP	bis(monoacylglycerol)phosphate
BSA	bovine serum albumine
BSL	bio-safety level
CA	constitutively active
Caco	colon cancer
Calu	lung cancer
Cas9	CRISPR-associated protein 9
CCR5	C-C motif chemokine receptor 5
CD	cluster of differentiation
CMFDA	5-chloromethylfluorescein diacetate
COVID	coronavirus disease
CPE	cytopathic effect
CRISPR	clustered regularly interspaced short palindromic repeats
cRNA	complementary RNA
CTD	C-terminal domain
C-type	calcium-dependent
CXCR4	C-X-C motif chemokine receptor 4
d	days
D	aspartic acid
Da	Dalton
DABV	Dabie virus
DC	dendritic cell
DC-SIGN	dendritic cell-specific intercellular adhesion molecule 3-grabbing non-integrin
DENV	Dengue virus
dH_2O	deionized water
DMEM	Dulbecco's modified Eagle's medium
DMSO	dimethyl sulfoxide
DNA	deoxyribonucleic acid
E	glutamic acid
E protein	envelope protein
E. coli	Escherichia coli
EDTA	ethylenediaminetetraacetic acid

EE	early endosome
EF2α	elongation factor 2α
EGFP	enhanced green fluorescent protein
EM	electron microscopy
E-PV	early-penetrating virus
ER	endoplasmic reticulum
ERGIC	ER-Golgi intermediate compartment
ESCRT	endosomal sorting complex required for transport
F	phenylalanine
FA	formaldehyde
FACS	fluorescence-activated cell sorting
FBS	fetal bovine serum
FPB	FACS permeabilization buffer
FSC	forward scatter
g	gram
G	glycine
Gc	glycoprotein C
GDP	guanosine diphosphate
GERV	Germiston virus
GMEM	Glasgow's minimal essential medium
Gn	glycoprotein N
GP	glycoprotein
GTP	guanosine triphosphate
GTPase	guanosine triphosphate hydrolase protein
H	Histidine
h	hours
HA protein	hemagglutinin protein
HCl	hydrogen chloride
HEK 293T cells	human embryonic kidney 293 cells that express the Simian virus 40 T-antigen
HeLa cells	Henrietta Lacks cells
HEPES	4-(2-hydroxyethyl)-1-piperazineethanesulfonic acid
HIV-1	human immunodeficiency virus 1
H-Lac	human lymphoid aggregate culture
HNE buffer	HEPES - NaCl – EDTA buffer
HR1	heptad repeat 1
HRTV	Heartland virus
Huh	human hepatoma
IAV	influenza A virus
IC_{50}	50% inhibitory concentration
IFITM2	interferon-induced transmembrane protein 2
iPSC	induced pluripotent stem cell
k	kilo
K	lysine
KREMEN1	Kringle containing transmembrane protein 1
L	liter
L	leucine
L segment	large segment

L-15	Leibovitz 15
LAMP1	lysosome associated membrane protein type 1
LDH	lactate dehydrogenase
LE	late endosome
L-PV	late-penetrating virus
Lrp1	low-density lipoprotein receptor-related protein 1
LSECtin	liver and lymph node sinusoidal endothelial cell C-type lectin
LY6E	lymphocyte antigen 6 complex, locus E
L-SIGN	liver/lymph node cell-specific intercellular adhesion molecule 3-grabbing non-integrin
m	milli
M	molar
M protein	membrane protein
M segment	medium segment
MDCK	Madin Darby canine kidney
MEM	minimal essential medium
MeOH	methanol
MERS	Middle East respiratory syndrome
MERS-CoV	Middle East respiratory syndrome coronavirus
MES	2-Morpholinoethanesulfonic acid
min	minutes
MLV	murine leukemia virus
MOI	multiplicity of infection
MOPS	3-(*N*-Morpholino)propane sulfonic acid
mRNA	messenger RNA
MT	microtubule
MT1-MMP	membrane-type 1 matrix metalloproteinase
n	nano
N	asparagine
N protein	nucleoprotein
NaCl	sodium chloride
NaOH	sodium hydroxide
NEAA	nonessential amino acids
NH_4Cl	ammonium chloride
NHS ester	N-Hydroxysuccinimide ester
NP protein	nucleoprotein
Nrp1	neuropilin 1
ns	nonsignificant
NSm protein	nonstructural protein M
nsp	nonstructural protein
NSs protein	nonstructural protein S
nt	nucleotide
NTD	N-terminal domain
ORF	open reading frame
P	proline
PBS	phosphate buffered saline
PEI	polyethylenimine
PFA	paraformaldehyde

pfu	plaque-forming units
PI	phosphoinositide
PI(3,5)P2	phosphatidylinositol 3,5-bisphosphate
PI3P	phosphatidylinositol 3-phosphate
PPMP	DL-*threo*-1-Phenyl-2-palmitoylamino-3-morpholino-1-propanol
PTV	Punta Toro virus
PVDF	poly-vinylidene difluoride
Q	glutamine
R	arginine
R&D	research & development
R18	octadecyl rhodamine B chloride
Rab	Ras-associated binding
RBD	receptor binding domain
RdRp	RNA-dependent RNA polymerase
RNA	ribonucleic acid
RNP	ribonucleoprotein
ROSA	Reverse oriented splice acceptor
rpm	rotations per minute
RPMI	Rosewell park memorial institute medium
rtTA	reverse tetracycline-controlled transactivator
RU	relative units
RVF	Rift Valley fever
RVFV	Rift Valley fever virus
RVFVΔNSs:EGFP	RVFV with NSs replaced by EGFP
S protein	spike protein
S segment	small segment
SARS	severe acute respiratory syndrome
SARS-CoV	severe acute respiratory syndrome coronavirus
SARS-CoV-2	severe acute respiratory syndrome coronavirus 2
SD	standard deviation
SDS-PAGE	sodium dodecyl sulfate polyacrylamide gel electrophoresis
sec	seconds
SEM	standard error of the mean
SFTSV	severe fever with thrombocytopenia syndrome virus
SFV	Semliki forest virus
siRNA	small interfering RNA
SSC	sideward scatter
STED	stimulated emission depletion
T	threonine
TBS	Tris-buffered saline
TBST	TBS-Tween
TCID50	50% tissue culture infectious dose
TGN	trans-Golgi network
THP	Tohoku Hospital Pediatrics
TIM1	T cell immunoglobulin and mucin domain 1
TM	transmembrane
TMEM16F	transmembrane protein 16F

TMPRSS	transmembrane protease serine
TOSV	Toscana virus
TPB	tryptose phosphate broth
Tris	Tris(hydroxymethyl)aminomethane
UUKV	Uukuniemi virus
vATPase	vacuolar-type H+-ATPases
VOC	variant of concern
VSV	Vesicular stomatitis virus
W	tryptophan
WB	western blot
WHO	world health organization
WT	wild type
Y	tyrosine

II. List of figures

III. List of tables

IV. Summary

Zoonotic viruses pose a global threat to both human and veterinary health, as recently demonstrated by the emergence of SARS-CoV-2, the causative agent of the COVID-19 pandemic. In addition to airborne viruses, highly pathogenic arthropod-borne viruses have emerged globally in recent decades, essentially due to human activities, global warming, habitat destruction, and globalization. Ideally, the prevention of the emergence and spread of emerging pathogens will require approaches that target the first steps of infection and that block the release of the viral genome into the cytosol, prerequisites for productive infection.

This PhD thesis work was dedicated to elucidating the entry mechanisms of two unrelated zoonotic emerging enveloped viruses, SARS-CoV-2 and Toscana virus (TOSV), at the cellular and molecular levels. TOSV is a sand fly-borne neurotropic pathogen of the family *Phenuiviridae* in the order *Bunyavirales*. TOSV is widely distributed in Mediterranean countries, where it is one of the most common causes of human meningitis during the summer. However, TOSV remains a neglected pathogen and little is known about its cell life cycle. Here, I developed sensitive, quantitative, and accurate assays involving flow cytometry, fluorimetry, and microscopy to decipher each step of the TOSV entry program, including virus binding, internalization, intracellular trafficking, and membrane fusion. Using fluorescently labeled TOSV particles, I showed that TOSV traffics along the endosomal machinery in induced pluripotent stem cell-derived human neurons and cell lines, first entering Rab5a+ early endosomes and then Rab7a+ and LAMP1+ late endosomal compartments. TOSV entry required intact late endosomes, from which acid-activated membrane fusion occurred. The pH threshold for fusion was optimal and faster at pH 5.5, but fusion also happened with prolonged pre-exposure of viral particles to the slightly acidic pH present in early endosomes. Unexpectedly for a class-II fusion virus like TOSV, the virus and other bunyaviruses remained infectious when exposed to low pH in the absence of a target membrane.

In parallel, I studied the mechanism of entry of SARS-CoV-2 into various cell lines representing the tissues targeted during infection. I found that authentic SARS-CoV-2 entered the cytosol from or near the plasma membrane in a rapid, pH-independent manner when host cells expressed the trypsin-like protease TMPRSS2. In contrast, in cells lacking TMPRSS2 expression, SARS-CoV-2 entry was slower and relied on both endosome maturation and acid-dependent endolysosomal cathepsins. Pre-activation of viral particles by proteases bypassed the need for acidification and cathepsin L activity. In addition, I established a microscopy-based cell-cell fusion assay and found that proteolytic

processing of S was necessary and sufficient to induce fusion, whereas acidification was not required.

In conclusion, my results expand our knowledge of the entry of emerging zoonotic viruses. TOSV makes atypical use of endosomal acidity to find its way out of the endocytic machinery, whereas SARS-CoV-2 uses different cellular proteases for membrane fusion and penetration independent of acidification. While the TOSV fusion process itself is triggered by low pH, SARS-CoV-2 requires acidification only for the activity of cathepsins that activate the viral particles. Overall, our study highlights the diversity of strategies developed by viruses to subvert cellular machinery and enter host cells and may provide a basis for the development of antiviral strategies.

V. Zusammenfassung

Zoonotische Viren stellen eine globale Bedrohung für die Gesundheit von Mensch und Tier dar, wie kürzlich das Auftreten von SARS-CoV-2, dem Erreger der COVID-19-Pandemie, gezeigt hat. Neben Viren, die über die Luft übertragen werden, sind in den letzten Jahrzehnten weltweit auch hoch pathogene, durch Arthropoden übertragene Viren aufgetreten, was im Wesentlichen auf menschliche Aktivitäten, die globale Erwärmung, die Zerstörung von Lebensräumen und die Globalisierung zurückzuführen ist. Idealerweise erfordert die Verhinderung des Auftretens und der Ausbreitung neu auftretender Krankheitserreger Ansätze, die auf die ersten Schritte der Infektion abzielen und die Freisetzung des viralen Genoms in das Zytosol blockieren, was die Voraussetzung für eine produktive Infektion ist.

In dieser Doktorarbeit wurden die Eintrittsmechanismen von zwei nicht verwandten zoonotischen, auftauchenden behüllten Viren, SARS-CoV-2 und Toscana-Virus (TOSV), auf zellulärer und molekularer Ebene aufgeklärt. TOSV ist ein von Sandfliegen übertragener neurotropischer Erreger aus der Familie der *Phenuiviridae* in der Ordnung der *Bunyavirales*. TOSV ist in den Mittelmeerländern weit verbreitet, wo es im Sommer eine der häufigsten Ursachen für menschliche Meningitis ist. TOSV bleibt jedoch ein vernachlässigter Erreger, und über seinen Zelllebenszyklus ist nur wenig bekannt. Hier habe ich empfindliche, quantitative und genaue Assays entwickelt, die Durchflusszytometrie, Fluorimetrie und Mikroskopie umfassen, um jeden Schritt des TOSV-Eintrittsprogramms zu entschlüsseln, einschließlich Virusbindung, Internalisierung, intrazellulärer Transport und Membranfusion. Unter Verwendung fluoreszenzmarkierter TOSV-Partikel konnte ich zeigen, dass TOSV in aus induzierten pluripotenten Stammzellen abgeleiteten menschlichen Neuronen und Zelllinien entlang der endosomalen Maschinerie wandert und zunächst in frühe Rab5a+-Endosomen und dann in späte Rab7a+- und LAMP1+-Endosomen-Kompartimente gelangt. Für den Eintritt von TOSV waren intakte späte Endosomen erforderlich, von denen aus eine durch Säure aktivierte Membranfusion stattfand. Der pH-Schwellenwert für die Fusion war bei pH 5,5 optimal und schneller, aber die Fusion erfolgte auch bei längerer Präexposition der Viruspartikel gegenüber dem leicht sauren pH-Wert in den frühen Endosomen. Unerwartet für ein Klasse-II-Fusionsvirus wie TOSV blieben das Virus und andere Bunyaviren infektiös, wenn sie einem niedrigen pH-Wert in Abwesenheit einer Zielmembran ausgesetzt waren.

Parallel dazu untersuchte ich den Mechanismus des Eindringens von SARS-CoV-2 in verschiedene Zelllinien, die die Zielgewebe der Infektion repräsentieren. Ich fand heraus, dass authentisches SARS-CoV-2 schnell und pH-unabhängig von oder nahe der Plasmamembran in das Zytosol eindringt, wenn die Wirtszellen die trypsinartige Protease TMPRSS2 exprimieren. Im Gegensatz dazu war der Eintritt von SARS-CoV-2 in Zellen ohne TMPRSS2-Expression langsamer und hing sowohl von der Endosomenreifung als auch von säureabhängigen endolysosomalen Kathepsinen ab. Die Voraktivierung der Viruspartikel durch Proteasen umging die Notwendigkeit der Ansäuerung und der Kathepsin-L-Aktivität. Darüber hinaus habe ich einen auf Mikroskopie basierenden Assay zur Zellfusion durchgeführt und festgestellt, dass die proteolytische Verarbeitung von S notwendig und ausreichend war, um die Fusion einzuleiten, während eine Ansäuerung nicht erforderlich war.

Zusammenfassend lässt sich sagen, dass meine Ergebnisse unser Wissen über den Eintritt neuer zoonotischer Viren erweitern. TOSV nutzt auf atypische Weise die endosomale Azidität, um aus der endozytischen Maschinerie herauszukommen, während SARS-CoV-2 verschiedene zelluläre Proteasen für die Membranfusion und -penetration unabhängig von der Azidifizierung nutzt. Während der TOSV-Fusionsprozess selbst durch einen niedrigen pH-Wert ausgelöst wird, benötigt SARS-CoV-2 eine Ansäuerung nur für die Aktivität von Kathepsinen, die die Viruspartikel aktivieren. Insgesamt unterstreicht unsere Studie die Vielfalt der Strategien, die Viren entwickelt haben, um zelluläre Mechanismen zu unterlaufen und in Wirtszellen einzudringen, und könnte eine Grundlage für die Entwicklung antiviraler Strategien bilden.

1. Introduction

1.1 Zoonotic emerging viruses

The term "zoonosis" is derived from the Greek words "zoon" and "nosos", meaning animal and illness. According to the World Health Organization (WHO), it includes any disease or infection that is transmitted from vertebrate animals to humans or vice versa (1). Many zoonotic viruses pose a major threat to humans and have caused numerous outbreaks. It has been reported that more than 60% of human pathogens are zoonoses and according to the R&D Blueprint list of priority pathogens published by the WHO, all eleven named priority pathogens are of zoonotic origin (2, 3). In addition, zoonotic viruses often have a wide range of hosts and can also infect animals and plants. Together, they pose a major threat to human and animal health and agricultural productivity.

Zoonotic viruses can be airborne, foodborne, transmitted directly from animals to humans, or vector-borne, transmitted indirectly from animals to humans via arthropod vectors such as mosquitoes and ticks. In the latter case, we speak of arthropod-borne viruses (arboviruses). While some viruses spread to humans only occasionally, others have caused major outbreaks and are now exclusively human pathogens, such as the human immunodeficiency virus 1 (HIV-1). Some zoonoses are considered emerging. As defined by the WHO, an "emerging zoonosis is a zoonosis that is newly recognized or newly evolved, or that has occurred previously but shows an increase in incidence or expansion in geographical, host or vector range" (4). Emerging zoonotic diseases are often caused by enveloped RNA viruses, which have an RNA genome encapsidated by a viral nucleoprotein surrounded by a lipid bilayer with transmembrane proteins. Important examples of emerging zoonotic viral diseases are Rift Valley fever (RVF), severe acute respiratory syndrome (SARS), Middle East respiratory syndrome (MERS), coronavirus disease (COVID), Ebola, or influenza. The emergence of new diseases is facilitated by globalization, habitat destruction, climate change, and loss of species and biodiversity (5).

Arboviruses constitute a large group of diverse viral families, most of which belong to the genera *Flavivirus*, *Alphavirus*, or the order *Bunyavirales*, and with a lower extent to *Rhabdoviridae*, *Orthomyxoviridae*, or *Reovirales*. Many arboviruses are emerging pathogens that have undergone dramatic geographic expansion in recent decades (6). Most arboviruses are not associated with human disease or are causing only mild illness, but others are of major medical importance and responsible for large epidemics on a global scale (7). Some examples of global health-threatening arboviruses are dengue

virus (DENV), Zika virus, yellow fever virus, chikungunya virus, and Rift Valley fever virus (RVFV), which are all small enveloped RNA viruses. The normal route of transmission to humans is through the bite of infected arthropod hosts during blood-feeding. The fact that arboviruses replicate in both vertebrate and invertebrate hosts makes the life cycle of these viruses dual and complex. After ingestion of viruses from an infected host, arboviruses cross the midgut epithelium and replicate in the arthropod vector before producing high titers in the salivary glands. The viruses are then transmitted to new hosts through a blood meal. The animal host is usually referred to as the reservoir host, which has a long history of co-evolution with the arbovirus, often in the absence of disease. In this animal-vector cycle, humans are often a coincidental host and are usually considered a dead end in the transmission chain.

WHO has published a blueprint list of twelve viral pathogens for which there is an urgent need to develop prevention, diagnostics, therapies, and research. Most of these pathogens, if not all, have emerged in human populations as a result of zoonotic diseases. In this context, the overarching aim of this PhD study was to characterize the early stages of infection by two emerging zoonotic viruses, one arbovirus, Toscana virus (TOSV), and one air-borne virus, SARS-CoV-2. TOSV belongs to the *Phenuiviridae* family in the order *Bunyavirales* and is transmitted by sand flies to humans. TOSV causes febrile illness and is associated with central nervous system manifestations. SARS-CoV-2 is a member of the *Coronaviridae* family, presumably derived from bats, and transmitted by air droplets. It is the causative agent of the COVID-19 pandemic of recent years.

1.1.1 Biological significance of phenuiviruses in the *Bunyavirales* order

The *Bunyavirales* is a large order with 14 virus families and about 500 virus isolates (8). The bunyaviral genome consists of multiple single-stranded RNA segments with a negative or ambisense coding strategy. They can infect a wide range of hosts, including vertebrates, invertebrates, and plants, and pose a major threat to livestock, agricultural productivity, and human public health (9). In addition to TOSV, the major viral families in the order, namely *Arenaviridae*, *Hantaviridae*, *Nairoviridae*, *Peribunyaviridae*, and *Phenuiviridae*, include important human pathogens associated with life-threatening disease and death.

The *Phenuiviridae* family includes more than 130 isolates, most of which are transmitted to vertebrates by sand flies and ticks, and rarely by mosquitoes. Phenuiviruses can cause a wide range of diseases in humans and animals, from asymptomatic to life-threatening.

Most human pathogenic members belong to the genera *Phlebovirus* and *Bandavirus*, with RVFV, Dabie virus (DABV) and TOSV causing severe disease in humans.

The highly pathogenic RVFV was first discovered in Kenya in 1930 (10) and has spread to several African countries and the Arabian Peninsula (11). RVFV is mainly transmitted by *Aedes* and *Culex* mosquitoes and primarily infects domestic animals such as sheep, goats, and cattle, where it causes high mortality rates in young animals and abortions in pregnant animals (11, 12). Human infections can range from mild symptoms such as fever or headache to life-threatening hemorrhagic fever in about 1-2% of cases. Mortality rates in severe cases ranging from 1% to 47% have been reported for various outbreaks (13). RVFV was one of the twelve pathogens prioritized by the WHO (3).

The tick-borne DABV, or formerly called severe fever with thrombocytopenia syndrome virus (SFTSV) is another human life-threatening phenuivirus. The tick-borne DABV was first reported in China in May 2007 and has since spread and been identified in South Korea, Japan, and Vietnam (14–17). Human infection has a high mortality rate of 6-27% and infections are characterized by fever, thrombocytopenia and leukopenia, but in severe cases can lead to multi-organ failure (18).

1.1.2 The phenuivirus Toscana virus (TOSV)

TOSV is transmitted to vertebrates and humans by sand flies and was first isolated in 1971 from *Phlebotomus perniciosus* and *Phlebotomus perfiliewi* sand flies in the Tuscany region of Italy (19). Most human TOSV infections in endemic areas are asymptomatic or cause mild influenza-like illness. In some cases, the febrile episode is followed by aseptic meningitis or meningoencephalitis with an estimated incubation period of 12 days (20). The disease is usually self-limiting, but in severe cases permanent sequelae or fatal outcomes have been reported (21, 22). Rare manifestations include hydrocephalus, erythema, intravascular coagulation, joint pain, deafness, speech impairment, paresis, testicular manifestations, and neuropathies with Guillain-Barré syndrome-like symptoms (23–31). TOSV has a wide distribution, especially in the Mediterranean, and is endemic from May to October, peaking at the same time as vector activity. During the summer season, the neurotropic TOSV is one of the leading causes of human meningitis and encephalitis in southern Europe (32). Phylogenetic analyses showed that three lineages of TOSV diverged, with different distributions in Mediterranean countries (**Figure 1**). Lineage A was detected in Italy, Cyprus and Algeria, whereas lineage B circulate in Spain, Morocco and Croatia (33). Both lineages co-circulate in France, Portugal, Turkey and Tunisia. To date, lineage C has only been detected at the genetic level in patient samples

from Croatia and Greece, but no virus has been isolated yet (34, 35). Serologic studies and case reports also suggested TOSV circulation in Bosnia-Herzegovina (36), Kosovo (37), Bulgaria (38), Romania (39), Algeria (40), Libya (41) and Djibouti (42). In addition, TOSV has been serologically confirmed in patients from Germany and the Netherlands with meningoencephalitis and no recent history of travel to endemic areas, suggesting that TOSV is more widespread than expected (43, 44). Although no viral genome has been detected to date, phlebotomine sand fly species capable of transmitting TOSV have been found in southern Germany (45, 46).

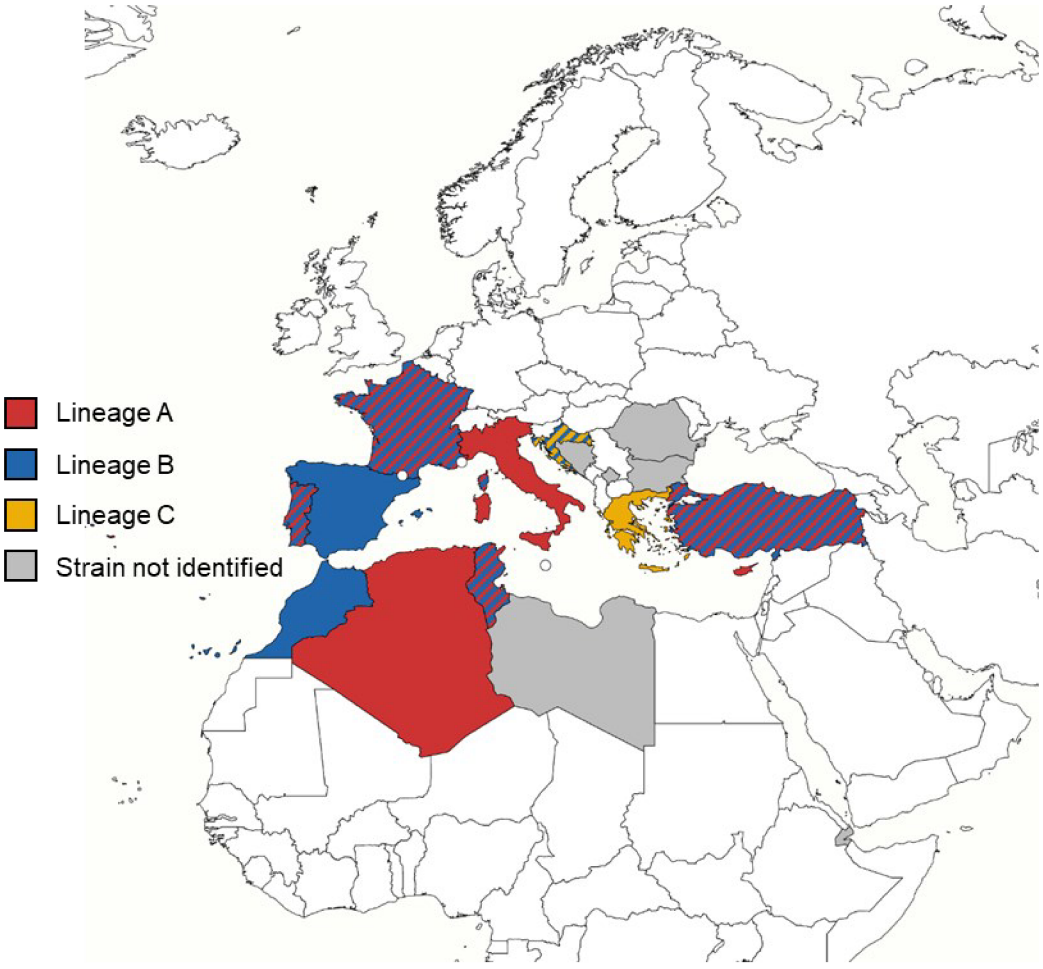

Figure 1. Circulation of TOSV in the Mediterranean countries.

Countries, where the TOSV genome was isolated from clinical samples or sand fly pools, were colored red, blue, or yellow depending on whether the lineages A, B, or C of TOSV, respectively, were identified. When two lineages co-circulate, the countries have been striped with the two colors corresponding to the TOSV lineage. Countries with TOSV seroprevalence but no lineage identified are shown in gray. The map was generated using the online tool mapchart.net.

After its discovery in 1971, TOSV was found in many other species of *Phlebotomus* and *Sergentomyia* sand flies (47–53). Transovarial and venereal transmission has been reported between sand flies (54–56). In addition, the demonstration that infectious TOSV persists in sugar meals for seven days suggests that horizontal transmission should also be considered as a route of TOSV transmission in the vector pool (57). Although TOSV could survive the winter in diapausing sand fly larvae in endemic countries (58), declining infection from generation to generation suggests that the virus cannot be maintained in the vector pool alone (59). To date, no reservoir animal has been defined for TOSV. Because of the short-lived viremia, it is unlikely that humans act as a reservoir for TOSV. Serologic studies have detected TOSV-specific antibodies in dogs, cats, livestock, bats and birds in several endemic countries. Although a high seroprevalence was found in the dog population in Turkey, experimental infection of dogs resulted in low viral loads and no excretion of virus (60, 61). High seroprevalence has also been reported in wild birds in Spain (62), and the TOSV genome has been isolated from wild birds in Turkey (63). The exact role of birds as reservoir hosts of TOSV remains to be investigated.

1.1.3 Biological significance of Coronaviruses

Members of the *Coronaviridae* family cause acute and persistent infections in mammals and birds. Only seven coronaviruses are known to cause human infections, all of which are zoonotic and originate from bats or rodents (5). While four of these viruses are associated with mild respiratory illness, SARS-CoV, MERS-CoV, and SARS-CoV-2 can cause severe disease, including death. Coronaviruses are classified into four genera called *Alpha*-, *Beta*- *Gamma*-, and *Deltacoronavirus*. Coronaviruses relevant to human health belong to *Alpha*- and *Betacoronavirus* genera, while most gamma- and deltacoronaviruses only infect birds (64). The *Betacoronavirus* genus is further divided into five subgenera. MERS-CoV belongs to the subgenus *Merbecovirus*, while SARS-CoV and SARS-CoV-2 belong to the subgenus *Sarbecovirus*.

The last two decades have been marked by the emergence of three human life-threatening betacoronaviruses, SARS-CoV, MERS-CoV, and SARS-CoV-2. It has been speculated that all three viruses originated in bats and were transmitted to humans via intermediate hosts. The first cases of SARS-CoV were reported in China in late 2002, followed by an outbreak in 29 countries with more than 8,000 cases, mostly in Asia and Canada, with a fatality rate of 11% (65). Palm civets have been proposed as the intermediate host for initial transmission to humans (66). The last known cases were reported in 2004. Approximately ten years later, in 2012, MERS-CoV emerged in Saudi

Arabia (67). MERS-CoV is transmitted from dromedary camels to humans. While the disease is asymptomatic in dromedaries, human infections have a fatality rate of 37.5% (68). The largest outbreaks occurred in Saudi Arabia and South Korea, and the virus is still circulating today (69). However, human-to-human transmission is not very efficient (70).

SARS-CoV-2 was first reported in China in December 2019 (71, 72) before causing a pandemic that has spread around the world with more than 680 million confirmed cases and approximately 6.8 million deaths to date. Transmission is mainly by direct contact, air droplets or aerosol (73). SARS-CoV-2 causes flu-like symptoms with fever, sore throat, cough, diarrhea, and breathing difficulties (74). Risk factors such as age, heredity, and pre-existing health conditions can contribute to the development of more severe disease, including pneumonia, lymphopenia, acute respiratory distress syndrome, multi-organ failure, and death (75). In addition, histological analysis of the lungs of deceased COVID-19 patients revealed multinucleated syncytia (76). Many patients also have persistent or recurrent COVID-19 symptoms after the acute phase of infection, also known as long COVID. An overall mortality rate of 0-2.5% was estimated during the first wave of infection, which varied widely between countries (77, 78). Due to the disease burden of SARS-CoV-2, several vaccines have been developed. Approved SARS-CoV-2 vaccines in Europe were based on messenger RNA (mRNA) lipid nanoparticles, nonreplicating adenoviral vectors and protein subunits. Several drugs have been approved for the treatment of SARS-CoV-2 infection. Specific antiviral treatments include inhibitors of viral proteases and RNA-dependent RNA polymerase (RdRp). In addition, monoclonal antibodies against the Spike protein were approved for specific uses during the pandemic. However, due to their significantly reduced efficacy against emerging variants, most of their approvals for treatment have been withdrawn.

1.1.4 History of emergence of SARS-CoV-2

SARS-CoV-2 shares 79.6% and 96.2% sequence identity with SARS-CoV and the bat coronavirus RaTG13, respectively (79). High sequence similarity of the spike receptor binding domain is also shared with pangolin coronaviruses (80). SARS-CoV-2 has a polybasic cleavage site at the S1/S2 junction that is not present in SARS-CoV or RaTG13, a close relative of bat SARS-CoV-2, but is found in other betacoronaviruses (69). The presence of this unexpected furin site has led to speculation about the natural origin of SARS-CoV-2. However, the high similarity to pangolin coronaviruses suggests a natural origin by zoonotic spillover. It has also been suggested that SARS-CoV-2 may be the

result of a recombination event between pangolin and bat coronaviruses (81). Traces of the first SARS-CoV-2 cases were linked to an animal market in Wuhan, China (82). Since no bats or pangolins were for sale, the first transmissions to humans likely occurred via an intermediate host animal (83, 84). From there, SARS-CoV-2 spread throughout the world, causing the COVID-19 pandemic in recent years.

During the pandemic, SARS-CoV-2 has evolved through various mutations, resulting in new variants of interest and variants of concern (VOCs). These VOCs were associated with increased rates of transmissibility, virulence, changes in symptoms, decreased effectiveness of public health measures or available diagnostics, vaccines and therapeutics (85). In Europe, further waves of infection have been caused primarily by the Alpha, Delta, and Omicron variants. Alpha was first documented in the United Kingdom in September 2020 and was dominant in Europe by early 2021. The Delta variant was first reported in India in October 2020 and caused another wave of infection in the fall of 2021 in Europe before being rapidly replaced by the Omicron variant. Omicron first appeared in South Africa in November 2021 and quickly spread around the world to become the predominant circulating variant by early 2022.

The following chapters first address general principles in the cell biology of virus entry, essential to understanding the specificities of the infectious entry process of bunyaviruses and coronaviruses, notably TOSV and SARS-CoV-2.

1.2 Cell biology of virus entry

1.2.1 Virus binding

As for all other viruses, the first step in the entry process of zoonotic viruses is the binding of viral particles to cell-surface receptors. This plays an important role in the host range and tissue tropism of pathogens. Some receptors can mediate viral entry without the help of additional factors. Alternatively, primary receptors often only limit particle movement or promote interaction with secondary receptors that then coordinate viral uptake. Such primary and secondary receptors are often referred to as attachment factors and co-receptors, respectively. Initial attachment often occurs by nonspecific binding to small

charged molecules through electrostatic interactions. These can include carbohydrates on glycoproteins or glycolipids, which are highly polar structures found on the surface of most mammalian cells (86). After binding to these primary receptors, viruses must interact with a specific receptor that either mediates the penetration of viral particles at the plasma membrane or leads to the internalization and sorting of virions into endosomes (**Figure 2**). In this second scenario, the viral particles traffic along the endocytic machinery until they reach the appropriate intracellular compartments to penetrate and reach the cytosol.

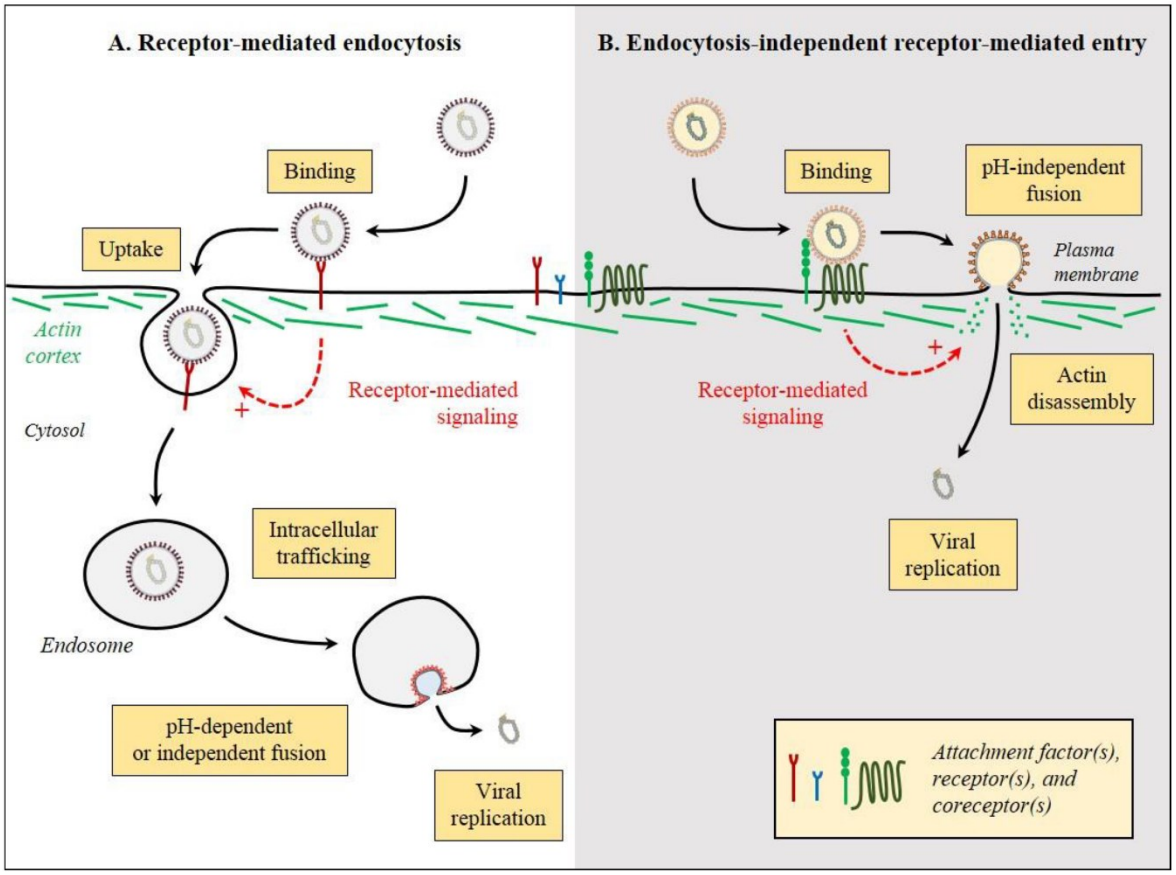

Figure 2. Strategies of viral entry.

In general, viruses can use two strategies to gain access to the cytoplasm, *i.e.*, either by endocytic internalization and then penetration from endosomal compartments in a process known as receptor-mediated endocytosis (A) or by direct penetration from the plasma membrane (B). Each step of the viral entry process is depicted. Although enveloped viruses are shown, non-enveloped viruses have developed similar strategies. Figure adapted from (86).

In this respect, non-enveloped viruses have developed specific mechanisms to open pores in target cell membranes, which are not reviewed here but discussed in detail elsewhere (87). Enveloped viruses, on the other hand, ensure their penetration into the cytosol by the fusion of their envelope with a cellular membrane. This ultimate step in the

virus entry program is essential for the release of their genome into the cytosol, a prerequisite for viral replication and amplification. Virus entry and fusion are evidently interesting targets to develop approaches aiming to inhibit and prevent infections by incoming viruses.

1.2.2 Exploitation of the endocytic machinery by viruses

After binding to specific receptors, most viruses are internalized into cells by receptor-mediated endocytosis. The uptake of viral particles can be either active, *i.e.*, binding to a receptor triggers internalization of the viral particles, or stochastic. Particle uptake occurs via several different pathways, which differ in their adaptor and coat proteins and in the size of the intracellular vacuoles. The best studied examples are clathrin-mediated endocytosis, caveolar and lipid raft-dependent endocytosis, and macropinocytosis (**Figure 3**). These pathways have in common that most of their cargo is delivered to the endosomal machinery as endocytic vesicles.

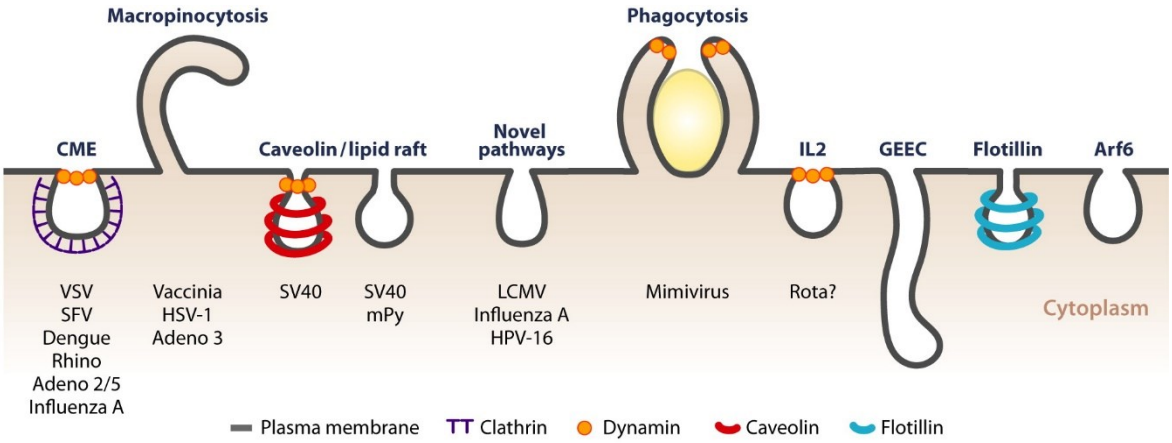

Figure 3. Endocytic uptake pathways used by viruses.
Viral particles can enter cells via different endocytic routes. The figure was adapted from (88). Adeno 2/5, adenovirus 2/5; Adeno 3, adenovirus 3; CME, clathrin-mediated endocytosis; HPV-16, human papillomavirus 16; HSV-1, herpes simplex virus 1; LCMV, lymphocytic choriomeningitis virus; mPy, mouse polyomavirus; SFV, Semliki Forest virus; SV40, simian virus 40; VSV, vesicular stomatitis virus.

In a simplified model, endosomes form a complex network of heterogeneous organelles that undergo continuous maturation, transformation, fusion, and fission (89). Roughly, the endocytic system can be divided into recycling and degradation pathways. In the recycling pathway, endocytosed plasma membrane components and ligands are returned to the

plasma membrane. In the degradation pathway, macromolecules are transported to lysosomes via late endosomes (LEs) and degraded. The degradative system is linked to an exchange pathway between the trans-Golgi network (TGN) and endosomes, which ensures the supply of new components to lysosomes and the recycling of sorting receptors from lysosomes back to the TGN. After endocytic uptake, cargos, as viral particles, enter early endosomes (EEs) and are sorted for either recycling or degradation. In general, most cargo is sorted for recycling and only a small fraction of mostly membrane components is transported to lysosomes.

EEs have heterogeneous structures with tubular and vacuolar domains. Cargo to be recycled is mostly concentrated in the tubular regions of EEs, whereas cargo destined for degradation is mostly found in the vesicular subdomains (89) (Figure 4). Due to their size, most viruses are too large for the tubular domains of EEs and are therefore localized in the vacuolar domains. One of the key players in lysosomal sorting is the endosomal sorting complex required for transport (ESCRT), which recognizes ubiquitinated cargo (90). Ubiquitination then serves as a signal for inward vesiculation of the limiting endosomal membrane, resulting in intraluminal vesicles (ILVs). These vacuolar subdomains with ILVs subsequently detach from the EEs to become multivesicular bodies that further mature into LEs. This complete maturation process from EEs to LEs is accompanied by many changes, including a decrease in pH, switch of Rab proteins, conversion of phosphoinositide (PI) species, switch of fusion partners, acquisition of lysosomal components, switch of motor proteins, movement to the perinuclear region, temperature sensitivity, and a change in morphology (89).

Rab proteins are small monomeric GTPases that exist in inactive GDP-bound and active GTP-bound states. By switching between these two states, Rab GTPases can recruit other proteins and regulate many functions of different organelles that shape organelle identity. Here, I will focus on the most important ones in the EE and LE maturation, which are Rab5 and Rab7. However, more than 60 *Rab* genes have been identified in humans and are reviewed in (91). For example, Rab5 determines the functions of EEs, whereas Rab7 has a corresponding role in LEs and lysosomes. Thus, Rab5 is converted to Rab7 during endosome maturation. It is thought that Rab5 recruits Rab7, resulting in a hybrid intermediate organelle with both markers (92). This in turn leads to Rab5 GTP hydrolysis and dissociation of Rab5. This Rab switch is also accompanied by changes in the tethering and fusion machinery. While EEs can undergo homotypic fusion with other EEs, Rab7-positive LEs lose the ability to fuse with EEs and can now fuse with each other and transiently or stably with lysosomes, resulting in endolysosomes (89). The Rab switch is

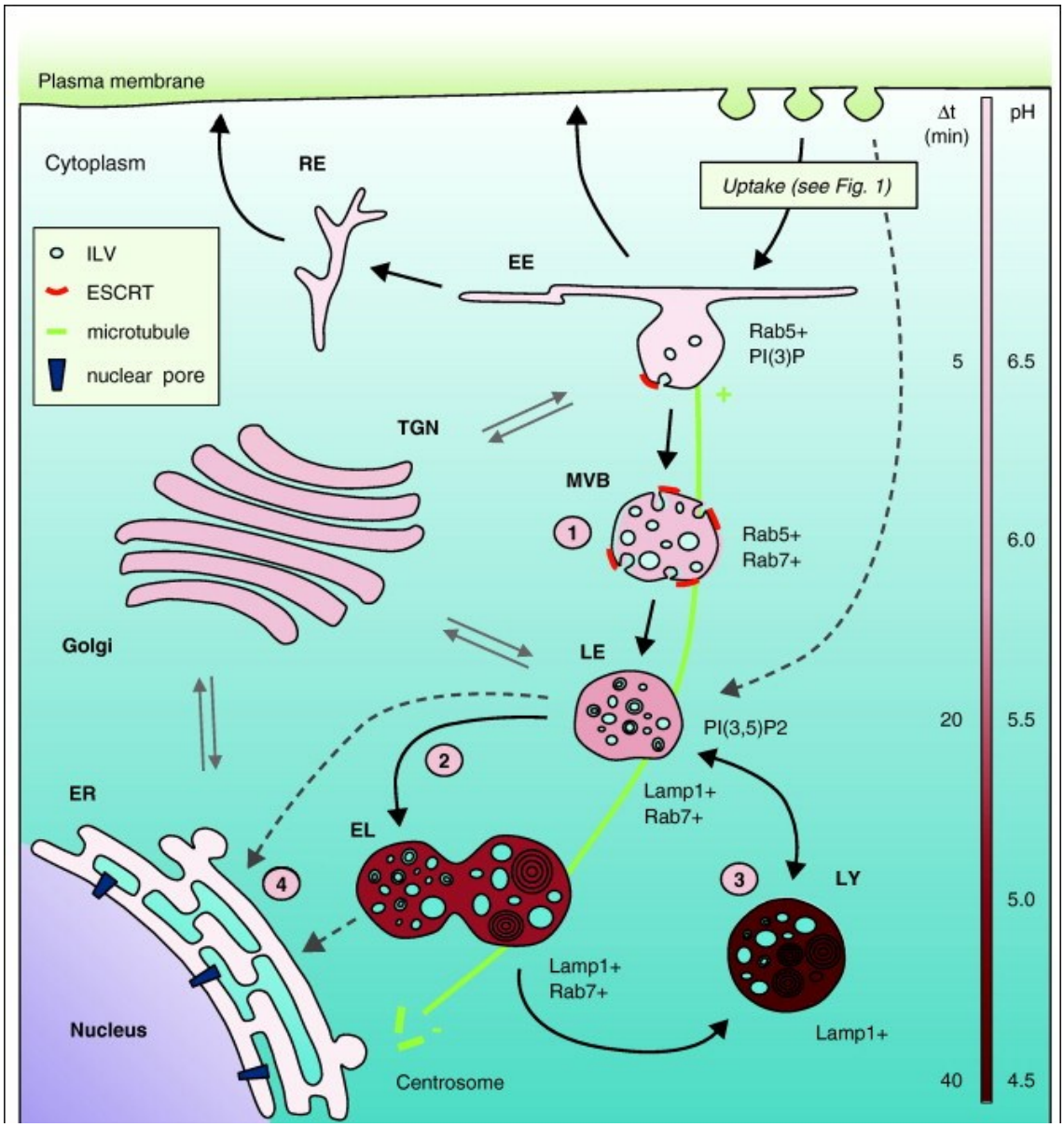

Figure 4. Intracellular trafficking of endocytosed viruses.

After uptake, viral particles are sorted into primary endocytic vesicles, which are mostly early endosomes (EEs). EEs then mature into MVBs and late endosomes, and ultimately, into endolysosomes. Diverse cues along the endocytic pathways can trigger the fusion of enveloped viruses with endosomal membranes or the opening of holes in cell membranes when viruses are not enveloped, resulting in the release of the viral genome into the cytosol. The scale on the right indicates the time required for a cargo to travel from the plasma membrane to the respective organelles and the pH within these organelles. The figure was modified from (93). EE, early endosome; EL, endolysosome; ER, endoplasmic reticulum; ESCRT, endosomal sorting complex required for transport; ILV, intraluminal vesicle; Lamp1, lysosomal-associated membrane protein 1; LE, late endosome; LY, lysosome; MVB, multivesicular body; PI(3)P, phosphatidylinositol 3-phosphate; PI(3,5)P2, phosphatidylinositol 3,5-biphosphate; Rab, Ras-associated binding; RE, recycling endosome; TGN, trans-Golgi network.

also tightly linked to the alteration of phosphoinositide (PI) lipid species through the recruitment of PI kinases such as PI 3-kinase and PIKfyve. As a result, PI 3-phosphate (PI3P) and PI 3,5-bisphosphate ($PI(3,5)P_2$) are formed on the cytosolic surface of EEs and LEs, respectively. These PI species then contribute to the identity of EEs and LEs by recruiting other proteins with corresponding PI-binding domains.

Along the endosomal pathway, the intraluminal pH continuously decreases from about pH 6.8-6.0 in EEs to 6.0-5.0 in LEs and down to pH 4.5 in lysosomes (94). This acidification is mediated by vacuolar-type ATPases (vATPases) and plays an important role in trafficking, sorting, and regulating the activity of lysosomal hydrolases. In addition to this pH gradient, the concentration of other ions fluctuates along the endosomal pathway. While Na^+ concentrations decrease along the endocytic pathway, K^+ concentrations increase (95). Ca^{2+} and Cl^- are both extruded into EEs, resulting in lower concentrations in EEs compared to the extracellular milieu. However, their concentrations appear to increase during maturation to LEs and progression to lysosomes (95, 96).

Maturation of EEs and LEs is also accompanied by a change in morphology. EEs are heterogeneous in shape and size and have tubular and vacuolar domains. A few ILVs with a diameter of 50-100 nm can be observed in the vacuolar domains (Figure 5) (89). In contrast, mature LEs typically have a round shape with a diameter of 250-1000 nm and many ILVs, but may also contain lamellar regions (89, 97).

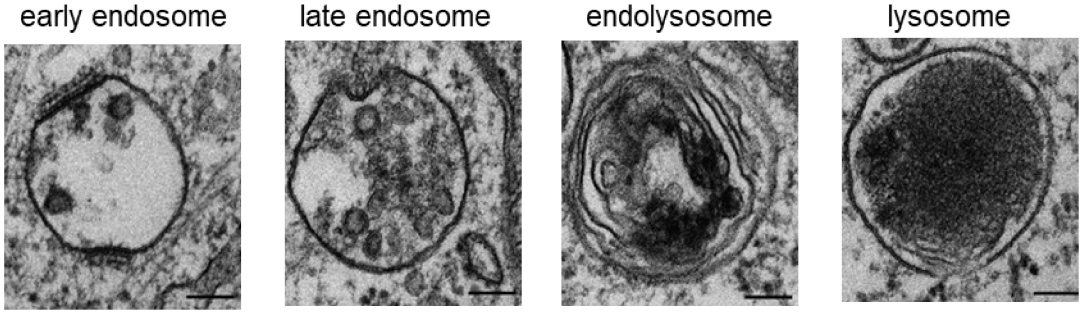

Figure 5. Morphology of endosomal vesicles during their maturation process.
Images are all from HeLa cells processed for thin-section electron microscopy. Few intraluminal vesicles are seen in early endosomes, which increase in number as they mature into late endosomes. Of note, the electron density of the lumen and the size of endosomal vesicles both increase during the maturation from early endosomes to lysosomes. Scale bar, 100 nm. Figure modified from (89).

The LE maturation is a highly dynamic process which involves the subcellular relocation of maturing endosomal vesicles. EEs are typically found in the periphery of cells, where they

undergo slow, short-range back-and-forth movements (89). In contrast, LEs undergo rapid long-range oscillatory movements with a net movement toward the nucleus. This change in motility is associated with a new set of microtubule-dependent motor proteins that allow movement toward perinuclear regions. Disruption of microtubules (MT) by nocodazole causes a dispersion of LEs and lysosomes throughout the cytosol, impairing endocytic trafficking to lysosomes in certain cell types (98). While initial acidification to about pH 6.0 can still occur, cargo transport to more acidic compartments is blocked (98, 99). Furthermore, EE formation is optimal at 37 °C in mammalian cells, although this process and the subsequent recycling is still active at 16°C. The maturation of LEs and their fusion with lysosomes are more sensitive to temperature and are completely blocked at temperatures below 20°C (100–102). Many of these steps in the LE maturation program are tightly linked and interdependent. Thus, perturbation of one step often results in a delay or inhibition of the entire LE maturation process.

Viruses hijack the endocytic machinery and use environmental cues to activate their fusion with a cellular membrane and gain access to the cytosol. Such triggers include various changes that occur along the endosomal pathway and may include acidic pH, changes in other ion concentrations, the presence of specific lipids, interactions with intracellular receptors, or proteolytic cleavage among others (more details on activating triggers are provided in section 1.2.3). Viruses entering cells by endocytosis can be classified as early- or late-penetrating viruses depending on the location in the endocytic pathway where fusion occurs. Early-penetrating viruses (E-PVs) penetrate from EEs, whereas late-penetrating viruses (L-PVs) are sorted to the degradative branch of the endocytic pathway. Some viruses like polyoma- and papillomaviruses, go even further since they have to reach the endoplasmic reticulum (ER) to penetrate the cytosol through interconnections between LEs and TGN. Whether fusion occurs from EEs or requires transport to downstream organelles can be estimated, at least in part, from the virus fusion threshold and the kinetics of viral penetration. E-PVs, such as Semliki Forest (SFV) or Vesicular stomatitis virus (VSV), typically require a pH of 6.3-6.1 and penetrate within 3-8 min after internalization (103, 104). In contrast, L-PVs often require a pH below 6, and penetration occurs in general 10-20 min after internalization but can also take several hours (93).

1.2.3 Virus Fusion

1.2.3.1 Fusion mechanisms of viruses

The virus fusion process is mediated by envelope fusion proteins that are anchored in the viral envelope and decorate the surface of virions. Three classes of fusion proteins have thus far been reported that share similarities with several cellular fusion proteins indicating that viral and cellular fusion proteins co-evolved. The different classes of viral fusion proteins share general mechanisms to mediate the fusion of the viral envelope with target cell membranes. The classes significantly differ, not only in their organization on the viral surface and their structure, but also in their biogenesis, priming, and cues of activation.

Each fusion protein contains a transmembrane (TM) anchor and a fusion unit, which can be either a peptide at the extremity of the protein or a small inner loop (Figure 6), that is inserted into a target membrane during the fusion process. Viral fusion proteins undergo a series of conformational changes from a pre-fusion to a post-fusion conformation to mediate fusion between the viral and cellular target membrane. However, viral fusion proteins can only act once (105). Therefore, their action must be tightly controlled in space and time to ensure that viral fusion proteins mediate fusion in a suitable environment for productive infection. Typically, two events lead to the transition from pre- to post-fusion conformation (105). The first event, called priming, converts the viral fusion protein to a fusion-competent state and is often a proteolytic cleavage. A second event, called activation or triggering, results in conformational changes in the fusion proteins upon induction by the binding of the fusion protein to cellular ligands, its exposure to signals such as the endosomal acidity, or its proteolytic cleavage in target cells. Activation of the fusion protein results in exposure and repositioning of the fusion unit toward the target membrane. Prior to activation, the fusion unit is usually buried within the structure or shielded and therefore inaccessible (106). Upon activation, the hydrophobic fusion unit is inserted into the lipid bilayer of a target membrane, causing small distortions and bending of the target membrane. Refolding of the viral fusion protein causes membrane apposition, hemi-fusion, *i.e.*, fusion of the two outer leaflets of each lipid bilayer, and ultimately fusion pore formation (Figure 7).

Fusion pore formation and pore expansion require multiple fusion proteins to act in concert. During this process, the viral fusion proteins adopt different conformations and undergo multiple conformational changes. After insertion of the fusion peptide/loop, an extended intermediate conformation, the so-called pre-hairpin, is formed, bridging the viral

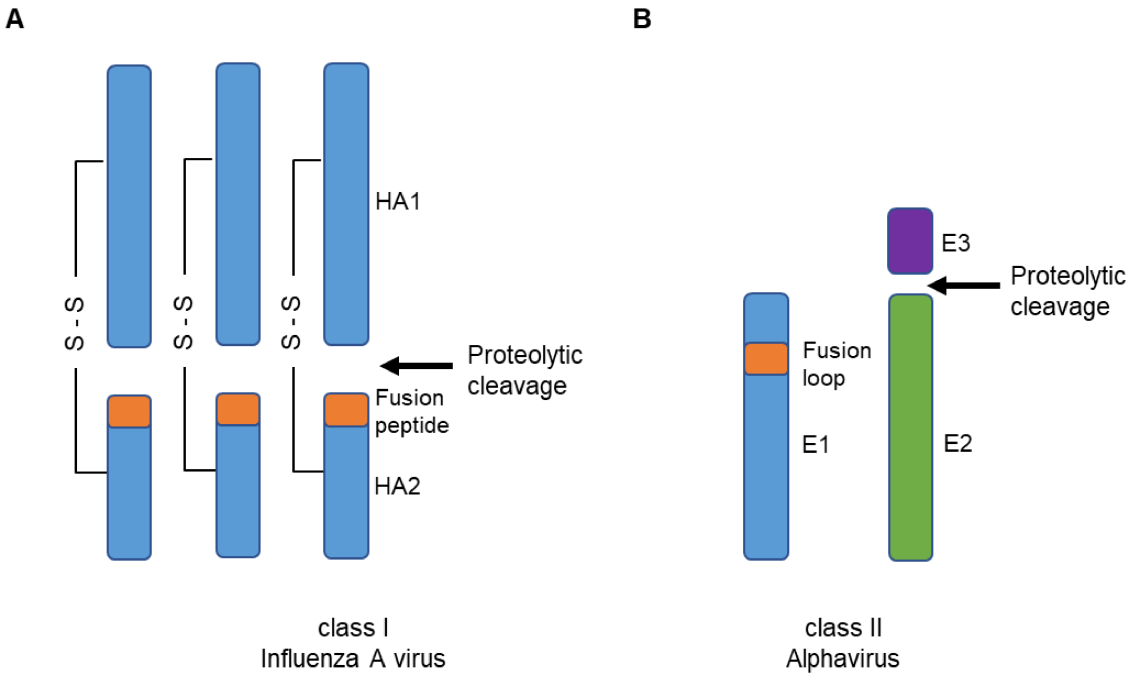

Figure 6. Processing and general organization of viral fusion proteins.
(A) Class-I fusion proteins are typically cleaved by proteases into an N-terminal subunit, often carrying the receptor-binding domain, and a C-terminal subunit with the fusion peptide (shown in orange) at or near the N-terminus. The two subunits can be covalently or noncovalently linked and usually form homotrimers on the viral surface. The hemagglutinin (HA) protein of influenza A virus is shown as an example of class-I viral fusion protein. (B) Class-II fusion proteins are expressed as polyproteins and are in general cleaved by proteases in the endoplasmic reticulum or Golgi, as exemplified by the envelope proteins E1, E2, and E3 of Semliki forest virus, a member of the *Alphavirus* genus in the *Togaviridae* family. This class of viral fusion proteins generally forms heterodimers with their accompanying protein (here E2/E3). E1 carries an internal fusion loop (shown in orange) and forms a dimer with its accompanying protein E2. In some alphaviruses, E3 dissociates from the E1-E2 heterodimer after particle release.

membrane via its TM domain and the target cell membrane via insertion of the fusion peptide/loop. Collapse and refolding of the bridging intermediate pulls the fusion peptide/loop and the transmembrane anchor closer together, ultimately bringing the envelope of the virus to the cell membrane. All viral fusion proteins form homotrimers in their stable post-fusion conformation and are therefore referred to as hairpin trimers. During membrane approach, a kinetic barrier must be overcome due to the repulsive forces of the hydration barrier, a layer of water associated with polar head groups of lipids. The energy to overcome this barrier comes from the irreversible refolding of metastable pre-fusion proteins of relatively high energy into energetically favored stable post-fusion conformations.

The viral segments inserted into a target cell membrane are called fusion peptides when they are at the N-terminus of the fusion protein, or fusion loops when they are internal. Most class-I fusion proteins contain a fusion peptide, while most class-II and -III fusion proteins contain a fusion loop. These fusion segments are usually highly enriched in alanine, glycine, proline, and aromatic residues (107). Alanine and glycine contribute to flexibility, proline and glycine to helix destabilization, and aromatic residues such as tryptophan or phenylalanine with their bulky side chains anchor the fusion segment in the membrane.

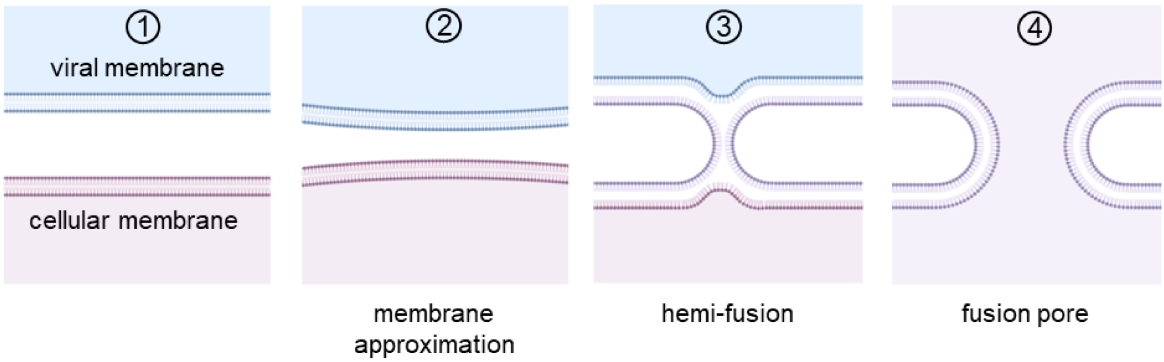

Figure 7. Fusion process of enveloped viruses.
Schematic representation of the viral fusion mechanism between a viral envelope and a cellular membrane. The viral and cellular bilayers are in apposition (1). Upon fusion initiation, the fusion peptide/loop of the viral fusion protein is inserted into the target cellular membrane. The two membranes are pulled closer together, resulting in membrane approximation (2) and lipid mixing between the outer layers (3), also known as hemi-fusion. Finally, the inner lipid layer also fuses through the action of multiple fusion proteins, forming a fusion pore (4). The figure was created with BioRender.

1.2.3.2 Classes of viral fusion proteins

Class I

A well-studied example of class-I viral fusion proteins is the influenza virus HA protein. In general, this class includes fusion proteins from retro-, orthomyxo-, paramyxo-, filo-, arena- and coronaviruses. Class-I fusion proteins are initially synthesized as inactive precursors that are cleaved by cellular proteases. This proteolytic cleavage results in an N-terminal fragment, often containing the receptor-binding domain, and a C-terminal fragment containing the hydrophobic fusion peptide at or near the N-terminus and a TM domain near the C-terminus (105). This initial cleavage primes the viral fusion protein, which is then metastable. The cleaved N- and C-terminal fragments remain associated and are mostly linked by disulfide bonds or noncovalent interactions (106). The

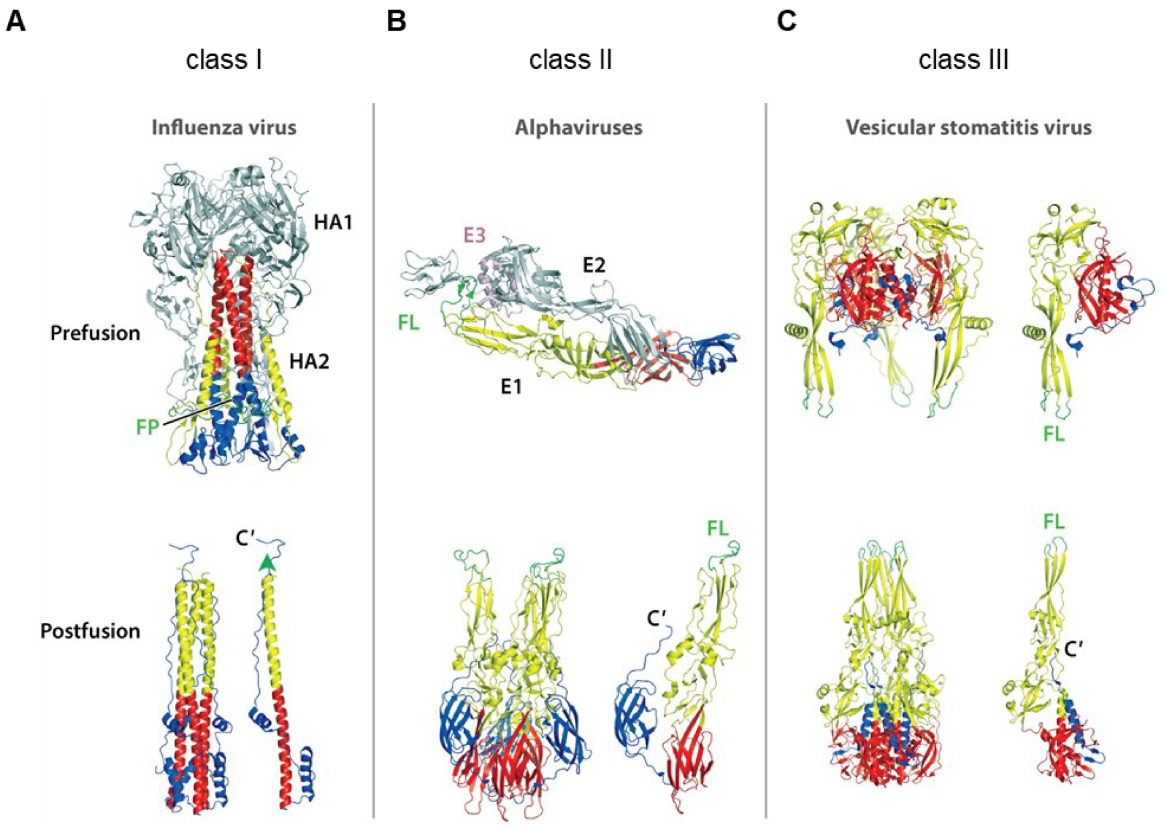

Figure 8. Typical structures of the three classes of viral membrane fusion proteins in their pre- and post-fusion conformations.

The domains of each fusion protein are color-coded, with the fusion peptide (FP)/fusion loop (FL) shown in green. Domains marked in yellow and red form the core trimers and blue indicates outer layers and structures that undergo large movements during the transition from pre- to post-fusion conformation. In the lower images, the post-fusion conformations are shown as a trimer on the left and as a single protomer of the trimer on the right. The C-termini attached to the transmembrane domains are indicated by C'. (A) Influenza virus HA protein as an example of a class-I fusion protein. HA1, shown in gray, and HA2 are shown in the pre-fusion trimer form, and HA2 alone is shown in the post-fusion form. The fusion peptide in the post-fusion structure is indicated by a green arrowhead. (B) Alphaviral E1, a class-II fusion protein, is shown in association with E2 and E3 (shown in gray and pink) in its pre-fusion conformation. The structure of trimeric E1 in its post-fusion form is shown in the lower image. (C) The rhabdoviral vesicular stomatitis virus G protein is shown as an example of a class-III viral fusion protein. The pre-fusion and post-fusion trimers are shown with a single chain shown on the right. Figure modified from (108).

structure of a class-I fusion protein is illustrated by the influenza HA protein in Figure 8A. The fusion protein HA2 is a trimer of largely α-helical structures with the fusion peptide buried within the trimer interface. Upon acidification, HA1 moves away from HA2 and the fusion peptide is released. Fusion occurs through a trimeric extended intermediate with fusion peptides inserted into the target membrane. The N-terminal fusion peptide and the

C-terminal TM anchor are both located at one end of the trimer. During folding, the C-terminal heptad repeats bind into the grooves of the N-terminal heptad repeats, bringing the membrane insertion site and the TM anchor closer together, *i.e.*, the cell membrane and viral envelope. The post-fusion conformation is a six-helix bundle with a trimer of hairpins forming a central coiled-coil structure (106).

Class II

The best studied examples of class-II viral fusion proteins are the alphaviral E1 and flaviviral E proteins. In general, the fusion proteins of toga-, flavi- and most bunyaviruses share a class-II fusion protein fold. In contrast to class-I fusion proteins, class-II fusion proteins are not assembled as trimers in their pre-fusion conformation, but rather build multimeric assemblies on the viral surface. They usually form heterodimers or heterotetramers with an accompanying protein. The accompanying protein acts as a chaperone, protecting the fusion protein and preventing premature fusion during egress along the secretory pathway of producer cells. In addition, accompanying proteins have been shown to be involved in receptor binding (109). In general, the fusion/accompanying protein complexes are arranged in an icosahedral symmetric lattice on the surface of mature virions.

Class-II fusion proteins are all synthesized as polyproteins with their accompanying proteins, which are cleaved in the ER by signal proteases. A second proteolytic cleavage occurs in the accompanying protein of alpha- and flaviviruses. This cleavage is mostly mediated by furin in TGN and is considered a priming event for fusion (110, 111). Interestingly, the accompanying proteins of bunya- and rubellavirus are not proteolytically processed (112). Protection from low pH along the secretory pathway and priming appears to use a distinct yet unknown mechanism from alpha- and flaviviruses.

The structure of the class-II fusion protein is largely composed of β-strands and β-sheets (Figure 8B). The three-domain architecture consists of a central β-sandwich (domain I) connected by a flexible hinge to two long loops with the hydrophobic fusion loop at its tip (domain II) and an immunoglobulin (Ig)-like fold as domain III. Domain III is attached to the TM anchor by a stem segment. In general, the structures of the accompanying proteins are less conserved, but also seem to derive from a common ancestor (109). Class-II fusion proteins are triggered by exposure to low pH. A schematic of the membrane fusion mechanism of alphaviruses is shown in Figure 9. Low pH induces movement and dissociation of the accompanying proteins E2 from the fusion protein E1. This results in the unshielding of the fusion loop, and its insertion into the target cell membrane. Insertion occurs as monomeric E1, which then reversibly associates with other E1 monomers to

form core trimers. Folding of the protein is promoted by interactions of conserved histidines resulting in a trimeric hairpin (113).

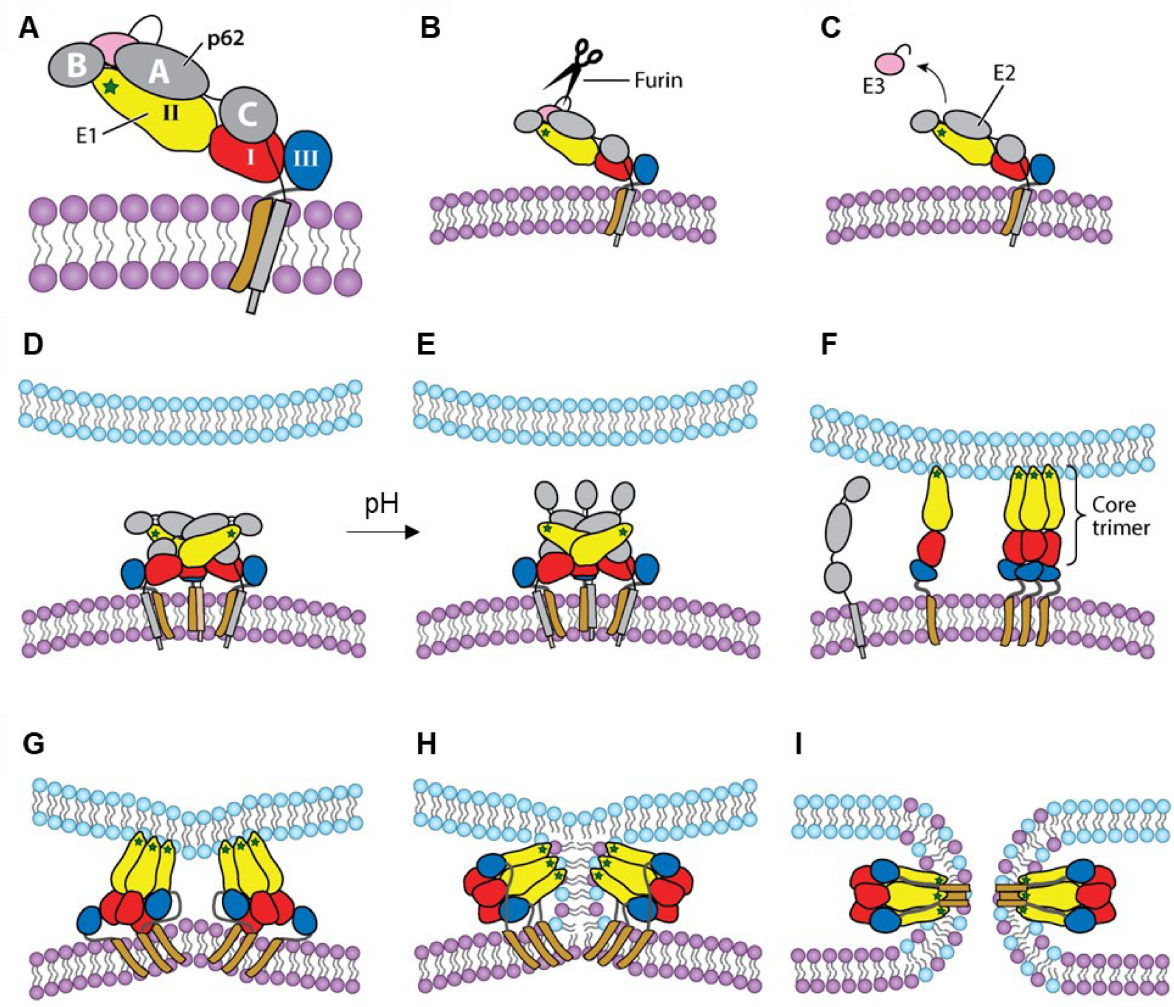

Figure 9. Schematic representation of alphavirus membrane fusion.

(A) E1 heterodimerizes with the immature viral polyprotein p62 (shown in gray and pink). The fusion loop is indicated by a green star. (B) p62 is processed by furin to E2 (gray) and E3 (pink). E3 remains associated by transport along the secretory pathway and is released at neutral extracellular pH for most alphaviruses (C). (D) Mature E2-E1 heterodimers are present on the viral surface. The viral envelope is shown in purple and the target cell membrane is shown in blue. (E) Upon acidification, E2 rearranges and the fusion loop of E1 is exposed. (F) Low pH triggers further conformational changes leading to the insertion of the fusion loop into the target cell membrane and followed by the dissociation of E1 and E2 and the trimerization of E1. (G) Upon refolding, the membranes are distorted and bent. Hemi-fusion (H) and fusion pore formation (I) follow. Figure modified from (108).

Class III

The third class of viral fusion proteins includes the G protein of rhabdoviruses, the gB protein of herpesviruses, and the gp64 protein of baculoviruses. Class-III fusion proteins

combine some features of both class-I and class-II. They contain both α-helical and β-structures and have two fusion loops in domain I with two long β-hairpins oriented around a central β-sandwich core module (domain IV) with other domains protruding from domain IV. The VSV G protein in its pre-fusion and post-fusion conformations is shown in Figure 8C. In contrast to class-I and -II fusion proteins, the fusion loops are not buried, but point down towards the viral membrane in the pre-fusion conformation. Upon triggering, dramatic rearrangements occur, resulting in a trimeric hairpin in the post-fusion conformation, as also observed in class-I and -II fusion proteins.

Class-III fusion proteins are usually displayed as trimers in both their pre- and post-fusion conformations. VSV G is an exception, consisting of monomers and trimers in its pre-fusion form, which are in equilibrium on the viral surface at neutral pH (114). This equilibrium then shifts to trimers at pH <6.5. For herpesviruses, gB-mediated fusion is more complex. Fusion activation by gB requires additional heterodimers of gH and gL and receptor or co-receptor binding by a fourth protein (115). Interestingly, there is no obvious priming event and most of the conformational changes are reversible in the absence of a target membrane, as is the case with the rhabdoviral G protein (116).

1.2.3.3 Triggers of viral fusion

General triggers

In general, there are four main triggers of fusion: exposure to low pH, interaction with receptors, binding to a receptor followed by exposure to low pH, and binding to a receptor followed by proteolytic cleavage. In most cases, the pH dependence of viruses correlates with their fusion site. Viruses that do not rely on proton binding to initiate fusion often fuse directly at the plasma membrane. Viruses that require acidification enter cells by endocytosis and mostly fuse from compartments of the endocytic machinery. In general, fusion occurs where all necessary and supportive environmental cues are present, *i.e.*, pH, receptors, ions, lipid composition, proteases, or other factors.

Exposure to low pH

Class-II viral fusion proteins, found in members of alpha-, flavi-, bunya-, and rhabdoviruses, are triggered by exposure to low pH, which is sufficient by itself for viral fusion. However, some class-I and class-III fusion proteins also undergo acid-activated membrane fusion. The underlying molecular mechanisms involve the protonation of amino acid residues, mostly histidines, at strategic sites in the protein. The pKa of solvent-exposed histidines is about 6.2, a pH that occurs during trafficking along the endosomal

pathway, whereas it depends on the immediate environment when histidines are unexposed (117). Protonation changes the net charge of the imidazole ring of the histidine to +1, allowing electrostatic interactions with other charged residues. These switch histidines play an important role in the conformational changes that occur during refolding. Many pH-sensitive fusion proteins have conserved histidines, and mutation of these histidines abolishes fusion activity (118–120). Similarly, the side chains of aspartic or glutamic acid have pKa values close to neutral pH and may be involved in triggering the transition from pre- to post-fusion in endosomes, as previously shown for the VSV G protein (121).

Triggering upon receptor binding

Most retroviruses and herpesviruses have been shown to be activated solely by binding to a receptor, albeit by different mechanisms. When murine leukemia virus (MLV) binds to its receptor, a disulfide bond between the receptor-binding domain and the fusion subunit is broken and they dissociate. The released fusion subunit can then exert its action (122). For the lentivirus HIV-1, fusion is also triggered by receptor binding. Binding of its envelope protein gp120 to its receptor CD4 exposes a binding site for co-receptors. Binding to co-receptors CXCR4 or CCR5 then triggers fusion (123). In the case of herpes- and paramyxoviruses, receptor binding and fusion are carried out by different proteins on the viral surface. Binding to a receptor induces conformational changes in the receptor-binding protein, which is then translocated directly or via other proteins to the fusion protein (115, 124).

Triggering by receptor binding followed by exposure to low pH

Certain viruses require both receptor binding and exposure to low pH. One example is avian sarcoma leukosis virus (ASLV). Upon binding at neutral pH, conformational changes are induced in the fusion subunit that result in insertion of the fusion loop into the target membrane. Refolding of the pre-hairpin into a six-helix bundle also requires low pH (106). Other viruses use an intracellular receptor located in endosomal compartments, as in the case of Lassa virus. The Lassa virus GP protein requires both binding to LAMP1 in endolysosomes and a low pH of 5 to enter host cells (125).

Triggering by receptor binding followed by proteolytic cleavage

Some retroviruses, coronaviruses, and paramyxoviruses use this strategy to enter host cells. For the coronavirus SARS-CoV, the viral spike protein is cleaved by cellular proteases in a pH-dependent or -independent manner after binding to its receptor ACE2 (discussed in more detail in section 1.4.2).

More complex triggering mechanisms

Other viruses, such as Ebolavirus, use even more complex mechanisms involving cleavage of the GP protein first by furin in producer cells and by low pH-dependent cathepsin proteases in target cells. These cleavages then expose a receptor binding site for the late endosomal/lysosomal protein Niemann-Pick C1, leading to low pH and calcium ion-dependent fusion mediated by GP2 (126, 127).

Other environmental factors involved in fusion

Lipids: Some viruses have been shown to require a specific lipid composition for fusion. SFV has a preference for membranes containing cholesterol and sphingomyelin (128, 129). Similarly, hantaviruses require high levels of cholesterol for fusion (130). Other viruses such as flaviviruses, the rhabdovirus VSV or the bunyavirus Uukuniemi (UUKV) have been shown to prefer fusion with membranes enriched in anionic lipids such as bis(monoacylglycerol)phosphate (BMP) (131–134). Interestingly, BMP is enriched in LEs and could be an additional environmental cue for preferential late endosomal entry of certain flaviviruses or bunyaviruses.

Ion concentrations: In addition to specific lipids, concentrations of specific ions may also play an important role during fusion. During endosomal trafficking, the concentration of luminal K^+ increases while that of Na^+ decreases. For some orthobunyaviruses, K^+ has been shown to be required for conformational changes during fusion or to promote infectivity (135). In addition to low pH, Ca^{2+} has been proposed to be required for rubella virus fusion. Ca^{2+} are thought to bind to a metal ion pocket in E1 protein, resulting in proper positioning of the two fusion loops (136).

1.3 Genome and structural organization of TOSV and SARS-CoV-2 particles

1.3.1 TOSV particles

As other vertebrate-infecting phenuiviruses, TOSV particles are enveloped, spherical with a diameter of 80-160 nm and have spike-like projections of 5-10 nm (**Figure 10A**) (137). Phenuiviruses have a trisegmented single-stranded RNA genome with a negative or ambisense coding strategy that encodes at least four proteins (**Figure 10B**). The large (L) segment encodes RdRp with endonuclease activity, which is required for replication and

transcription of the viral genome. The medium (M) segment encodes a polyprotein precursor that is cleaved by host cell signal peptidases into the two envelope glycoproteins, Gn and Gc. The M segment of some phenuiviruses also encodes a nonstructural protein NSm. Gn and Gc are located on the viral surface, form spike-like projections, and are involved in host cell entry and particle budding (64). They are also the major target of neutralizing antibodies, making them the primary target for vaccine development. The small (S) segment has an ambisense coding strategy and encodes the nucleoprotein N in negative polarity, which encapsulates the RNA genome and forms ribonucleoprotein (RNP) complexes with the RdRp. Most phenuiviruses additionally encode a nonstructural protein (NSs) in positive polarity on the S segment. NSs is thought to be the major virulence factor of phenuiviruses and is involved in the inhibition of the host interferon antiviral response (138). The total genome of the prototype phenuivirus RVFV consists of ~11,800 nt, with the L, M, and S segments contributing ~6,300, ~3,900, and ~1,600 nt, respectively (139). Each segment contains 3' and 5' noncoding regions with complementary end sequences that allow the formation of a stable panhandle secondary structure capable of interacting with RdRp.

Most structural information on phenuiviral particles has been obtained from studies of RVFV, UUKV, DABV, and Heartland virus (HRTV). The two envelope glycoproteins Gn and Gc form heterodimers on the viral surface and are arranged as dimers in 12 pentons and 110 hexons, forming an icosahedral lattice with a triangulation number of T = 12 (**Figure 10C**) (140, 141). The first structure of phenuivirus Gc came from X-ray crystallography of RVFV Gc in the pre-fusion conformation, which showed that Gc has a class-II fusion protein fold similar to unrelated alpha- and flaviviruses (142). In further studies post-fusion structures of RVFV and of the two bandaviruses DABV and HRTV were obtained, all of which showed a class-II fusion protein fold (143–145). The structure of RVFV Gc in the post-fusion form revealed the presence of a conserved interaction pocket for a glycerophospholipid head group (143). In recent years, the N-terminal ectodomain of RVFV and SFTSV Gn has been determined by X-ray crystallography, revealing a mixed α-helical/β-stranded N-terminal domain (domain A), a β-ribbon domain, and a domain B (146, 147). Although both proteins have a similar overall fold, relatively large differences were observed between members of the two genus groups, suggesting that Gn is less conserved than Gc. These new structures were then used to fit the crystal structures of RVFV Gn and Gc into cryo-EM tomographic reconstructions of purified viral particles. These reconstructions showed that the N-terminal region of Gn is localized membrane-distally and covers Gc at neutral pH. Gn probably shields the fusion loop of

Gc, thereby preventing premature fusion (147). This model is also consistent with data showing that neutralizing antibodies preferentially target Gn (148).

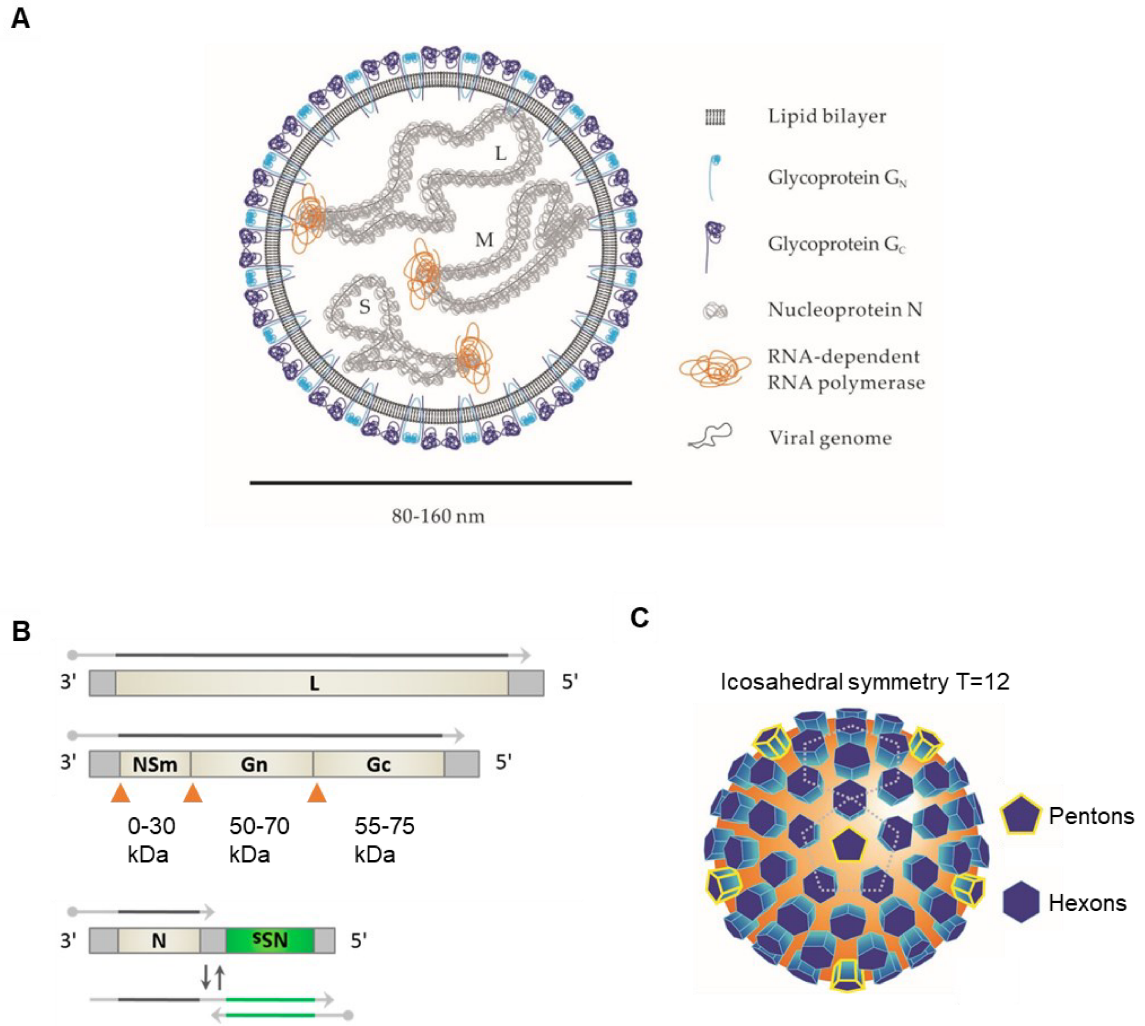

Figure 10. Structural and genomic organization of *Phenuiviridae.*

(A) Schematic representation of a phenuiviral particle. The figure is adapted from (149). (B) Coding strategy of the L, M, and S segments. Orange rectangles indicate cleavage sites by host cell proteases in the polyprotein M. Figure was modified from (138). (C) Arrangement of Gn/Gc heterodimers on the surface of phenuiviral particles. The figure was modified from (149). L, RNA-dependent RNA polymerase; NSm, a non-structural protein in the M polyprotein; NSs, a non-structural protein encoded by the S segment.

1.3.2 SARS-CoV-2 particles

Coronavirus particles are enveloped and nearly spherical with an average diameter of 118-136 nm and spike-like projections of 16-21 nm with a stalk and bulbous distal ends (**Figure 11A**) (64). The genome consists of large, nonsegmented positive-strand RNA of ~30 kilobases (kb) in size. Starting at the 5' end, about two-thirds of the genome is occupied by two large open reading frames (ORFs), ORF1a and ORF1b, which frameshift to encode sixteen nonstructural proteins that make up the replicase-transcriptase complex (**Figure 11B**). Many of these proteins have enzymatic functions and act as proteases, polymerases, helicases, and nucleases, among others (150). Four structural proteins are encoded at the 3' end: the spike (S), the nucleocapsid (N), the membrane (M) protein, and the envelope (E) protein. S and M are major and E is a minor component of the viral envelope.

S contains the receptor binding domain (RBD) and is a class-I fusion protein. M contains three TM domains and functions mainly as a scaffolding protein in the assembly of viral particles by interacting with itself, S, and the N protein (151, 152). E is involved in various steps of the life cycle such as assembly, budding, and contributes to pathogenesis (150). A role as viroporin, a membrane ion-conducting pore to selectively transport cations, has been proposed for oligomerized E proteins (153). In addition to the primary role of N protein in packaging the viral genome, N also functions in cell cycle regulation, stress response, and influencing the immune system (150). Due to a large genome but normal particle diameter for RNA viruses, the genome is packaged by N and the RNPs together form supercoiled structures (154). In addition, several accessory proteins are interspersed among the genes for the structural proteins. The number of accessory proteins varies among coronaviruses, and up to eleven have been proposed for SARS-CoV-2 (155). They are mainly involved in virus-host interactions and contribute to the pathogenesis of infection (150, 155).

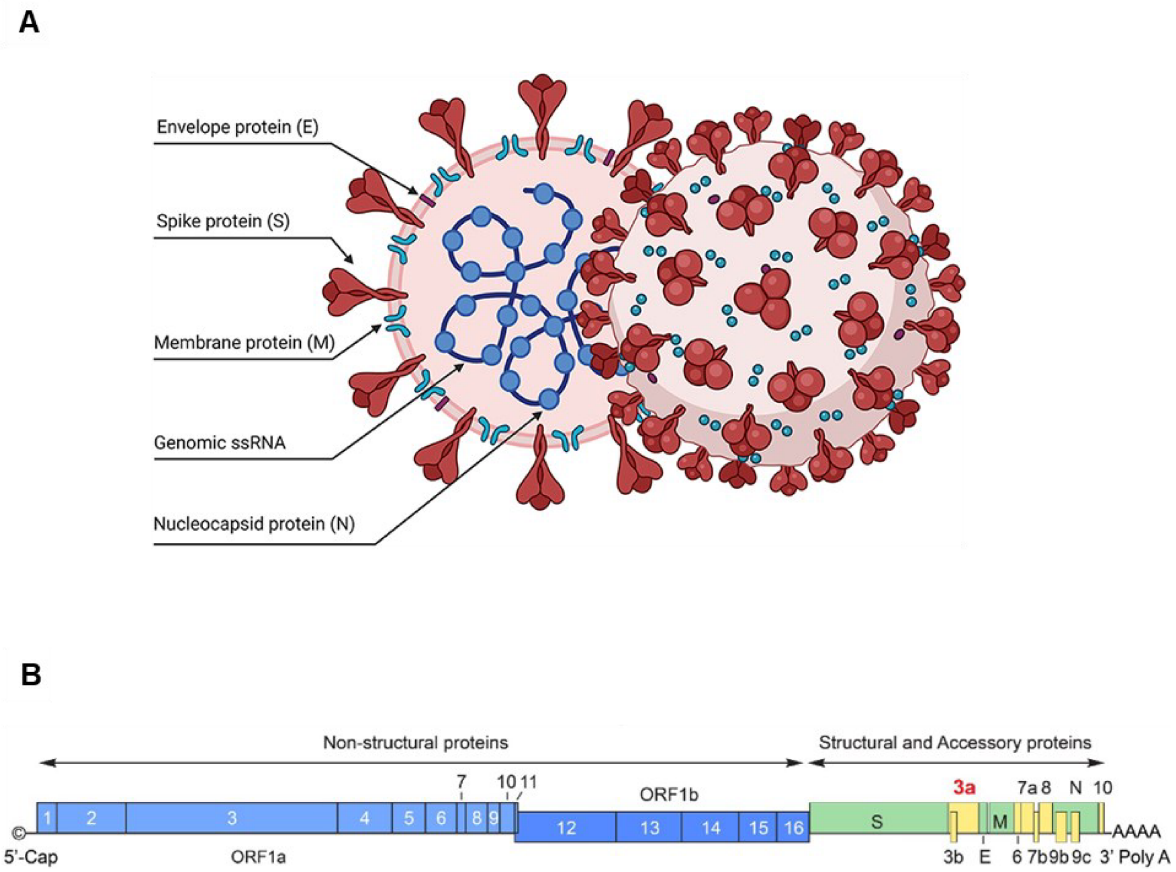

Figure 11. Structural and genomic organization of SARS-CoV-2.

Schematic representation of SARS-CoV-2 particle (A) and genome organization (B). ORF, open reading frame. Figure in (A) was adapted from (156) and (B) from (157).

1.4 Infection Cycles of TOSV and SARS-CoV-2

1.4.1 Replication cycle of TOSV and related phenuivirus

The cell life cycle of a virus can be divided into three major stages, namely entry, replication, and egress. Briefly, during entry, viral particles bind to cellular receptors, resulting in viral uptake into cells. For TOSV, there are is only a very limited number of studies at the cellular and molecular levels of infection. The few studies using the closely related RVFV, DABV, and UUKV showed that phenuiviruses travel along the endosomal pathway and enter host cells by acid-activated membrane fusion (**Figure 12**). As a result, the viral genome is released into the cytosol where it is replicated and viral proteins are synthesized. The polyprotein encoded by the M segment is processed in the ER and Golgi. Assembly and budding occur at the Golgi, and new virions are released by exocytosis.

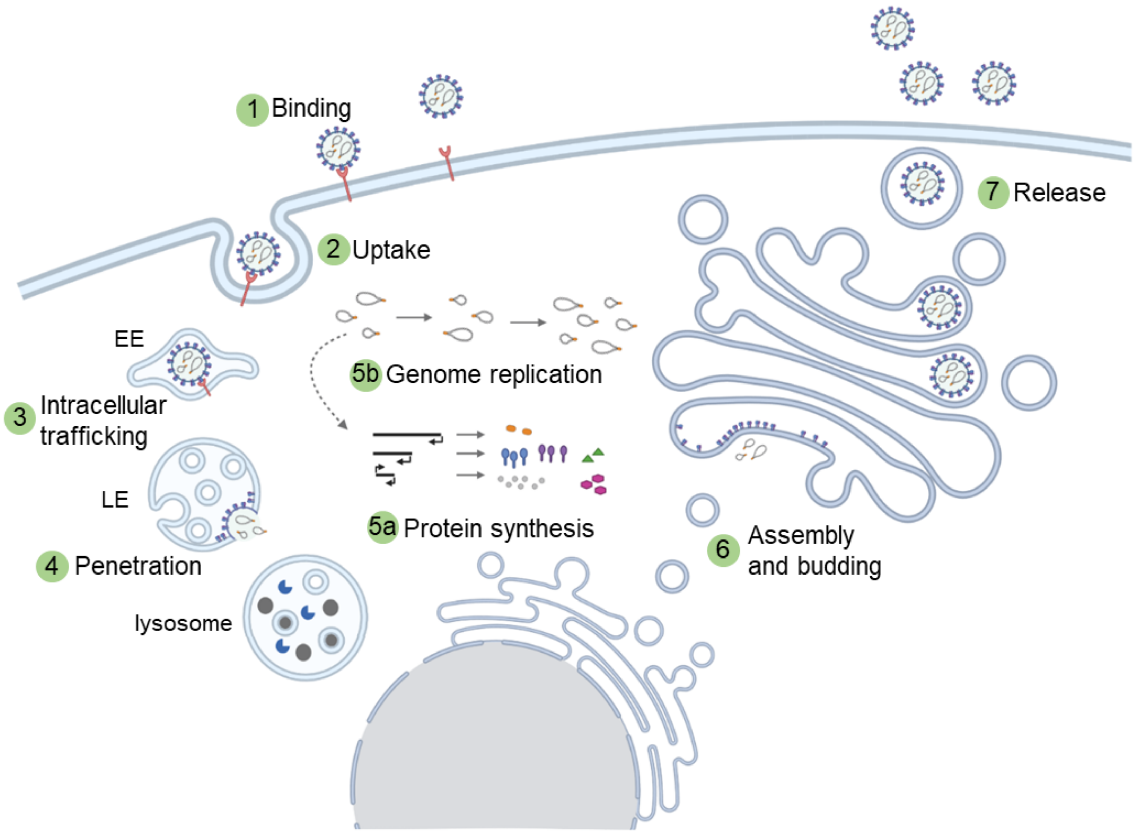

Figure 12. Life cycle of phenuiviruses in mammalian cells.

The infection cycle of phenuiviruses begins with binding to receptors at the cell surface. Particles enter cells by receptor-mediated endocytosis and travel along the endocytic pathway until penetration by acid-activated membrane fusion occurs in late endosomes. The viral replication is exclusively cytosolic. First, the negative-sense genome is transcribed to produce the viral mRNAs necessary for the biosynthesis of all the viral proteins. The polyprotein, which is encoded by the M segment, is processed co-translationally in the endoplasmic reticulum (ER). The replication of the viral genome involves a positive-sense RNA intermediate, usually named as viral cRNAs for complementary RNAs, which is used as template to produce new viral RNA genomic segments. Then particles assemble and bud into the Golgi lumen. Virions are believed to leave host cells by exocytosis. The figure was created with BioRender. EE, early endosome; LE, late endosome.

Cellular receptors and phenuiviral uptake into mammalian cells

The first step in viral entry is viral binding to receptors exposed on the cell surface. For phenuiviruses, there is a limited number of studies and only a few receptors, attachment factors and co-receptors are known (**Table 1**).

Viruses often bind to common attachment factors such as carbohydrates on glycoproteins or glycolipids, that act as initial docking sites through electrostatic interactions with viral glycoproteins. For RVFV and TOSV, the glucosaminoglycan heparan sulfate has been

shown to facilitate infection and act as an attachment factor (158–160). A dose-dependent inhibitory effect on TOSV infection could be observed by adding bovine lactoferrin that competitively binds to heparan sulfate glucosaminoglycans on the cell surface (160).

Many phenuiviruses have been shown to use the C-type lectin dendritic cell-specific intercellular adhesion molecule-3-grabbing non-integrin (DC-SIGN) to enter cells (161–165). DC-SIGN is a high-mannose-specific lectin functional at the cell surface under the form of tetramers, which can be achieved only when the lectin is highly expressed. Such high levels are mainly observed on dermal dendritic cells (DCs). DC-SIGN is expressed by other cell types such as macrophages, megakaryocytes, some B cells, and platelets, but with a much lower expression (166, 167). High expression of DC-SIGN rendered cell lines permissive for RVFV, UUKV, TOSV, Punta Toro virus (PTV) and DABV (161–164). The DC-SIGN-mediated entry of RVFV depends on specific *N*-linked glycans in the viral glycoproteins Gn and Gc (165). Since high-mannose *N*-glycans are typical for insect-derived glycoproteins and dermal DCs are located in the anatomical site of arbovirus transmission, interactions between DC-SIGN and phenuiviruses are thought to be particularly relevant (9, 161). In addition to viral binding, DC-SIGN molecules accumulate at the binding site and trigger a signaling cascade leading to viral uptake by clathrin-mediated endocytosis. This indicates that DC-SIGN acts as a true endocytic receptor for phenuiviruses, leading to viral uptake into cells (161).

Besides DC-SIGN, the C-type lectins liver-specific intercellular adhesion molecule-3-grabbing non-integrin (L-SIGN) and liver and lymph node sinusoidal endothelial cell C-type lectin (LSECtin) have also been proposed as receptors for RVFV, TOSV, UUKV, and DABV (162, 163, 168, 169). In contrast to DC-SIGN, L-SIGN is believed to act as an attachment factor (169). Recently, low-density lipoprotein receptor-related protein 1 (Lrp1) was identified as another receptor for RVFV by a CRISPR/Cas9 screening approach (170). Lrp1 was later found to function as a general host factor for many RNA viruses (171). Finally, nonmuscle myosin heavy chain type IIA was found to be involved in DABV entry, but it is not clear whether it acts as a receptor or attachment factor (172).

After viral binding to receptors, phenuiviruses are internalized into cells by endocytosis. Studies using various perturbants of the endocytic machinery such as siRNA, chemical inhibitors, and inactive and active mutants revealed heterogeneity in the pathways used by phenuiviruses to enter cells. While clathrin-mediated endocytosis was shown to be the entry pathway of DABV (173), its role in the uptake of RVFV or UUKV was less clear. Association of UUKV with clathrin was observed after binding of UUKV to DC-SIGN (161). However, in cells lacking DC-SIGN, UUKV was rarely observed in clathrin-coated vesicles

and silencing of the clathrin heavy chain had no significant effect on UUKV infection (174). Several routes of entry for RVFV have been proposed. While clathrin was shown to play a role in the uptake of a nonspreading mutant of RVFV (120), a role for caveolin-mediated endocytosis or macropinocytosis was proposed for the RVFV vaccine strain MP12 (175, 176). Overall, this demonstrates the ability of phenuiviruses to use alternative internalization pathways that can vary between virus species, but also between cell types and possibly even between individual cells.

Table 1. Receptors for phenuiviruses in mammalian hosts

Receptor/cofactor	Species	References
DC-SIGN	DABV, ppDABV, PTV, RVFV, TOSV, UUKV	(174, 162–165)
L-SIGN	ppDABV, RVFV, TOSV, UUKV	(162, 163, 168, 169)
LSECtin	ppDABV	(163)
Heparan sulfates	RVFV, TOSV	(158–160)
NMMHC-IIA	DABV	(172)
LRP1	RVFV, SFSV	(170, 171)

DABV, Dabie virus; DC-SIGN, dendritic cell-specific intercellular adhesion molecule-3-grabbing non-integrin; L-SIGN, liver-specific intercellular adhesion molecule-3-grabbing non-integrin; LRP1, low-density lipoprotein receptor–related protein 1; LSECtin, liver and lymph node sinusoidal endothelial cell C-type lectin; NMMHC-IIA, nonmuscle myosin heavy chain IIA; ppDABV, rhabdovirus pseudotyped with the glycoproteins G_N and G_C of Dabie virus; PTV, Punta Toro virus; RVFV, Rift Valley fever virus; SFSV, Sandfly fever Sicilian virus; TOSV, Toscana virus; UUKV, Uukuniemi virus. Table was modified from (149).

Intracellular trafficking

After viral uptake, virions are sorted into endosomal vesicles and travel along the endosomal pathway until they reach a compartment from which they enter host cells (**Figure 13**). Penetration is triggered by environmental cues such as a decrease in the luminal pH of endosomes. For phenuiviruses, endosomal acidification has been shown to play a key role in entry, as inhibition of vacuolar acidification blocked infection by RVFV, UUKV, and DABV (120, 173, 174). For several phenuiviruses, acid-dependent entry occurred 20-60 min after internalization into cells (120, 173, 174). For RVFV and other acid-dependent viruses, entry was also dependent on RNASEK, a factor associated with the vATPase (177). However, the exact role of RNASEK in viral entry remains elusive.

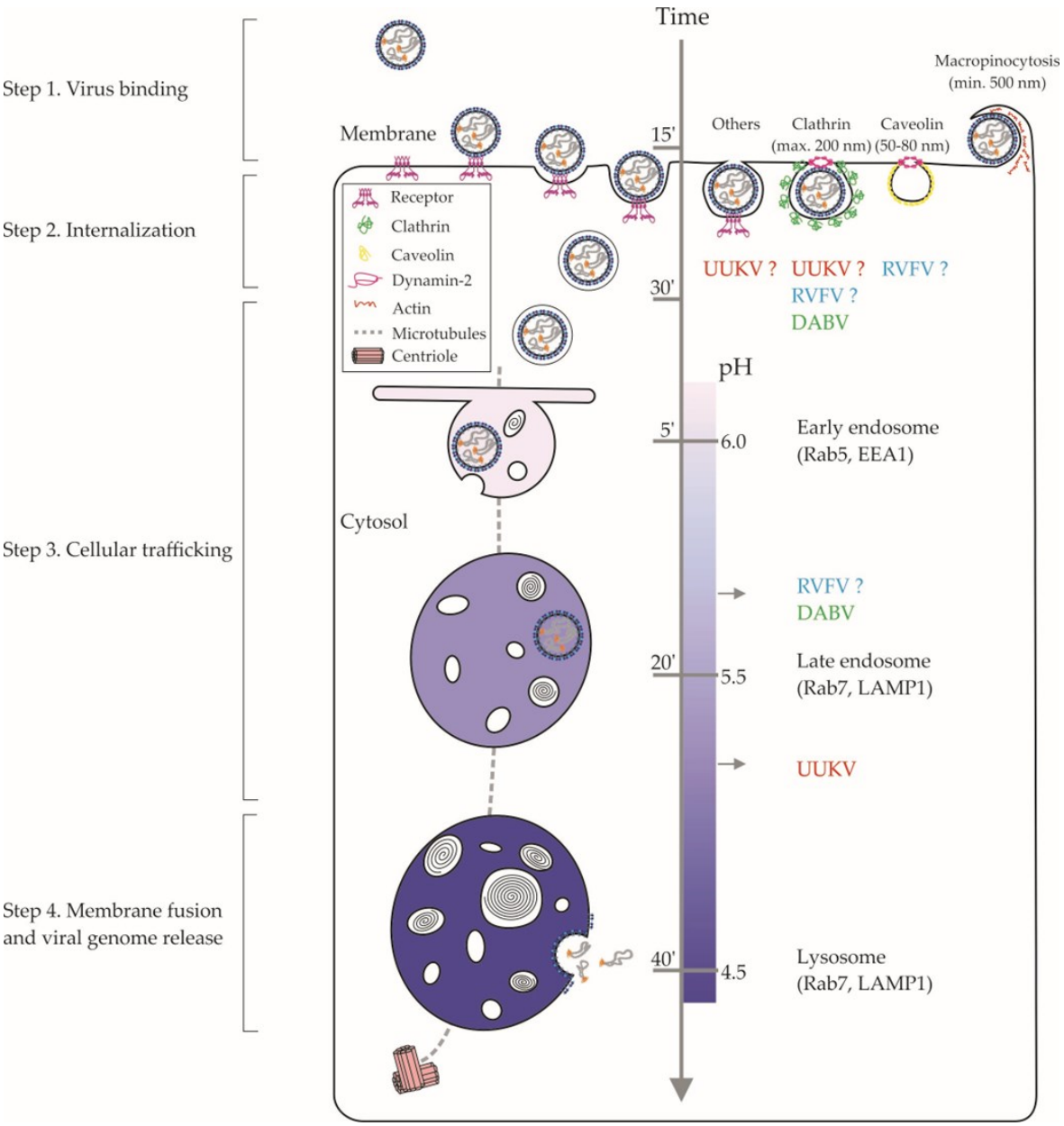

Figure 13. Entry of phenuiviruses into mammalian host cells.

Phenuiviruses bind to host cells through specific interactions with cell surface receptors. Particles then enter cells via various endocytic uptake mechanisms such as clathrin- or caveolin-dependent endocytosis, macropinocytosis, or via a clathrin-independent uptake pathway. Endocytosed particles travel along the endosomal pathway from early to late endosomes. Particles penetrate from endosomal compartments by acid-activated membrane fusion when intraluminal conditions are optimal for fusion. The scales in the middle indicates typical pH values found in the endosomal lumen and the time it typically takes for cargo to reach each compartment. The figure was adapted from (149). DABV, Dabie virus; EEA1, early endosome antigen 1; LAMP1, lysosome-associated membrane protein 1; Rab5 and Rab7, Ras-associated binding protein 5 and 7; RVFV, Rift Valley fever virus; UUKV, Uukuniemi virus.

Microscopy-based studies have shown that phenuiviruses traffic along the endosomal pathway and transit through EEs. UUKV and DABV were observed in vesicles positive for the early endosomal marker Rab5a, and UUKV infection was inhibited by expression of dominant-negative and constitutively active mutants of Rab5 (173, 174). Transport to downstream organelles of EEs was observed for UUKV, which co-localized with Rab7a, a marker of LEs, and DABV, which was found in LAMP1+ and endolysosomal-like compartments (173, 174). The maturation of EEs to LEs is also dependent on the MT network. Disruption of the MT network by nocodazole or colcemid blocked infection by UUKV and DABV (173, 174). The kinetics of penetration, co-localization with resident proteins of late endosomal vesicles, and susceptibility to inhibitors of the functional microtubule network suggest that phenuiviruses rely on LE maturation for productive infection and belong to the diverse group of L-PVs.

Fusion

Viral fusion with a target cell membrane is mediated by the glycoprotein Gc, which has a class-II fusion protein fold similar to that of alpha- and flaviviruses. The general mechanism of viral membrane fusion and that of class-II fusion proteins is described in more detail in section 1.2.3.. Similar to other class-II fusion proteins, fusion of phenuiviruses is activated by low pH. For the phenuiviruses UUKV, DABV, and RVFV, the optimal pH for fusion was found to be at pH 5.4, 5.6, and 5.7, respectively (120, 173, 174). Such a low pH is usually present in LEs, which is another indication that phenuiviruses are L-PVs. For UUKV and RVFV, acidification was shown to be sufficient to induce fusion, whereas DABV required cleavage of Gn and/or Gc by serine proteases in addition to low pH (120, 131, 162). In addition, the lipid composition of the target cell membrane may modulate fusion efficiency. UUKV fusion was enhanced in the presence of anionic lipids, as BMP, a lipid species increased in LEs, and glycerophospholipids facilitated RVFV fusion (131, 143).

Based on recent advances in the structures of Gn and Gc, a fusion model for phenuiviruses has been proposed. Similar to other class-II fusion proteins, Gc forms heterodimers with Gn, its accompanying protein, on the viral surface in its pre-fusion form. Together they form hexameric and pentameric structures consisting of six and five heterodimers, respectively. At neutral pH, the N-terminal region of Gn is localized membrane-distally, covering Gc and thereby shielding the fusion loop of Gc, preventing premature fusion (147). Upon acidification, Gn is thought to reorient laterally, resulting in the release of the Gc fusion loop and allowing insertion into a target membrane (**Figure 14A**).

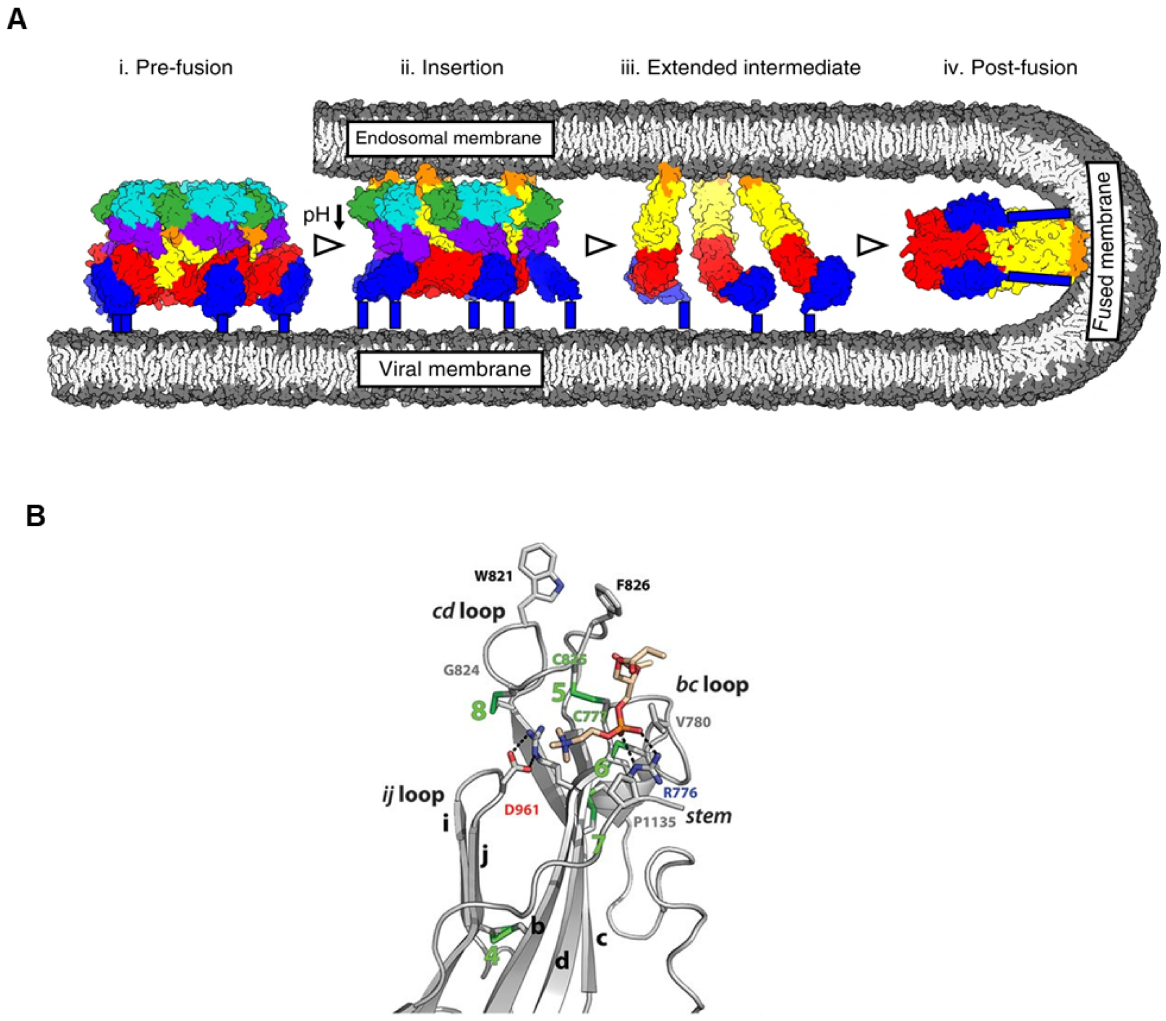

Figure 14. Gc-mediated fusion mechanism of phenuiviruses.

(A) The different domains of the class-II fusion protein Gc are colored in red, yellow and blue as shown in Figures 8 and 9. The different domains of Gn are shown in green, cyan, and purple. The fusion loops of Gc (orange) are buried within the Gn-Gc interface in the pre-fusion form at neutral pH (i). Upon low pH triggering and exposure to a target membrane, Gn is expected to move laterally, exposing the fusion loops at the tip of domain II. This is followed by a full extension of Gc, resulting in the insertion of the fusion loops into the target membrane (ii). Gn and Gc dissociate and the extended intermediates of Gc reassemble into trimers (iii). Gc folds back to its post-fusion conformation, resulting in the fusion of the two membranes (iv). Figure adapted from (147). (B) Schematic representation of the tip of domain II of RVFV with its *bc* and *cd* loops. A dipropionyl phosphatidylcholine molecule is shown in the glycerophospholipid-specific binding pocket. Figure adapted from (143).

The fusion loop of phenuiviruses is located in domain II of Gc. The *cd* loop is the major fusion loop, but the adjacent *bc* loop is likely to also contribute to membrane insertion (**Figure 14B**) (143). The *cd* fusion loop of phenuiviruses consists of bulky hydrophobic

amino acids such as W821 and F826 in RVFV. F826 is conserved in the fusion loops of other phenuiviruses, whereas W821 is replaced by an isoleucine in sand fly-borne phleboviruses or an alanine in tick-borne uuku- or bandaviruses. The nature and location of hydrophobic residues in RVFV and DABV are very important for their fusogenicity, as shown by several unsuccessful rescue attempts of virus variants with mutated amino acids in the *bc* and *cd* loops. Similar to other pH-sensitive fusion proteins, conserved histidines in RVFV and DABV Gc have been proposed to play a role in the transition from pre- to post-fusion (120, 144). The protonation of histidines upon acidification introduces new stabilizing salt bridges or destabilizing repulsive charges that are thought to drive the conformational changes. Thus, conserved histidine residues act by stabilizing the pre- or post-fusion conformation, especially at the domain I/III interface, or by allowing interactions with phospholipids in the target membrane.

Virus replication and release of infectious viral particles

Viral genome replication and transcription of phenuiviruses occurs exclusively in the cytoplasm of infected cells and is mediated by the viral RdRp. Viral replication begins at the 3' end of the viral genome with transcription of a complementary RNA (cRNA) that is shorter than the full-length genome and serves as a mRNA for translation of viral proteins (**Figure 15**). During elongation, the N protein is shed from the RNP complexes. Translation of viral proteins begins with a cap-snatching mechanism in which the viral RdRp "steals" a short 5' fragment of cellular mRNAs by cleaving at a position near the 5' end. The snatched fragment of approximately 10-25 nucleotides then serves as a primer for viral mRNA transcription using the vRNA as a template. Since phenuiviral genomes do not contain a poly(U) stretch, viral mRNAs do not have a poly(A) tail and transcription stops at termination signal sequences in the untranslated region of the genome. When the N protein is sufficiently expressed, the RdRp switches to transcribing full-length cRNAs. This cRNA, which is predominantly positive sense, then serves as a template for RdRp to produce new negative sense viral genome RNAs (vRNA) in the same manner. After termination, RdRp re-bonds to the panhandle structure at the 3' and 5' ends of newly generated viral RNA.

N and RdRp proteins are synthesized in the cytoplasm and form RNP complexes with newly synthesized viral RNA. Proteins encoded by the M segment are synthesized as polyprotein precursors. Signal peptides direct translocation to the ER membrane. In the ER, the polyprotein is processed co-translationally by signal peptidases to NSm (if present), Gn and Gc, and *N*-linked glycosylations are added to Gn and Gc. Gn/Gc heterodimers are transported to the Golgi and inserted into the Golgi membrane. The

cytoplasmic tails of Gn interact with RNPs in the cytosol to package the viral genome into particles. However, genome packaging appears to be heterologous and nonselective, as nearly 40% of newly produced RVFV virions lack at least one segment (178). Budding occurs in the Golgi lumen and virus-containing vesicles exit the cells via the secretory pathway.

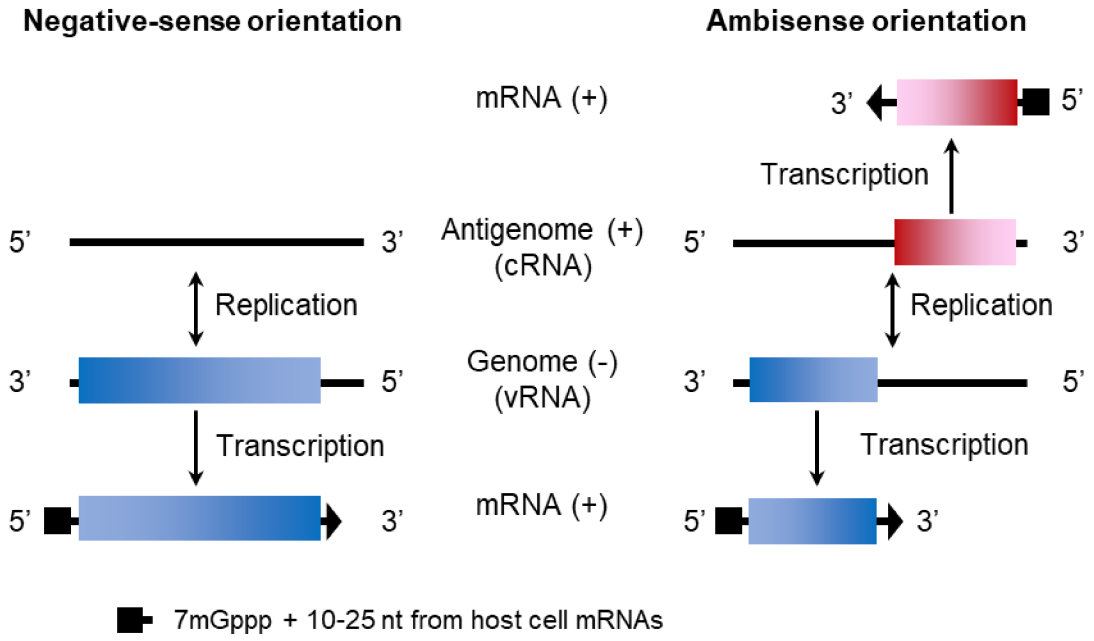

Figure 15. Coding strategies for phenuivirus replication and transcription.
The schema depicts the strategies developed by phenuiviruses to transcribe and replicate their RNA genome. The L and M segments are in negative-sense orientation while the S segment has an ambisense coding strategy. The viral mRNAs contain host cell-derived caps at their 5' ends, but no polyA tail.

1.4.2 Replication cycle SARS-CoV-2 and related coronaviruses

The coronavirus Spike protein

Receptor binding and entry into host cells is mediated by the S protein. S is a large, highly glycosylated protein with a length of 1,273 amino acids and a size of 180-200 kDa. It is also a type-I membrane protein and belongs to the group of class-I fusion proteins. Like other class-I fusion proteins, S forms homotrimers on the viral surface, giving the particles their crown-like appearance. It is the major antigen and target of neutralizing antibodies and has been used in vaccine development. An average of 20-50 spike homotrimers are found on each virion (179–181).

S consists of two subunits, S1 and S2, which are cleaved by host cell proteases and remain noncovalently attached. The S1 subunit contains an N-terminal domain (NTD), a receptor binding domain (RBD) and two C-terminal domains (CTDs) and is mainly involved in binding to cell surface receptors (**Figure 16**). The S2 subunit carries the fusion peptide, a central helix, two heptad repeats, a TM domain and a short cytosolic tail. S2 is highly conserved, whereas S1 is the major target of neutralizing antibodies, especially epitopes in NTD and RBD.

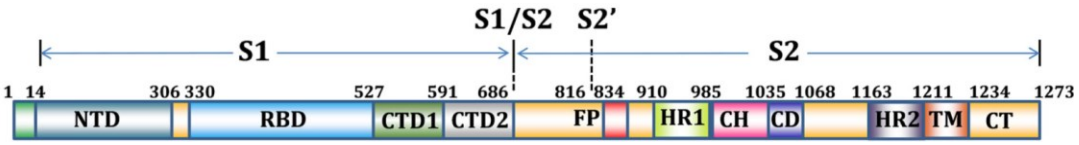

Figure 16. Domains of the SARS-CoV-2 Spike protein (S).

Schematic representation of the domains in the spike (S) protein of SARS-CoV-2. Cleavage of S at the S1/S2 site results in two subunits, S1 and S2, which remain noncovalently linked. A second cleavage site exists at the S2' position in S2 upstream of the fusion peptide (FP). S1 is mainly responsible for receptor binding and consists of an N-terminal domain (NTD), a receptor binding domain (RBD), and two C-terminal domains (CTD1 and CTD2). S2 exhibit the fusion activity and carries the fusion peptide (FP), two heptad repeats (HR1 and HR2), the central helix (CH), the connector domain (CD), the transmembrane domain (TM), and a cytosolic tail (CT). The figure was modified from (182).

Binding of S to cellular receptors

Binding to cellular receptors is mainly mediated by the RBD of S. The RBD of SARS-CoV-2 is very similar to that of SARS-CoV. For example, both use angiotensin-converting enzyme 2 (ACE2) as a receptor (183). ACE2 is a type-I TM protein mainly expressed in lung, heart, kidney and intestine. Its main role is the regulation of vasoconstriction and blood pressure by acting as a carboxypeptidase. However, the catalytic domain of ACE2 does not overlap with the virus binding site. The RBD of S adopts two different conformations: an "up" position that allows interaction with receptors, and a "down" position that prevents receptor binding. Both conformations appear to be in a dynamic equilibrium, with approximately one RBD per trimer in the up position (184). Upon receptor binding, the NTD shifts slightly outward while the positioning of the S2 subunit remains unaffected.

Several host factors have been proposed to be involved in viral attachment. One of the attachment factors could be the highly abundant proteoglycan heparan sulfate. Heparan sulfate may participate in the initial binding of SARS-CoV-2 before S is redirected to

ACE2. In addition, heparan sulfate may promote the ACE2-accessible up conformation of the RBD (185–187). In recent years, a growing number of potential receptors or adhesion factors have been proposed that could contribute to infection of cell types and tissues lacking ACE2 expression. Several of these factors have been shown to render cells susceptible when overexpressed, or infection has been reduced by treatment with antibodies targeting the factor. Neuropilin 1 (Nrp1) has been proposed to contribute to TMPRSS2-dependent entry (188, 189). Nrp1 is widely expressed on respiratory and olfactory endothelial and epithelial cells and may contribute to SARS-CoV-2-induced anosmia (190). Other factors include C-type lectins (191), TIM1 (192, 193), AXL (194), CD147/basigin (195), KREMEN1 (196), ASGR1 (196), and many others. However, conflicting results have been reported for many factors, and further experimental studies are needed to understand their roles during SARS-CoV-2 infection.

Fusion

Coronaviruses do not all use the same triggers for fusion. For some viruses, exposure to low pH is sufficient to induce fusion, such as the infectious bronchitis virus (197), whereas others, including MERS-CoV or SARS-CoV, require initial binding to a receptor followed by proteolytic cleavage (198). SARS-CoV-2 is thought to require cleavage at two sites to exert its fusogenic role. A first cleavage, called priming, occurs at the S1/S2 junction, which contains with RRAR a noncanonical polybasic furin cleavage site compared to the classical RX(R/K)R furin cleavage motif. The second cleavage occurs immediately upstream of the fusion peptide and leads to activation of the class-I fusion protein. Cleavage at the S1/S2 boundary is a prerequisite for cleavage at the S2' site in SARS-CoV (199). Since SARS-CoV does not contain a furin cleavage site at the S1/S2 boundary, both sites are cleaved by host cell proteases in target cells. For SARS-CoV-2, it has been proposed that furin cleaves S in Golgi compartments of producing cells. A second proteolytic cleavage occurs in target cells at the S2' site, which is well conserved among coronaviruses. In other coronaviruses, several proteases such as cathepsins, trypsin, trypsin-like proteases, or elastase have been shown to be involved in priming and activation of S (69, 150).

The transmembrane protease serine 2 (TMPRSS2) is often associated with coronaviruses and is widely expressed on epithelial cells in the respiratory, gastrointestinal, and urogenital tracts (200). Its exact physiological role is unknown, but it has been implicated in the regulation of sodium currents in the lung and inflammatory responses in the prostate (201, 202). TMPRSS2 has been shown to cleave SARS-CoV and MERS-CoV S and is critical for rapid entry into cells (203, 204). In SARS-CoV-2, TMPRSS2 can cleave

S at its S2' site after a single arginine residue (205). However, it is uncertain whether the protease also has activity at the S1/S2 site (205, 206). Other proteases often associated with coronaviruses are cathepsins. Cathepsin L is a cysteine protease that is active at acidic pH in endolysosomes, where it is involved in proteolytic degradation, energy metabolism, and immune responses (207). S of SARS-CoV, MERS-CoV and SARS-CoV-2 has predicted cleavage sites for several cathepins, including cathepsin L (208–210). These include cleavage sites close to the polybasic furin site at the SARS-CoV-2 S1/S2 junction and close to the TMPRSS2 cleavage site at S2'.

Thus, a multistep fusion model has been proposed in which binding of S RBD to ACE2 leads to conformational changes in S1. This is followed by dissociation of the S1 subunit and exposure of the S2' cleavage site (184). Neither trypsin cleavage nor acidic pH alone could induce conformational changes from pre-fusion to post-fusion in the absence of ACE2 binding (211). Dissociation of one S1 subunit of the trimer upon interaction with ACE2 could then promote dissociation of the other two S1 subunits. In the pre-fusion conformation, the heptad repeat 1 (HR1) forms a long coiled-coil with the central helix. Upon exposure and cleavage at the S2' site, the unstructured HR1 undergoes a dramatic refolding to a helical conformation that triggers insertion of the fusion peptide into a target membrane. Upon insertion of the fusion peptide, three highly conserved hydrophobic grooves on HR1 are exposed. The HR2 folds back, attaches to the hydrophobic grooves of HR1, and brings the two membranes together. Two entry pathways have been proposed for SARS-CoV and MERS-CoV: an early pathway by fusion from the plasma membrane or a late pathway from LEs (**Figure 17**) (198). Which entry pathway is used depends on the host cell protease that cleaves at S2'. When S is activated by TMPRSS2 on the cell surface, viruses enter via the fast pathway, whereas when cleaved by cathepsins, entry occurs from endolysosomes.

During the course of the pandemic, novel and highly mutated variants appeared, mainly with deletions and substitutions in S. Mutations in these circulating variants were mainly associated with altered transmissibility and antigenicity. Altered transmissibility can be conferred in a variety of ways, including stabilized S protein, increased receptor binding, or increased cleavage. The D614G mutation appeared early in the pandemic and was present in all VOCs. It is associated with a stabilized S protein that reduces premature shedding of noncovalently bound S1. This in turn may prevent activation of conformational changes in S2 in a suboptimal environment and virus inactivation (212, 213). Others have proposed that the D614G mutation leads to an increased likelihood of S adopting the open conformation capable of binding to receptors, resulting in increased infectivity (214–216).

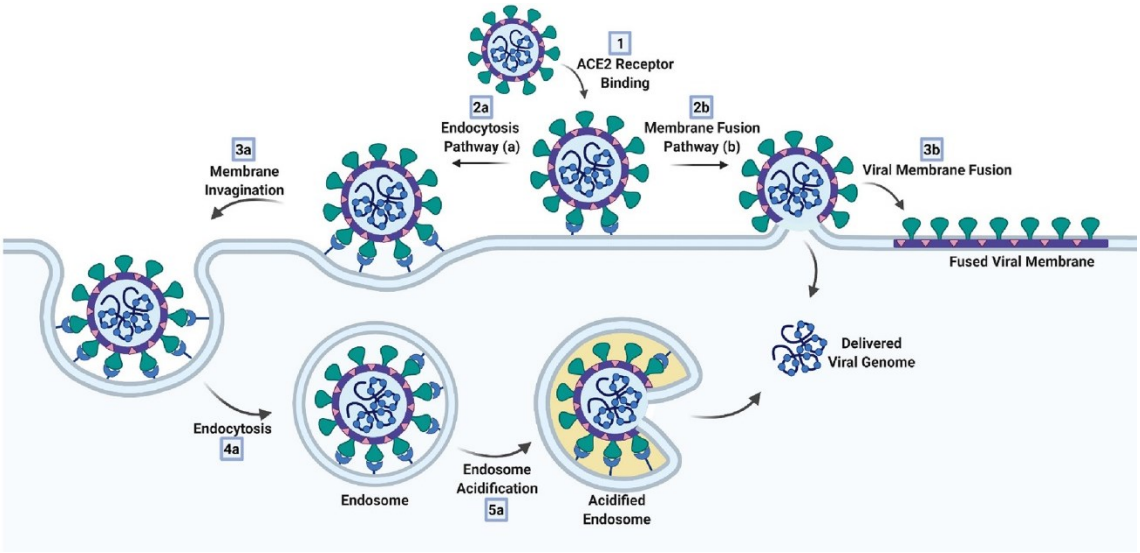

Figure 17. Entry routes of coronaviruses.

Coronaviruses can use multiple pathways to enter cells. Coronaviral particles bind to cell-surface receptors such as angiotensin-converting enzyme 2 (ACE2). Particles can then enter cells by receptor-mediated endocytosis and travel along the endocytic pathway before the spike (S) is cleaved by proteases, such as cathepsin L, in endolysosomes. Alternatively, S can be cleaved by cell-surface proteases, leading to fusion at or nearby the plasma membrane. The figure was adapted from (217).

In addition, increased transmissibility is achieved by increased affinity for ACE2, as proposed for the N501Y mutation within the RBD (218, 219), or by mutations at or near the furin cleavage site, such as the P681R/H mutation (220). Under the pressure of the immune system, mutations in VOCs have emerged that also show reduced sensitivity to neutralization by antibodies from recovered or vaccinated patients. These mainly include mutations in the RBD, such as K417N/T, L452R, E484K/Q and N501Y, which have been associated with escape from neutralizing antibodies (220).

Replication, assembly, and egress

The incoming positive-sense, single-stranded RNA genome has a 5' cap and a poly(A) tail and serves multiple functions. It can act directly as mRNA for translation of two large polyproteins and also serves as a template for replication and transcription (**Figure 18**). The two polypeptides pp1a and pp1ab are processed by viral proteases into 15-16 nonstructural proteins, nsp1-16. Together, they have important functions during replication and protein synthesis, such as forming the replicase-transcriptase complex, having proteolytic activity, or contributing to the formation of replication organelles. The replicase-transcriptase complex is involved in genome replication, transcription, and polyprotein

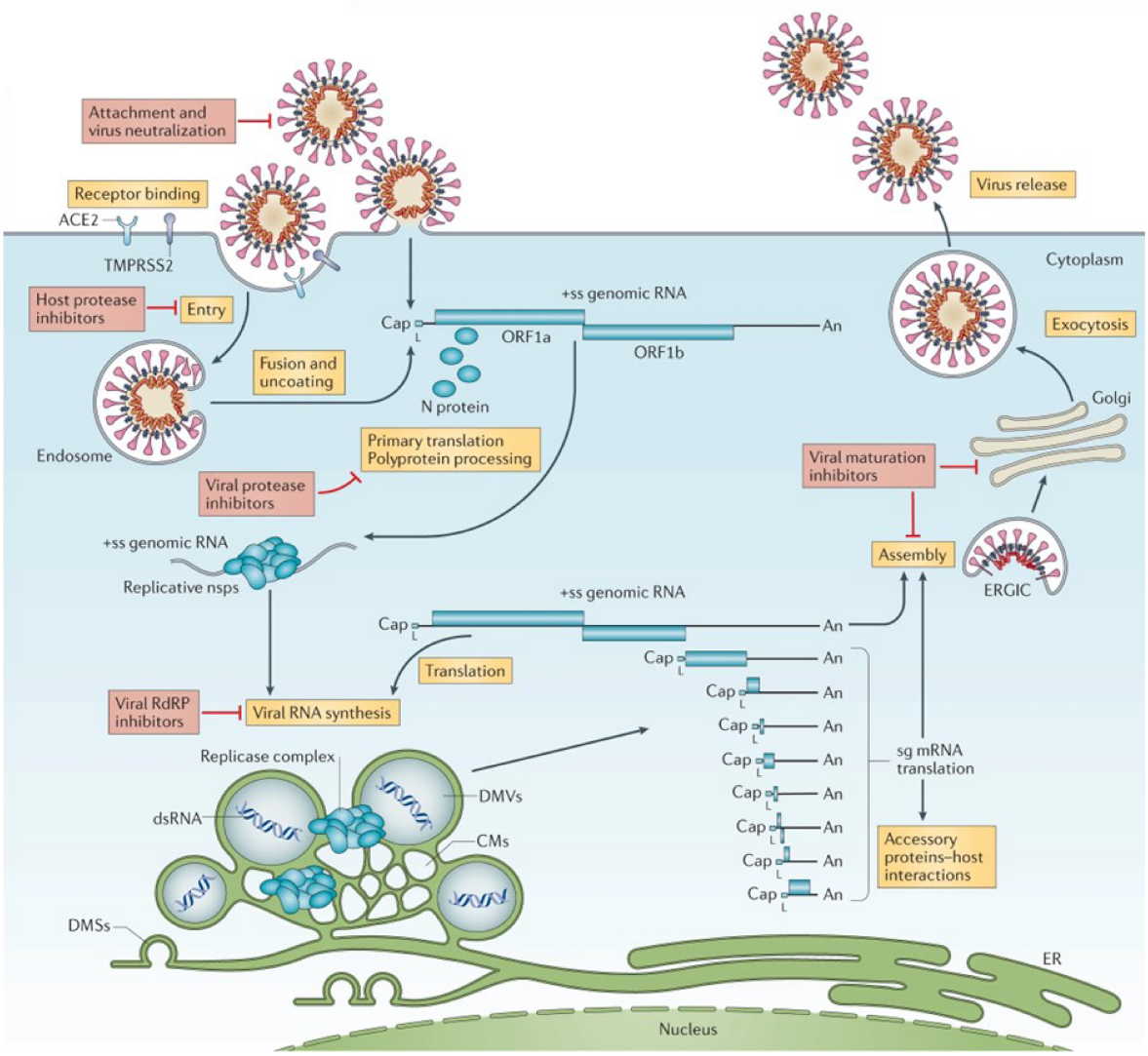

Figure 18. Replication cycle of coronaviruses.

Coronaviruses attach to cells through interactions between the spike (S) protein and cell-surface receptors, such as angiotensin-converting enzyme 2 (ACE2). Entry into host cells can occur at or near the plasma membrane or from intracellular compartments. The release of incoming viral genomic RNAs is directly followed by the translation of the two large open reading frames (ORFs). The resulting polyproteins, pp1a and pp1ab, are processed into nonstructural proteins that form the replication-transcription complex. Genome replication occurs in viral replication factories consisting of double-membrane vesicles and convoluted membranes derived from endoplasmic reticulum membranes. In addition, structural and accessory proteins are translated from subgenomic mRNAs. Assembly occurs at the ER-Golgi intermediate compartment (ERGIC). Viral particles bud into the ERGIC lumen and are secreted by exocytosis. Figure was adapted from (221). An, 3′ polyA sequence; cap, 5′ cap structure; dsRNA, double-stranded RNA; L, leader sequence; RdRP, RNA-dependent RNA polymerase.

processing. All structural and accessory viral proteins encoded at the 3' end of the genome are synthesized from individual small subgenomic RNAs. Using the viral genome as a template, replication occurs through synthesis of a full-length complementary negative-strand RNA. This then serves as a template to produce full-length positive-polarity viral RNA. Genomic replication and transcription occur in replication factories, which are membrane rearrangements of the endoplasmic reticulum. SARS-CoV-2 induces double-membrane vesicles, which together form a network of folded membranes. S, M and E are inserted into the ER membrane and traffic to ER-Golgi intermediate compartments (ERGIC) where they are retained and accumulate. Assembly and budding occurs in ERGIC, where M interacts with S proteins and RNP complexes to ensure packaging of the viral genome. Particle egress occurs via the secretory or lysosomal exocytic pathway (156).

1.5 Objectives of this thesis

More and more viruses are emerging or re-emerging due to globalization, habitat destruction, and global warming. As viral vectors expand geographically, many arboviruses, including phenuiviruses, are at risk of being introduced into new geographical areas in Europe and spreading further northwards. This is also the case for sand fly-borne TOSV, which is already widespread in many Mediterranean countries. Despite being one of the leading causes of viral meningitis during the summer season, there is very little information on the molecular and cellular biology of TOSV infection of human cells.

Therefore, the first part of my PhD project aims to characterize the entry route and early virus-host cell interactions of TOSV in induced pluripotent stem cell-derived human neurons and other tissue culture cells. To this end, I first established and optimized protocols for the production and fluorescent labeling of TOSV particles. This laid the foundation for the establishment of several sensitive, quantitative and accurate assays based on flow cytometry, lipid-mixing fluorimetry, and a combination of microscopy-based techniques to address individual steps of the viral entry process including binding, internalization, intracellular trafficking, and membrane fusion. In addition, the morphology of viral particles was studied by cryo-electron microscopy.

For intracellular trafficking, fluorescently labeled TOSV particles were generated and their co-localization with endosomal markers was followed and analyzed by confocal microscopy. The subcellular localization and dynamics of host cell entry as well as the triggers for membrane fusion were analyzed in more detail. Here, I wanted to investigate

whether TOSV shares with other phenuiviruses the characteristic of being a L-PV. This was done using several complementary approaches, including chemical inhibitors and mutant proteins, and using newly synthesized viral proteins as a read-out. In parallel, fusion events could be directly monitored by fluorimetry in a lipid-mixing assay using TOSV labeled with the self-quenching lipid dye octadecyl rhodamine B chloride (R18). These R18-labeled viruses were then used to study the dynamics of the viral fusion process in correlation with the endosomal pH values.

In the second part of my thesis, I focused on the cell entry mechanisms of SARS-CoV-2, the causative agent of the COVID-19 pandemic. With the onset of the pandemic, there has been a debate about how SARS-CoV-2 enters host cells and how particles are primed and activated for fusion. Using similar approaches previously established for TOSV, I analyzed whether SARS-CoV-2 enters host cells from the plasma membrane or from intracellular compartments after endocytosis. Therefore, several permissive epithelial cell types were used to investigate the dependence of SARS-CoV-2 entry on proteolytic processing and endosomal acidification, and how the expression of different proteases can drive entry pathways. This was accomplished by using a combination of overexpression of proteases, different perturbants and mutant proteins. In addition, the kinetics of each step of the entry program were analyzed by time-of-addition experiments using different specific inhibitors. Furthermore, a cell-cell fusion model was developed to study the triggers required for membrane fusion.

2 Material and Methods

2.1 Material

2.1.1 Cell Lines

Cell line	Culture medium	Information
A549	DMEM (10% FBS, 1% NEAA)	(222)
A549-ACE2 (=A549*)	DMEM (10% FBS)	(223)
A549 EF2α-TMPRSS2	DMEM (10% FBS)	(223)
A549-ACE2 EF2α-TMPRSS2 (=A549* TMPRSS2+)	DMEM (10% FBS)	Provided by Prof. Bartenschlager
A549-ACE2 ROSA-TMPRSS2	DMEM (10% FBS)	Provided by Prof. Bartenschlager
BHK-21	GMEM (5% FBS, 10% TPB)	(224)
Caco-2	DMEM (10% FBS)	(225, 226)
Calu-3	DMEM (10% FBS)	(227)
HEK293T	DMEM (10% FBS)	(228)
DF-1	DMEM (10% FBS)	(229)
HeLa	DMEM (10% FBS)	(230)
Huh-7	DMEM (10% FBS)	(231)
iPSC-derived neurons	B27/Neurobasal (5% FBS, 1X GlutaMAX)	(232)
Jurkat	RPMI (10% FBS)	(233)
L929	DMEM (10% FBS)	(234, 235)
LLE/LULS40	L-15/H-Lac/L-15B (15% FBS, 7% TPB, 1X GlutaMAX)	(236)
LLE/LULS45	L-15B (5% FBS, 10% TPB, 1X GlutaMAX)	(237)
MDCK	DMEM (10% FBS)	(238, 239)
PPL/LULS49	L-15B/H-Lac (13% FBS, 5% TPB, 1X GlutaMAX)	(237)
Raji	RPMI (10% FBS)	(240)
SUP-T1^{R5}	RPMI (10% FBS)	(241, 242)
SH-SY5Y	MEM:F12 (1:1; 10% FBS)	(243, 244)
THP-1	RPMI (10% FBS)	(245)
U87^{44}	DMEM (10% FBS)	(226, 246, 247)
Vero E6	DMEM (10% FBS)	(248, 249)

2.1.2 Viruses

Virus	Producer cell	Reference
Germiston virus (GERV)	BHK-21 cells	(250)
Influenza A virus (IAV) (provided by Prof. Kräusslich)	MDCK cells	(251, 252)
Rift Valley fever virus ΔNSs:EGFP	Vero E6 cells	(253)

SARS-CoV-2 (BavPat1, Wuhan strain)	Vero E6 cells	(254)
SARS-CoV-2 (Delta variant) (provided by Prof. Bartenschlager)	Vero E6 cells	(255)
Semliki Forest virus (SFV)	BHK-21 cells	(256)
Toscana virus (TOSV) Strain H4906 (lineage B)	BHK-21 cells	(257, 258)
Uukuniemi virus	BHK-21 cells	(259, 260)

2.1.3 Plasmids

Plasmid	Notes	Reference
pEGFP-Rab5	Expression plasmid for eGFP-tagged Rab5a WT	(174)
pEGFP-Rab5 Q79L	Expression plasmid for eGFP-tagged constitutively active mutant of Rab5a	(174)
pEGFP-Rab5 S34N	Expression plasmid for eGFP-tagged dominant-negative mutant of Rab5a	(174)
pEGFP-Rab7	Expression plasmid for eGFP-tagged Rab7a WT	(174)
pEGFP-Rab7 Q67L	Expression plasmid for eGFP-tagged constitutively active mutant of Rab7a	(174)
pEGFP-Rab7 T22N	Expression plasmid for eGFP-tagged dominant-negative mutant of Rab7a	(174)
pLAMP1-EGFP	Expression plasmid for eGFP-tagged LAMP1	(174)

2.1.4 Antibodies

Primary Antibodies			
Antibody	Species	Dilution and Method	Information
anti-ACE2	Rabbit	1:1,000 WB	Abcam, #ab108252
anti-actin	rabbit	1:1,000 WB	Sigma-Aldrich, Merck, A2066
anti-cathepsin L	Mouse	1:1,000 WB	Thermo Fisher Scientific, #BMS1032
anti-EF2α	goat	1:1,000 WB	Santa Cruz, #SC-13004
anti-GERV	Guinea pig	1:16,000 flow cytometry 1:1,000 WB	(258)
anti-IAV N	Mouse	1:250 flow cytometry	Merck Millipore, #MAB8257
anti-SARS-CoV NP	Mouse	1:500 flow cytometry and microscopy 1:1,000 TCID50	Sino Biologicals, #40143-MM05
anti-SARS-CoV Spike	rabbit	1:1,000 WB	Thermo Fisher Scientific, #PA1-41165
anti-SFV E2	Mouse	1:400 flow cytometry	Provided by Prof. Margeret Kielian; (261)
anti-TMPRSS2	Rabbit	1:1,000 WB	Abcam, #ab92323
anti-TOSV	Guinea pig	1:1,000 WB	(258)

anti-TOSV	Mouse	1:4,000 flow cytometry 1:1000 WB	Kindly provided by Prof. Robert Tesh; (169)
anti-TOSV Gc	Guinea pig	1:1,000 WB	(258)
anti-TOSV Gn	Guinea pig	1:1,000 WB	(258)
anti-TOSV N	Guinea pig	1:1,000 WB	This study.
anti-tubulin	Mouse	1:1,000 WB	Sigma-Aldrich, Merck, #T5168
anti-UUKV N	mouse	1:400 flow cytometry	Provided by Dr. Anna Överby; (262)
Secondary Antibodies			
Antibody	Species	Dilution and Method	Information
Anti-goat IRDye 800CW	donkey	1:10,000 WB	LiCOR, #926-32214
Anti-guinea pig AF488	goat	1:500 flow cytometry	Thermo Fisher Scientific, #A-11073
Anti-guinea pig IRDye 680RD	donkey	1:10,000 WB	LiCOR, #926-68077
Anti-guinea pig IRDye 800CW	donkey	1:10,000 WB	LiCOR, #926-32411
anti-mouse IRDye 800CW	donkey	1:10,000 WB	LiCOR, #926-32212
anti-mouse AF405	goat	1:500 flow cytometry	Thermo Fisher Scientific, #A-31553
anti-mouse AF488	goat	1:500 flow cytometry	Thermo Fisher Scientific, #A-11001
Anti-mouse AF647	goat	1:1,000 microscopy	Thermo Fisher Scientific, #A-21241
anti-mouse IRDye 680RD	donkey	1:10,000 WB	LiCOR, #926-68072
anti-rabbit IRDye 800CW	donkey	1:10,000 WB	LiCOR, #926-32213
anti-rabbit IRDye 680RD	donkey	1:10,000 WB	LiCOR, #926-68073

2.1.5 Reagents

Reagent	Solvent	Stock concentration	Provider, Cat#
Alexa Fluor 488 NHS ester	DMSO	10 $mg.mL^{-1}$	Thermo Fisher Scientific, #A20000
Ammonium chloride (NH_4Cl)	H_2O	1 M	Sigma-Aldrich, Merck, #254134
Aprotinin	H_2O	25 mM	Cayman Chemical, #Cay14716
ATTO647N NHS ester	DMSO	5 $mg.mL^{-1}$	ATTO-TEC, #AD 647N-31
Bafilomycin A1	DMSO	100 µM	BioViotica, Adipogen Life Sciences, # BVT-0253

Camostat mesylate	H_2O	50 mM	Sigma-Aldrich, Merck, #SML0057
Chloroquine diphosphate	H_2O	10 $mg.mL^{-1}$	Sigma-Aldrich, Merck, #C6628
Colcemid	DMSO	10 mM	Cayman Chemical, #Cay15364-1
Concanamycin B	DMSO	50 µM	BioViotica, Adipogen Life Sciences, # BVT-0252
Furin	Tris and glycerol-based	200 $µg.mL^{-1}$	R&D Systems, # 1503-SE-010
MG-132	DMSO	40 mM	Selleck Chemicals, #SEL-S2619
Nocodazole	DMSO	20 mM	Calbiochem, Merck, #487928
Octadecyl rhodamine B chloride (R18)	Ethanol	10 mM	Invitrogen, Thermo Fisher Scientific, #O246
SB412515	DMSO	10 mM	Cayman Chemical, #Cay23249
Taxol (=Paclitaxel)	DMSO	10 mM	Sigma-Aldrich, Merck, #T7402
Thermolysin	PBS	10 $mg.mL^{-1}$	Sigma-Aldrich, Merck, #T7902
Trypsin	PBS	1 $mg.mL^{-1}$	Sigma-Aldrich, Merck, #T1426

2.1.6 Buffers

Buffer	Composition
Agarose overlay solution (BHK-21)	2.5% FBS, 1% agarose, 0.4% sodium bicarbonate in GMEM
Agarose overlay solution (SARS-CoV-2)	4% FBS, 0.1% agarose in DMEM
Coomassie destaining solution	10% acetic acid in dH_20
Coomassie fixative solution	40% methanol, 10% acetic acid in dH_2O
Coomassie staining solution	0.25% Coomassie brilliant blue, 50% methanol, 10% acetic acid in dH_2O
Crystal violet staining solution	0.3% crystal violet, 10% ethanol, 4% formaldehyde in dH_2O
FACS permeabilization buffer (FPB)	2% FBS, 5 mM EDTA, 0.02% NaN_3, 0.1% Saponin in 1X PBS
Freezing medium	90% FBS, 10% DMSO
HNE	10 mM HEPES, 150 mM NaCl, 1 mM EDTA in dH_2O and adjusted to pH 7.3
Infection medium (TOSV, GERV, RVFV, SFV, IAV) for A549 and Vero cells	20 mM HEPES, 0.2% BSA in DMEM
LB agar	13% agarose in LB medium
LB medium	1% tryptone, 0.5% yeast extract, 171 mM NaCl in dH_2O
Lysis buffer	25 mM Tris-HCl pH 7.5, 50 mM NaCl, 2 mM EDTA, 0.6% NP-40, 0.1% SDS, 1x complete protease inhibitor in dH_2O

Mowiol	6 g glycerol, 2.4 g polyvinyl alcohol 4-88, 6 mL dH_2O, 12 mL 100 mM Tris-HCl pH8.5; mixed for 48 h, centrifuged at 5,000 rpm for 15 min
pH buffers	All based on DMEM, 0.2% BSA, pH adjusted and sterile filtered through 0.22 µm
pH 7.4, pH 7.0	30 mM HEPES
pH 6.0, 5.8, 5.6	30 mM MES
pH 5.5	1.6 $g.L^{-1}$ citric acid, 4.7 $g.L^{-1}$ sodium citrate
pH 5.25	2.0 $g.L^{-1}$ citric acid, 4.3 $g.L^{-1}$ sodium citrate
pH 5.0	2.4 $g.L^{-1}$ citric acid, 4.0 $g.L^{-1}$ sodium citrate
TBS-Tween (TBST)	0.1% Tween in 1X TBS
TPB	29.5% in dH_2O
Tris-buffered saline (TBS)	20 mM Tris base, 150 mM NaCl in dH_20, adjusted to pH 7.6

2.1.7 Chemicals and Media

Chemical	Provider
Acetic acid	Merck
Agarose, ultra-pure	Invitrogen, Thermo Fisher Scientific
Agarose (for LB agar plates)	Carl Roth
Albumin Fraction V, powder (BSA)	Carl Roth
B-27 Plus Supplement (50x)	Gibco, Thermo Fisher Scientific
Bovine Albumin Fraction V (7.5 % solution)	Gibco, Thermo Fisher Scientific
Citric acid monohydrate	Sigma-Aldrich, Merck
CMFDA	Invitrogen, Thermo Fisher Scientific
collagen	Sigma-Aldrich, Merck
Coomassie brilliant blue G-250	Thermo Fisher Scientific
Crystal violet	Sigma-Aldrich, Merck
D(+)-Saccharose	Carl Roth
Dimethyl sulfoxide (DMSO)	Merck
DMEM, high glucose, GlutaMAX supplement	Gibco, Thermo Fisher Scientific
DMEM, high glucose, no glutamine, no phenol red	Gibco, Thermo Fisher Scientific
DMEM/F-12, GlutaMAX Supplement	Gibco, Thermo Fisher Scientific
DRAQ5	Thermo Fisher Scientific
Ethanol	Merck
Ethylenediaminetetraacetic acid (EDTA)	Carl Roth
Ethylenediaminetetraacetic acid (EDTA) 0.5 M pH8	Invitrogen, Thermo Fisher Scientific
Fetal bovine serum (FBS)	Gibco, Thermo Fisher Scientific
Fetal bovine serum (FBS)	Capricorn Scientific
Formaldehyde solution 37 % (for flow cytometry)	Merck
G-418 Solution	Roche, Merck
Glasgow's MEM (GMEM)	Gibco, Thermo Fisher Scientific
GlutaMAX	Thermo Fisher Scientific
Glutaraldehyde	Carl Roth
Glycerol	Labochem international
Hank’s Balanced Salt Solution (HBSS)	Sigma-Aldrich, Merck

HEPES (1M)	Gibco, Thermo Fisher Scientific
Hoechst 33258	Thermo Fisher Scientific
Intercept (TBS) Blocking Buffer	LI-COR
Kanamycin	Carl Roth
L-15 medium	Gibco, Thermo Fisher Scientific
Lactalbumine hydrosylate	Sigma-Aldrich, Merck
LB Medium Powder	Carl Roth
Lipofectamine 2000 transfection reagent	Invitrogen, Thermo Fisher Scientific
Lipoprotein	MP Biomedicals, Thermo Fisher Scientific
MEM nonessential amino acids solution (100X)	Gibco, Thermo Fisher Scientific
MEM, GlutaMAX Supplement	Gibco, Thermo Fisher Scientific
MES (2-(N-morpholino)ethanesulfonic acid)	Carl Roth
Methanol	VWR International
Milk powder, blotting grade	Carl Roth
Mowiol 4-88	Sigma-Aldrich, Merck
Neurobasal Plus Medium	Gibco, Thermo Fisher Scientific
NP-40	Merck
NuPAGE LDS Sample Buffer (4X)	Invitrogen, Thermo Fisher Scientific
NuPAGE MOPS SDS Running Buffer (20X)	Invitrogen, Thermo Fisher Scientific
NuPAGE Sample Reducing Agent (10X)	Invitrogen, Thermo Fisher Scientific
NuPAGE Transfer Buffer (20X)	Invitrogen, Thermo Fisher Scientific
Opti-MEM	Gibco, Thermo Fisher Scientific
Paraformaldehyde solution, 16 % w/v, methanol free (for imaging)	Alfa Aesar
Penicillin-Streptomycin 100X solution	Pan Biotech
Phosphate buffered saline (PBS)	Merck
PPMP	Cayman Chemical
Protease inhibitor cocktail tablets	Roche, Merck
Protein Standard, SeeBlue Plus2 Prestained	Invitrogen, Thermo Fisher Scientific
Puromycin	Invivogen
RPMI 1640 Medium, GlutaMAX Supplement	Gibco, Thermo Fisher Scientific
Saponin	Serva
Sodium azide (NaN_3)	Merck
Sodium bicarbonate solution 7.5 %	Gibco, Thermo Fisher Scientific
Sodium chloride (NaCl)	Bernd Kraft
Sodium citrate monobasic	Sigma-Aldrich, Merck
Sodium dodecyl sulfate (SDS)	Serva
Tris base	Carl Roth
Triton X-100	Merck
Trypan blue solution 0.4 %	Gibco, Thermo Fisher Scientific
Trypsin 0.25%	Pan Biotech
Trypsin/EDTA 10X	Pan Biotech
Tryptone	Sigma-Aldrich, Merck
Tryptose phosphate broth (TPB)	Sigma-Aldrich, Merck
Tween 20	Carl Roth
Yeast extract	Sigma-Aldrich, Merck

2.1.8 Kits and Consumables

Media, Kits and Consumables	Provider
Centrifuge tubes, polyclear	Seton
CytoTox 96® Non-Radioactive Cytotoxicity Assay	Promega
E. coli DH5α competent bacteria	Gibco, Thermo Fisher Scientific
FACS micro tubes	Thermo Fisher Scientific
Lab-Tek 8-well (#155411)	Thermo Fisher Scientific
NucleoBond PC 500 plasmid extraction kit	Macherey-Nagel
Nunc cell culture tubes	Thermo Fisher Scientific
PD Minitrap™ G-25	Cytiva, Merck
Precast Protein gels, 10 % Bis-Tris, NuPAGE	Thermo Fisher Scientific
Transfer stack, PVDF (iBlot)	Invitrogen, Thermo Fisher Scientific

2.1.9 Machines

Machine	Company
Bacteria centrifuge Avanti J-20 XP	Beckman Coulter
Bacteria incubator	Memmert
Bacteria shaker Multitron Pro	Infors HT
Blotting system (iBlot gel transfer device)	Invitrogen, Thermo Fisher Scientific
Cell culture incubator C200	Labotect
Cell culture wide field microscope	Nikon
Electrophoresis Power Supply EV231	Consort
ENVAIR eco safe Comfort Safety workbench	ENVAIR
Flow cytometer BD FACSCelesta	BD Bioscience
Heraeus Fresco 21 Centrifuge	Thermo Fisher Scientific
Heraeus Megafuge 40R Centrifuge	Thermo Fisher Scientific
Infinite M200Pro plate reader	Tecan
JA-10 rotor	Beckman Coulter
LabGard class II safety cabinet	Nuaire
Leica TCS SP8 confocal microscope	Leica Microsystems
LI-COR Odyssey CLx	LI-COR
Magnetic Stirrer Hei-Standard	Heidolph Instruments
Microcentrifuge MiniStar silverline	VWR
Mini-gel electrophoresis system	Thermo Fisher Scientific
Nanophotometer NP80 Touch	Implen
Optima L-90K Ultracentrifuge	Beckman Coulter
pH-meter FiveEasy	Mettler-Toledo
Precision scale EW220-3NM	Kern
Rocker Polymax 1040	Heidolph

Rotor SW 32 Ti	Beckman Coulter
Rotor SW 60 Ti	Beckman Coulter
Scale 650-2NM	Kern
Spectrofluorometer FP-8000 series	Jasco
STED/ RESOLFT microscope	Abberior Instruments
Thermomixer C	Eppendorf
Vortex-Genie 2	Scientific Industries
XCell SureLock Mini-Cell Electrophoresis chamber	Invitrogen, Thermo Fisher Scientific

2.1.10 Software

Software	Notes
BioRender	Figure Design
FlowJo (Treestar)	Flow cytometry data
GraphPad Prism v8.0.1	Analysis, figure design
ImageJ	Image analysis

2.2 Methods

2.2.1 Cells

2.2.1.1 Cell Culture

All mammalian cell lines were cultured at 37°C in a humified atmosphere with 5% CO_2. BHK-21 cells were cultured in GMEM supplemented with 5% FBS and 10% TPB. A549, Caco-2, Calu-3, DF-1, HeLa, HEK293T, Huh-7, L929, MDCK, U87 and Vero cells were all cultivated in DMEM supplemented with 10% FBS. For A549 cells, the medium was additionally supplemented with 1X nonessential amino acids (NEAA). A549 cells overexpressing ACE2 and TMPRSS2 were a kind gift from Prof. Bartenschlager. Caco-2 and Calu-3 cells were grown on collagen-coated flasks and plates. For coating, collagen was dissolved to 1% in 60% ethanol and added to flasks or plates for at least 30 min at 37°C. The surfaces were extensively washed with PBS before seeding of cells. Jurkat, Raji, Sup-T1 and THP-1 cells were grown in RPMI supplemented with 10% FBS while SH-SY5Y were cultivated in MEM/F12 supplemented with 10% serum. The sand fly cell lines LLE/LULS40, LLE/LULS45 and PPL/LULS49 were kept at 28°C in sealed, flat Nunc tubes. LLE/LULS40 was cultured in a mix of L-15, H-Lac and L-15B, LLE/LULS45 in L-15B and PPL/LULS49 in a mix of L-15B and H-Lac. All cell lines were grown in the presence of

100 units.mL^{-1} penicillin and 100 mg.mL^{-1} streptomycin. Cells were monitored regularly with a widefield microscopy and split according to their confluency.

For passaging of adherent mammalian cells, cells were washed with PBS before trypsin/EDTA was added to detach cells. Medium was added and cells were resuspended. Suspension cells were split by resuspending the cell suspension. Sand fly cell lines were passaged by resuspending cells and transferring to new tubes. For long-term storage, cells were cryopreserved at -80°C or in liquid nitrogen. For freezing, cells were pelleted by centrifugation at 300 x g for 5 min and resuspended in freezing medium. Cell suspension was transferred to cryo-tubes in an isopropanol tank and placed overnight at -80°C.

Human induced pluripotent stem cells (iPSCs)-derived glutamatergic neurons were prepared and provided in a collaboration by Alessandra Albertelli from the Claudio Acuna group in Heidelberg as previously described (232). Briefly, iPSC were infected with two lentiviruses, one was expressing a reverse tetracycline-controlled transactivator (rtTA) under an ubiquitin promoter. The second lentivirus was designed to express neurogenin-2 and puromycin in an inducible manner driven by the rtTA promoter. After one day, doxycycline was added to induce neurogenin-2 and puromycin expression. Two days later, puromycin was added for selection of transduced iPSCs. Remaining cells were re-plated on Matrigel-coated coverslips with primary mouse glial cells that were prepared as previously described (263). From then on, half of the medium was changed every second day for 8 d, and 2.5% FBS was added to support astrocyte viability. After day 10, induced neurons were cultured in B27/Neurobasal medium supplemented with 5% FBS for a minimum of 21 days before infection with TOSV. For a complete list of cell lines and media, see section 2.1.1.

2.2.1.2 Cytotoxicity assay

Cytotoxicity of all used inhibitor concentrations were assessed using the CytoTox96 Non-Radioactive Cytotoxicity colorimetric assay according to the provider's recommendations. This assay measures lactate dehydrogenase that is released into the extracellular medium upon cell death and lysis. Cells were treated for 9 h at 37°C with drugs in the range of concentrations used to study entry. PPMP, a ceramide analog that impairs ceramide maturation and cell membrane integrity, was used as a positive control. Absorbance was measured at 490 nm using a plate reader.

2.2.2 Plasmid preparation and transfection of mammalian cells using Lipofectamine

For amplification of plasmid, chemically competent *E. coli* DH5α cells were thawed on ice and 50 ng of plasmids were added to 25 µL of bacteria. After 30 min incubation on ice, a heat shock at 42°C for 30 sec was performed before bacteria were placed back on ice for 2 min an 1 mL of LB medium was added. The bacteria were incubated at 37°C for 1 h while shaking. 100 µL of transformed bacteria were plated on LB-agar plates supplemented with kanamycin for selection. Single colonies were picked the next day to inoculate 250 mL of LB. Bacterial cultures were grown overnight at 37°C at 180 rpm. Bacteria were pelleted at 6,000 x g for 15 min at 4°C and plasmids were extracted using the NucleoBond PC 500 Kit according to the manufacturer's instructions. Plasmids were resuspended in dH_20 and DNA yield was measured by a nanophotometer.

Plasmids were transfected into A549 and Vero cells using Lipofectamine 2000 transfection reagent according to the manufacturer's instructions. Transfection were performed in a 24-well plate format. $8x10^4$ A549 cells or $5x10^4$ Vero cells were seeded. The next day, A549 and Vero cells were transfected the next day with 0.5 µg and 0.75 µg plasmid DNA and 1 µL and 1.9 µL Lipofectamine 2000, respectively. The medium was changed after 5 h. For imaging-based transfections, cells were seeded on glass cover slips.

2.2.3 Viruses

2.2.3.1 Virus production

GERV, SFV, and TOSV were produced in BHK-21 cells, and RVFVΔNSs:EGFP and SARS-CoV-2 in Vero E6 cells according to protocols previously described (250, 253, 256, 258, 264). Briefly, BHK-21 and Vero cells at a confluency of 60-80% were washed with serum-free GMEM (GMEM, 10% TPB), serum-free DMEM (RVFVΔNSs:EGFP) or DMEM containing 2% FBS (SARS-CoV-2). Cells were infected in 15 mL with TOSV, GERV, SFV, RVFVΔNSs:EGFP, or SARS-CoV-2 at low multiplicities of infection (MOIs) of 0.01, $5x10^{-5}$, 0.05, 0.02 and 0.1, respectively. The input virus was replaced after 1 h at 37°C by 33 mL serum-free medium, or for SARS-CoV-2, medium containing 2% FBS. Virus was harvested at approximately 50% cytopathic effect (CPE) reached after around 72 h, 33 h, 24 h, 72 h for TOSV, GERV, SFV and SARS-CoV-2, respectively. For RVFVΔNSs:EGFP, infection of the eGFP-expressing virus was assessed by a widefield fluorescence microscope and virus-containing supernatant was harvested after 120 h. For TOSV, GERV, SFV, and RVFVΔNSs:EGFP, supernatant was supplemented with 20 mM HEPES,

cleared by centrifugation at 1500 x g for 20 min at 4°C and subsequently purified by ultracentrifugation through a sucrose cushion. SARS-CoV-2 containing supernatant was cleared by centrifugation at 800 x g for 5 min at room temperature and subsequently filtered through 0.45 µm. All virus stocks were aliquoted and stored at -80°C.

GERV and RVFVΔNSs:EGFP were produced jointly with the lab rotation student Alicia Rosenberger. UUKV was produced and provided by Zina Uckeley, a former group member and the production was described elsewhere (260). IAV was produced with the reverse genetics system on MDCK cells and kindly provided by Vera Sonntag-Buck, a technician in the group of Prof. Kräusslich, Virology, Heidelberg according to standard protocols (265). The SARS-CoV-2 Delta variant was produced on Vero cells by Marie Bartenschlager and kindly provided by Berati Cerikan, a former group member of Prof. Bartenschlager (255).

2.2.3.2 Purification of viral particles

Semi-purification through sucrose cushion

The infectious supernatant were semi-purified through a 25% (GERV, RVFVΔNSs:EGFP, SFV) or a 30% sucrose cushion (TOSV). Thereby, virus containing supernatant in SW32 centrifugation tubes was carefully underlaid by 2.5 mL of respective sucrose cushion and ultracentrifuged at 96,000 x g for 2 h at 4°C using a SW32 rotor. Supernatant was discarded, 300 µL of HNE buffer was added and tubes were rested on ice for 1 h. Viral pellets were resuspended, aliquoted, stored at -80°C and characterized by titration and protein quantification.

Gradient-purification of TOSV particles

For cryo-EM or remove unbound dyes during fluorescent labeling, TOSV particles were purified over a sucrose density gradient. A linear sucrose gradient was prepared in SW60 tubes by layering 900 µL of sucrose solutions of 60, 45, 30 and 15% on top of each other. After each layer, the tubes were placed at -80°C until the solutions were frozen. Gradients were thawed overnight at 4°C to allow linearization of the gradient. Labeled TOSV was then added carefully on top of the gradient and ultracentrifugation was performed at 100,000 x g at 4°C for 90 min in a SW60 Ti rotor with deceleration set to a minimum. A milky band at 40-45% sucrose was extracted using a syringe. Labeled virus was then analyzed by plaque-forming unit (pfu) titration, Coomassie staining and in-gel fluorescence.

Purification of SARS-CoV-2 by buffer exchange columns

Labeled SARS-CoV-2 was purified from unbound dye over PD MiniTrap G-25 buffer exchange columns according to manufacturer's recommendations. Briefly, the column was equilibrated two times by applying 500 µL DMEM containing 2% FBS and allowing the medium to enter by gravity. 500 µL medium was applied a third time and column was spun at 1000 × g for 2 min. Labeled virus was added on top of the matrix and eluted by centrifugation at 1000 × g for 2 min. Labeled SARS-CoV-2 was then analyzed by pfu titration and fluorescence microscopy.

2.2.3.3 Titration

Titration by plaque-forming unit assay

Infectivity of TOSV, GERV and SFV was analyzed by pfu titration assay on BHK-21 cells while TOSV was additionally titrated on A549 cells. $3x10^5$ BHK-21 or $1x10^6$ A549 cells were seeded in a 6-well plate format. The next day, cells were washed in serum-free medium and infected in duplicates with 10-fold dilutions in 500 µL. After 1 h at 37°C, cells were overlaid with 4 mL of agarose solution and incubated at 37°C. After 1 h, the plates were inverted when the agarose turned solid and incubated at 37°C for 96 h (TOSV), 72 h (GERV) and 48 h (SFV).

SARS-CoV-2 titers were determined by semi-solid pfu titration on Vero and A549* cells. For pfu titration, $1x10^4$ Vero and $1.2x10^4$ A549* cells were seeded in a 24-well plate format and infected with 250 µL of 10-fold dilutions of SARS-CoV-2 in DMEM 2% FBS the next day. After 1 h, 150 µL of DMEM 2% FBS and 400 µL of 2X agarose overlay was added and incubated for further 72 h at 37°C. To visualize plaques in pfu assays, agarose was removed, the cell layer was fixed with 4% formaldehyde (FA) and stained with crystal violet solution for 20 min. SARS-CoV-2 plates were additionally plunged in containers with 6% FA for 30 min before they could leave BSL3 environment. Stained plates were washed in H_2O and viral titers in $pfu.mL^{-1}$ were calculated by the number of plaques and corrected for the dilution factor.

Titration by TCID50 assay

SARS-CoV-2 susceptibility and titers were additionally determined by 50% tissue culture infectious dose (TCID50) titration assay on Vero, Caco-2, Calu-3, HeLa, HeLa DC-SIGN, A549 and HEK293T cells. $3x10^4$ cells were seeded in a 96-well plate format and infected the next day with 10-fold dilutions of SARS-CoV-2 in DMEM containing 2% FBS. Infected

cells were fixed after 24 h by incubating 10 min in 4% FA and plunging the plate for 30 min in 6% FA. After extensive washing of the plate, cells were permeabilized in 0.5% triton X-100/PBS for 15 min at room temperature. Samples were blocked in Li-COR blocking buffer for 30 min before subjected to immunostaining using the anti-SARS-CoV NP antibody at a dilution of 1:1,000 for 1 h. After extensive washing, an IRDye 800CW-coupled anti-mouse antibody and DRAQ5 diluted 1:10,000 were added for 45 min. Cells were washed and fluorescence was scanned on Li-COR Odyssey CLx. TCID50 titers were calculated by the Spearman and Kärber algorithm as previously described (266).

Titration of RVFVΔNSs:EGFP by fluorescence microscopy

As pfu titration of RVFVΔNSs:EGFP did not result in plaques, A549 cells were infected with different volumes of semi-purified virus stock and the percentage of infected cells was determined. Infection was allowed for 9 h at 37°C ensuring only a single round of infection. Cells were then fixed and fluorescence resulting from eGFP expression was analyzed by widefield fluorescence microscopy.

2.2.3.4 Quantification of viral proteins by Coomassie blue staining

To quantify the concentration of individual viral proteins in the semi-purified virus stocks and to verify the purity of the stock, virus was mixed with 4X SDS sample buffer and viral proteins were separated by SDS-PAGE on a 10% Bis-Tris gel. For quantification, different volumes of virus stocks (2.5, 5 and 10 µL) were loaded together with a bovine serum albumin (BSA) standard of known concentrations ranging from 0 – 1,000 ng on the gel. Gel electrophoresis was performed under nonreducing conditions in a MOPS SDS running buffer at 125 V for 90 min. The gel was incubated in the fixative solution for 1 h before proteins were stained in a Coomassie staining solution for 1 h. Destaining was achieved by multiple washing steps in dH_2O and Coomassie destaining solution overnight. The destained gel was scanned and intensities of viral and BSA bands were analyzed by ImageJ. A standard curve could be determined using the BSA standard enabling quantification of viral proteins.

2.2.3.5 Fluorescent labeling of virions

TOSV envelope glycoproteins were labeled with amine-reactive fluorescent NHS ester dyes as previously described for other phenuiviruses (267). Briefly, the concentration of TOSV glycoproteins was determined as described in section 2.2.3.4 and roughly 100 ng

of glycoproteins were labeled with Alexa Fluor (AF) 488 NHS or ATTO647N NHS in a molar ratio of viral protein to dye of 1:1 and 1:2, respectively. Alternatively, to label the viral membrane and perform lipid-mixing assays, roughly $3x10^9$ infectious TOSV particles were mixed with the fluorescent autoquenching dye R18 at a final concentration of 25 µM. Dyes were dissolved in 50 µL HNE buffer, added dropwise to virus stocks and incubated for 2 h at room temperature in the dark with gentle shaking. Labeled viruses were then purified and extracted by sucrose density ultracentrifugation.

SARS-CoV-2 particles were labeled with R18 using a similar protocol as for TOSV but with different concentrations. 500 µL SARS-CoV-2 stocks were incubated with R18 at a concentration of 1 µM for 2 h to allow labeling of the viral membrane. Labeled particles were then purified by buffer exchange columns.

2.2.4 Flow Cytometry-based infection assays

2.2.4.1 Infection assay

Cells were seeded and infected the following day at indicated MOIs of TOSV, SFV, GERV, RVFVΔNSs:EGFP, IAV, SARS-CoV-2 and UUKV. Infections were carried out in the respective serum-free medium containing 20 mM HEPES and 0.2% BSA (infection medium) or DMEM supplemented with 2% FBS in the case of SARS-CoV-2. MOIs provided in figure legends are given according to titration on BHK-21 (TOSV, GERV, SFV, UUKV), A549 (RVFVΔNSs:EGFP), MDCK (IAV) or Vero (SARS-CoV-2). After 1 h at 37°C, virus input was removed if not stated otherwise, and replaced by complete medium. Infection experiments to assess entry were usually stopped after another 5 h for TOSV, 7 h for SFV, GERV, RVFVΔNSs:EGFP, IAV and UUKV, and 8 h for SARS-CoV-2. Cells were then harvested and infection was monitored by flow cytometry (specified in section 2.2.4.6).

For inhibition experiments, compounds were serially diluted in infection medium for TOSV (DMEM, 0.2% BSA, 20 mM HEPES) or SARS-CoV-2 (DMEM, 2% FBS) in the presence of similar amounts of solvents. Cells were pretreated in a 24-well plate format at 200 µL 1.5-fold concentrations of inhibitors for 30 min, except for colcemid, nocodazole and taxol that were added for 3 h at 4°C. Controls with respective amount of solvent were included and used for normalization of infections. 100 µL of diluted virus was added to reach a final inhibitor concentration of one-fold. To assess inactivation by pretreatment at low pH, virions were first buffered to different pH values in 100 mM citric acid (pH 5.0 – pH 6.5) or 100 mM MES (pH 7.0) and incubated for 5 min at 37°C, or 10 min for SARS-CoV-2.

Virions were re-neutralized to pH 7.4 by addition of 0.1 N NaOH and stabilized by addition of 20 mM HEPES before adding to cells. For proteolytic processing, SARS-CoV-2 was pretreated with trypsin (100 µg.mL^{-1}), furin (1 µg.mL^{-1}) or thermolysin (1 mg.mL^{-1}) for 15 min at 37°C before adding to cells.

2.2.4.2 Binding and internalization assay with fluorescently-labeled viral particles

Binding of viral particles to the cell surface was achieved by adding viral particles to cells in suspension at 4°C for at least 1 h. Cells were detached with 0.5 mM EDTA and washed in complete medium to remove EDTA. Cells were pelleted by 300 x g for 4 min, washed in infection medium and cooled down on ice for 10 min. Pre-cooled virus suspension was added to 2x10^5 cells and incubated on ice for 60-90 min. Virus input was removed after centrifugation at 300 x g for 4 min at 4°C and washed twice in cold PBS before fluorescence of bound viral particles was analyzed by flow cytometry. To assess binding of pH pretreated virus particles, pH pretreatment was performed as described in section 2.2.4.1. before virus was added to cells on ice. For binding competition of TOSV and SFV, cells were first exposed to indicated amounts of unlabeled TOSV and SFV for 45 min before AF488-TOSV corresponding to 15 nM viral glycoproteins was added and left for another 60 min on ice.

For internalization assays, AF488-TOSV was bound to cells in suspension. Cells were either kept on ice, or washed in warm infection medium and the temperature was rapidly shifted to 37°C in a water bath to allow endocytosis of particles. After indicated timepoints, cells were washed with cold PBS and kept on ice until acquisition of fluorescence by flow cytometry. To differentiate between plasma membrane-bound and internalized particles, each sample was split into half, and 0.01% trypan blue was added to one half directly before acquisition.

2.2.4.3 Plasma membrane-fusion assay (endocytic bypass experiment)

To analyze the optimal pH for TOSV fusion, an endocytic bypass experiment was performed as previously described for other viruses (104, 174). Briefly, virus binding at MOI 10 was synchronized on ice as described in section 2.2.4.2. After binding, prewarmed buffers at indicated pH were added, and the plate was quickly transferred to a 37°C water bath for 90 sec. Cells were extensively washed, complete medium

supplemented with 50 mM NH_4Cl was added and incubated at 37°C for 7 h before harvesting and analysis of infection by flow cytometry.

2.2.4.4 Drug-addition and removal time courses

To determine kinetics of inhibitor-sensitive steps during entry of viruses, binding of viral particles at indicated MOIs was synchronized on ice in infection medium. The inoculum was removed and prewarmed complete medium supplemented with 20 mM HEPES was added. The temperature was rapidly shifted to 37°C in a water bath for 20 min followed by incubation in an incubator at 37°C for the remaining time period. For addition time courses, inhibitors were added at different time points and at indicated concentrations. For removal time courses, inhibitors were added in complete medium supplemented with 20 mM HEPES directly when the inoculum was removed. Inhibitors were removed and cells were extensively washed at indicated time points. Samples without inhibitor and with inhibitor kept during complete infection were included as controls. TOSV samples were harvested 5-6 h, and SARS-CoV-2 and UUKV samples 8 h after the warm shift.

2.2.4.5 Temperature entry assay

To assess the dependence of TOSV entry on temperature, virus was bound to cells on ice. SFV was used as a control. Virus inputs was removed, complete medium buffered with 20 mM HEPES was added temperature was shifted to indicated temperatures for 50 min. Samples were then transferred to 37°C, 50 mM NH_4Cl was added and incubated for further 6 h. To investigate the impact of temperature on TOSV fusion, an endocytic bypass experiment was performed at different temperatures as described in section 2.2.4.3. After TOSV binding to cells on ice, pH 5.0 and 7.4 buffers adjusted to indicated temperatures were added and samples were transferred to different temperatures for 90 sec. Cells were then washed with infection medium, prewarmed complete medium with 50 mM NH_4Cl was added and cells were incubated for 7 h at 37°C.

2.2.4.6 Cell fixation and immunostaining for flow cytometry

For harvesting, cells were washed with PBS and detached with trypsin. Detached cells were resuspended in complete medium and transferred to tubes or 96-well V-bottom plates. Cells were pelleted by 400 x g for 3 min, washed in PBS and resuspended in 4% FA for fixation. TOSV-, GERV-, RVFVΔNSs:EGFP-, SFV-, IAV-, and UUKV-infected

samples were fixed for 20 min at room temperatures whereas SARS-CoV-2 infected cells were fixed for 30 min in 4% PFA under BSL3 conditions before fixed samples could be handled under BSL2 conditions. After fixation, cells were washed in PBS and all further steps were performed in a saponin-based FACS permeabilization buffer (FPB) . Cells were first incubated in FPB for 5 min before resuspended in primary antibody diluted in 100 µL FPB and incubated for 1 h at room temperature or 4°C overnight. After washing, cells were incubated in AF488- or AF405-conjugated secondary antibody for 1 h at room temperature in the dark. Cells were extensively washed, resuspended in PBS and kept on ice until measurement with the flow cytometer. Data were analyzed with the software FlowJo v10.8.1. More information about primary and secondary antibodies and their dilutions are provided in section 2.1.4.

2.2.5 Imaging-based assays

2.2.5.1 Binding and internalization assays

To assess viral binding by microscopy, cells were seeded on 12 mm round glass cover slips in a 24-well plate format or in Lab-Tek chambers. The next day, cells were washed in cold infection medium, cooled down on ice for 10 min and viral particles were added. Samples were kept on ice for 60-90 min before cells were washed twice in cold PBS and fixed in cold 4% methanol-free PFA for 20 min on ice followed by 10 min at room temperature. Nuclei were stained with Hoechst 33258 at a concentration of 0.5 µg.mL^{-1} for 5 min at room temperature and washed in PBS. Cells in Lab-Tek chambers were kept in PBS and stored at 4°C. Cells grown on glass cover slips were washed once in dH_20, air-dried, mounted in 4 µL mowiol on a microscopy slide and dried overnight at room temperature. Cells were imaged by confocal microscopy on a Leica TCS SP8 confocal microscope.

For internalization assays, AF488-TOSV was bound to adhered cells in Lab-Tek chambers before cells were kept on ice (0 min timepoint) or washed in warm infection medium and the temperature was rapidly shifted to 37°C in a water bath to allow endocytosis of particles. After 0 and 30 min at 37°C, cells were washed with cold PBS and fixed for confocal imaging. Nuclei were stained by Hoechst and cells were imaged, before 0.02% trypan blue was added and the same cell was imaged again.

2.2.5.2 Co-localization analysis of TOSV with EGFP-tagged endosomal markers

A549 cells were transfected on glass cover slips with EGFP-tagged endosomal markers as described in section 2.2.2., before ATTO647N-TOSV at MOI 1 was bound to cells on ice 22 h post-transfection. Internalization of viral particles was allowed by rapid shifting to 37°C for indicated timepoints before cells were returned back on ice. Fixation and mounting were performed as described in section 2.2.5.1.

2.2.5.3 Cell-cell fusion assay of SARS-CoV-2

$5x10^4$ A549*, $5x10^4$ A549* TMPRSS+ or $2x10^4$ Vero cells were seeded in 8-well Lab-Tek chambers and infected with SARS-CoV-2 at MOI 0.1 and 0.2, respectively. After 24 h, non-infected CMFDA-labeled target cells were added and co-cultured for 5 h. For labeling and preparation of target cells, CMFDA was added at a concentration of 2.5 µM to cells for 30 min at 37°C. Cells were washed in PBS and detached with EDTA as described in section 2.2.4.2. Detached cells in suspension were then added to SARS-CoV-2 infected donor cells at a ratio of donor to target cell of 2:1. After 5 h, co-cultured cells were left untreated or exposed to furin (1 $\mu g.mL^{-1}$) or trypsin (100 $\mu g.mL^{-1}$) for 5 min at 37°C. Cells were gently washed and left to incubate for 1 h prior to fixation. Alternatively, cells were first treated with trypsin, left resting for 1 h at 37°C before buffers at pH of 7.4, 6.0 and 5.0 were added for 5 min at 37°C. The co-cultured cells were again washed and left to incubate for 1 h at 37°C before fixation. To assess the role of TMPRSS2, camostat mesylate (100 µM) was added during the whole 5 h of co-culture. Cells were fixed in 4% methanol-free PFA/ 0.2% glutaraldehyde in PBS for 10 min before plunging in 6% FA bath for 30 min. Cells were extensively washed in PBS and permeabilized in 0.1% triton X-100/PBS for 5 min at room temperature. Samples were blocked in 5% BSA/PBS overnight at 4°C and infected cells were stained with anti-SARS NP and incubated overnight at 4°C. After washing, an anti-mouse antibody coupled to AF647 was added for 1 h at room temperature in the dark. Nuclei were stained in Hoechst. Formation of syncytia was evaluated by fluorescence confocal microscopy.

2.2.5.4 Confocal fluorescence microscopy and image analysis

3D stacks of samples were acquired by confocal microscopy on a Leica TCS SP8 confocal microscope equipped with an HC PL APO CS2 63x/1.4 N.A. oil immersion objective. Images were recorded with an excitation wavelength of 405, 488, 561 and 640 nm. Stacks had a z-spacing of 200 -1000 nm with 200 nm used for co-localization

analysis of TOSV with endosomal markers, and 1000 nm for SARS-CoV-2 cell-cell fusion assays. Images were analyzed by Image J. For binding assays, 3D stacks of cells were inverted and minimal projected. The noise was reduced with the Gaussian Blur filter and particles were selected by applying a threshold. A Watershed algorithm was applied to separate overlapping particles. Each cell was selected individually to count puncta with the “analyze particles” plugin. For co-localization analysis, the total number of particles per cell and the number of particles co-localizing with vesicles positive for endosomal markers were counted. In the SARS-CoV-2 cell-cell fusion assay, syncytia formation was determined by counting all cells and nuclei in CMFDA-positive cells. A fusion index *f* was calculated based on the equation $f = (1 - [c/n])$ where *c* is the number of cells and *n* is the number of nuclei in a field of view. An average field of view contained roughly 30 Vero or 60 A549* nuclei.

2.2.5.5 Super resolution microscopy of TOSV particles

ATTO647N-TOSV particles were imaged by super resolution microscopy with a 2-color STED microscope equipped with an x100 Olympus UPlanSApo (NA 1.4) oil immersion objective. Virus particles were mounted in mowiol on PEI-coated coverslips and imaging was performed by Dr. Susann Kummer, a former member of the Kräusslich group, Heidelberg, as previously described (268). The pixel size was set to 60 nm (confocal) and 15 nm (nondiffracted). Minor adjustments of contrast and brightness of images and the Richardson–Lucy deconvolution with a regularization parameter of 0.001 stopped after 30 iterations were carried out using Imspector software 16.1.7098 (Abberior instruments).

2.2.5.6 Cryo-EM sample preparation and image acquisition

For cryo-EM imaging, semi-purified TOSV was further purified over a linear sucrose gradient as described in section 2.2.3.2. To remove sucrose, particles were washed in HNE buffer and pelleted by ultracentrifugation at 100,000 x g for 90 min at 4°C. Virus pellet was resuspended in 4% methanol-free PFA and flash-frozen in liquid nitrogen. Particles were imaged by Dr. Martin Obr, a former member of the Florian Schur lab at IST Austria, as recently described (250). Briefly, virus was applied to degassed Quantifoil R2/2 Cu grids and vitrified in liquid ethane by a plunge freezer. Images were acquired on a Thermo Fisher Scientific Glacios transmission electron microscope using SerialEM software. The nominal magnification was 73,000x, resulting in a pixel spacing of 2.019 Å. Cryo-EM images were further analyzed by ImageJ. Diameter of virions and membrane-to-

membrane distance were measured by the distance of peaks in density profiles on the opposite side of the viral particle. The largest and smallest diameters of each particle were measured to determine the sphericity.

2.2.6 R18-based fusion assays

R18-labeled TOSV was used to evaluate fusion with host cell membranes. To analyze dequenching of R18-TOSV upon dilution of the dye, particles diluted in HNE buffer were analyzed in a cell-free dequenching assay. The fluorescence emission of quenched R18-TOSV was measured by a Jasco FP-8500 spectrofluorometer. Triton X-100 was added to disrupt the membrane to a final concentration of 1% and fluorescence was measured again. To assess kinetics of penetration from endosomes, R18-TOSV was bound to A549 cells in suspension at MOI 10 on ice in phenol-free infection medium. Cells were pelleted after virus binding and resuspended in prewarmed complete phenol-free medium supplemented with 20 mM HEPES before cell suspension was transferred into a cuvette placed inside a spectrofluorometer warmed to 37°C. Fluorescence emission was measured every min over 90 min at 37°C. As control, 50 mM NH_4Cl was added to one sample to block acidification of endosomes. To analyze fusion kinetics with the plasma membrane, R18-TOSV was allowed to bind to cells on ice. After 90 min binding on ice, cells were pelleted by centrifugation at 4°C and resuspended in PBS prewarmed to 37°C directly before acquisition in a spectrofluorometer. Fluorescence emission was recorded every sec for 600 sec. After 30 sec, a pre-defined volume of pH buffers was injected into the sample to reach the indicated pH value ranging from pH 5.0-7.4 in the cell suspension. After 550 sec, triton X-100 was added. Data were normalized to input and background fluorescent increase from pH 7.4 sample was subtracted. Kinetics were analyzed using GraphPad Prism. For kinetics of pH pretreated TOSV, pH pretreatment was performed as described in section 2.2.4.1. before binding to cells on ice.

2.2.7 Protein analysis by SDS-PAGE and western blotting

For lysis of cells, cells were washed in PBS, detached by scraping in cold PBS and cells were pelleted by centrifugation for 300 x g for 4 min. Cell pellet was resuspended in cold lysis buffer and incubated for 20 min on ice. The lysed cells were centrifuged at 10,000 rpm in a table-top centrifuge for 20 min at 4°C and the supernatant was stored at -20°C until subjected to SDS-PAGE and western blotting. Cell lysates were mixed with 4X SDS sample buffer and boiled at 95°C for 5 min before loaded on a precast 10% Bis-Tris

gel. Electrophoresis was performed under nonreducing conditions, if not stated otherwise, in MOPS SDS running buffer at 125V for 90 min. Proteins were then transferred to a polyvinylidene difluoride (PVDF) membrane by using the iBlot dry blotting system. Membranes were blocked in 5% milk/ TBST for at least 1 h at room temperature on a rocker before incubated in primary antibody diluted in 5% BSA/ TBST overnight at 4°C on a shaker. The membrane was washed thrice for 10 min in TBST and transferred to Li-COR secondary antibodies diluted in Li-COR intercept blocking buffer for 1 h at room temperature in the dark. More information about primary and secondary antibodies and their dilutions are provided in section 2.1.4. Membranes were again washed thrice for 10 min in TBST and acquired on a Li-COR Odyssey CLx scanner. Band intensities were analyzed by ImageJ.

2.2.8 Statistical analysis

Graph plotting and statistics were performed with Prism v8.0.1. Figures show means ± standard deviation (SD) if not stated differently. Figure legends indicate number of independent experiments performed in duplicates or triplicates (n), statistical method and p values when appropriate.

3 Results

3.1 Characterization and fluorescent labeling of TOSV produced from mammalian cells

3.1.1 Production and purification of TOSV from BHK-21 cells

In this thesis, I used TOSV, a representative phenuivirus transmitted by phlebotomine sand flies, and aimed to study its entry into human host cells. This work is currently under revision as a single first author in PLOS Pathogens (269). Before TOSV could be used for entry experiments, protocols for its production, purification, titration, and characterization had to be established and optimized. In addition, protocols for fluorescent labeling of viral particles were established to enable qualitative and quantitative fluorophore-based assays.

TOSV could be produced from the fibroblastic baby hamster kidney (BHK)-21 cells. The collected supernatant containing viral particles was semi-purified by ultracentrifugation through a 30% sucrose cushion. Viral proteins were then separated by nonreducing SDS-PAGE and stained with Coomassie blue (**Figure 19A**). TOSV Gn and Gc showed molecular weights of approximately 46 kDa, while that of the N protein was about 27 kDa. For immunodetection, I mainly relied on antibodies that were homemade. Antibodies were raised in guinea pigs either against viral particles, which allowed to detect all structural proteins, the nucleoprotein N and the glycoproteins Gn and Gc, with a single polyclonal antibody, or against individual peptides derived from the Gn, Gc, and N proteins (258). The individual peptides enabled to generate polyclonal antibodies specific for Gn, Gc, and N proteins. When the viral proteins were separated by SDS-PAGE followed by western blotting, Gn, Gc and N could be detected with the antibody directed against the structural proteins at the same sizes as the bands appearing in the Coomassie staining (**Figure 19B**). In addition, antibodies directed against a single viral protein detected only Gn, Gc and N. Two unspecific bands of weak intensity at approximately 58 and 64 kDa appeared with the antibodies against Gn and TOSV raised in guinea pigs in mock-infected samples, but did not represent a limitation for my future analysis.

The concentration of viral proteins was quantified from Coomassie stained gels by plotting a curve of the band intensities of a BSA standard with determined quantities (**Figure 19C**, **D**). For all virus productions, N and glycoprotein concentrations were included in the range

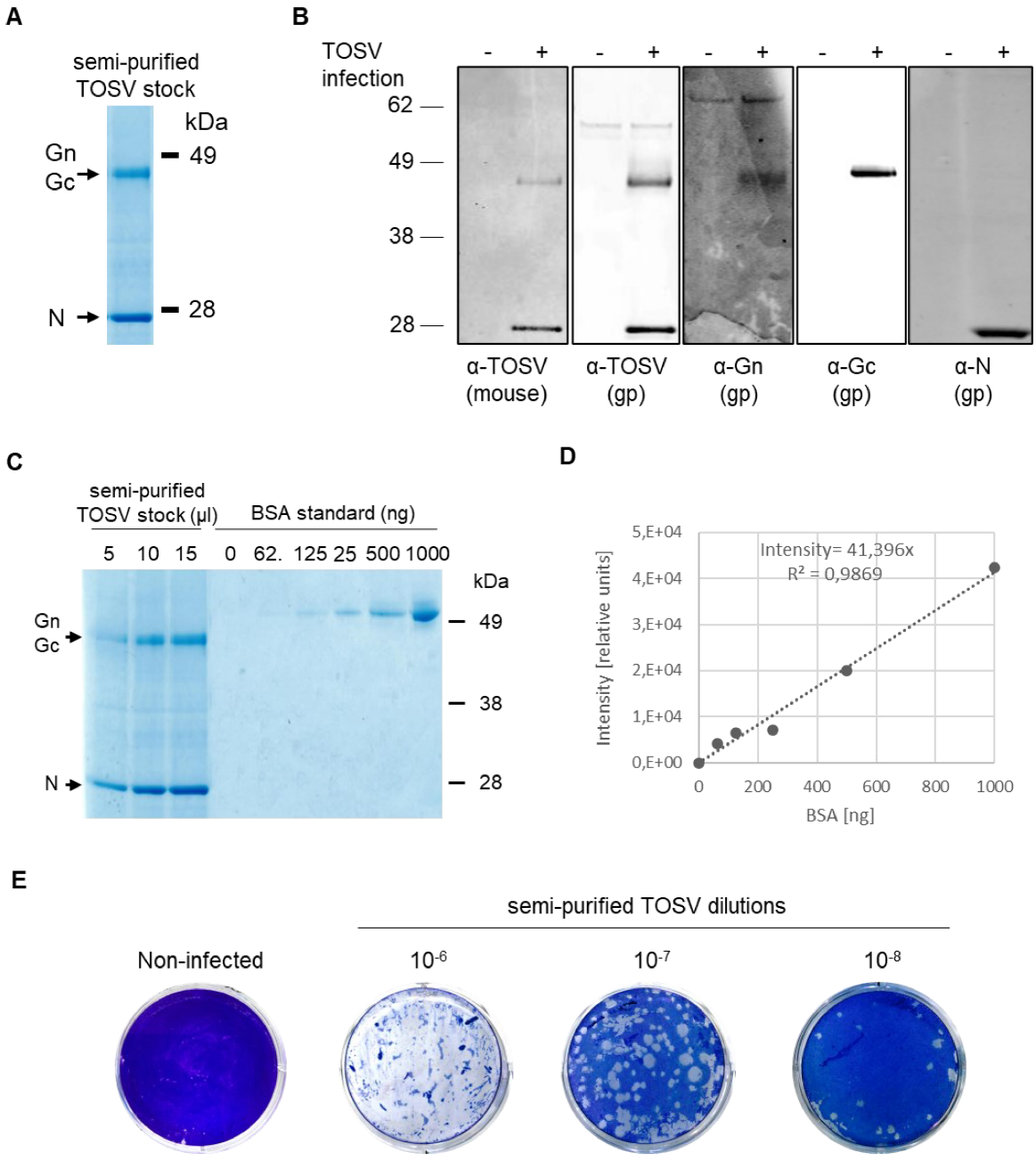

Figure 19. Characterization of TOSV proteins and titer after amplification in BHK-21 cells.

(A) Proteins from viral particles purified through sucrose cushion were separated by SDS-PAGE followed by Coomassie blue staining. (B) Cell lysate of noninfected or TOSV-infected A549 or HEK293T cells (for N protein) were subjected to SDS-PAGE followed by western blotting. Viral proteins were visualized using mouse and guinea pig (gp) antiserum raised against TOSV, or guinea pig antibodies individually against TOSV Gn, Gc, or N protein. (C) Viral proteins of semi-purified TOSV together with a BSA standard scale were subjected to SDS-PAGE and stained with Coomassie blue. (D) Band intensities of BSA standard were plotted against their quantities in ng. Concentrations of viral proteins could be determined by comparison to the standard curve. (E) TOSV titers were determined by plaque-forming unit (pfu) assay on BHK-21 cells using 10-fold dilutions of the virus stock. After four days of incubation at 37°C, cell layers were fixed and plaques were visualized by crystal violet staining.

55 - 320 µg.mL^{-1} and 84 - 370 µg.mL^{-1}, respectively, with a glycoprotein to N protein ratio between 0.7 – 1.8.

The infectivity of TOSV was measured as titrated by plaque-forming titration assays on BHK-21 cells (**Figure 19E**). Virus could be produced to titers as high as 10^7 – 10^8 pfu.mL^{-1} in the supernatant of infected BHK-21 cells and 10^9 - 10^{10} pfu.mL^{-1} after concentration during the semi-purification ultracentrifugation step.

3.1.2 Cryo-EM imaging of TOSV particles

TOSV particles were washed in HNE buffer to remove sucrose, fixed in 4% PFA, and vitrified prior to cryo-EM. Cryo-EM was performed in collaboration with Dr. Martin Obr from the Florian Schur lab (IST Austria). The particles appeared to be enveloped, nearly spherical with a diameter of 121 ± 11 nm and spike-like protrusions of 9 ± 2 nm (n=96) (**Figure 20A, B**). The roundness coefficient, *i.e.*, the ratio of perpendicular width to length, reflected the sphericity of virions and was close to 0.92 ± 0.06. The closer the sphericity index is to 1, the more spherical the viral particles are.

3.1.3 TOSV can infect cell types from a broad range of species and tissues

TOSV causes a variety of symptoms in humans, and seroprevalence of TOSV has been reported in various animal species, including horses, cats, dogs, cattle, goats, bats, and birds (60, 62, 270–274). This suggested a broad tissue tropism and a wide host range. To test this, the susceptibility of 19 cell lines representing different cell types from different species to TOSV infection was determined. Infection was allowed for 18 h and was assessed in a flow cytometry-based assay after immunostaining with the mouse-derived antibody directed against all TOSV structural proteins (**Table 2**). 16 of 19 cell lines were susceptible to infection, including a wide range of different epithelial cell types of human and mammalian origin. In addition, all three sand fly-derived cell lines allowed TOSV infection. The phlebotomine PPL/LULS49, derived from the natural vector of TOSV, showed higher susceptibility compared to sand fly cell lines derived from Lutzomyia sand flies (PPL/LULS40 and PPL/LULS45). Cells of the myeloid or lymphoid lineage had low susceptibility to TOSV infection.

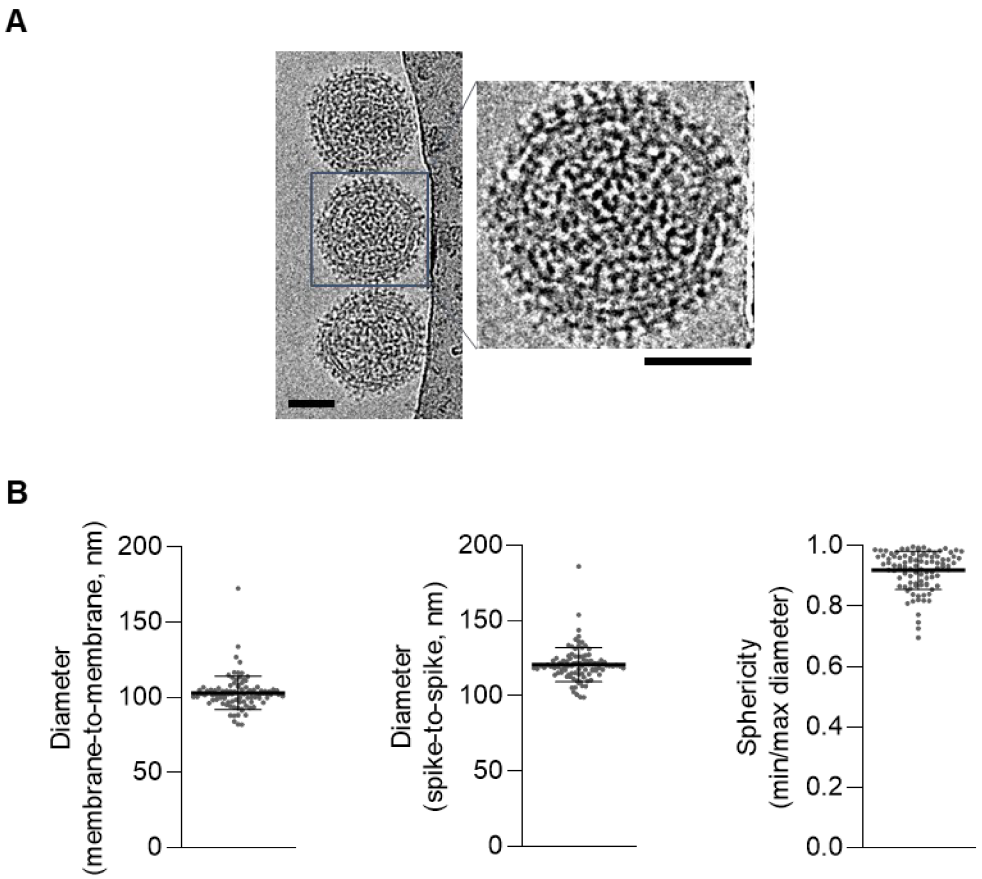

Figure 20. Structural organization of TOSV particles.

(A) Purified TOSV particles were fixed with paraformaldehyde, vitrified, and analyzed by cryo-EM. Martin Obr (formerly Florian Schur group, IST Austria) performed the Cryo- EM workflow and imaging. The right panel shows a representative image of the cryo-electron micrograph of TOSV particles, and the left panel shows an enlarged view. Scale bar, 50 nm. (B) The membrane-to-membrane and spike-to-spike diameter of TOSV particles were determined (n=96). The sphericity was determined by calculating the ratio of minimal to maximal diameter (n=96). The results were published in (269).

TOSV production by pfu titration unit assay was evaluated in eight TOSV-susceptible cell lines that are adherent. Plaques appeared after 72 h in seven of the eight cell lines, suggesting that most TOSV-susceptible cell lines support complete TOSV replication cycles in which new infectious virions are produced and released (**Table 2**).

Since TOSV can cause meningoencephalitis in humans, the sensitivity of brain cells to TOSV infection was tested. Human functional glutamatergic neurons were generated from human iPS cells by expression of the transcription factor neurogenin-2 in collaboration with the group of Claudio Acuna in Heidelberg (232). Human induced mature neurons were then exposed to different MOIs of TOSV for up to 48 h. Infection of the cells was

Table 2. Susceptibility and permissiveness of different mammalian and sand fly cell lines to TOSV infection.

Cell Lines	Specie	Tissue	Sensitivity to TOSV infection[a]	Production of new viral particles[b]
A549	Human	Lung epithelial	+++	+++
HEK293T	Human	Embryonic kidney	+	n.d.
HeLa	Human	Cervix epithelial	+	+++
Huh-7	Human	Liver epithelial	+++	++
iPSC-derived neurons	Human	Neurons	++	n.d.
Jurkat	Human	T lymphoblast	-	n.d.
Raji	Human	B lymphocyte	+	n.d.
SUP-T1^{R5}	Human	T lymphoblast	-	n.d.
SH-SY5Y	Human	Neuroblast	+++	n.d.
THP-1	Human	Monocyte	-	n.d.
U87[44]	Human	Glial cells	++	n.d.
BHK-21	Hamster	Kidney fibroblast	+++	+++
DF-1	Chicken	Embryonic fibroblast	+	++
L929	Mouse	Fibroblast	+	-
MDCK	Dog	Kidney epithelial	+	++
Vero E6	Monkey	Kidney epithelial	+++	++
LLE/LULS40	Sand fly	Embryonic	+	n.d.
LLE/LULS45	Sand fly	Embryonic	+	n.d.
PPL/LULS49	Sand fly	Larva	++	n.d.

Data were generated by lab rotation student Nina Rolfs in our lab under the supervision of Zina Uckeley, except for PPL/LULS49 that were analyzed by Qilin Xin, and iPSC-derived neurons, LLE/LULS40 and LLE/LULS45 that were assessed by myself. [a]Cells were exposed to TOSV for 18 h at MOI 1 and infection was analyzed by flow cytometry after immunostaining against TOSV structural proteins. Sensitivity to TOSV infection is expressed as the percentage of infected cells and is given as follows: +++ greater than 30%, ++ between 10% and 30%, + from 1% to 10%, and – less than 1%. [b]The production of TOSV was assessed in certain cell lines shown to be sensitive to TOSV infection. Production of virus was assessed by pfu titration assay after exposition to TOSV stocks at dilutions of 10^{-6} – 10^{-8} for 72 h. Diameter of plaques were determined. Level of production was given according to the size of plaques with +++ greater than 1 mm, ++ between 0.5 and 1 mm, + less than 0.5 mm and – no plaques observable. n.d., not determined. The table was published in (269).

quantified by flow cytometry after immunostaining with the mouse-derived antibody directed against all TOSV structural proteins. An example of the gating strategy is shown in **Figure 21A**. After setting a gate on the cell population and selecting only single cells, infected cells were detected by an increase in fluorescence due to immunofluorescence

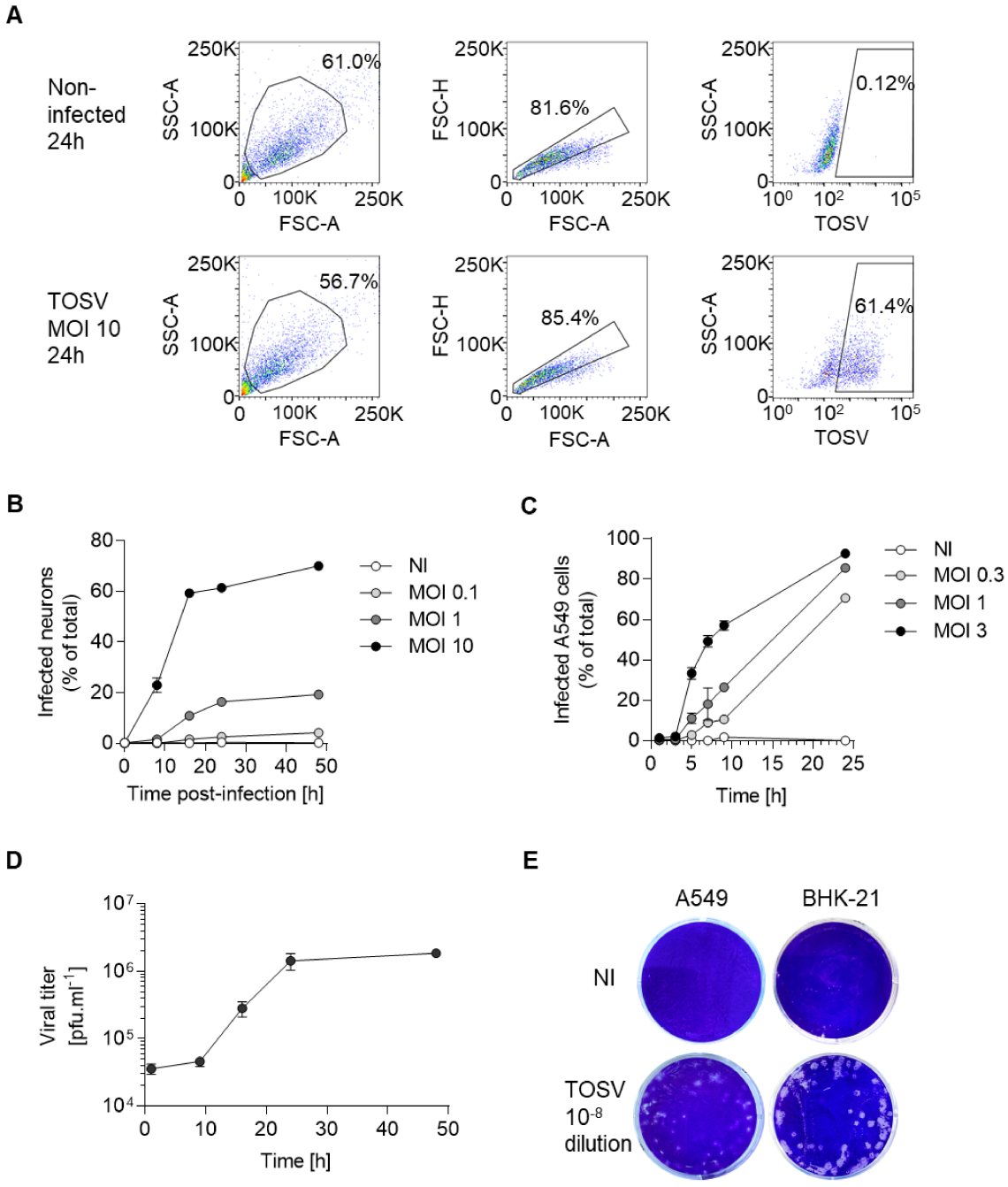

Figure 21. Characterization of TOSV infection in iPSC-derived neurons and A549 cells.

(A) Induced neurons were generated from human iPSC cells and provided by Alessandra Albertelli (formerly Claudio Acuna group, Heidelberg University, Germany). Mature, glutamatergic neurons were exposed to TOSV at MOI 10 for 24 h. Infection was analyzed by flow cytometry after immunostaining of viral proteins. Representative gating strategy of flow-cytometry workflow is shown starting with a cell gate in the forward scatter (FSC) and the sideward scatter (SSC) plot. Single cells were selected based on the FSC-A (area) and FSC-H (height) plots. Infected and noninfected cells could be distinguished based on their fluorescence intensity after immunostaining. Gates were set in non-infected samples and applied to infected samples. (B) iPSC-derived neurons were infected with TOSV at indicated MOIs and infection was monitored over 48 h using the flow cytometry-based assay described in A. n = 1. (C) A549 cells were exposed

to TOSV at indicated MOIs up to 24 h. Infection was analyzed by flow cytometry. Data show one out of three representative experiments in triplicates. (D) Supernatant of A549 cells infected with TOSV at MOI 2 was collected after indicated time points, and infectivity was determined by pfu assay on BHK-21 cells. Data show a representative experiment of two in triplicates. (E) Representative images of pfu titration assay on BHK-21 and A549 cells of semi-purified TOSV at a dilution of 10^{-8}. The figure was adapted in a modified version from (269).

staining with the antibody directed against newly synthesized TOSV proteins. Around 70% of the induced neurons were infected after 48 h at MOI of 10 (**Figure 21B**). The percentage of infected cells increased with higher MOI and over time, reaching a plateau after 16-24 h. This indicates that the fluorescence signal detected in this assay corresponds to the synthesis of new viral proteins and not to the input virions.

The human lung epithelial cell line A549 was highly susceptible to TOSV infection, supported a complete viral replication cycle (**Table 2**). This cell line represents the advantage to divide every 24 h and is easier to handle in larger quantities compared to the complex iPSC-derived mature neurons. To evaluate infection kinetics, A549 cells were infected at different MOIs and allowed to infect for up to 24 h. Similar to induced neurons, the percentage of infected A549 cells increased over time and also when higher MOIs were used for infection (**Figure 21C**). 57% of A549 cells were infected after 9 h at MOI 3, which increased to over 90% after 24 h. The supernatant of infected A549 cells was collected and titrated on BHK-21 cells. An initial increase in viral titers was observed between 9 and 16 h and reached a plateau between 24-48 h (**Figure 21D**). Taken together, this suggests that TOSV completes a round of infection from binding and internalization to release of newly produced infectious progeny within 9-16 h in A549 cells. In addition, I also observed plaques on a monolayer of A549 cells infected with TOSV (**Table 2**, **Figure 21E**). The titer of TOSV on A549 cells was similar to that on BHK-21 cells, although the plaques in A549 cells were smaller and more diffuse.

3.1.4 TOSV particles were labeled with fluorescent NHS ester or membrane dyes

To follow the entry steps of TOSV by fluorescence-based techniques, the viral envelope glycoproteins Gn and Gc were labeled with fluorescent NHS ester dyes. Dyes with excitation wavelengths of 488 and 647 nm, respectively, were coupled to free lysine residues of TOSV glycoproteins using an adapted protocol as published by our group for the labeling of UUKV (267). Labeling conditions for TOSV were set to find a balance between brightness and loss of infectivity, allowing detection by sensitive imaging and

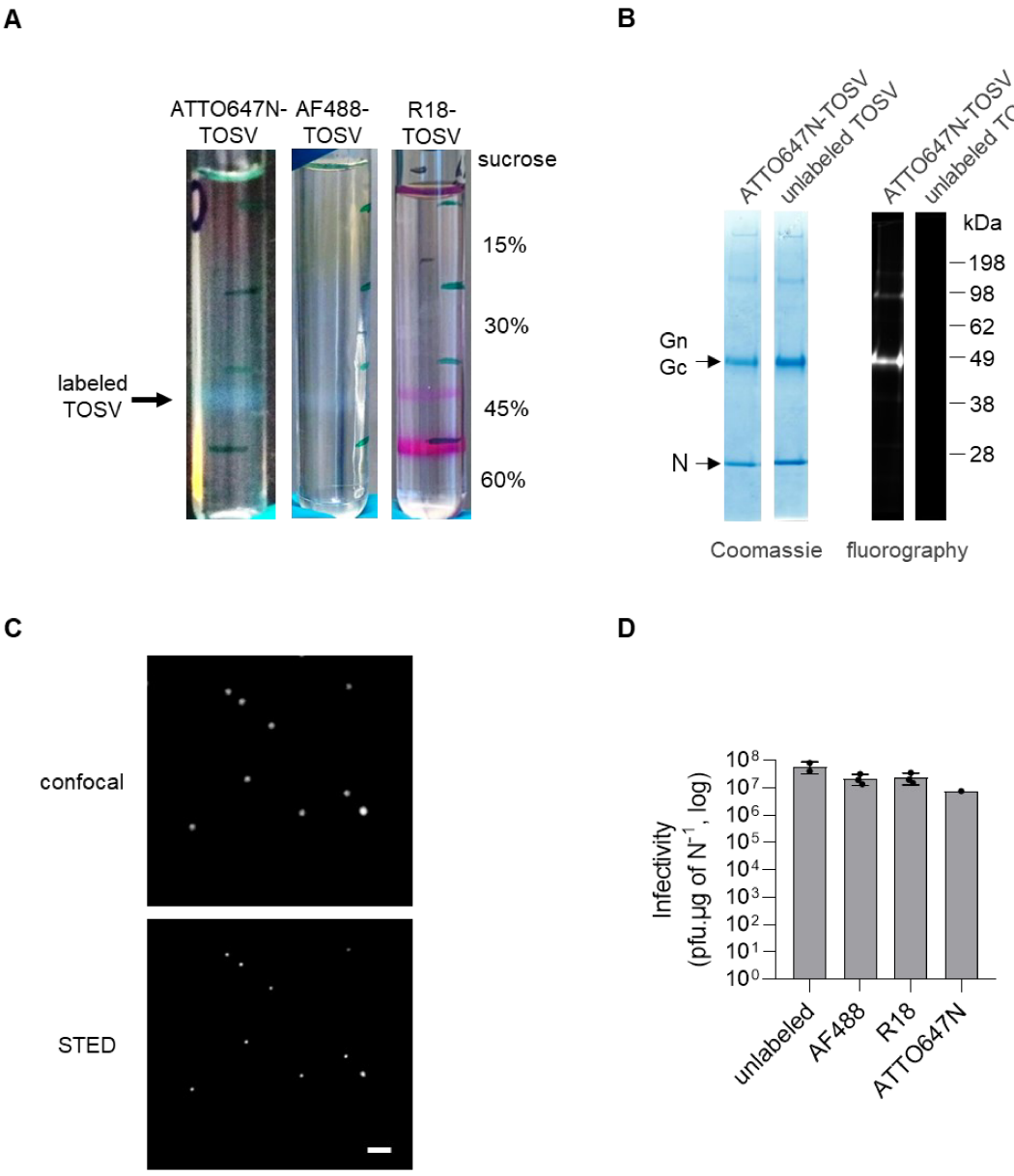

Figure 22. Labeled TOSV particles are fluorescent and infectious.

(A) TOSV particles were labeled with the NHS ester dyes ATTO647N and AF488, or the membrane dye R18. Particles were purified over a linear sucrose gradient by ultracentrifugation. Banded virus appeared at 40-45% sucrose whereas excessive ATTO647N and AF488 could be detected on top of the gradient and for R18 at around 50-55% sucrose. (B) ATTO647N-labeled und unlabeled TOSV were extracted from the gradient and fluorescence of individual viral proteins was analyzed by fluorography after SDS-PAGE. After imaging, all proteins were visualized by Coomassie blue staining. (C) Fluorescence of ATTO647N-TOSV particles was analyzed by confocal microscopy (top panel) and by stimulated emission depletion (STED) microscopy (lower panel). Imaging was performed by Dr. Susann Kummer (formerly in Hans-Georg Kräusslich group, University Hospital Heidelberg, Germany). Scale bar, 1 µm. (D) Infectivity of unlabeled and labeled TOSV was determined by pfu titration assay on BHK-21 and normalized to N protein amount. n = 1-3. The figure was adapted from (269).

flow cytometry-based approaches while maintaining infectivity. After semi-quantification of glycoprotein concentration using a BSA standard, virus corresponding to approximately 100 µg of glycoproteins was labeled with AF488 and ATTO647N dyes at a glycoprotein to dye molar ratio of 2:1 and 1:1, respectively. Alternatively, the viral envelope was labeled with the lipophilic dye R18. A high concentration of R18 in labeled virus membranes leads to auto-quenching of its own fluorescence. Thus, R18-labeled virus allows the study of fusion events by measuring an increase in fluorescence signal upon dilution of the dye after fusion with target cell membranes.

Labeled virus particles were purified by density ultracentrifugation through a 0-60% sucrose gradient to remove unbound dye. As a control, TOSV was mixed with the solvent used to prepare the dye stocks (unlabeled TOSV) and purified in parallel of the dye-labeled virus. ATTO647N- and AF488-labeled TOSV appeared as a fluorescent band at 40-45% sucrose of blue and green color, respectively, whereas unlabeled virus appeared milky white (**Figure 22A**). Unbound ATTO647N and AF488 NHS ester dyes were observed at the top of the gradient, while excessive unbound R18 appeared as a band at 50-55% sucrose concentration. The banded virus was extracted, viral proteins were separated by SDS-PAGE, and fluorescence of viral proteins was analyzed using an in-gel fluorescence gel imager followed by Coomassie blue staining, as shown for ATTO647N-TOSV (**Figure 22B**). The structural proteins of Gn, Gc, and N could be detected by Coomassie blue staining in both labeled and unlabeled TOSV. In contrast, only the band corresponding to the viral envelope proteins Gn and Gc of the ATTO647N-labeled virus was fluorescent, but not the N protein or any protein of a unlabeled control. This indicates that the fluorescent labeling of the virus particles was successful and that the particles were still intact after the labeling process.

I then visualized the fluorescently labeled particles by microscopy. Confocal and super-resolution stimulated emission depletion (STED) microscopy revealed single spherical particles (**Figure 22C**). Spots of varying intensity could indicate partial clustering of 2-3 virions that appear as one spot due to the diffraction limit of confocal microscopy, but better resolved by STED microscopy. Infectivity normalized to viral protein N quantities, which reflects the total number of viral particles, infectious or not, revealed that infectivity of labeled virus was similar to that of unlabeled virus (**Figure 22D**). This suggests that fluorescently labeled viral particles are still able to enter cells and complete the viral life cycle.

ATTO647N-TOSV was then added to A549 cells at MOI 1 and bound to the cell surface on ice. This allows for synchronized binding of virions without internalization. Fluorescent

particles bound to the cell surface were imaged by confocal microscopy as bright fluorescent spots (**Figure 23A**). Viral particles were visible on the cell surface of the cells in individual focal planes. Combining all focal planes of the z-stack, the total number of bound particles per cell was 10.5 ± 8.5 (n = 151) at an MOI of 1. This indicates that most

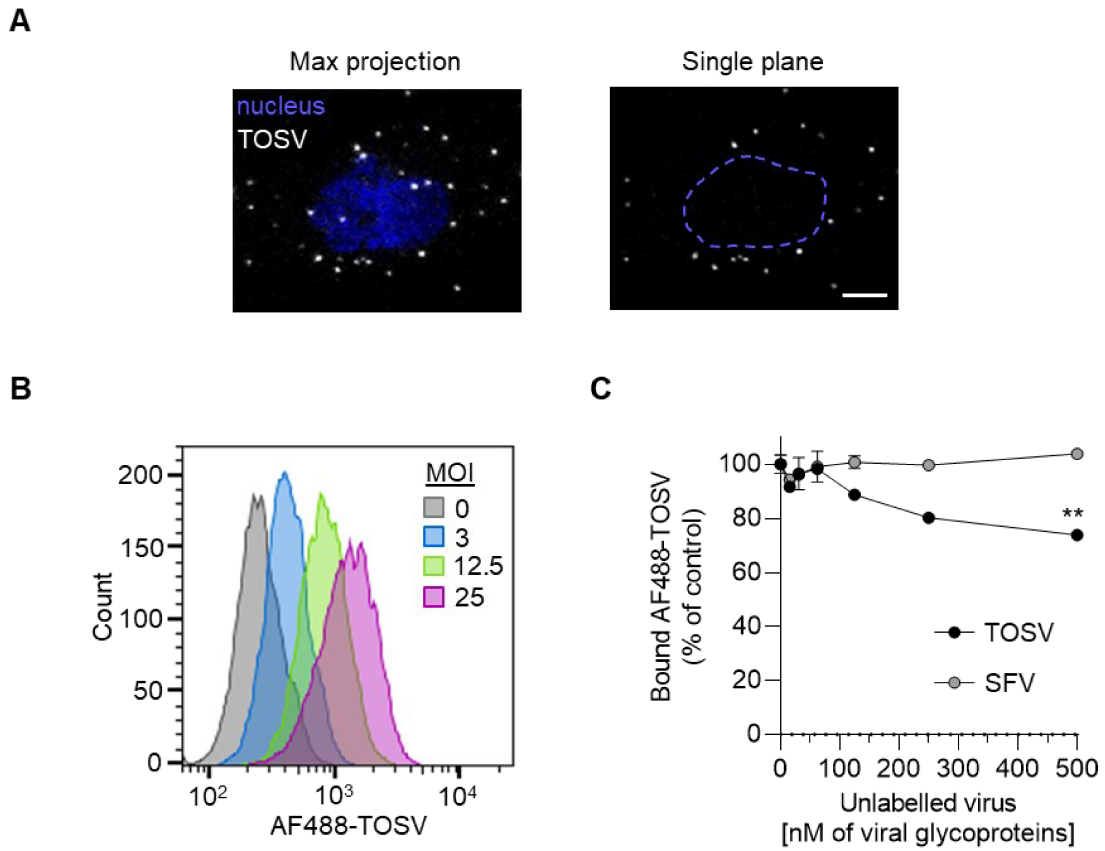

Figure 23. Labeled TOSV specifically bind to cells.

(A) ATTO647N-TOSV particles at MOI 1 were bound to A549 cells on ice for 90 min, fixed, and nuclei were stained with Hoechst. Cells were imaged by confocal microscopy. Left panel shows a maximum projection of a cell with associated virions (in white) acquired in the 647 nm channel. A single plane of the same cell is shown on the right side with nuclei border marked in blue dashed lines. Scale bar, 5 µm. (B) AF488-TOSV at indicated MOIs were bound to A549 cells on ice and washed before the analysis of cell-associated fluorescence by flow cytometry. Histograms of intensities in the AF488 channel of representative samples are shown. (C) A549 cells were first exposed to increasing amounts of unlabeled TOSV and SFV for 45 min on ice. Then AF488-TOSV at a quantity equivalent to 15 nM of viral glycoproteins Gn and Gc was allowed to bind to cells for another hour. Input viruses were removed, cells were washed, and fluorescence was analyzed by flow cytometry. Data were normalized to samples without pre-bound unlabeled TOSV or SFV. T-test with Welch's correction was applied at the highest concentration of unlabeled virus. Data show one out of two representative experiments in duplicates. **, p = 0.0039. The figure was modified from (269).

of the bound particles are non-infectious and gives a ratio of infectious to non-infectious virions inferior to 1:10. Bound fluorescent particles were also detected by flow cytometry. AF488-TOSV binding to A549 cells was detectable at MOI 3 and the fluorescence signal increased at higher MOIs (**Figure 23B**).

To assess the specificity of TOSV binding to A549 cells, a competitive binding approach was performed. Briefly, A549 cells were first exposed to increasing concentrations of unlabeled TOSV before fluorescent AF488-TOSV was added. As a control, A549 cells were pre-bound with SFV, an unrelated virus of the *Alphavirus* genus. Pre-binding of increasing concentrations of TOSV resulted in a dose-dependent reduction in binding of fluorescent TOSV, indicating competition for binding to the same receptor and/or attachment factors (**Figure 23C**). Conversely, pre-binding of SFV did not affect the level of AF488-TOSV binding, suggesting binding to alternative receptor(s). Complete inhibition of binding could not be achieved because the necessary concentration of unlabeled virus could not be achieved under my experimental conditions. Taken together, these data demonstrate that TOSV binds to A549 cells in a specific manner.

3.2 TOSV enters cells by acid-activated membrane fusion from late endosomes

3.2.1 TOSV particles are internalized within 10 min into A549 cells

According to previous reports on phenuivirus entry, virions enter cells by endocytosis and fuse from endosomal compartments. To follow the viral entry of TOSV, I first analyzed whether TOSV particles are internalized into cells. A trypan blue-based internalization assay was performed to distinguish between internalized and surface-bound virions (**Figure 24A**). The assay is based on the property of membrane-impermeable trypan blue to quench green-emitting dyes such as AF488. Thus, the fluorescence of surface-bound AF488-labeled viruses is quenched, whereas the fluorescence intensity of internalized particles is not affected by the cell-impermeable trypan blue. Binding of AF488-TOSV to A549 cells was synchronized on ice, and viral endocytosis was allowed by rapid warming to 37°C for 30 min before returning to ice. Without warming, AF488-TOSV could be detected by confocal imaging as single spots bound to the cell surface (**Figure 24B**). Fluorescence of viral particles was undetectable upon addition of trypan blue, suggesting that all particles were surface-bound and none were internalized when samples were kept on ice. Strikingly, fluorescence of approximately three-quarters of AF488-TOSV was still

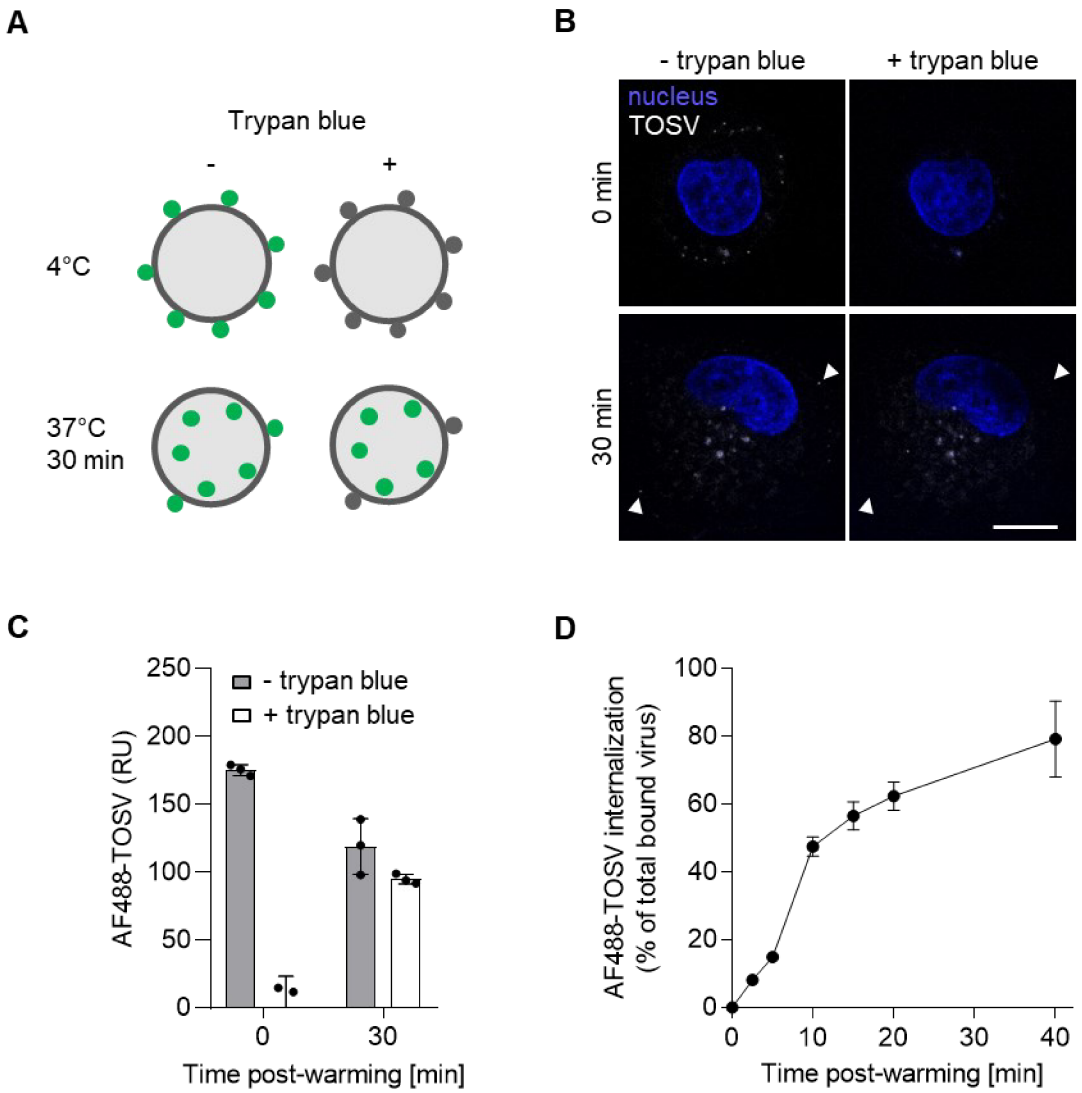

Figure 24. Internalization of TOSV particles into cells.

A) Principle of the trypan blue-based internalization assay. Trypan blue is membrane-impermeable and can only quench the fluorescence of cell-surface exposed AF488-TOSV but not of internalized particles. Uptake of particles into cells is triggered by the rapid warming of bound particles to 37°C. (B) AF488-TOSV at MOI 10 was bound to A549 cells on ice. Input virions were removed, and the temperature was rapidly shifted to 37°C for 30 min before cells were washed and fixed. For the 0 min time point, cells were washed after binding and left on ice until fixation. Nuclei were stained with Hoechst, and cells were imaged by confocal microscopy. Trypan blue (0.02%) was added and the same cell was imaged again. Arrowheads in the 30 min sample indicate fluorescent particles at the cell surface, which were quenched by adding trypan blue. Single planes of representative images are shown. Scale bar, 10 µm. (C) AF488-TOSV was bound to A549 cells at MOI 10 in suspension. After binding, the input virus was removed and cells were rapidly shifted to 37°C for 30 min or left on ice. Cells were washed, and fluorescence was analyzed by flow cytometry after the addition, or not, of trypan blue. RU, relative unit. Data show a representative experiment of three in triplicates. (D) Internalization of AF488-TOSV was performed as described in (C) for indicated time periods. Internalization is given as the percentage of the fluorescent signal before

and after the addition of trypan blue. The fluorescent signal of A549 cells without bound AF488-TOSV was subtracted as background. n = 3. The figure was adapted from (269)

detectable after warming to 37°C for 30 min and addition of trypan blue. Notably, the fluorescence of internalized particles appeared less punctate, suggesting that the viral envelope with labeled glycoproteins had already fused to an intracellular membrane.

To quantitatively assess internalization, I bound AF488-TOSV to A549 cells at a MOI of 10 and used flow cytometry as a readout. Similar to confocal imaging, the fluorescence of AF488-TOSV was completely quenched by trypan blue if samples were not warmed before analysis, and the fluorescence intensity of the samples was at the background level, *i.e.*, of cells without bound virus (**Figure 24C**). In contrast, after warming to 37°C for 30 min, approximately 80% of the fluorescence signal remained upon addition of trypan blue. Taken together, the data obtained by both confocal microscopy and flow cytometry suggest that the majority of viral particles are taken up by the cells within the first 30 min.

In order to determine the kinetics of internalization, I analyzed the rate of internalization, *i.e.*, the ratio of the signal with and without trypan blue, over time in a flow cytometry-based approach. The first events of internalization could be detected as early as 2.5 min and increased with time (**Figure 24D**). Half-maximal intensity was reached at 9.1 ± 2.4 min and plateaued 10-30 min later. Taken together, these data show that TOSV particles are internalized into A549 cells in a rapid and rather synchronous manner.

3.2.2 TOSV requires vacuolar acidification for infection

To investigate whether the acidic pH in endosomes is required for infection, TOSV was allowed to infect induced neurons and A549 cells in the presence of inhibitors of endosomal acidification. Ammonium chloride (NH_4Cl) and chloroquine diphosphate are both weak lysosomotropic bases that neutralize the drop in intraluminal pH in endosomes. Since my goal was to study the impact of endosomal acidification on virus entry, I limited the infection to a single round in this series experiments and also in all subsequent experiments, *i.e.*, to exactly 6 and 8 h in A549 and induced neurons, respectively. For each cell line, MOIs were chosen to achieve approximately 20-30% infection. This range allows detection of a potential inhibitory or enhancing effect of an interfering agent without reaching saturation while maintaining a significant detectable signal. TOSV infection in the presence of NH_4Cl and chloroquine resulted in a dose-dependent reduction of infection in both induced neurons and A549 cells (**Figure 25A, B**).

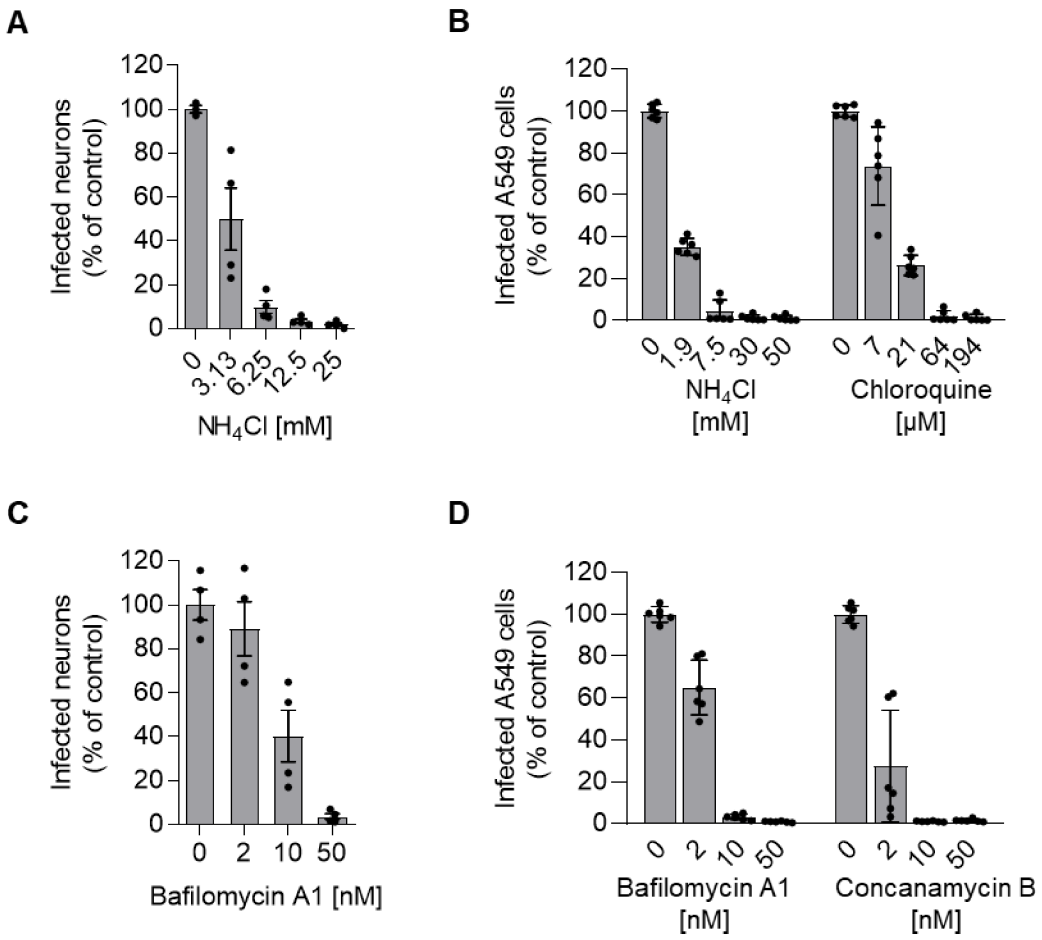

Figure 25. TOSV infection is sensitive to inhibitors of vacuolar acidification.

(A to D) iPSC-derived neurons (A and C) and A549 cells (B and D) were pretreated with NH_4Cl (A and B), chloroquine (B), bafilomycin A1 (C and D), and concanamycin B (D) before the exposure to TOSV at MOI 10 for 8 h or MOI 2 for 6 h, respectively, in the continuous presence of inhibitors of endosomal acidification. Infection was analyzed by flow cytometry and normalized to infections without inhibitor treatment. n = 2-3. The figure was published in (269).

Alternatively, acidification of the vacuolar pH was blocked by bafilomycin A1 and concanamycin B, both of which inhibit the vacuolar-type ATPase from pumping protons into the lumen of endosomes. Similar to the weak lysosomotropic bases, treatment with bafilomycin A1 and concanamycin B resulted in a dose-dependent reduction of TOSV infection in induced neurons and A549 cells (**Figure 25C, D**). Taken together, these data indicate that TOSV infection is dependent on vacuolar acidification during entry into human cells. Of note, all inhibitors used here and later were evaluated for cytotoxicity in a strain of A549 cells overexpressing TMPRSS2 from another lab by a lactate dehydrogenase release assay (section 3.3.2., **Figure 38**), which were recently confirmed to show the same results in my A549 cell line strain (250). Upon cell death and lysis,

lactate dehydrogenase is released and can be detected in the extracellular medium. All inhibitors were used at concentrations that were not toxic to the cells (**Figure 38**).

3.2.3 TOSV traffics through early endosomes and reaches late endosomes

To assess whether TOSV particles are trafficked within endosomes, I used A549 cells that transiently overexpress a variety of fluorescently tagged proteins that typically reside in endosomal compartments. A549 cells were transfected with an expression vector encoding the small GTPase Rab5a, the master regulator of EE functions, tagged with monomeric enhanced green fluorescent protein (EGFP). Subsequently, the binding of ATTO647N-TOSV to cells was synchronized on ice and internalization was allowed for different time points through warming to 37°C. Confocal microscopy revealed that TOSV co-localized with EGFP-Rab5-positive vesicles as early as 5 min after heating (**Figure 26A**). Quantification over time revealed a peak of co-localization events at 5-10 min post-warming and a decline thereafter (**Figure 26B**).

TOSV was then tested for co-localization with EGFP-tagged late endosomal markers Rab7a and LAMP1. Rab7a drives the identity of LEs and LAMP1 is a heavily glycosylated membrane protein highly enriched in LEs and lysosomes. TOSV particles were observed in vesicles positive for EGFP-Rab7 and LAMP1-EGFP, albeit at later time points compared to Rab5 co-localization (**Figure 26C-F**). Here, co-localization with both EGFP-Rab7 and LAMP1-EGFP increased over time and was maximal 40 min after warming. Notably, some particles were located in the center of vesicles, indicating that they had not yet fused with the limiting membrane, while some spots localized to the membrane of vesicles and appeared more fuzzy. Taken together, these data demonstrate that after internalization, TOSV is sorted into EEs and trafficked along the endosomal pathway to LEs.

3.2.4 TOSV requires late endosomal maturation for infection of A549 and iPSC-derived neurons

In order to analyze whether TOSV entry depends on the passage through the EEs, I examined the TOSV infection in the presence of a constitutively active (CA) mutant of Rab5 (Rab5 Q79L). The Rab5 GTPase cycles between the active GTP-bound state and the inactive GDP-bound state. In these two states, Rab5 serves as a master regulator of EE biogenesis, acting through different Rab effectors. Expression of the Rab5 CA mutant typically results in enlarged EEs and blockage of cargo trafficking to lysosomes due to

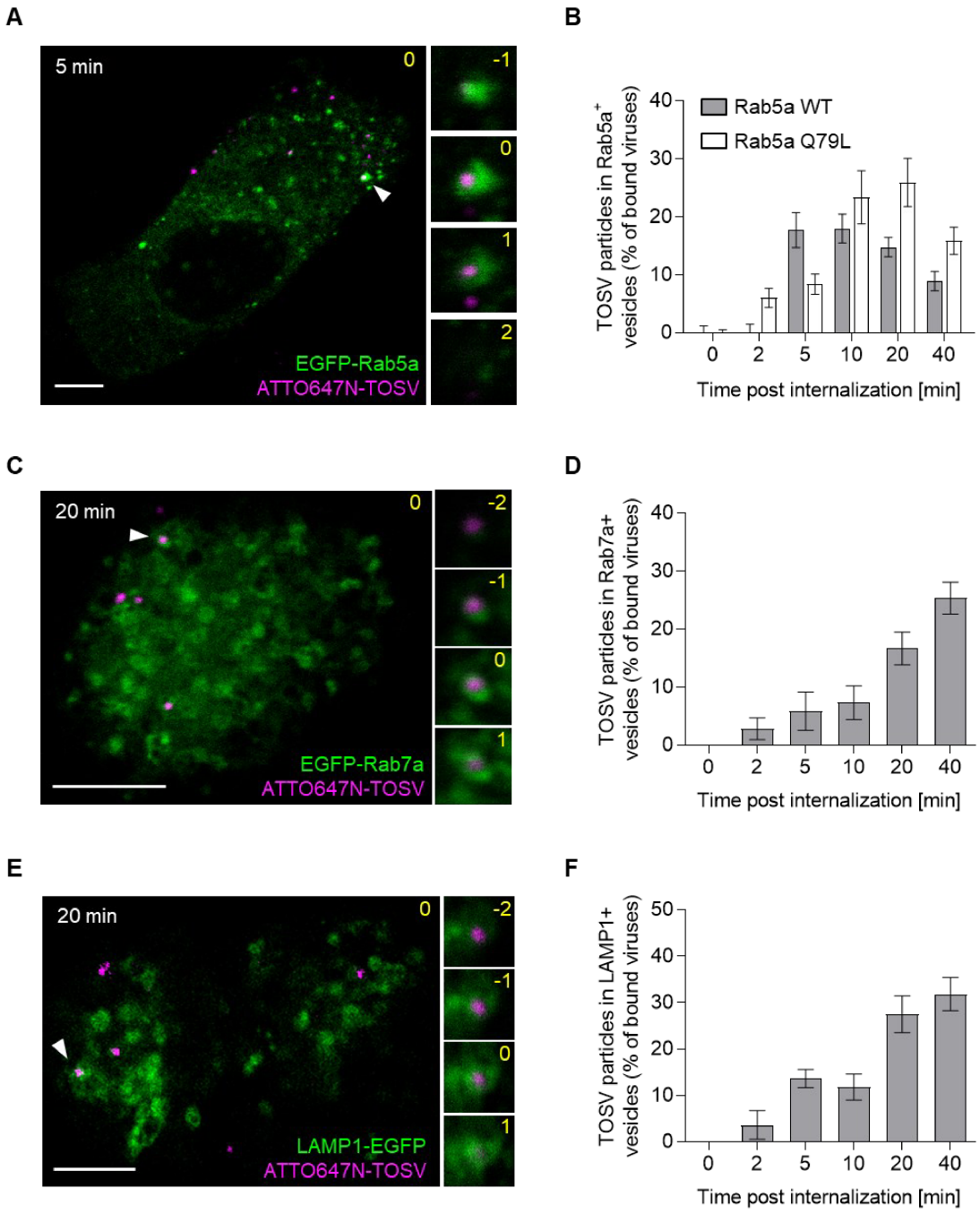

Figure 26. TOSV enters early endosomes and then late endosomal compartments.

(A) A549 cells were transfected with a plasmid encoding EGFP-tagged Rab5a, and 22 h later, exposed to ATTO647N-TOSV at MOI 1 for 90 min on ice. Cells were rapidly warmed to 37°C for 5 min to allow internalization. Cells were washed, fixed on ice, and imaged by confocal microscopy. The large image shows a single plane with TOSV particles (in magenta) and Rab5a (in green). Arrowhead indicates a co-localization event of ATTO647N-TOSV and Rab5a-positive vesicle. Higher magnifications are shown on the right side as a z-stack series indicated by yellow numbers in the top right corner with the original plane being marked with 0. Representative images are shown. Scale bar, 5 µm. (B) Quantification of co-localization of ATTO647N-TOSV with vesicles positive for wild-type (WT) Rab5a or constitutively active mutant Q79L. Internalization of the virus

was allowed for indicated time periods into transfected cells before fixation and analysis of co-localization by confocal microscopy. Co-localization is expressed as the percentage of total particles per cell that are associated with respective vesicles. A minimum of 6 cells were analyzed per time point. Data shows mean ± SEM, n = 1. (C to F) Internalization of ATTO647N-TOSV was allowed into A549 cells transiently expressing EGFP-tagged late endosomal markers Rab7a and LAMP1 as described in (A). Representative images are shown 20 min post-warming (C and E). Co-localization of virus particles with Rab7a and LAMP1 (D and F) was analyzed over time as described in (B). A minimum of 9 cells were analyzed per condition. Data shows mean ± SEM, n = 1. Scale bar, 5 µm. The figure was published in (269).

impaired LE maturation (275). This enlarged EEs morphology after transient expression of EGFP-tagged Rab5 CA mutant in A549 cells was also observed here (**Figure 27A**). Furthermore, co-localization events between ATTO647N-TOSV and Rab5 CA mutant were visualized by confocal microscopy. Co-localization started after 2 min of warming and reached a maximum after 20 min (**Figure 26B**). In contrast to Rab WT, which showed a decrease in co-localization after 10 min, co-localization with the CA mutant of Rab5 decreased after 20 min, suggesting an impairment of LEs maturation and cargo transport to LEs and lysosomes. In addition, cells with similar EGFP-Rab5 expression levels were evaluated for TOSV infection by flow cytometry. TOSV infection was impaired by 80% by Rab5 CA expression (**Figure 27B**). Expression of an EGFP-tagged dominant-negative mutant of Rab5 (S34N) also reduced TOSV by more than 60%. This mutant abolishes newly formed EEs. This suggests that TOSV traffics within EEs and requires functional compartments downstream of EEs to enter host cells.

To test whether TOSV relies on transit through LEs, the organelle downstream of EEs, I took advantage of Rab7 GTPase mutants. Rab7 is a key player in LE identity and orchestration of its functions (276). Infection with TOSV was impaired by 80% when a dominant negative mutant of Rab7 (T22N) was transiently expressed in A549 cells (**Figure 27C**). In contrast, expressing a constitutively active Rab7 mutant (Q67L) did not affect TOSV infection and resulted in infection levels similar to those observed with Rab7 WT.

To further investigate the importance of LE maturation in TOSV infection, I examined the role of functional microtubules (MT). The sorting of cargo in EEs to LEs and the transport of endosomes to the perinuclear region have been shown to be mediated along MT in several cell types. Furthermore, MT and its motors are central to the orchestration of the fusion of LEs with other LEs and lysosomes. Thus, disruption of MT results in impaired maturation of LEs and prevents cargo from reaching compartments with a pH low enough to induce fusion (89). Here, treating induced neurons and A549 cells with the MT-

destabilizing drugs nocodazole and colcemid inhibited TOSV infection by 40-60% (**Figure 28A, B**). In contrast, MT stabilization by taxol treatment had no effect on TOSV infection in A549 cells (**Figure 28C**).

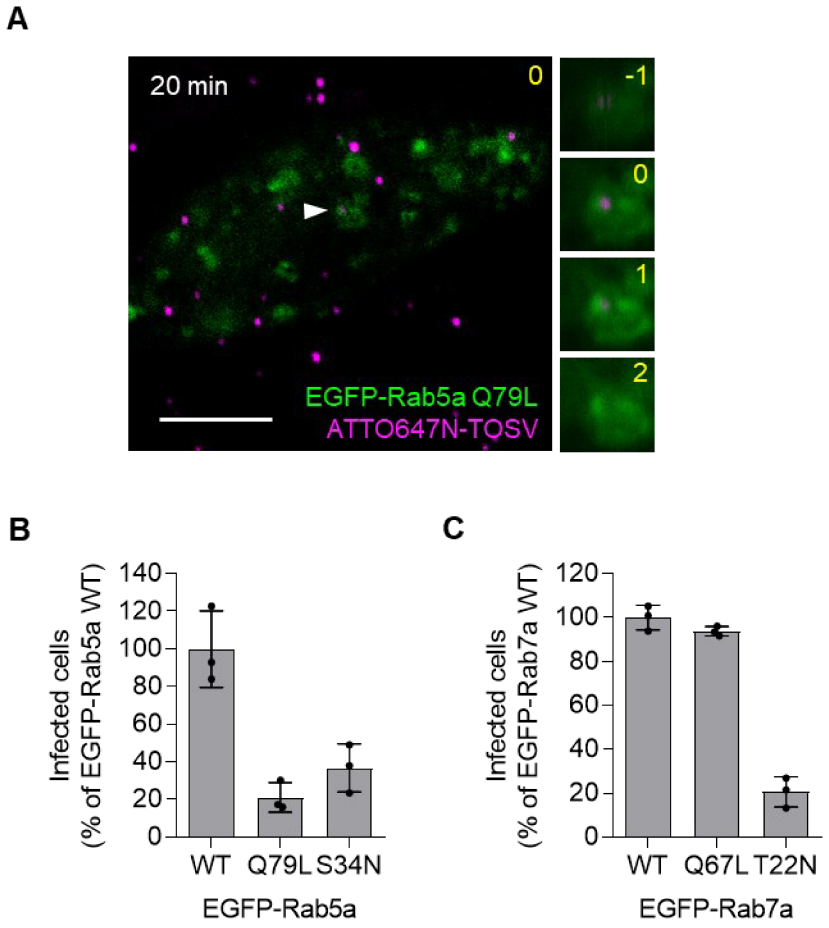

Figure 27. TOSV relies on transfer to functional late endosomes for infection.

(A) ATTO647N-TOSV was allowed to enter A549 cells transiently expressing the EGFP-tagged constitutively active Rab5a mutant Q79L as described in Figure 26. Internalization was allowed for 20 min and a white arrowhead illustrates a co-localization event between ATTO647N-TOSV (in magenta) and Rab5a Q79L (in green). A representative image is shown. Scale bar, 5 µm. (B) A549 cells were transfected with an expression vector coding for EGFP-tagged Rab5a WT, the constitutively active Q79L or dominant-negative S34N mutant. Transfected cells were exposed to TOSV at MOI 4 for 6 h. Infection was analyzed by flow cytometry in cell populations with similar expression levels of EGFP-tagged Rab5a. Infection was normalized to Rab5a WT. Data show one out of three representative experiments in triplicates. (C) A549 cells transiently expressing EGFP-tagged Rab7a wild-type (WT), the constitutively active Q67L, or the dominant-negative T22N were challenged with TOSV at MOI 4 for 6 h. Infection was analyzed by flow cytometry as described in (B). Data were normalized to infection in Rab7a WT-expressing cells. Data show a representative experiment of three in triplicates. The figure was adapted from (269).

Furthermore, sorting of cargo in EEs to LEs is mediated by the ESCRT machinery, where ubiquitin serves as a sorting signal. Disruption of ubiquitin-dependent endosomal sorting by treatment of induced neurons and A549 cells with MG-132 resulted in a dose-dependent reduction of infection (**Figure 28D**). Collectively, these data demonstrate that TOSV requires trafficking to functional LEs for productive infection and suggest that TOSV is a L-PV.

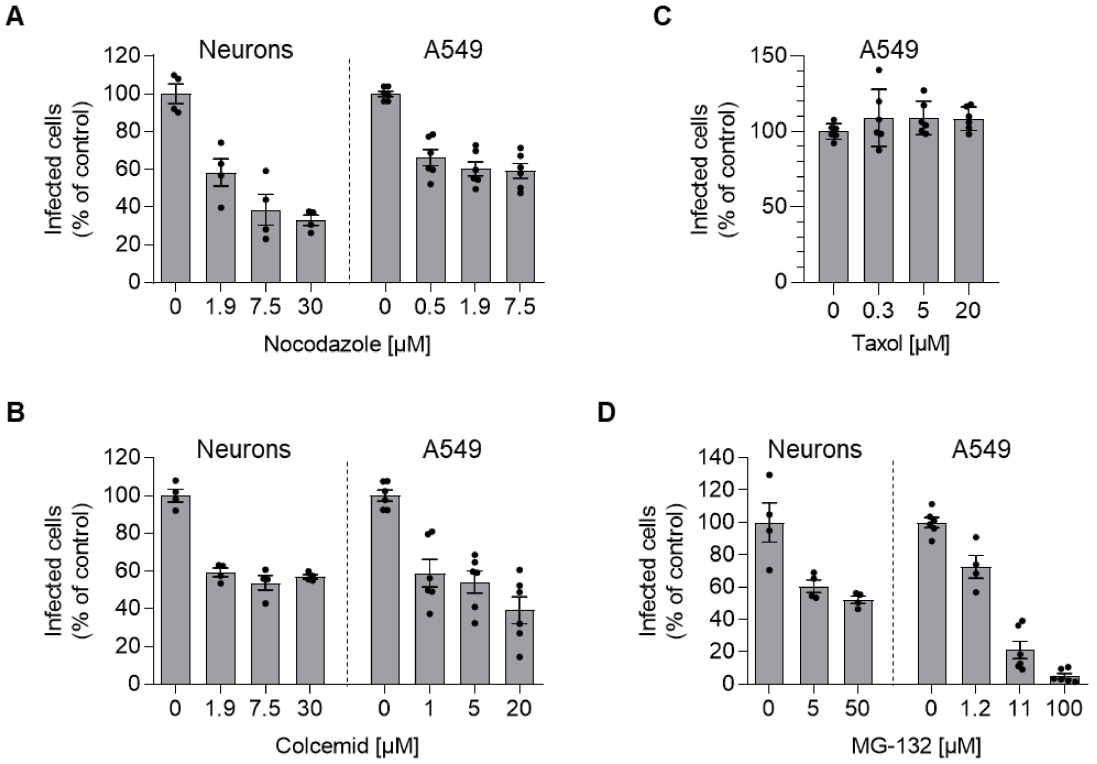

Figure 28. TOSV depends on late endosome maturation for infection.

(A to D) iPSC-derived neurons and A549 cells were pretreated with nocodazole (A), colcemid (B), taxol (C), or MG-132 (D) before being exposed to TOSV. TOSV infection was allowed at MOI 10 for 8 h or MOI 2 for 6 h in induced neurons and A549 cells, respectively. Infection was analyzed by flow cytometry and normalized to samples without inhibitor treatment. n = 2-3. The figure was adapted from (269).

3.2.5 TOSV penetrates host cells by acid-activated membrane fusion

The observation that TOSV relies on vacuolar acidification and transport to functional LEs led me to hypothesize that TOSV requires low pH for acid-activated membrane fusion. To further test this possibility, fusion of TOSV directly with the plasma membrane was attempted by lowering the pH of surface-bound virions in a bypass assay (**Figure 29A**). Briefly, TOSV binding to A549 cells was synchronized on ice prior to a rapid temperature shift to 37°C for 90 sec in buffers of varying pH ranging from pH 7.4 - 5.0, representing the

acidification that occurs during endosomal trafficking. After extensive washing, NH_4Cl, which neutralizes endosomal acidification, was added to the medium to block endosomal entry and to record only infection events resulting from fusion at the plasma membrane. No infection was detected when a pH 7.4 buffer was added to induce TOSV fusion at the plasma membrane (**Figure 29B**). In sharp contrast, infection was high when a pH 5.0 buffer was added. Infection began to increase at pH 5.8 and increased rapidly until a plateau was reached at pH 5.5 and below. Half-maximal infection was recorded at pH 5.6. This suggests that lowering the pH is sufficient to induce TOSV fusion.

To determine when viral particles penetrate host cells by acid-activated membrane fusion, TOSV was bound to the surface of A549 cells and induced neurons on ice before the temperature was rapidly shifted to 37°C to allow internalization. NH_4Cl was added to the medium at different time points to block TOSV internalization. I exploited the fact that NH_4Cl acts almost immediately and raises endosomal pH (277). When added directly after shifting the cells to 37°C, no infection was observed in either A549 cells or induced neurons (**Figure 29C, D**). In A549 cells, infection began to occur after 5 min post-warming and increased over time, reaching a plateau after 40-60 min. Half of the particles passed the acidification-dependent step, *i.e.*, penetrated the host cells, within the first 15 min after warming to 37°C. TOSV penetration into induced neurons was rather asynchronous, and infection increased steadily over time. This may be due to a higher degree of spatial compartmentalization (278) with longer distances to traffic in the neuronal endosomal system, as well as the heterogeneity of cell preparations typical of induced neurons.

This penetration kinetics is consistent with penetration occurring in late endosomes. To pursue this hypothesis, I exploited the temperature dependence of LE formation. While endocytosis and LE formation occur at temperatures above 16°C, maturation transport of cargo to LEs is blocked at temperatures below 21°C (100). To address this experimentally, TOSV binding was synchronized on ice before A549 cells were shifted to different temperatures for 50 min. The temperature was then raised to 37°C and NH_4Cl containing medium was added to block further penetration. No infection could be observed at temperatures of 21°C and below, suggesting that such low temperatures do not allow TOSV penetration into host cells (**Figure 29E**). In addition, TOSV infection was compromised at 30°C and 25°C by 40 and 85%, respectively. As a control, SFV was used, which already penetrates host cells in EEs and does not rely on LE formation (279). Unlike TOSV, SFV infection was unaffected at 30°C compared to 37°C. In addition, SFV infection could still be detected at 21°C and 16°C. This further suggests reinforced the view that TOSV is a L-PV.

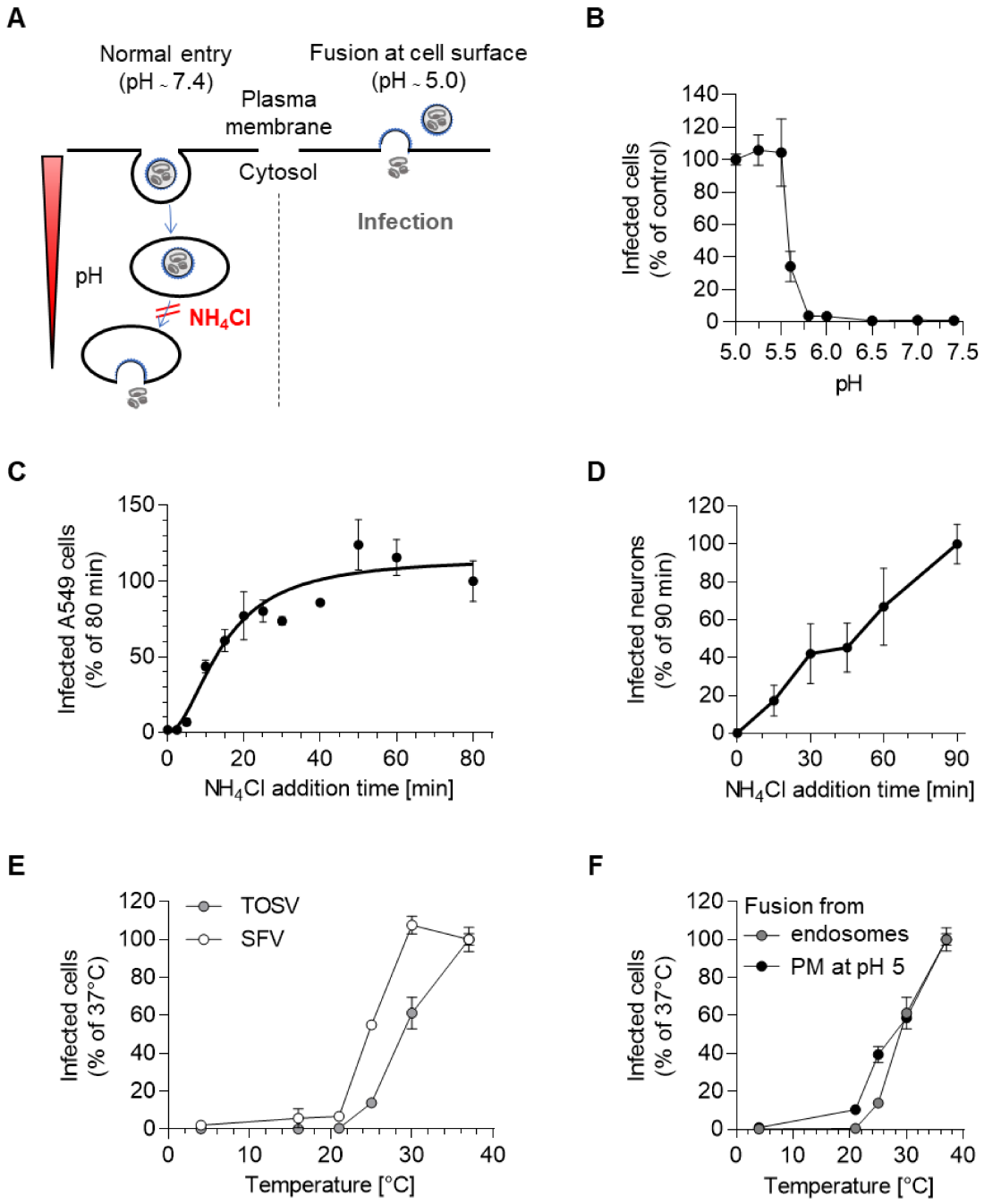

Figure 29. TOSV fusion occurs at an optimal pH of 5.5 and penetration is completed within 50 min in A549 cells.

(A) Schematic representation of the endocytic bypass experiment to assess fusion of TOSV. (B) TOSV is bound to A549 cells on ice at MOI 10 before buffers at indicated pH were added for 90 sec at 37°C. Cells were washed and incubated for 7 h at 37°C in presence of 50 mM NH_4Cl to block penetration from endosomes. Infection was quantified by flow cytometry and normalized to that induced by the addition of pH 5.0 buffer. n = 2-4. (C and D) TOSV was bound to A549 cells (C) or iPSC-derived neurons (D) on ice at MOI of 1 and 15, respectively. Cells were then rapidly shifted to 37°C and NH_4Cl (50 mM) was added at indicated time points. Infection was stopped after 6 h (A549) or 8 h (induced neurons) after the warm shift and analyzed by flow cytometry. Data were

normalized to infection after 80 min (A549) or 90 min (induced neurons) NH_4Cl addition time. N = 2-3. (E) TOSV and SFV were bound to A549 cells on ice at MOI 1 and 150, respectively. Temperatures were then shifted to indicated temperatures for 50 min before NH_4Cl was added to block further penetration. Samples were incubated for further 7 h at 37°C, and infection was analyzed by flow cytometry. Infection was normalized to samples incubated throughout at 37°C. Data are representative of one experiment in triplicate out of two. (F) TOSV was bound to A549 cells on ice for 90 min before a buffer at pH 5 was added at indicated temperatures for 90 sec. Afterward, cells were extensively washed and incubated for 7 h at 37°C in a complete medium supplemented with 50 mM NH_4Cl to block further penetration. Infection was analyzed by flow cytometry and normalized to sample treated at 37°C. Data show a representative experiment out of two in triplicates. The figure was modified from (269).

To rule out that the fusion process itself is the limiting factor of infection at temperatures below 21°C, I used the bypass assay described above and forced fusion of TOSV directly at the plasma membrane at pH 5 at different temperatures. At 30°C, the level of penetration from endosomes is similar to that of forced fusion from the plasma membrane at pH 5, indicating that fusion is the bottleneck of infection at 30°C (**Figure 29F**). Conversely, at 25°C, fusion was impaired by 60% while penetration was inhibited by nearly 90%. At 21°C, fusion was still happening, although reduced by 90%, while endosomal penetration was completely abolished. This suggests that at 21°C, fusion is not the bottleneck of infection, but the block in infection is due to impaired LE formation.

So far, most fusion assays have relied on immunofluorescent staining of newly synthesized viral proteins. To directly monitor fusion events, I established a fluorescent lipid-mixing assay using the auto-quenching lipophilic dye R18. Particles with high concentrations of R18 incorporated into viral membranes showed a low level of fluorescence that increased upon dilution of the dye, *i.e.*, upon fusion with a target cell membrane (**Figure 30A**). Changes in fluorescence intensity were measured in a time-resolved manner using a spectrofluorometer. Disruption of the viral membrane by the detergent triton X-100 resulted in an approximately nine-fold increase in fluorescence (**Figure 30B**). This indicated that the fluorescence in the viral particles was auto-quenched, while the infectivity was still close to that of unlabeled virus (**Figure 22D**).

I then investigated whether R18-labeled TOSV could enter and penetrate host cells from late endosomal compartments as unlabeled virus. R18-TOSV was bound to A549 cells in suspension on ice, and virus internalization was allowed by a rapid shift to 37°C within the spectrofluorometer. Fluorescence intensity increased over time, reaching a 2-4-fold increase after 90 min compared to baseline (**Figure 29C**). As a control, the

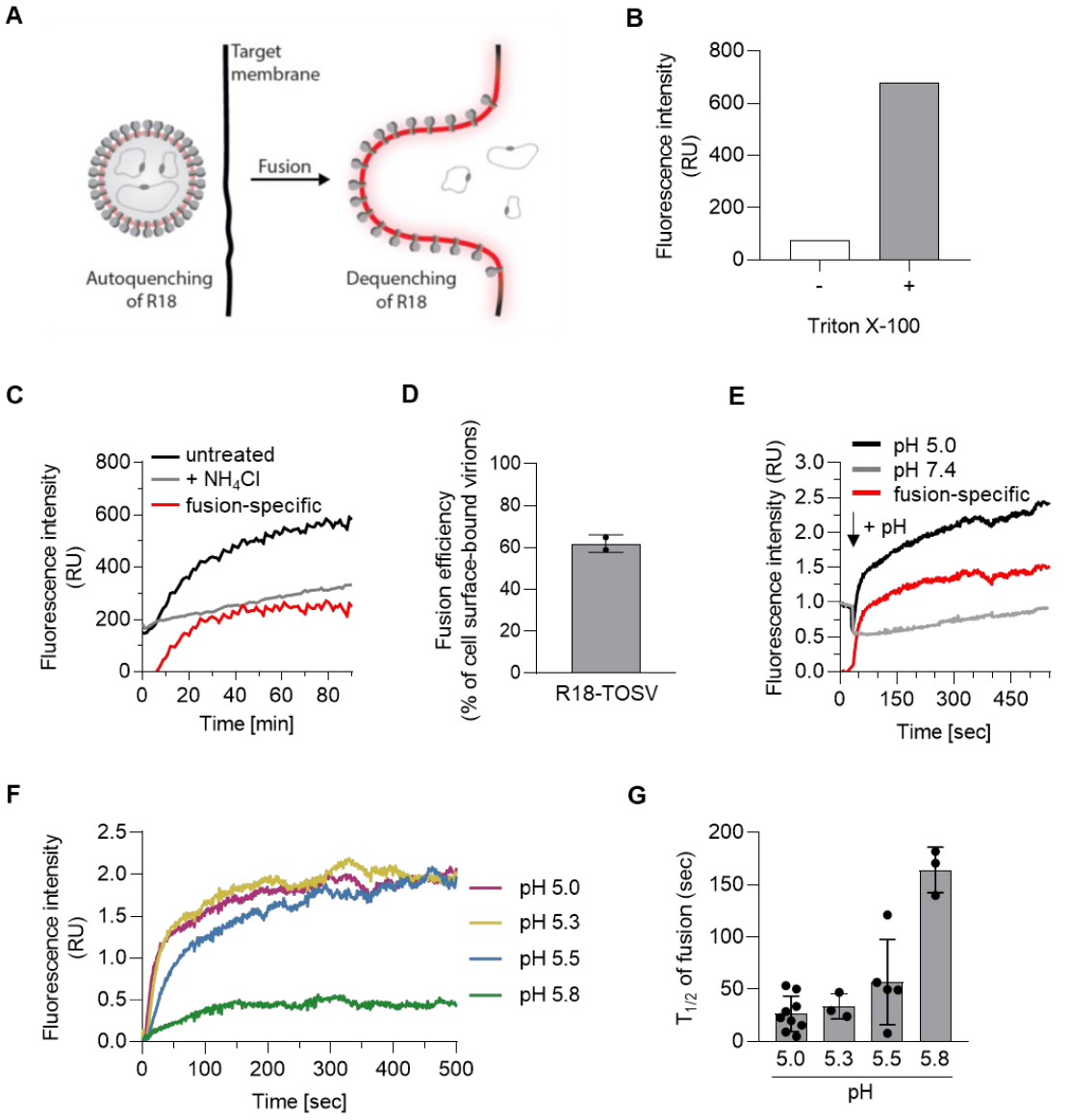

Figure 30. Penetration and fusion dynamics of TOSV can be assessed by R18-based lipid-mixing fusion assays.

(A) Scheme of R18-based lipid-mixing fusion assay. Fluorescence of R18-TOSV particles is autoquenched. Upon fusion with a target cell membrane, R18 is diluted in the membrane resulting in an increase in fluorescence. (B) The fluorescence increase of R18-TOSV was evaluated in a cell-free dequenching assay. Fluorescence emission was measured in a spectrofluorometer before and after the addition of triton X-100 to disrupt viral membranes. n = 1. RU, relative unit. (C) R18-TOSV was bound to A549 cells at MOI 10 on ice for 90 min. After washing, cells were resuspended in a prewarmed complete medium to allow internalization, and fluorescence emission was measured inside a spectrofluorometer at 37°C for 90 min. NH_4Cl was used as a control to block fusion with endosomal membranes and to determine the background signal due to the natural flip-flop of the dye between nearby membranes. The fluorescent background (grey line) was subtracted from the inhibitor-untreated sample (black curve) to obtain the fusion-specific kinetic (shown in red). Representative curves are shown. RU, relative unit. (D) To determine the efficiency of fusion from

endosomes, an assay was performed as described in (C) but triton X-100 was added after incubation for 90 min at 37°C. Triton X-100 disrupts all membranes resulting in full dequenching of all bound R18-TOSV particles. Data shows fluorescence after 90 min at 37°C normalized to fluorescence after the addition of triton X-100. Data were obtained by lab rotation student Lea Woltereck under my supervision. (E) R18-TOSV was bound to A549 cells on ice at MOI 10. Infected cells were then transferred into a spectrofluorometer, and the temperature was rapidly shifted to 37°C. The fluorescence signal was recorded for 550 sec. After 30 sec, a pre-defined volume of pH buffers was added reaching pH 5.0 or 7.4 in the cell suspension (indicated by '+ pH'). Data were normalized to input virions, *i.e.*, timepoint 0 sec. Background fluorescence obtained at pH 7.4 (grey curve) due to free diffusion of R18 was subtracted from the values obtained at pH 5 (black curve) to determine the fusion-specific kinetic (red curve). Representative curves are shown. RU, relative unit. (F) R18-TOSV was bound to A549 cells and buffers in the range of 5.0 to 5.8 were added at time point 0 as described in (E). Data were normalized to time point 0, and background fluorescence at pH 7.4 was subtracted. Representative curves are shown. RU, relative unit. (G) The kinetics of half-maximal intensities ($t_{1/2}$) were determined from curves shown in (F). n = 3-9. The figure was adapted from (269).

penetration of R18-TOSV was blocked by NH_4Cl. The increase in fluorescence was significantly reduced, although not completely eliminated, compared to the sample without NH_4Cl. This nonspecific, slight increase in fluorescence could be due to spontaneous translocation of R18 from the viral to a cellular membrane or flip-flop of the lipid dye between the two leaflets of the viral membrane. Subtraction of the nonspecific fluorescence increase resulted in a fusion-specific curve that began to increase after a lag time of 6 min, reached half-maximal intensity at 18.2 ± 2.3 min, and plateaued at 40-50 min. When triton X-100 was added after 90 min at 37°C to disrupt all membranes and release the maximum fluorescence of R18-TOSV, the fluorescence continued to increase. Approximately 60% of the full signal was reached after allowing R18-TOSV to enter the cells for 90 min (**Figure 30D**). This indicates that approximately 60% of all surface-bound particles have fused with a cellular membrane. These penetration kinetics data obtained from lipid mixing assays with R18-TOSV were very similar to those obtained from the NH_4Cl addition time course in A549 cells (**Figure 29C**). This demonstrates that R18-labeled TOSV has the same penetration kinetics as unlabeled virus and can be used in further approaches to assess viral fusion. Although it is not possible to distinguish between hemi-fusion and complete fusion pore formation in R18-based assays, it serves as a good correlate of fusion.

To determine the dynamics of the fusion process itself, I aimed to bind R18-TOSV to A549 cells and force fusion with the plasma membrane by lowering the pH to 5.0, as previously described in the bypass assay. Here, the increase in fluorescence due to fusion of the

virus with the plasma membrane was measured in real time in a spectrofluorometer. Briefly, R18-TOSV bound to A549 cells was rapidly warmed to 37°C and buffers of different pH were added after 30 seconds. Fluorescence increased rapidly upon addition of a pH 5 buffer, reaching half-maximal intensity after 27 ± 16 sec and a plateau approximately 90 sec later (**Figure 30E**). In stark contrast, there was only a marginal change in fluorescence when the pH was maintained at 7.4 throughout the measurement.

As a next step, I wanted to study the dynamics of TOSV fusion in the range of pH 5.0 - 5.8 in real time using the R18 approach. Buffers at these pH values have previously been shown to force TOSV fusion at the plasma membrane of A549 cells to varying degrees (**Figure 29B**). Viral fusion could be detected at pH 5.8 and below, with fusion occurring more rapidly at lower pH (**Figure 30F**). While fusion at pH 5.0, 5.3, and 5.5 occurred at comparable rates with half-maximal kinetics ($t_{1/2}$) of 27, 34, and 57 sec, respectively, fusion at pH 5.8 was slower, reaching its $t_{1/2}$ after 164 sec (**Figure 30G**). This suggests that TOSV can also achieve fusion at higher pH, although it requires longer exposure times.

3.2.6 TOSV is not inactivated by exposure to pHs below its fusion threshold

Phenuiviral Gc has a class-II viral fusion protein fold. It has been described that the conformational change from pre- to post-fusion conformation of class-II fusion proteins is triggered by low pH, is irreversible, and the proteins can only act once (105). To test whether the fusion process of TOSV is an irreversible step, I investigated whether exposure of viral particles to low pH in the absence of a target membrane would lead to virus inactivation. In such an assay, conformational rearrangement to the post-fusion conformation would be induced upon exposure to the optimal low pH. If this process is irreversible, it would render the particles noninfectious. To test this, viral particles were pretreated in pH buffers ranging from pH 5.0 - 7.4 for 5 min at 37°C, re-neutralized to pH 7.4, and added to cells. Surprisingly, infection of A549 cells was not reduced when viral particles were pretreated at low pH (**Figure 31A**). Pretreatment at pH 5.5 and 5.0 resulted in similar infection rates compared to neutral pH pretreatment. Interestingly, pretreatment at mildly acidic pH 6.5 and 6.0 caused an approximately 1.8-fold increase in infection compared to pretreatment at pH 7.4.

To determine whether resistance to low pH pretreatment is unique to TOSV or can be extended to other viruses, I analyzed a variety of related and unrelated viruses harboring class-II and class-I viral fusion proteins. RVFV and GERV, both members of the order *Bunyavirales*, as TOSV, have been shown (142, 143) or predicted by our lab to have a

class-II fusion protein (unpublished data). In addition, the alphavirus SFV, another class-II fusion protein, and the influenza A virus (IAV), which carries a class-I fusion protein, both unrelated to TOSV, were used as controls. While SFV has previously been shown to enter host cells from EEs and has an optimal pH of 6.2, RVFV, GERV, and IAV are late penetrating viruses and fuse at pHs below 6.0 (120, 250, 256, 280). Infection conditions were established for all viruses and their respective cell lines prior to evaluating their inactivation by low pH pretreatment. RVFV, like TOSV, belongs to the *Phlebovirus* genus, but is transmitted by mosquitoes instead of sand flies. Here, an RVFV construct was used in which NSs, a nonstructural protein and virulence factor, was replaced by EGFP (RVFVΔNSs:EGFP). RVFV particles were pretreated with pH buffers and infected using a protocol similar to TOSV. Similar to TOSV, pretreatment of RVFVΔNSs:EGFP with low pH did not negatively affect infectivity in A549 cells (**Figure 31B**). Again, pretreatment with mildly acidic pH in the range of pH 6.0 - 6.5 further enhanced infection. GERV belongs to the *Orthobunyavirus* genus, a genus from a different family than *Phenuiviridae* in the large order of *Bunyavirales*. Similar to TOSV and RVFV, pretreatment of GERV was not affected by low pH pretreatment (**Figure 31C**). Strikingly, the lower the pH pretreatment, the higher the infectivity of GERV in A549 cells.

In contrast, pH pretreatment of two unrelated viruses, SFV and IAV, resulted in a significant decrease in their infectivity in BHK-21 and A549 cells, respectively (**Figure 31D – F**). Infectivity decreased gradually with decreasing pH pretreatment. Compared to neutral pH, more than 97% of SFV and 93% of IAV particles were inactivated at pH 5.5 and pH 5.0, respectively. To evaluate whether this marked reduction in SFV infectivity was due to the use of BHK-21 cells instead of A549 cells, infection conditions for TOSV were established in the two mammalian cell lines BHK-21 and Vero. Pretreatment of TOSV and infection also resulted in a drop in infectivity with decreasing pH (**Figure 31E**). Although the infectivity of TOSV was reduced, 20% of the virions were still infectious at pH 5.5, which is significantly higher than the remaining barely 3% of SFV particles after pH 5.5 pretreatment. Infection of Vero cells with pH pretreated TOSV resulted in a similar pattern compared to TOSV infection of BHK-21 cells. This suggests that the resistance to low pH pretreatment can be extended to other bunyaviruses, but does not appear to be shared with viruses outside the viral order.

To examine which step in the viral entry process is favored by low pH pretreatment, I first analyzed binding to host cells. ATTO647N-TOSV was pretreated at different pHs, re-neutralized and bound to A549, BHK-21 and Vero cells on ice prior to confocal microscopy imaging. Approximately 10-15 TOSV particles were bound per cell after pretreatment at neutral pH (**Figure 32A, B**). While pretreatment at mildly acidic pH

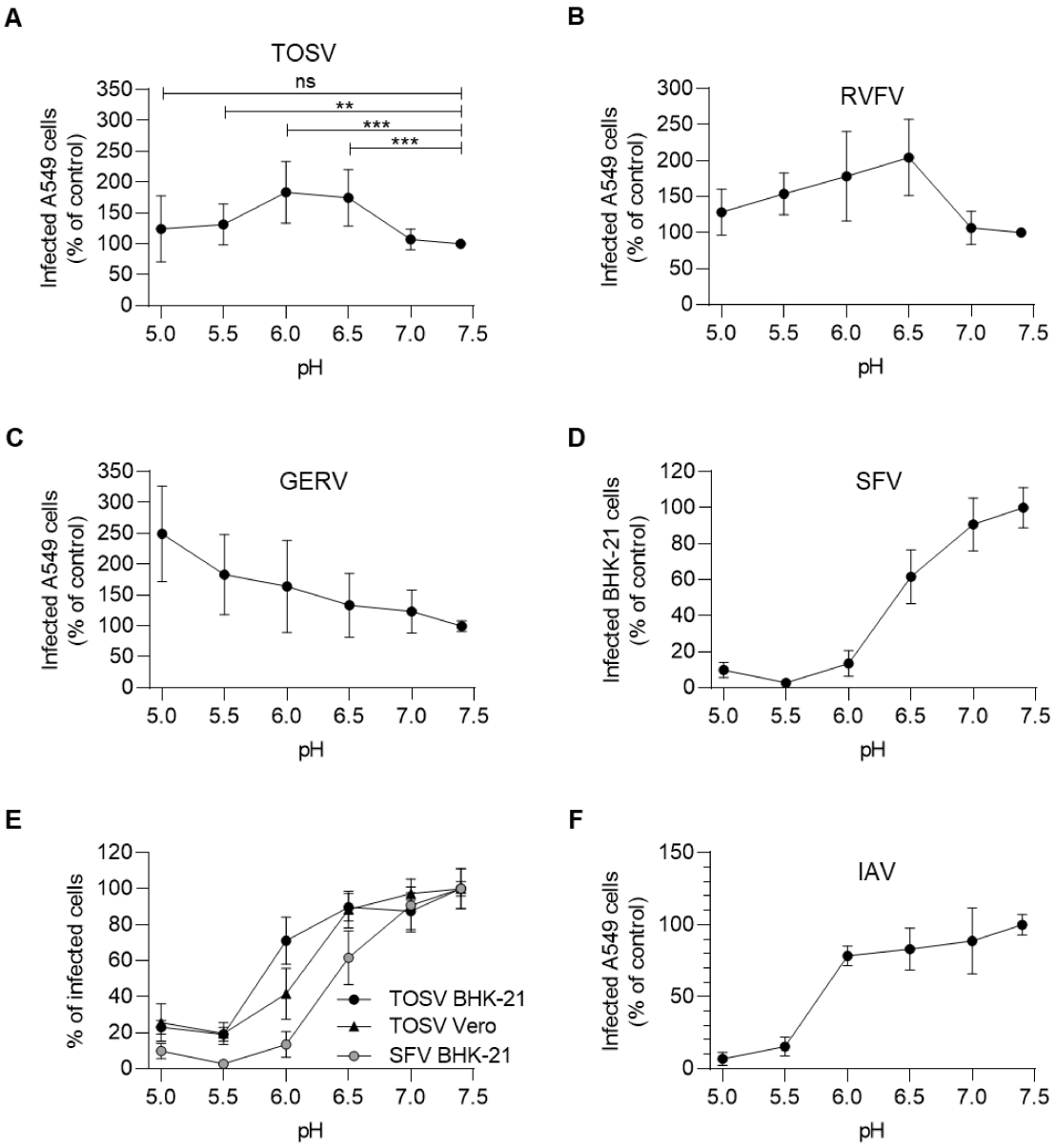

Figure 31. Low pH pretreatment does not inactivate TOSV and other bunyaviruses.

(A) TOSV was pretreated at indicated pH for 5 min at 37°C, reversed to pH 7.4, and added to A549 cells at MOI 2. Infection was allowed for 6 h at 37°C and quantified by flow cytometry. Data were normalized to samples kept at pH 7.4 during pretreatment. T-test with Welch's correction was applied. n = 5, p values: pH 6.5 vs. 7.4, ***, p <0.0001; pH 6.0 vs. 7.4, ***, p <0.0001; pH 5.5 vs. 7.4, **, p = 0.0025; pH 5.0 vs. 7.4, ns, p = 0.1001. Data were obtained jointly by my lab rotation student Alicia Rosenberger and myself. ns, not significant. (B to F) Rift Valley fever virus (RVFV) coding enhanced green fluorescent protein (RVFVΔNSs:EGFP; B), Germiston virus (GERV; C), Semliki Forest virus (SFV; D and E), and influenza A virus (IAV; F) were pretreated at low pH as described in (A). RVFVΔNSs:EGFP, GERV, and IAV were added to A549 cells at MOIs 0.4, 5, and 0.1, respectively. BHK-21 cells were exposed to SFV at MOI 0.05 and to TOSV at MOI 0.8 while TOSV was added to Vero E6 cells at MOI 0.8. Infection was allowed for 8 h at 37°C. Data in (B and C) were obtained jointly by my lab rotation student Alicia Rosenberger and myself. Data in (F) were

obtained by my lab rotation student Aiste Kudulyte under my supervision. IAV was kindly provided by Vera Sonntag-Buck (Hans-Georg Kräusslich group, University Hospital Heidelberg, Germany). n = 2-5. The figure is a modified version published in (269).

increased viral binding to ~20 particles per cell, pretreatment at more acidic pH of 5.5 and below resulted in decreased binding compared to neutral pH. This indicated that increased infection in A549 cells after pretreatment at pH 6.5 and 6.0 could be explained by increased binding. However, reduced binding at pH 5.5 pretreatment could not explain the higher infection in A549 cells. Calculating the ratio of infectious to bound virus revealed differences between A549 and BHK-21 and Vero cells. While the infectious/bound ratio decreased with lowering the pH in Vero and BHK-21 cells, the ratio remained stable between pH 7.4 and 6.0 and increased rapidly at pH 5.5 and 5.0 in A549 cells (**Figure 32C**). Notably, no difference in fluorescence intensity of ATTO647N-TOSV particles was observed, suggesting that the ATTO647N dye is pH stable.

Since increased infection after low pH pretreatment cannot be explained solely by its effect on binding, I then investigated whether the fusion process itself is affected. R18-TOSV was pretreated at mildly acidic pH 6 and bound to the surface of A549 cells under neutral conditions. Fusion of the viral membrane with the plasma membrane was then forced by the addition of a pH 5.8 buffer, a pH range previously shown to be capable of inducing fusion, albeit with slow kinetics (**Figure 30F**). Pretreatment at pH 6.0 resulted in significantly faster fusion at pH 5.8 compared to pretreatment at neutral pH (**Figure 32D, E**). With pH 6 pretreatment, the $t_{1/2}$ decreased from 169 to 62 sec, which is in a similar range to fusion at pH 5.5 without pretreatment (**Figure 30F, G**). This suggests that prolonged exposure to the mildly acidic pH present in EEs may prime TOSV and result in faster fusion.

3.2.7 TOSV remains infectious in the endocytic machinery for long periods

Since TOSV shows a high degree of stability to acidity and seems to be able to fuse at a variety of pH values, I hypothesized that TOSV would be less susceptible to inactivation in the endocytic machinery. To test how long TOSV is still able to enter cells, I reversed the approach of adding NH_4Cl. This approach is based on the fact that NH_4Cl effect is reversible almost instantaneously. TOSV was bound to A549 cells on ice and endocytosis was allowed by a rapid shift to 37°C in the presence of NH_4Cl. The weak base was then washed out after different periods of time and infection of A549 cells was evaluated by flow cytometry after immunofluorescence staining for viral proteins. Approximately 60% of

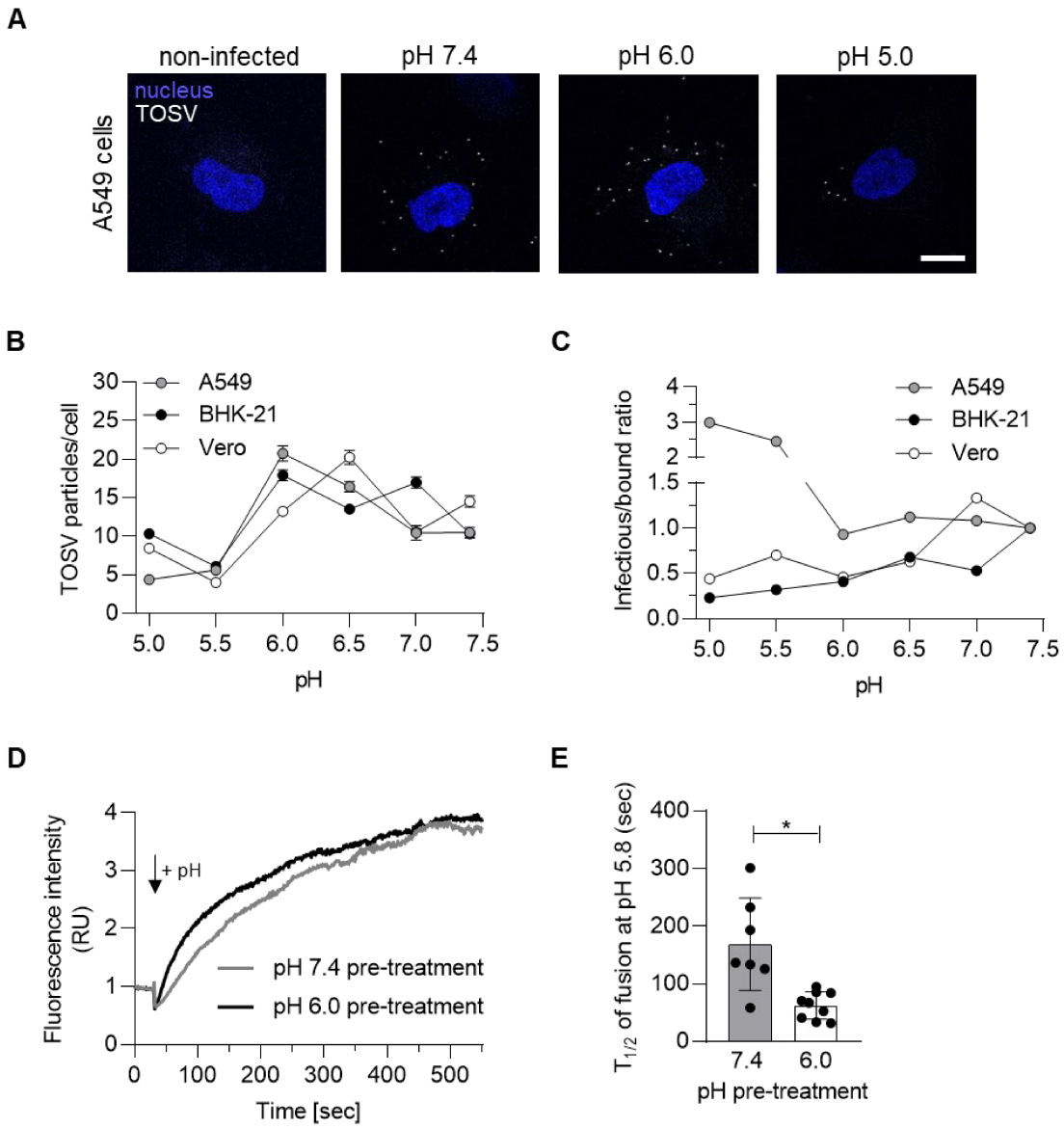

Figure 32. TOSV shows higher binding at faster fusion when pretreated at pH 6.0.

(A) ATTO647N-TOSV was pretreated at different pH as described in Figure 31A before allowed to bind to A549 cells at MOI 1 on ice for 90 min. Cells were washed and fixed, and nuclei were stained with Hoechst before cells imaging by confocal microscopy. Nuclei are shown in blue and ATTO647N-TOSV particles in white. Scale bar, 10 µm. (B) Quantification of binding assay of pH pretreated ATTO647N-TOSV to A549, Vero, and BHK-21 cells as described in (A). A minimum of 124 cells were analyzed per condition. (C) The ratio of infectious-to-bound TOSV particles in A549, Vero, and BHK-21 cells was calculated for each pH from data obtained in B and Figures 31A, and 31E. (D) R18-TOSV was pretreated at pH 6.0 and 7.4 as described in Figure 31A before being bound to A549 cells at MOI 10 on ice for 90 min. Cells were then rapidly warmed to 37°C within a spectrofluorometer, and the fluorescence signal was measured over 550 sec. Virus fusion was assessed by adding a pH 5.8 buffer after 30 sec (indicated by '+ pH'). Data were normalized to time point 0. Representative curves are shown. RU, relative unit. (E) Quantification of fusion kinetics of R18-TOSV pretreated at pH 6.0 and 7.4. The half-maximal intensities ($t_{1/2}$) were

calculated from the data shown in (D). n = 3. T-test with Welch's correction was applied. *, p = 0.0119. The figure was adapted from (269).

TOSV particles lost infectivity when incubated in the endocytic machinery without penetration (**Figure 33**). Thereafter, infectivity declined at a slower rate. Approximately 20% of the particles could still be acid-activated after 80 min in endosomes. This suggests that TOSV infectivity remains high even when the virus remained blocked in the degradative branch of the endocytic machinery for long periods of time.

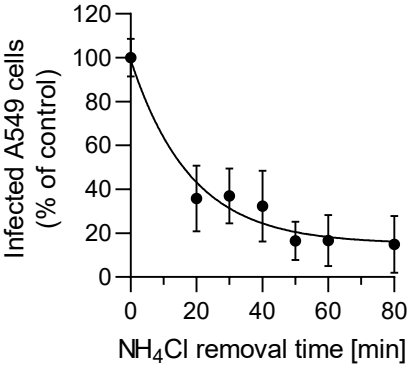

Figure 33. TOSV remains acid-activable in endosomal environment for long periods.
TOSV was bound to A549 cells at MOI 1 for 90 min on ice before the temperature was rapidly shifted to 37°C in the presence of NH_4Cl (50 mM). NH_4Cl was washed out after indicated time periods to allow acid-activated penetration. Infection was stopped 6 h after warming and analyzed by flow cytometry. Infection was normalized to those samples where NH_4Cl was removed directly at time point 0. n = 3. The figure was published in (269).

Taken together, these data demonstrate that TOSV enters host cells by acid-activated membrane fusion. TOSV traffics along the endosomal pathway until it reaches the low pH of late endosomal compartments, from which it enters host cells. In the process, TOSV displays remarkable resistance and adaptability to environments with acidic pHs. This feature of reversibility during the fusion process appeared to be share with other bunyaviruses and unique to this virus order.

3.3 SARS-CoV-2 enters host cells via acid-dependent and acid-independent entry pathways

3.3.1 Characterization of the SARS-CoV-2 life cycle in Caco-2 and Vero cells

This work was done in collaboration with the group of Steeve Boulant (formerly at CIID Heidelberg, now at the University of Florida). I worked on this project jointly with Zina Uckeley, a PhD student in my lab. We published this project together as shared first

authors in the EMBO Journal (264). First, large quantities of SARS-CoV-2 stocks were produced in Vero cells. Vero cells at about 80% confluency were infected at MOI 0.1 with a passage-2 SARS-CoV-2 stock (BavPat1) kindly provided by Prof. Bartenschlager. The BavPat1 strain was isolated from a patient and corresponds to the original Wuhan strain (254). The virus was harvested after 72 h, when a CPE of about 50% was observed. SARS-CoV-2 was then titrated on Vero cells using a TCID50 assay. Briefly, cells were infected with 10-fold dilutions of SARS-CoV-2 stock in a 96-well plate format. After 24 h, cells were fixed and stained for the viral nucleoprotein NP. Typically, SARS-CoV-2 was able to establish infection in Vero cells after a dilution of 10^{-3} - 10^{-5} of the original stock.

Prior to studying cell entry, several cell lines of human and mammalian origin were tested for SARS-CoV-2 susceptibility and permissiveness. Cells were infected with authentic SARS-CoV-2 at various dilutions for 24 h in a TCID50 assay prior to fixation and immunofluorescence staining for the viral NP protein. Infection was detected in the cell lines Calu-3, derived from human lung, Caco-2, which originates from human colon, and Vero E6, which are African green monkey kidney epithelial cells (**Figure 34**). Infection could be detected in Caco-2 and Vero cells at dilutions up to 10-4, while infection could be established in Calu-3 cells up to a 10^{-5} dilution. In contrast, no infection could be detected in HeLa cells with or without expression of the C-type lectin DC-SIGN, a known receptor/co-receptor of many enveloped viruses including SARS-CoV (281). In addition, SARS-CoV-2 was unable to establish infection in either the human lung epithelial A549 cells or the human embryonic kidney HEK293T cells.

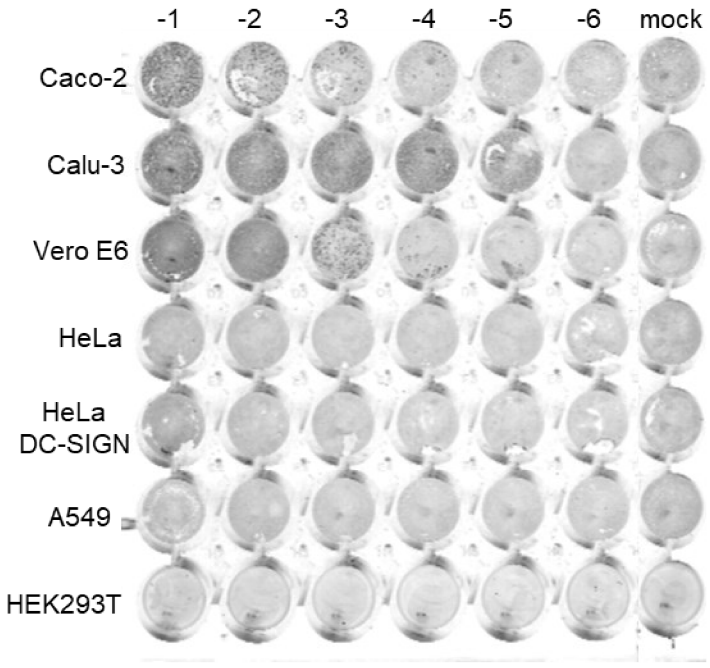

Figure 34. Susceptibility and permissiveness of various cell lines to SARS-CoV-2.
Cells were exposed to SARS-CoV-2 at indicated 10-fold dilutions for 24 h at 37°C. Cells were fixed and immunostained against viral NP protein, and fluorescence signal was measured on a Li-COR scanner. Infection can be seen in a greyscale. n = 1.

Therefore, Caco-2 and Vero cells were used to characterize SARS-CoV-2 infection in terms of virus replication and production. SARS-CoV-2 infection was analyzed in a flow cytometry-based assay after immunofluorescence staining for viral NP protein. Infection with SARS-CoV-2 at MOI 0.1 resulted in a steady increase in mean fluorescence and percentage of infected cells over time (**Figure 35A, B**). This suggests that the increase in fluorescence signal corresponds to newly synthesized viral NP protein during infection and not to input virions. Infection of Caco-2 cells began to increase more rapidly, reaching approximately 20-25% of infected cells after 8 h and reaching a plateau after 16 h. In contrast, it took longer to establish SARS-CoV-2 infection in Vero cells. After 8 h and MOI 0.1, only about 2% of the cells produced NP protein. Only after 24 h, infection increased steadily over time to reach more than 70% of total cells.

Next, I investigated whether SARS-CoV-2 was able to complete a full cycle in Vero and Caco-2 cells. To this end, cells were infected at MOI 0.1, the supernatant was collected after various time periods and titrated on Vero cells to assess the release of *de novo* produced infectious particles. Infectious particles were found to be released within the first 12 h of infection (**Figure 35C**). While the initial increase was observed between 8 h and 12 h in Vero cells, it appeared to be more rapid in Caco-2, where an increase was recorded between 4 and 8 h. In both cell lines, a plateau was reached after 16 h. At all time points, the release of infectious SARS-CoV-2 particles appeared to be higher in Caco-2 cells compared to Vero cells. Taken together, these data show that SARS-CoV-2 can complete its full cycle in both Caco-2 and Vero cells. The viral replication and virus production were somewhat increased and faster in Caco-2 cells. In all of the following assays, I have limited the infection to 8 h to restrict it to a single cycle of viral entry, as this is the focus of my study. In addition, the MOIs for each cell line were chosen such that infection was in the range of 20-30% of total cells. This range allows the detection of possible inhibitory or enhancing effects of a perturbant.

3.3.2 Cell lines exhibit different expression of cellular proteases involved in SARS-CoV-2 entry

Several host proteases have been proposed to play a role in priming and activating the spike protein by cleaving at specific sites. Prior to my study, the most prominent proteases were TMPRSS2, cathepsin L, and furin. Furin cleavage seems to occur mainly in producing cells, whereas TMPRSS2 and cathepsin L act in target cells. To test the role of TMPRSS2 and cathepsin L during SARS-CoV-2 entry into target cells, I analyzed the expression of the two proteases in four different cell lines, namely Vero, Caco-2, Calu-3,

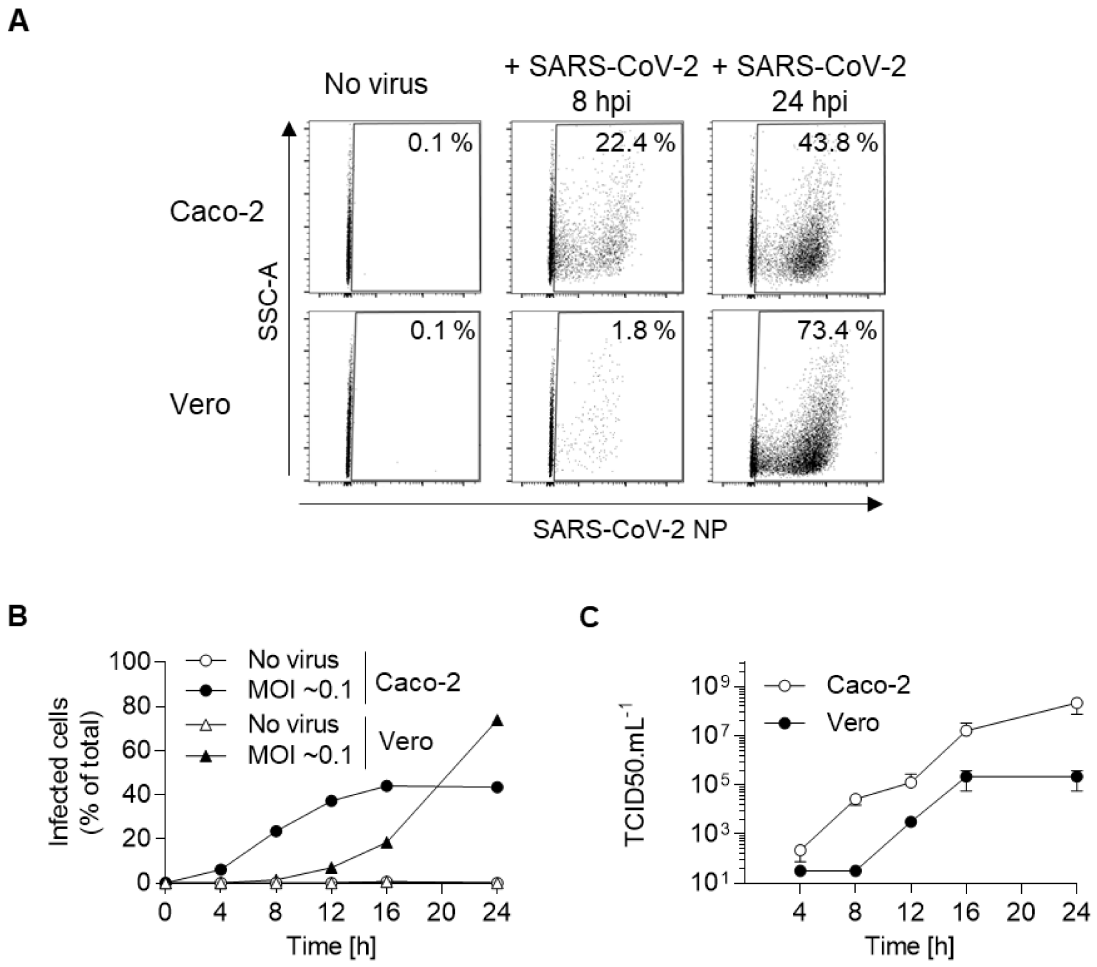

Figure 35. Quantification of SARS-CoV-2 infection.

(A) Vero and Caco-2 cells were exposed to SARS-CoV-2 at MOI 0.1, and infection was stopped after 8 and 24 h. Infection was analyzed in a flow cytometry-based assay after immunostaining of viral NP protein. Gate for NP-positive cells was set in samples not exposed to the virus and applied to infected samples. Representative plots are shown. SSC, sideward scatter. (B) Vero and Caco-2 cells were infected with SARS-CoV-2 at MOI 0.1, and infection was monitored over 24 h in a flow cytometry-based infection assay as described in (A). Data show one of 2-3 representative experiments in triplicates. (C) The supernatants of infected cells were collected from time course in (B) and assessed for *de novo* production of SARS-CoV-2 particles in a $TCID_{50}$ assay in duplicates on Vero cells. Data shows one representative experiment out of 2-3. The seeding of Caco-2 cells was performed by Patricio Doldan. All data collection was done jointly with Zina Uckeley. The figure was published in a modified version in (264).

and A549 cells. A549 cells genetically engineered to stably overexpress the SARS-CoV-2 receptor ACE2 (hereafter referred to as 'A549*') were kindly provided by Prof. Bartenschlager. Expression of ACE2 was shown to render A549 cells susceptible to SARS-CoV-2 infection (223). Cathepsin L expression was detected in all four cell lines with different extents as analyzed by SDS-PAGE and western blotting (**Figure 36A**).

Bands corresponding to pro-cathepsin L at 35-38 kDa were prominent in A549*, Caco-2, and Calu-3, whereas a band at around 28 kDa was predominant in Vero cells. This shows that versions of cathepsin L are expressed in all four cell lines. However, the conversion of pro-cathepsin L to cathepsin L is particularly strong in Vero cells. High levels of TMPRSS2 expression were detected in Calu-3 cells (**Figure 36B**). TMPRSS2 was also expressed to a lesser extent in Caco-2, while no expression was detected in Vero and A549* cells. In Caco-2, TMPRSS2 was observed as two bands. The lower band at 42 kDa may represent a cleaved version as observed in other cell lines (282). Taken together, this indicates that cathepsin L versions are expressed in all four cell lines, whereas only Caco-2 and Calu-3 cells express TMPRSS2 at detectable levels. From now on I distinguished between TMPRSS2-positive (+) cells, *i.e.*, Caco-2 and Calu-3, and TMPRSS-negative (-) cells, namely Vero and A549*.

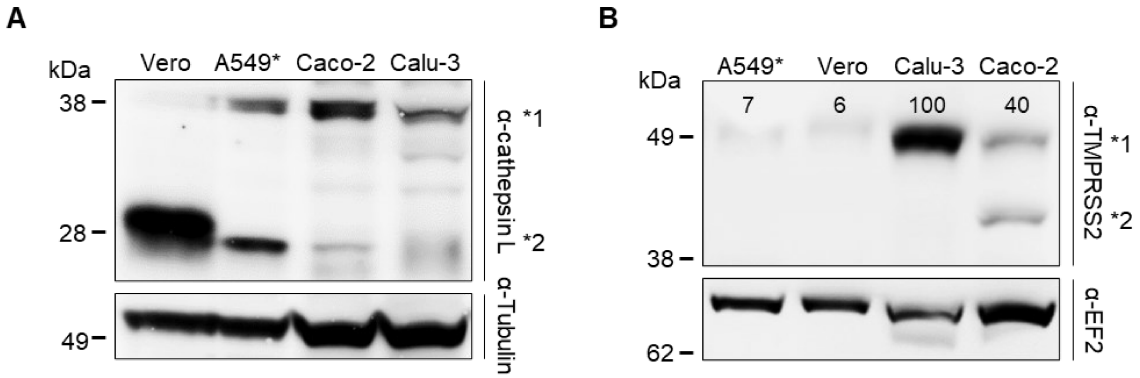

Figure 36. SARS-CoV-2 permissive cell lines have different expression levels of the host cell proteases TMPRSS2 and cathepsin L.

(A and B) Lysates of Vero, A549-ACE2 (=A549*), Caco-2, and Calu-3 cells were subjected to SDS-PAGE under reducing (A) or nonreducing conditions (B) followed by western blotting against cathepsin L (A) and TMPRSS2 (B). TMPRSS2 expression levels are indicated as percentages of Calu-3 cells normalized to the loading control EF2. *1 indicates pro-cathepsin L (A) and TMPRSS2 (B) while *2 shows cathepsin L (A) and a cleaved form of TMPRSS2 (B). EF2, elongation factor 2. Data were jointly collected with Zina Uckeley. The figure was published in (264).

To evaluate the role of TMPRSS2 and cathepsins in SARS-CoV-2 entry, I took advantage of specific inhibitors of the two proteases. In the two TMPRSS2+ cell lines Caco-2 and Calu-3, the inhibition of TMPRSS2 by aprotinin, a serine protease inhibitor, correlated with a block in infection in a dose-dependent manner (**Figure 37A**). In contrast, SARS-CoV-2 infection in the two TMPRSS2- cell lines A549* and Vero was unaffected by the addition of aprotinin. Similar results were observed when TMPRSS2 was inhibited by camostat mesylate, a more specific inhibitor of TMPRSS proteases (**Figure 37B**). In contrast, treatment of TMPRSS2+ cells with SB412515, a cathepsin L-specific inhibitor, had no

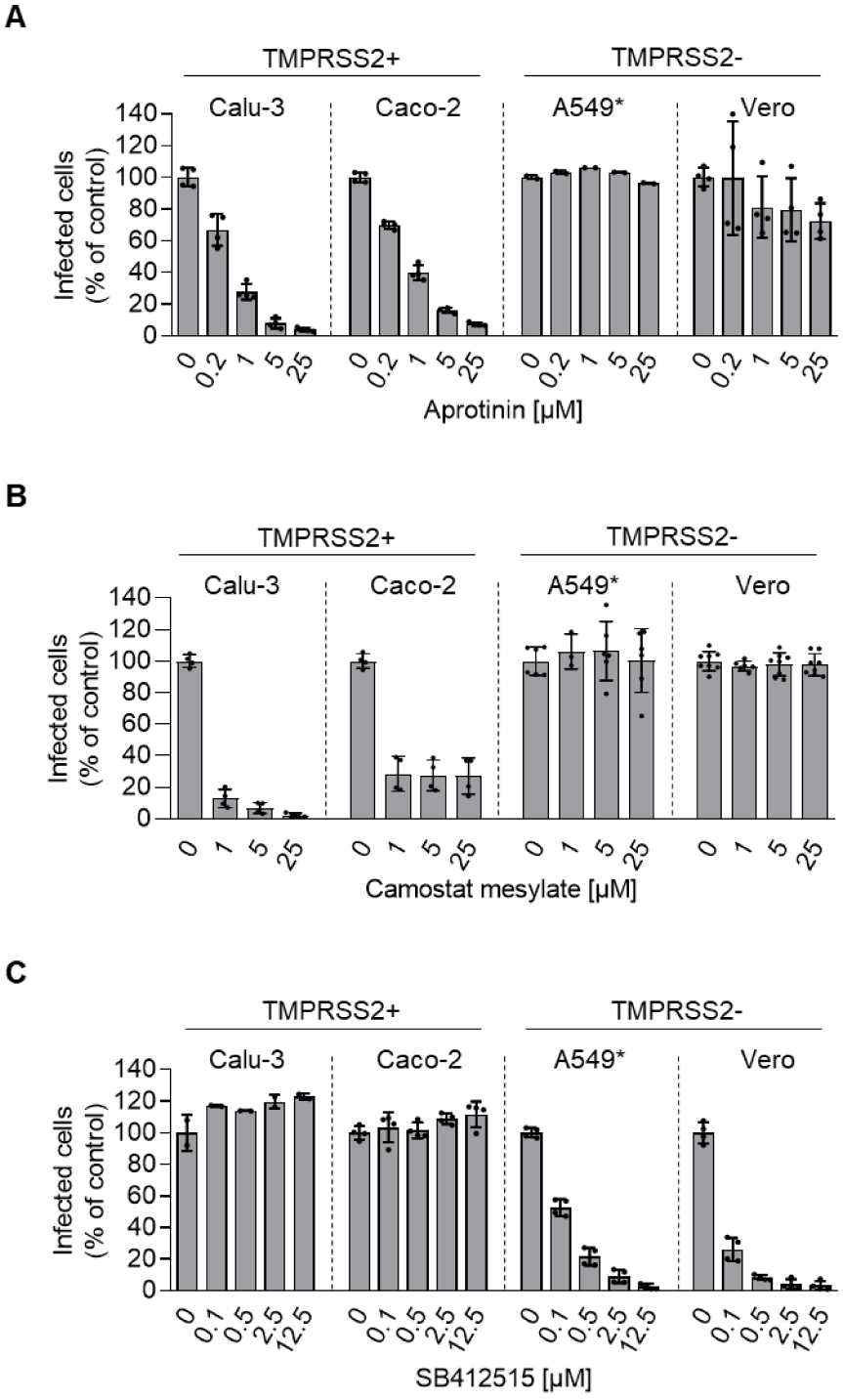

Figure 37. SARS-CoV-2 infection relies on different proteases in TMPRSS2+ and TMPRSS2- cells.

(A to C) Cells were pretreated with indicated concentrations of TMPRSS2 inhibitors aprotinin (A) and camostat mesylate (B) or the cathepsin L inhibitor SB412515 (C). Calu-3, Caco-2, A549*, and Vero cells were then infected with SARS-CoV-2 at MOI 0.3, 0.4, 0.2, and 0.3, respectively, in the continuous presence of inhibitors. Infection was stopped after 8 h (Caco-2, A549*, and Vero) or 24 h (Calu-3) and then analyzed by flow cytometry. Data were normalized to samples without inhibitor. n = 1-4. The seeding of Caco-2 and Calu-3 cells was performed by Patricio Doldan. All

data were obtained in collaboration with Zina Uckeley. The figure is a modified version published in (264).

negative effect on SARS-CoV-2 infection, whereas infection in Vero and A549* cells was dose-dependently reduced (**Figure 37C**). This suggests that in TMPRSS2+ cells, TMPRSS2 plays a role during infection that cannot be taken over by cathepsin L. Of note, all inhibitors used here and later were evaluated for cytotoxicity by a lactate dehydrogenase release assay as described in the study of TOSV entry. Upon cell death and lysis, lactate dehydrogenase is released and can be detected in the extracellular medium. All inhibitors were used at concentrations that were not toxic to the cells (**Figure 38**).

To investigate whether protease activity is required during the entry process of SARS-CoV-2 and to determine the kinetics of protease dependence, time-of-addition assays were performed. Briefly, SARS-CoV-2 binding to the cell surface was synchronized by incubation on ice for 2 h, and the internalization was induced by a rapid shift to 37°C. After various time periods, the cathepsin L inhibitor SB412515 or the TMPRSS2 inhibitor aprotinin was added either to A549* and Vero cells or to Calu-3 and Caco-2 cells, respectively. When SB412515 was added to A549* and Vero cells immediately after warming to 37°C, no infection could be detected (**Figure 39A, B**). The initial increase in infection occurred between 15-30 min post-warming and increased over time, reaching a plateau in A549* at about 90 min, which was slightly faster in Vero cells, *i.e.*, at about 60 min. Half of the particles passed the cathepsin L-sensitive step after 59 min and 37 min in A549* and Vero cells, respectively.

When aprotinin was added to Calu-3 and Caco-2 cells, a faster increase in SARS-CoV-2 infection was observed (**Figure 39C, D**). Half-maximal kinetics were reached at about 10 min and plateaued at about 20 min. Taken together, these data demonstrate that the protease activity of both cathepsin L and TMPRSS2 is required during the entry process. While the cathepsin L-sensitive step occurred after approximately 30-90 min, the requirement for TMPRSS2 was overcome more rapidly during the viral life cycle, occurring within the first 20 min of SARS-CoV-2 infection. This differential kinetics of the protease-sensitive step may be explained by the different subcellular localization of the proteases. TMPRSS2 is located on the cell surface and therefore a fast cleavage is expected. In contrast, cathepsin L is active in endolysosomes. Consequently, SARS-CoV-2 would first have to traffic through the endocytic machinery and reach endolysosomes to be activated by cathepsins in the absence of TMPRSS2. These results also suggested that viral fusion is rather concomitant with the proteolytic activation of S in target cells.

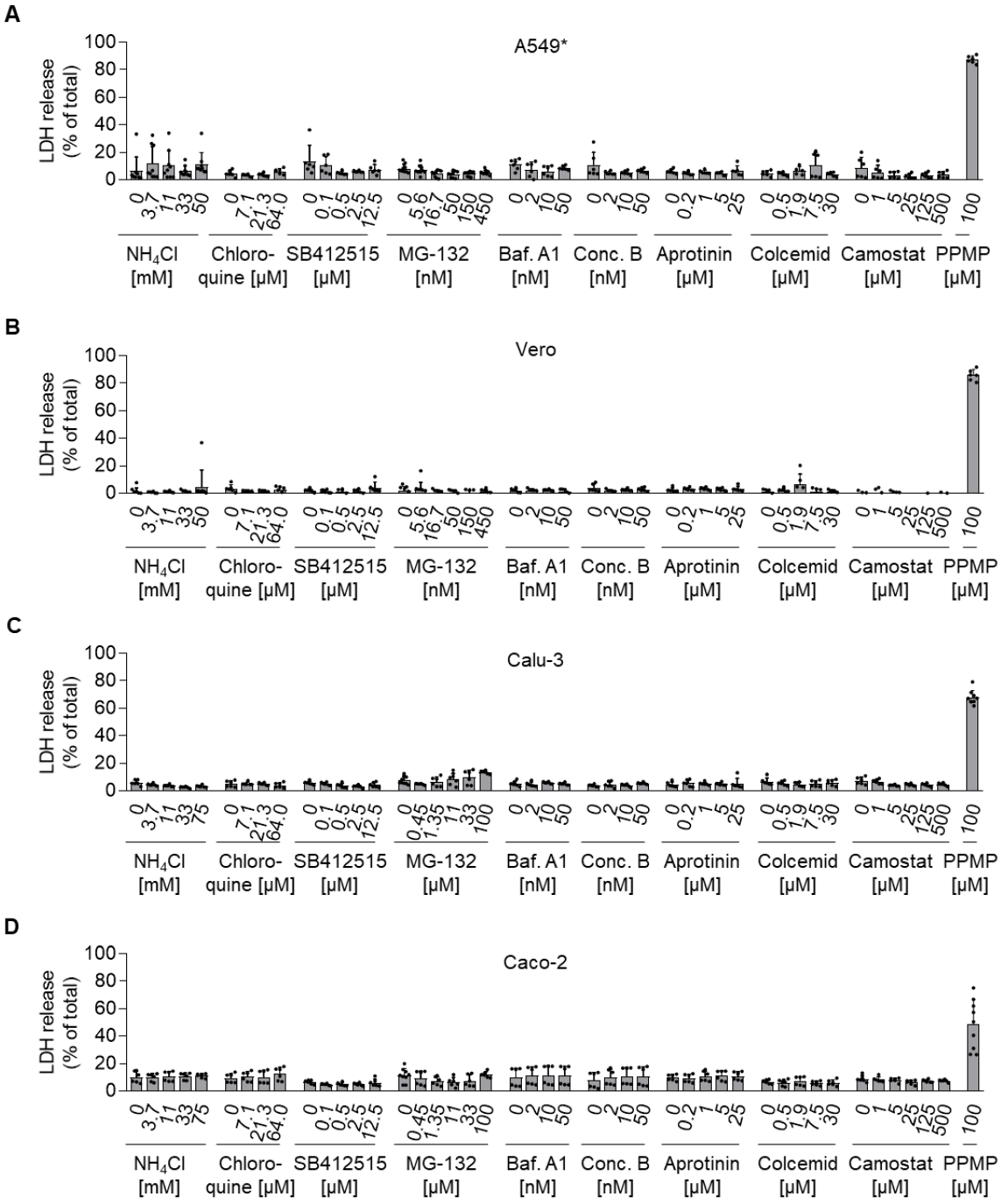

Figure 38. Inhibitors are not cytotoxic to cells at used concentrations.

(A to D) Drugs were added at indicated concentrations to A549* (A), Vero (B), Calu-3 (C), and Caco-2 (D) for 9 h at 37°C. Cytotoxicity of drugs was tested using the CytoTox96 Non-Radioactive Cytotoxicity colorimetric assay. PPMP, a ceramide analog, was used as a positive control. Values were normalized to those of untreated cells after lysis that shows the maximal release of lactate dehydrogenase (LDH) into the extracellular medium. n = 2-3. Baf. A1, bafilomycin A1, Conc. B, concanamycin B. The seeding of Caco-2 and Calu-3 cells was performed by Patricio Doldan. Data were obtained in collaboration with Zina Uckeley. The figure was adapted from (264).

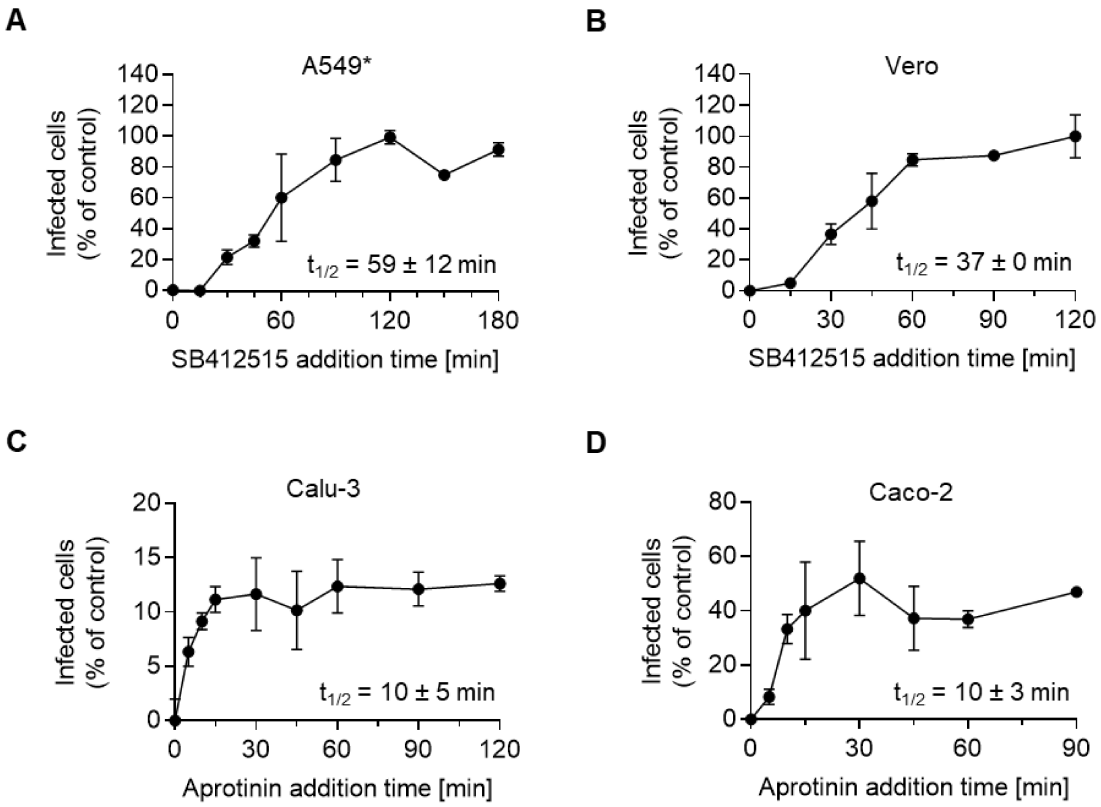

Figure 39. Differential dynamics of proteolytic cleavage in TMPRSS2+ and TMPRSS2- cells. (A to D) SARS-CoV-2 was bound to A549* (A), Vero (B), Calu-3 (C), and Caco-2 (D) on ice for 2 h at MOI 0.2, 0.3, 0.6, and 0.5, respectively. Cells were then rapidly warmed to 37°C, and cathepsin L inhibitor SB412515 (10 µM, A and B) or TMPRSS2 inhibitor aprotinin (30 µM, C and D) were added at indicated times to block further proteolytic cleavages. Infection was allowed for 8 h (A, B, and D) or 24 h (C) after the temperature shift at 37°C. Infection was analyzed by flow cytometry and normalized to samples without inhibitors. Representative results out of 2-3 experiments are shown. The seeding of Caco-2 and Calu-3 cells was performed by Patricio Doldan. All data were obtained in collaboration with Zina Uckeley. The figure is a modified version published in (264).

3.3.3 SARS-CoV-2 entry depends on endosomal acidification in TMPRSS2- cells

To explore the possibility that transport to endolysosomes is required during the entry process of SARS-CoV-2 into TMPRSS2-deficient cells, I investigated the importance of endosomal acidification for infectious entry. Similar to approaches used to study TOSV entry, vacuolar acidification was inhibited by the weak lysosomotropic bases NH_4Cl and chloroquine, or the two vATPase inhibitors bafilomycin A1 and concanamycin B. Blocking endosomal acidification resulted in a dose-dependent reduction of SARS-CoV-2 infection in all four cell lines, A549*, Vero, Caco-2, and Calu-3 (**Figure 40A-D**). However, when comparing the concentration required to inhibit 50% of the infection (IC_{50}), it became clear

that SARS-CoV-2 infection was more dependent on acidification in the two TMPRSS2- cell lines, A549* and Vero, compared to the TMPRSS2+ cell lines, Caco-2 and Calu-3. While the IC_{50} values for NH_4Cl, bafilomycin A1 and concanamycin B were 2 to 8-fold higher in TMPRSS2-expressing cells, and the difference for chloroquine even reached 200-fold (**Table 3**).

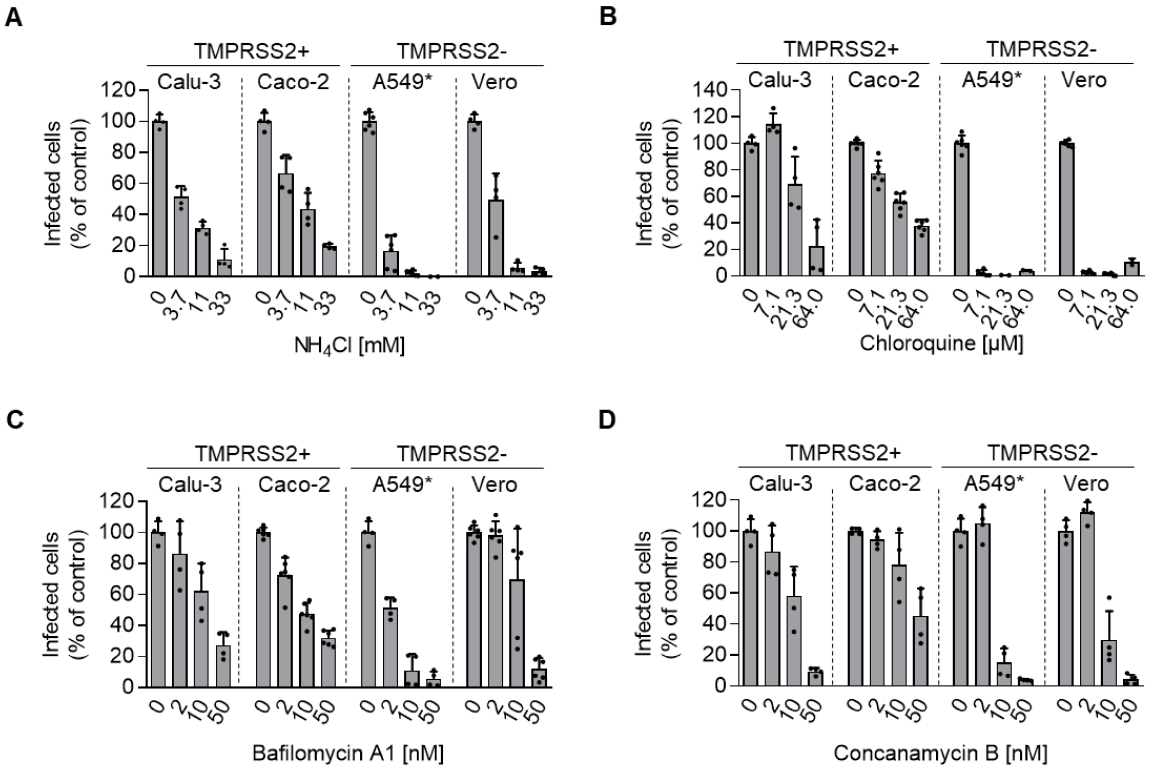

Figure 40. SARS-CoV-2 infection depends on vacuolar acidification.

(A to D) Cells were pretreated with the lysosomotropic bases NH_4Cl (A) and chloroquine (B) or the vATPase inhibitors bafilomycin A1 (C) and concanamycin B (D). Calu-3, Caco-2, A549*, and Vero cells were exposed to SARS-CoV-2 at MOI 0.3, 0.4, 0.2, and 0.3, respectively, in the continuous presence of drugs. Infection was stopped after 8 h (Caco-2, A549*, and Vero) or 24 h (Calu-3) and analyzed by flow cytometry. Data were normalized to samples without inhibitors. n = 2-3. The seeding of Caco-2 and Calu-3 cells was performed by Patricio Doldan. All data were jointly obtained with Zina Uckeley. The figure was modified from (264).

Similar to the protease inhibitors, time-of-addition assays were performed to assess the importance and kinetics of the acidification-dependent step during SARS-CoV-2 entry. As with TOSV, a time course of NH_4Cl addition with SARS-CoV-2 was performed in all four cell lines. In the two TMPRSS2- cell lines A549* and Vero, NH_4Cl addition at later time points correlated with higher infection. Half-maximal infection was reached at 48 and 52 min in Vero and A549* cells, respectively, and plateaued at approximately 90 min (**Figure 41A**). This kinetic resembled the dynamics of the cathepsin L-dependent step and

Table 3. Half-maximal inhibitory concentration (IC_{50}) of inhibitors against SARS-CoV-2.

IC50 ± SD	TMPRSS2+		TMPRSS2-	
	Calu-3	Caco-2	A549*	Vero
Aprotinin [µM]	0.4 ± 0.1	0.6 ± 0.0	x	x
Camostat mesylate [nM]	72.9 ± 36.5	806 ± 680	x	x
SB412515 [nM]	x	x	125.7 ± 29.9	36.9 ± 10.9
NH_4Cl [mM]	4.4 ± 0.9	7.9 ± 2.4	2.2 ± 0.1	2.5 ± 0.6
Chloroquine [µM]	50.1 ± 24.4	27.4 ± 4.0	0.3 ± 0.0	0.2 ± 0.1
Bafilomycin A1 [nM]	16.3 ± 6.6	10.4 ± 3.2	2.0 ± 0.6	18.6 ± 7.7
Concanamycin B [nM]	12.2 ± 5.8	50.3 ± 30.4	6.0 ± 1.2	8.6 ± 2.2
MG-132 [nM]	670 ± 205	5249 ± 2129	4.4 ± 1.4	16.4 ± 5.6

Table was published in (264).

indicated an important role of acidification during viral entry into cells lacking TMPRSS2 expression. In contrast, the addition of NH_4Cl at different time points in Caco-2 and Calu-3 cells did not result in an increase in infection, even when added hours later. This could indicate a side effect of the high concentrations of NH_4Cl specific to these cells, affecting other steps of the SARS-CoV-2 life cycle, such as viral replication, during the viral life cycle. Therefore, concanamycin B was used as an alternative for addition time course experiments in TMPRSS2 expressing cell lines. Concanamycin B is a specific inhibitor of vATPase and therefore blocks acidification, somehow, more specifically than the weak base NH_4Cl that neutralize vacuolar acidification in general. When concanamycin B was added to the cells immediately before warming at 37°C, SARS-CoV-2 infection could still be detected in both Caco-2 and Calu-3 cells (**Figure 41B**). This suggests that SARS-CoV-2 entry into TMPRSS2+ cells is insensitive to endosomal acidification.

To rule out the possibility that concanamycin B was not effective in blocking endosomal acidification in these cells, late-penetrating UUKV was tested in parallel. UUKV requires endosomal acidification and trafficking to late endosomes for productive infection (174). Addition of concanamycin B early in the time course completely inhibited UUKV infection, indicating that endosomal acidification is blocked by concanamycin B in Caco-2 cells (**Figure 41B**). Addition at later time points increased infection, suggesting that the UUKV had already entered the host cells and was no longer dependent on acidification.

Contrasting with the observations made for TMPRSS2+ cells, SARS-CoV-2 infection was sensitive to concanamycin B when the virus was bound to A549* and Vero cells, and the kinetics of concanamycin B sensitivity resembled those obtained with UUKV in these cells (**Figure 41C**). Neutralizing the pH with chloroquine had similar effects on virus entry compared to concanamycin B. While infection of SARS-CoV-2 in the TMPRSS2+ cell lines

Caco-2 and Calu-3 was nearly insensitive to the addition of chloroquine, infection in A549* and Vero cells was completely blocked when chloroquine was added directly after the shift of temperature to 37°C (**Figure 41D**). The later chloroquine was added, the higher the infection, reaching half-maximal kinetics and plateaus in a similar range as for NH_4Cl. Taken together, these data show that SARS-CoV-2 enters cells by two distinct entry routes. In cells expressing TMPRSS2, SARS-CoV-2 entry is rapid and pH-independent, whereas entry into cells lacking TMPRSS2 is slower, more asynchronous, and acidification dependent.

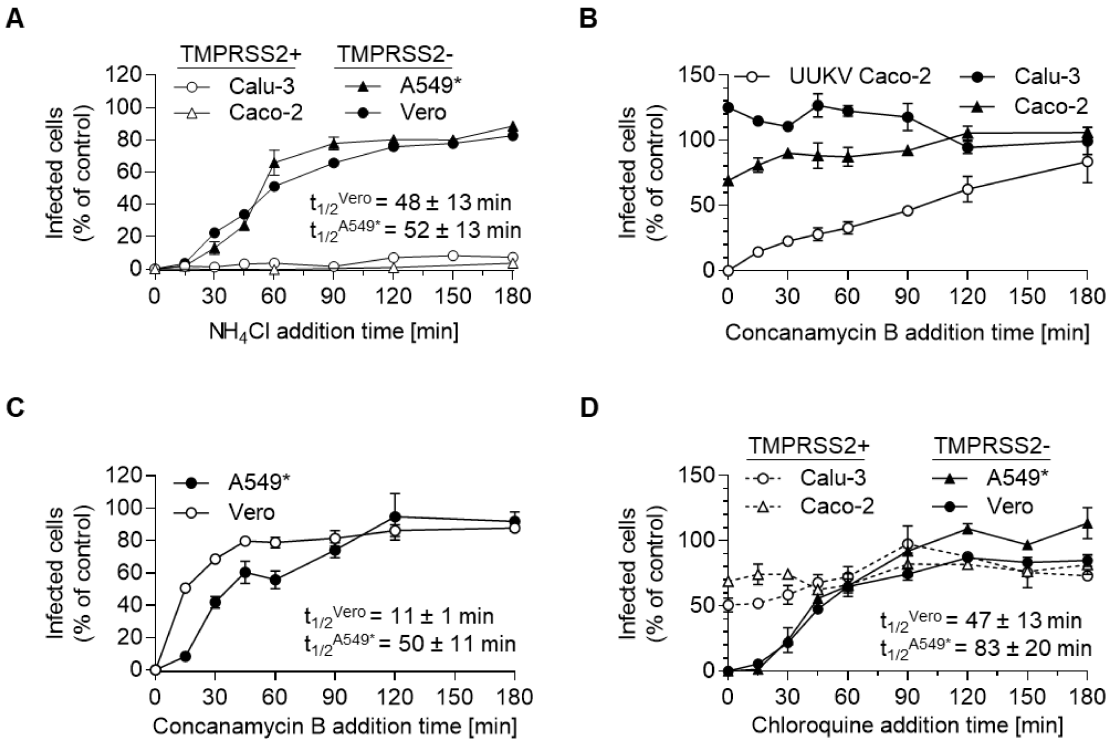

Figure 41. SARS-CoV-2 entry relies on endosomal acidification in cells lacking TMPRSS2 expression.

(A) SARS-CoV-2 was bound to Calu-3, Caco-2, A549*, and Vero cells on ice for 2 h at MOI 0.5, 0.6, 0.2, and 0.3, respectively. Temperature was rapidly shifted to 37°C and NH_4Cl (50 mM for A549* and Vero cells, and 75 mM for Calu-3 and Caco-2 cells) was added at indicated time points to block endosomal acidification. Caco-2, A549*, and Vero cells were harvested 8 h after the shift to 37°C and Calu-3 after 24 h. Infection was analyzed by flow cytometry and normalized to samples without NH_4Cl. (B and C) Same as in (A) but with the addition of concanamycin B (50 nM) instead of NH_4Cl. Uukuniemi virus (UUKV) was added as a control for Caco-2 cells and bound at MOI 150 to these cells. (D) Same as in (A) but with chloroquine instead of NH_4Cl. Chloroquine was added at a concentration of 64 µM. Representative results out of 2-3 experiments are shown. The seeding of Caco-2 and Calu-3 cells was performed by Patricio Doldan. All experiments were jointly conducted with Zina Uckeley. The figure was adapted from (264).

3.3.4 TMPRSS2 expression drives pH- and cathepsin L-independent entry of SARS-CoV-2

To correlate TMPRSS2 expression with a cathepsin L- and pH-independent pathway, TMPRSS2 was stably overexpressed in A549 cells, which normally lack TMPRSS2 expression. Overexpression of TMPRSS2 under the EF2α promoter (hereafter referred to as 'A549* TMPRSS2+') was confirmed by SDS-PAGE of cell lysates followed by western blotting (**Figure 42A**). SARS-CoV-2 infection in A549* cells expressing TMPRSS2 or not was then assayed for its sensitivity to inhibitors of TMPRSS, cathepsin L, and vATPases. While the infection of parental A549* cells lacking TMPRSS2 was unaffected by the TMPRSS inhibitor camostat mesylate, infection was reduced by 70-85% when cells expressed TMPRSS2 (**Figure 42B**). Conversely, inhibition of cathepsin L by the drug SB412515 resulted in a dose-dependent reduction of SARS-CoV-2 infection in cells lacking TMPRSS2 (**Figure 42C**). No effect on infection was observed when cells overexpressed TMPRSS2. Furthermore, TMPRSS2-deficient A549* cells showed a dose-dependent reduction with over 90% inhibition at 50 nM bafilomycin A1, whereas infection in TMPRSS2-expressing cells was only marginally reduced by 15% at the same concentration of bafilomycin A1 (**Figure 41D**). Taken together, these data demonstrate that TMPRSS2 expression drives pH- and cathepsin L-independent entry of SARS-CoV-2 into A549 cells.

To assess how different expression levels of TMPRSS2 affect the entry routes, TMPRSS2 was expressed in A549* cells under the weaker promoter ROSA26 (hereafter referred to as A549* ROSA-TMPRSS2). While cells lacking TMPRSS2 were completely dependent on cathepsin L activity for SARS-CoV-2 infection, cells strongly overexpressing TMPRSS2 were almost completely dependent on TMPRSS2 for infection (**Figure 42B, E**). Weaker expression of TMPRSS2 in A549* ROSA-TMPRSS2 cells did not result in complete inhibition by the TMPRSS2 and cathepsin L inhibitors (**Figure 42E**). Blocking the TMPRSS2 pathway resulted in 55% inhibition of SARS-CoV-2 infection, while a block in the cathepsin L-dependent pathway resulted in 65% inhibition of infection. Notably, A549 cells lacking expression of the ACE2 receptor but strongly overexpressing TMPRSS2 were not susceptible to SARS-CoV-2 infection at all. This shows that infectious entry of SARS-CoV-2 depends on the expression of its receptor ACE2 and suggests that the expression levels of individual proteases, among others, may influence which entry pathway is used by SARS-CoV-2.

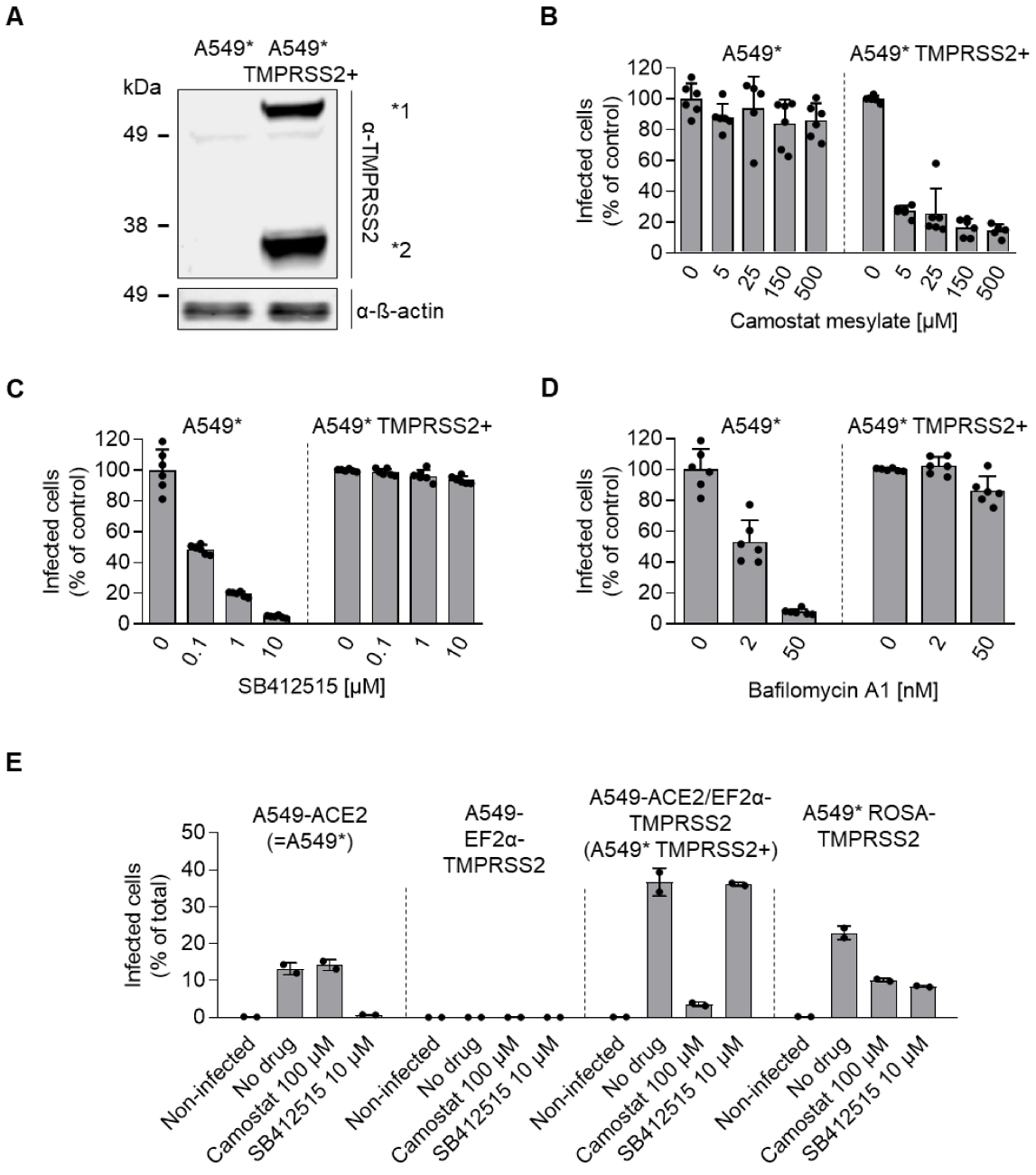

Figure 42. SARS-CoV-2 infection becomes pH- and cathepsin-independent upon TMPRSS2 overexpression.

(A) Lysates of A549* cells and A549* cells overexpressing TMPRSS2 (A549* TMPRSS2+) was subjected to nonreducing SDS-PAGE and western blotting against TMPRSS2. *1 indicates the full-length and *2 a cleaved form of TMPRSS2. (B to D) A549* and A549* TMPRSS2+ cells were pretreated at indicated concentrations of the TMPRSS2 inhibitor camostat mesylate (B), the cathepsin L inhibitor SB412515 (C), or the vATPase inhibitor bafilomycin A1 (D). Cells were infected with SARS-CoV-2 at MOI 0.2 in presence of inhibitors for 8 h at 37°C. Infection was quantified by flow cytometry and data were normalized to infection in samples where inhibitors had been omitted. n = 3. Data (A to D) were obtained in collaboration with Zina Uckeley. (E) A549 cells with different expression patterns of ACE2 and TMPRSS2 (A549* (=A549-ACE2), A549-EF2α-

TMPRSS2, A549-ACE2/EF2α-TMPRSS2 (=A549* TMPRSS2+), and A549* ROSA-TMPRSS2) were pretreated with camostat mesylate or SB412515 and challenged with SARS-CoV-2 at MOI 0.2 for 8 h. Infection was quantified by flow cytometry. Raw values of one representative experiment out of two are shown. The figure was adapted and modified from (264).

3.3.5 SARS-CoV-2 relies on endosomal maturation for infection of TMPRSS2- cells

My results suggested that SARS-CoV-2 enters cells through the endocytic machinery when TMPRSS2 is absent, and conversely, that the virus penetrates from the plasma membrane or early endosomes when TMPRSS2 is expressed in target cells. To further test the possibility that SARS-CoV-2 reaches endolysosomes for infection in TMPRSS2- cells, I used perturbants of several factors important for LE maturation. These approaches were similar to those described in the study of TOSV entry (section 3.2.4). One of these factors is Rab7a, the small GTPase associated with late endosomal vesicles. Transient expression of EGFP-tagged Rab7a in Vero cells resulted in an increase in SARS-CoV-2 infection with increasing Rab7 WT expression levels, reaching a 1.4-fold increase at the highest Rab7 WT expression level (**Figure 43A**). While a low level of overexpression of the constitutively active mutant Q67L resulted in an increase in infection compared to WT Rab7, a higher level of overexpression resulted in a decrease in infection. In contrast, expression of the dominant negative mutant T22N reduced SARS-CoV-2 by up to 50% compared to WT at the respective expression level. The combination of increased infection with higher Rab7 WT expression and inhibition with dominant-negative mutant expression suggests a role for proper LE formation and maturation in the cathepsin L-dependent entry of SARS-CoV-2 into Vero cells.

Transport of cargo to LEs and lysosomes is dependent on ubiquitin-dependent endosomal sorting in EEs. Depletion of the free ubiquitin pool by the proteasomal inhibitor MG-132 resulted in a dose-dependent reduction of SARS-CoV-2 infection with IC_{50} values of 4.4 and 16.4 nM in A549* and Vero cells, respectively (**Figure 43B, Table 3**). To link the effect of MG-132 to the entry process of SARS-CoV-2, and to rule out side effects of MG-132 on later stages of the viral life cycle, I determined the timing at which SARS-CoV-2 becomes insensitive to MG-132 in an addition time course similar to those described above. I observed that the kinetics of penetration in cells treated with MG-132 was similar to those obtained for inhibitors of cathepsin L and vacuolar acidification (**Figure 43C**). In both A549* and Vero cells, the kinetics reached a half-maximal level at approximately 45 min and reached a plateau at approximately 60 to 90 min. This suggests that MG-132 affects SARS-CoV-2 entry in cells lacking TMPRSS2 expression. LE maturation also depends on MT-mediated transport to the nuclear periphery. Depolymerization of MT

induced by colcemid treatment in Vero cells resulted in a 40-50% reduction in SARS-CoV-2 infection (**Figure 43D**). Collectively, these data demonstrate that SARS-CoV-2 relies on functional LEs for infectious entry into TMPRSS2- cells.

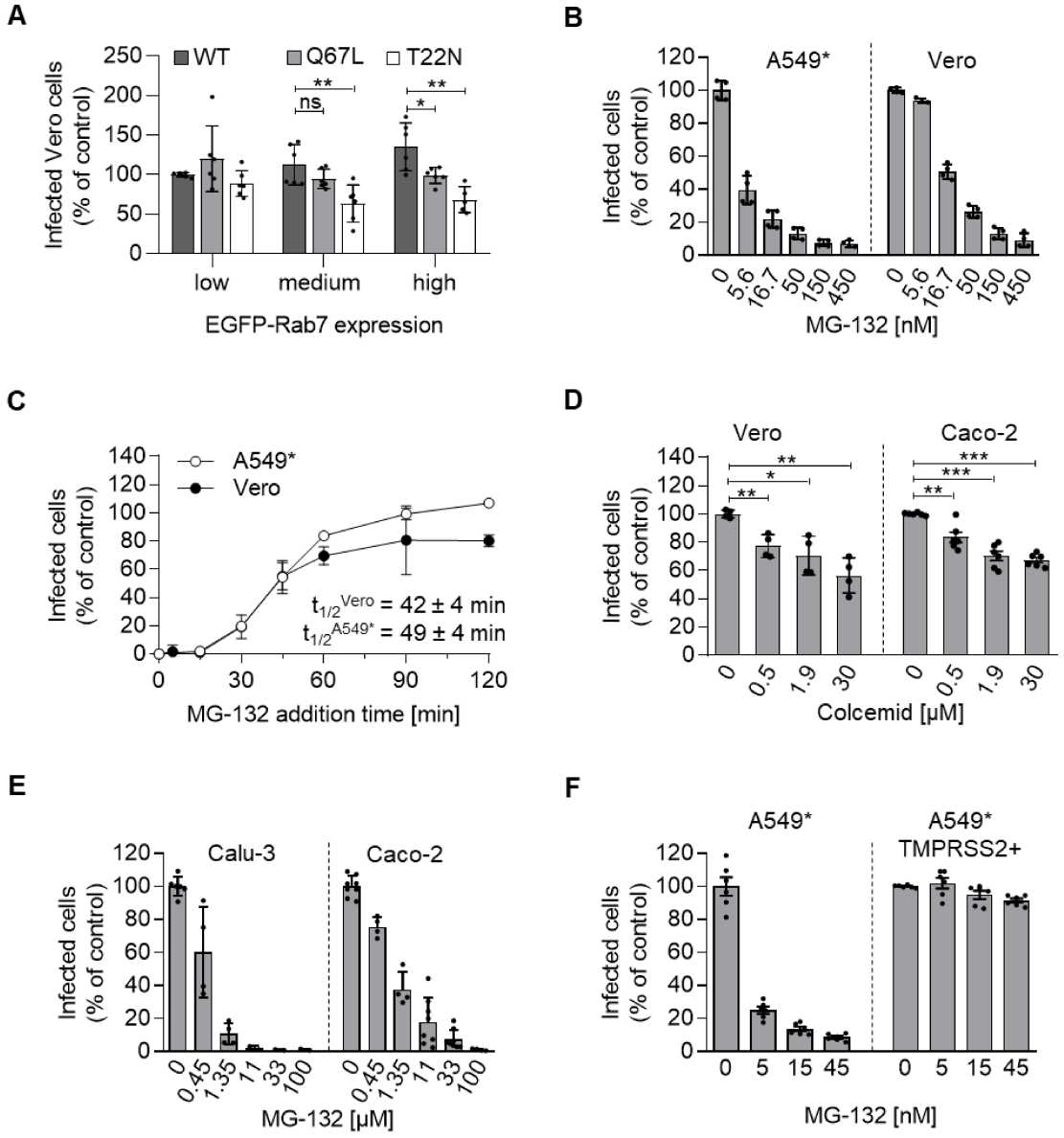

Figure 43. Endosomal maturation is required for SARS-CoV-2 entry into TMPRSS2- cells.
(A) Vero cells were transfected with expression vector coding for EGFP-tagged Rab7a wild-type (WT) and its constitutively active, Q67L, and dominant-negative, T22N, mutants. 22 h post-transfection, cells were exposed to SARS-CoV-2 at MOI 0.3 for 8 h. Cell populations with varying expression levels of EGFP-Rab7a were selected and SARS-CoV-2 infection was analyzed in each population by flow cytometry. Infection was normalized to cells with the lowest expressing levels of EGFP-Rab7a WT. Unpaired t-test with Welch's correction was applied to compare infection in cell populations with similar expression levels of EGFP-Rab7a. n = 2, p values: WT medium vs. Q67L medium, ns, p = 0.1655; WT medium vs. T22N medium, **, p = 0.0062; WT high vs. Q67L high, *,

p = 0.0317; WT high vs. T22N high, **, p = 0.0017. ns, not significant. (B) A549* and Vero cells were pretreated with MG-132 and infected with SARS-CoV-2 at MOI 0.2 and 0.3, respectively, in the continuous presence of drugs. Cells were harvested after 8 h, and infection was analyzed by flow cytometry and normalized to samples without inhibitor added. n = 2. (C) SARS-CoV-2 particles were bound to A549* and Vero cells at MOI 0.2 and 0.3, respectively, on ice for 2 h. Cells were rapidly shifted to 37°C, and MG-132 (3.7 µM) was added at indicated time points. Cells were harvested 8 h after the temperature shift, and infection was quantified by flow cytometry. Data were normalized to infection in samples without MG-132 treatment. Representative experiment out of two is shown. (D) Cells were pretreated with indicated concentrations of colcemid for 3 h on ice before being challenged with SARS-CoV-2 at MOI 0.3 for Vero and 0.4 for Caco-2 for 8 h. Infection was quantified by flow cytometry and normalized to samples where colcemid had been omitted. n = 2-3, p values: Vero 0 vs. 0.5 µM, **, p = 0.0075; 0 vs. 1.9 µM, *, p = 0.0202; 0 vs. 30 µM, **, p = 0.0047; Caco-2 0 vs. 0.5 µM, **, p = 0.0062; 0 vs. 1.9 µM, ***, p = 0.0003; 0 vs. 30 µM, ***, p <0.0001. (E and F) Calu-3 and Caco-2 (E), as well as A549* and A549* TMPRSS2+ (F), were pretreated with MG-132 and infected with SARS-CoV-2 at MOIs 0.3, 0.4, 0.2, and 0.2, respectively, in the continuous presence of the drug. Infection was allowed for 8 h (Caco-2, A549*, and A549* TMPRSS2+) or for 24 h (Calu-3) and was then analyzed by flow cytometry and normalized to samples without inhibitor. n = 1-4. The seeding of Caco-2 and Calu-3 cells was performed by Patricio Doldan. Data were obtained jointly with Zina Uckeley. The figure was modified from (264).

Perturbation of the MT network also reduced SARS-CoV-2 infection in TMPRSS2+ Caco-2 cells, although the inhibitory effect was lower compared to TMPRSS2- cells (**Figure 43D**). This could be explained by a broader role of the MT network during SARS-CoV-2 infection in addition to its role during entry. To investigate whether SARS-CoV-2 requires sorting to LEs when TMPRSS2 is expressed, Caco-2 and Calu-3 cells were infected in the presence of MG-132. MG-132 caused a dose-dependent inhibition of SARS-CoV-2 infection in both Caco-2 and Calu-3 cells, although the IC_{50} values were up to 1,200-fold higher compared to those observed in TMPRSS2- A549* and Vero cells (**Figure 43E, Table 3**). When TMPRSS2 was overexpressed in A549* cells, MG-132 had only a marginal effect on SARS-CoV-2 infection, *i.e.*, less than 10% decrease in infection at the highest concentration of the drug (**Figure 43F**). Overall, these data demonstrated that entry of SARS-CoV-2 into cells expressing TMPRSS2 is not dependent on LE maturation.

3.3.6 Proteolytic processing of the Spike protein drives membrane fusion

To mediate fusion of the viral membrane with host cell membranes, the S protein must be processed by proteases at two distinct sites. The first cleavage, priming, occurs at the junction between the S1 and S2 domains, and the second cleavage, activation, takes

place in the S2 domain upstream of the fusion peptide. For priming, furin processing in producer cells or cleavage by serine or cathepsin proteases in target cells have been proposed (198). To evaluate the rate of cleaved S protein released from producer cells, viral proteins from the SARS-CoV-2 virus stock were separated by SDS-PAGE followed by western blotting using a primary antibody recognizing the S2 fragment. A strong band was detected at approximately 160 kDa corresponding to the full-length unprocessed S, S0 (**Figure 44A**). The cleaved S2 fragment appeared at approximately 75 kDa with weaker intensity than S0. I quantified the signal and determined a ratio between the cleaved S2 signal and the total signal (S0 + S2). This allowed to show that approximately one third of the S was cleaved by producer cells in the virus stock (**Figure 44B**). When virus particles were treated with trypsin prior to SDS-PAGE, the S2 band became more prominent and the ratio of S2/(S0 + S2) was greater than 0.9, indicating that more than 90% of the S proteins were cleaved at the S1/S2 junction. The addition of exogenous furin slightly increased processing, reaching about 50% of cleavage.

Next, I wanted to determine whether increased proteolytic processing would affect infection of the cells. To assess this, SARS-CoV-2 was pretreated with exogenous trypsin or furin before being added to cells. Trypsin pretreatment resulted in a 1.8- and 2.5-fold increase in infection in Caco-2 and Vero cells, respectively, compared to untreated virus (**Figure 44C**). Additional processing with furin resulted in a slight increase of 20% in Caco-2 cells, whereas it had no effect on infection of Vero cells. These results suggest that proteolytic cleavage of virus particles in producer cells was incomplete and that approximately one third of S was proteolytically processed upon release. In other words, one S molecule per trimer was already cleaved after the virus release. Taken together, these data indicated that additional proteolytic processing of the S protein on input viruses favors SARS-CoV-2 infectivity regardless of the presence of TMPRSS2 in target cells.

To investigate the requirements for SARS-CoV-2 fusion and to assess whether proteolytic processing is essential, an imaging-based cell-cell fusion assay was established. Briefly, cells were infected with SARS-CoV-2 for 24 h to achieve more than 90% infection. Infected cells (donor cells) were then co-cultured for 5 h with noninfected cells (target cells), which were previously labeled with the green cytosolic dye CMFDA (**Figure 45A**). After 5 h of co-culture, cells were fixed and immunofluorescence staining for viral NP protein allowed detection of infected cells. Confocal imaging visualized infected donor cells in magenta and CMFDA-labeled target cells in green. Fusion events between donor and target cells could then be detected as multinucleated cells stained in both magenta and green. This assay is based on the property of CMFDA that the dye can pass freely through membranes when added to cells, but is converted to a cell-impermeable

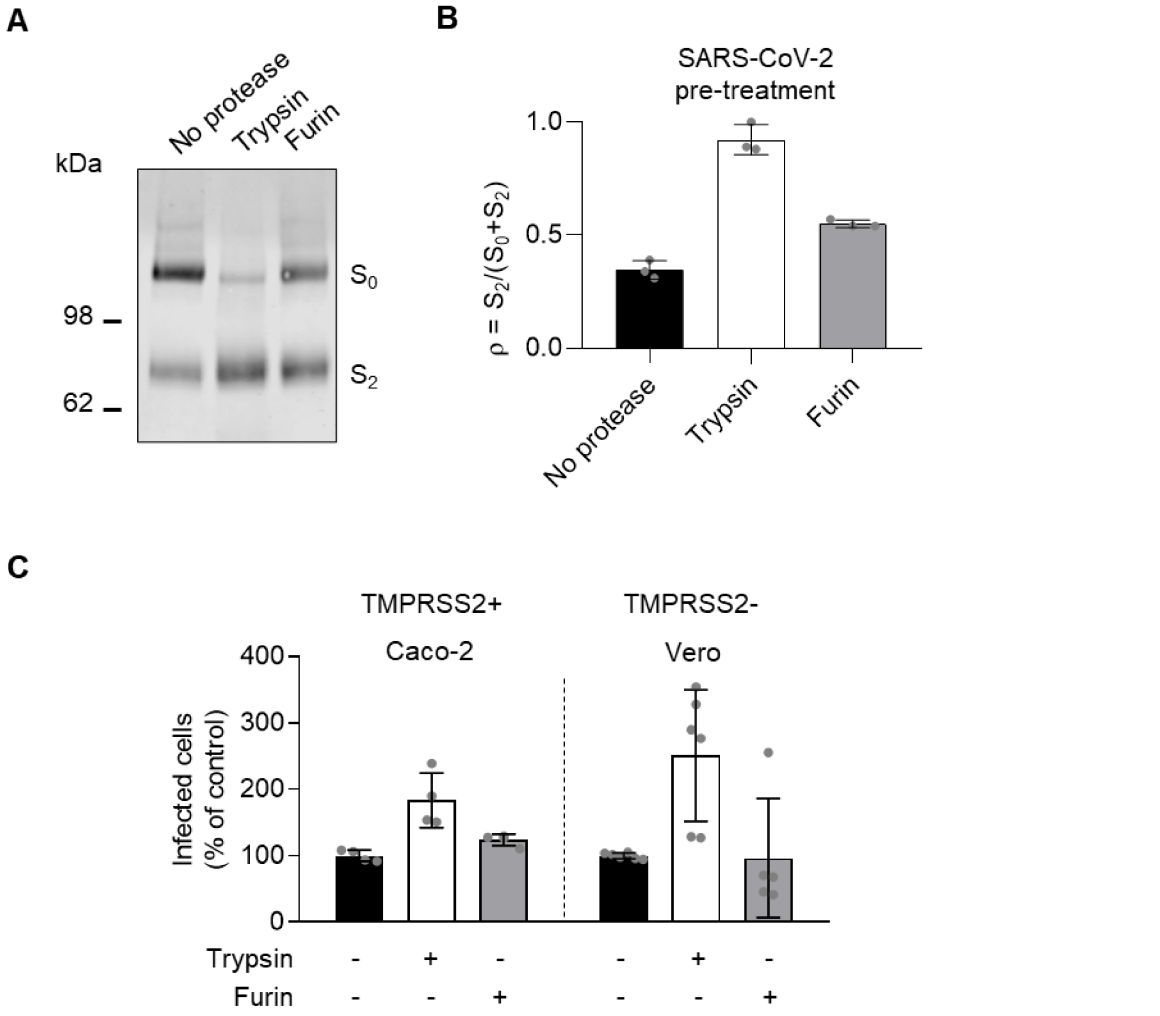

Figure 44. Proteolytic activation of SARS-CoV-2 particles is incomplete when released from producer cells.

(A) SARS-CoV-2 particles were left untreated or were treated with exogenous trypsin or furin for 15 min at 37°C before subjected to reducing SDS-PAGE and western blotting using a polyclonal antibody targeting S2 region of the Spike protein. Representative blot is shown. S_0, full-length Spike. (B) S_0 and S_2 were semi-quantified from (A). The fraction of S_2 compared to sum of S_0 and S_2 is shown. (C) SARS-CoV-2 were pretreated with proteases as explained in (A) and added to Caco-2 and Vero cells at MOI 0.4 and 0.3, respectively. Cells were harvested after 8 h, and infection was quantified by flow cytometry. Data were normalized to infection with untreated SARS-CoV-2 particles. The seeding of Caco-2 cells was performed by Patricio Doldan. Data were obtained jointly with Zina Uckeley. The figure was modified from (264).

fluorescent dye once inside the cells. The degree of fusion was expressed as a fusion index ranging from 0 to 1. 0 means that no multinucleated cells of green and magenta color appeared in a microscopic field of view, and a fusion index of 1 indicates that all cells have fused with each other.

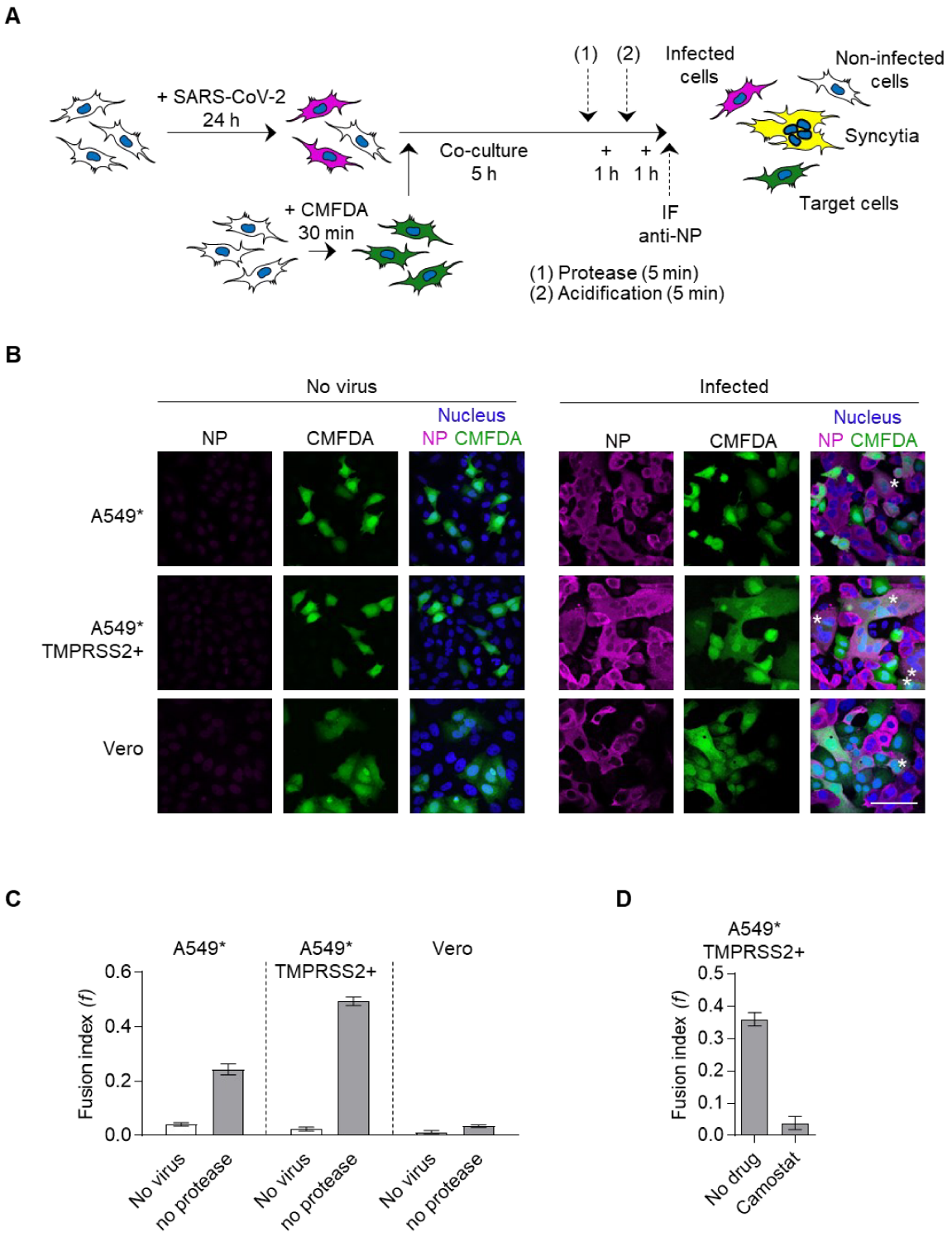

Figure 45. SARS-CoV-2 fusion is increased upon TMPRSS2 expression.

(A) Principle of my cell-cell fusion assay. In this approach, donor cells infected with SARS-CoV-2 were immunostained against the viral NP protein (magenta) and target cells fluorescently labeled with CMFDA (green). Cell-cell fusion events results in the formation of syncytia, and in turn, in the merge of both colors (yellow). CMFDA, cytosolic green dye. (B) A549*, A549* TMPRSS2+, and Vero cells were first left noninfected or were infected with SARS-CoV-2 at MOI 0.1 for 24 h. Cells were then co-cultured with noninfected, CMFDA-labeled cells (shown in green) for 5 h. Co-culture

was fixed, and infected cells were subjected to immunofluorescent staining against viral NP protein (in magenta). Nuclei were stained with Hoechst (in blue). Co-culture was imaged by confocal microscopy. White asterisks indicate syncytia formation between donor and target cells. The multinucleated cells appeared in yellow. Representative images are shown. Scale bar, 100 µm. (C) Cell-cell fusion from (B) was quantified. Fusion was expressed in a fusion index *f* given as *f* = 1 – [(number of green cells in a field)/(number of nuclei in green cells)]. A minimum of 30 fields were quantified for samples without viruses and a minimum of 80 for infected samples. Data show mean ± SEM. (D) Co-culture was performed with A549* TMPRSS2+ cells as described in (B) but in the presence of the TMPRSS2 inhibitor camostat (100 µM). A minimum of 30 fields. The figure was modified from (264).

Using Vero cells as donor and target cells, almost no fusion events were observed after 5 h of co-culture (**Figure 45B, C**). In A549* cells, some fusion events were observed, reaching a fusion index of 0.24, which increased approximately 2-fold upon overexpression of TMPRSS2. Conversely, inhibition of TMPRSS2 by camostat strongly reduced syncytia formation (**Figure 45D**). This suggests that cell surface expression of TMPRSS2 promotes syncytia formation.

To determine whether the addition of exogenous proteases could increase fusion formation, cells were treated with trypsin or furin for 5 min after 5 h of co-culture. Trypsin treatment resulted in a 7- and 2.8-fold increase in syncytia formation in Vero and A549* cells, respectively (**Figure 46A, B**). However, the addition of exogenous trypsin to A549* TMPRSS2+ cells only marginally increased syncytia formation from 0.49 to 0.54, while it significantly enhanced the formation of syncytia with A549* cells, from 0.24 to 0.68. The addition of exogenous furin to the co-culture had little or no effect on fusion formation. This demonstrates that the cell-cell fusion assay established here is functional and that fusion between donor and target cells can be visualized and quantified by microscopy. Proteolytic processing by TMPRSS2 and trypsin can induce fusion, whereas the addition of furin does not appear to be effective. Furthermore, these data suggest that proteolytic cleavage is both necessary and sufficient to induce SARS-CoV-2 fusion.

3.3.7 Low pH does not inactivate SARS-CoV-2 and is not sufficient to trigger viral membrane fusion

SARS-CoV-2 does not appear to depend on endosomal acidification for infectious entry into TMPRSS2+ cells. This suggests that acidification is not required for the fusion process itself, but rather for proteolytic processing by cathepsin L in TMPRSS2- cells. To further assess the role of acidification in SARS-CoV-2 fusion, I first determined whether

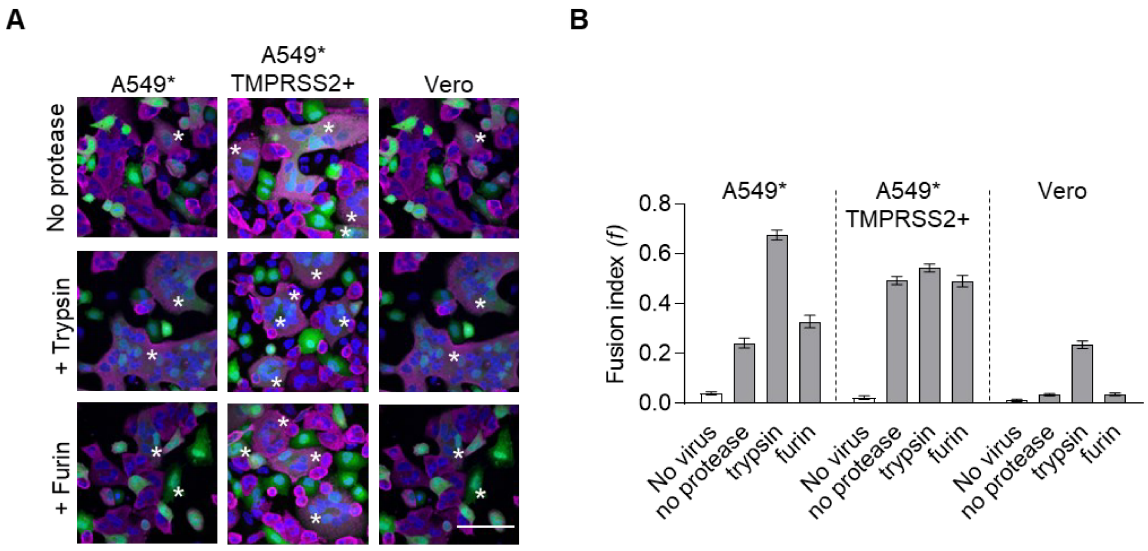

Figure 46. Proteolytic processing triggers SARS-CoV-2 membrane fusion.

(A) Cell-cell fusion assay was performed as in Figure 45B but 5 h after adding non-infected, CMFDA-labeled green cells, co-culture was treated with proteases for 5 min at 37°C and subsequently recovered for 1 h at 37°C before fixation. White asterisks indicate syncytia formation. Representative images are shown. Scale bar, 100 µm. (B) Cell-cell fusion from (A) was quantified as described in Figure 45C. A minimum of 30 fields were quantified for samples without viruses and a minimum of 60 for infected samples. Data shows mean ± SEM. The figure was modified from (264).

SARS-CoV-2 could be inactivated by low pH treatment prior to infection, as previously shown for TOSV and several other viruses (section 3.2.6). Briefly, virus particles were exposed to pH buffers ranging from 5.0 to 7.4, similar to the acidification that occurs during trafficking in the endosomal system. Prior to cell infection, the virus particles were neutralized to pH 7.4 and added to the cells. Viruses with acid-activated membrane fusion are usually inactivated when pretreated at the pH that induces fusion, which is caused by the conversion of the viral fusion protein from the pre-fusion to the post-fusion conformation. Low pH treatment of SARS-CoV-2 resulted in only a 20% reduction at pH 6.0 and approximately a 50% reduction at pH 5.0 in both Vero and Caco-2 cells (**Figure 47A**). This reduction is minimal compared to SFV and IAV, which were inactivated by approximately 95% at pH 5.5 (**Figure 31D, F**).

To further investigate the role of acidification on SARS-CoV-2 fusion, the effect of low pH was tested in my established cell-cell fusion assay. Buffers of different pH were added for 5 min after 5 h of co-culture. Low pH did not affect syncytia formation in either Vero, A549* or A549* TMPRSS2+ cells (**Figure 47B**). To investigate whether there is a synergistic effect of proteolytic cleavage and acidification on fusion, cells were first treated

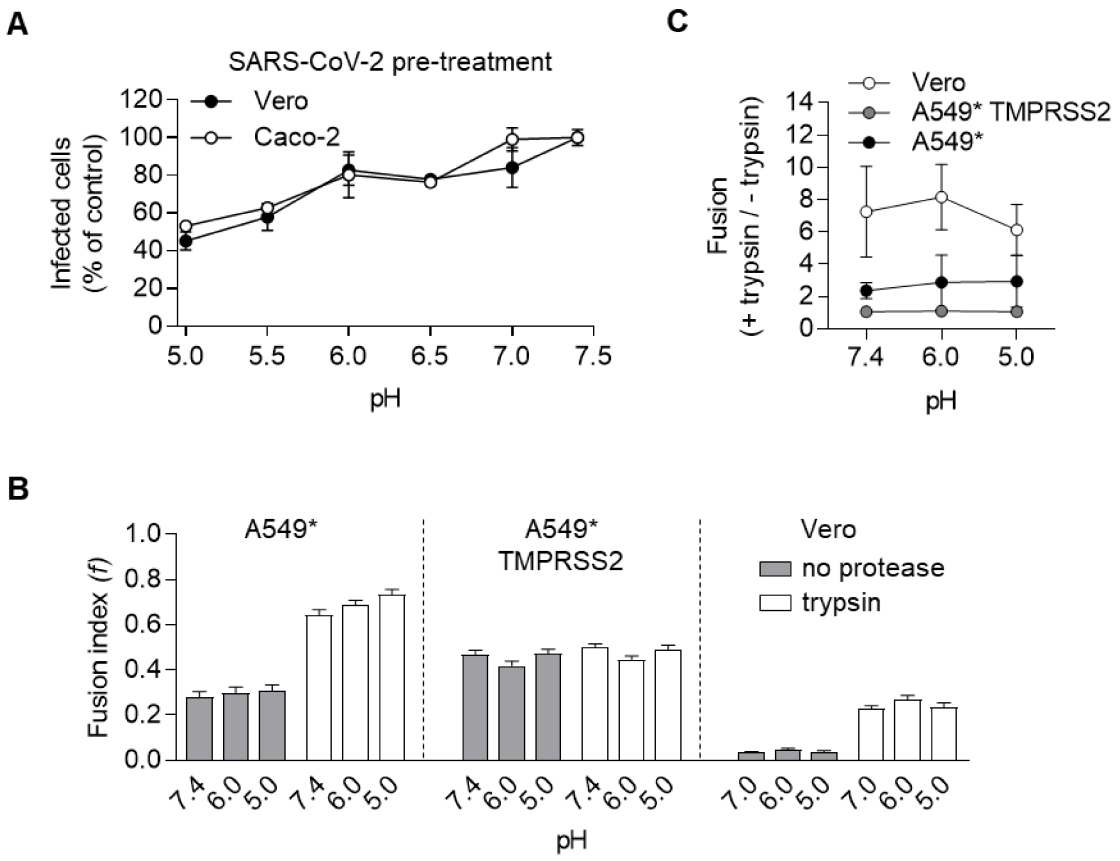

Figure 47. SARS-CoV-2 membrane fusion is not acid-activable.

(A) SARS-CoV-2 particles were pretreated at indicated pH for 10 min at 37°C and then the pH was neutralized before the addition of the virus to Vero and Caco-2 cells at MOI 0.3 and 0.4, respectively. Cells were harvested 8 h later, and infection was quantified by flow cytometry and normalized to samples pretreated at pH 7.4. One representative out of two experiments is shown. The seeding of Caco-2 cells was performed by Patricio Doldan. Data were obtained jointly with Zina Uckeley. (B) SARS-CoV-2 fusion was assessed at various pH values in my cell-cell fusion assay as described in Figure 45B and 46A. After trypsin treatment, cells were left at 37°C for 1 h and then culture medium was exchanged against buffers at indicated pH for 5 min at 37°C. After washing and a further incubation of 1 h at 37°C, cells were fixed. At least 50 microscopy fields were analyzed per condition, and the fusion index was calculated as described in Figure 45C. Data show mean ± SEM. (C) Ratio of fusion of cells treated with trypsin to those of untreated cells was calculated for each cell line from the data obtained in (B). The figure was modified from (264).

with trypsin and then exposed to different pH buffers and tested in the cell-cell fusion assay. Again, very little or no difference was observed after trypsin treatment followed by exposure to low pH compared to neutral pH (**Figure 47B**). Notably, proteolytic processing by trypsin again resulted in a 6-7-fold increase in Vero cells, and a 2-3-fold increase in A549* and almost no effect on syncytia formation in A549* cells overexpressing TMPRSS2 (**Figure 47B, 46B**). In all three cell lines, the fusion index was similar and

appeared independent on acidification (**Figure 47C**). Taken together, these data demonstrate that endosomal acidification alone is not sufficient to induce membrane fusion of SARS-CoV-2. In addition, the results showed that virus particles have a high resistance to low pH treatment with preservation of their infectivity.

3.3.8 Low pH is required for endolysosomal proteases that activate/prime viral fusion

Acidification is required for entry into TMPRSS2- cells, but fusion does not depend on low pH. I therefore postulated that acidification may be required for the activity of endolysosomal cathepsins that prime and activate SARS-CoV-2 fusion. To test this hypothesis, I evaluated whether SARS-CoV-2 particles pre-activated with exogenous proteases also require endosomal acidification for the infection of TMPRSS2- cells. Viral particles were pretreated with trypsin or thermolysin and then added to cells. Thermolysin was previously shown to cleave SARS-CoV S protein and induce a cleavage pattern in the Ebolavirus glycoprotein GP similar to that of cathepsin L (283, 284). In contrast to the activity of cathepsin L that relies on endosomal acidification, thermolysin has the advantage to be functional at neutral pH. The use of thermolysin thus allows to decouple proteolytic processing from low pH. With this approach, I observed that the block of vATPases by bafilomycin A1 almost completely abolished infection of TMPRSS2- A549* cells by SARS-CoV-2 (**Figure 48A, 40C**). Conversely, when viral particles were pretreated with trypsin or thermolysin, infection could be rescued. While trypsin cleavage could increase infection from 8% to 59%, thermolysin treatment could completely rescue infection. Similar observations were made in the TMPRSS2- Vero cells.

The loss of dependence on endosomal acidification upon protease treatment of the virus was additionally tested by determining the kinetics of the acid-requiring step in an NH_4Cl addition time course. Briefly, SARS-CoV-2 was pretreated with or without trypsin and added to cells on ice to synchronize binding. The temperature was then rapidly shifted to 37°C, and NH_4Cl was added at various time points to neutralize endosomal acidification. In stark contrast to untreated virus, the addition of NH_4Cl did not inhibit infection of trypsin-pretreated SARS-CoV-2 in both A549* and Vero cells (**Figure 48B**). The curve was similar to that of SARS-CoV-2 entering the TMPRSS2- cell lines Caco-2 and Calu-3 (**Figure 41B, D**). These data demonstrate that SARS-Co-2 particles are no longer dependent on endosomal acidification when processed and activated by cellular proteases.

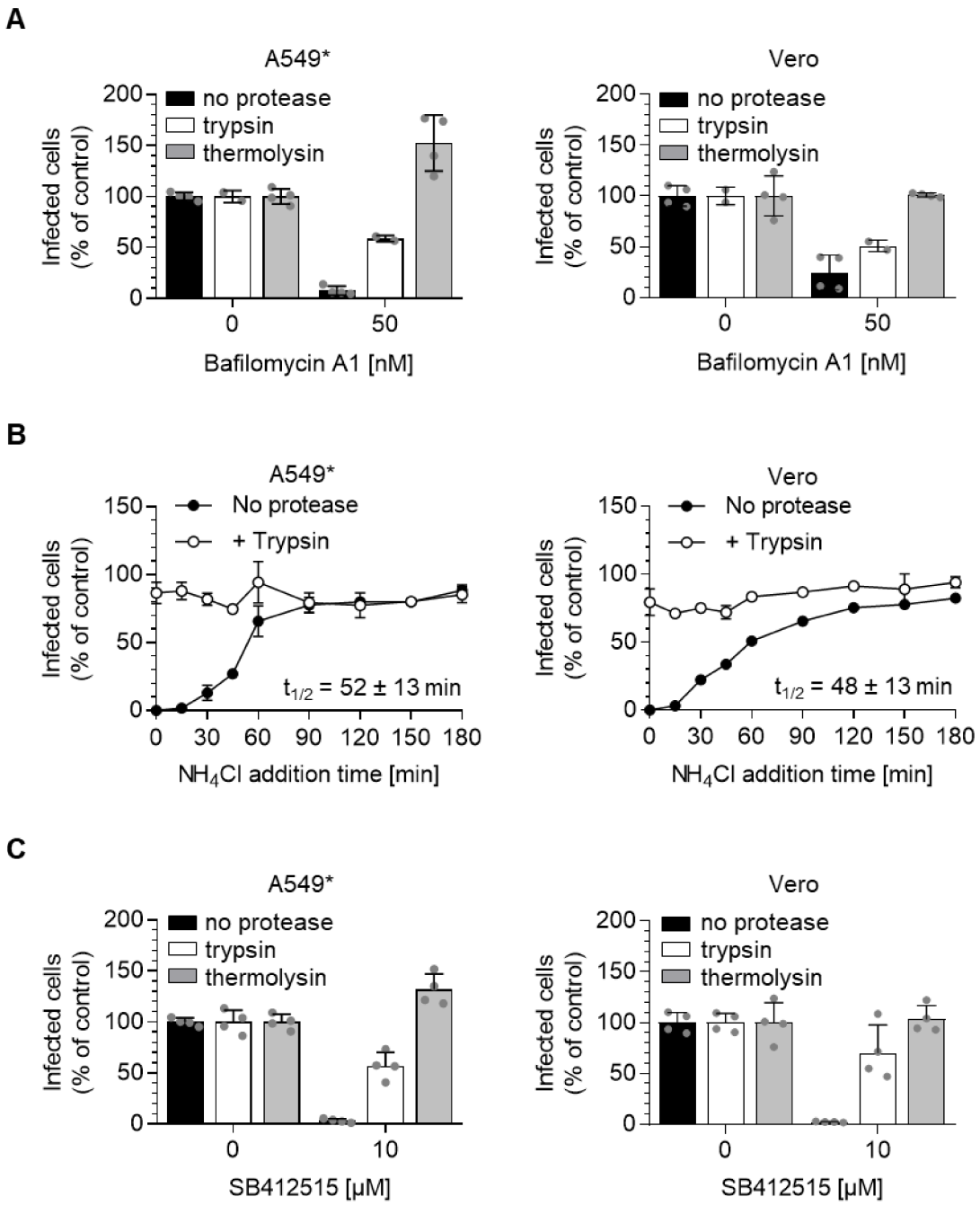

Figure 48. Protease-pretreated SARS-CoV-2 does no longer rely on low pH and cathepsin L activity.

(A) A549* and Vero cells were infected with SARS-CoV-2 pretreated with trypsin or thermolysin at MOI 0.2 and 0.3, respectively, in the continuous presence of bafilomycin A1. Infection was analyzed 8 h later by flow cytometry, and data were normalized to infection without bafilomycin A1. n = 1-2. (B) SARS-CoV-2 particles were pretreated with trypsin as described in (A) before the virus was allowed to bind to A549* and Vero cells on ice for 2 h, at MOI 0.2 and 0.3, respectively. Cells were rapidly warmed to 37°C and NH_4Cl (50 mM) was added at indicated time points to prevent endosomal acidification and cathepsin activity. Cells were harvested after 8 h, and infection was quantified by flow cytometry. Data were normalized to samples without NH_4Cl. One representative

experiment out of two is shown. (C) Same as in (A) but in the continuous presence of cathepsin L inhibitor SB412515 instead of NH_4Cl. n = 2. Data were obtained collectively with Zina Uckeley. The figure was modified from (264).

In a next step, the requirement for cathepsin L was tested when viral particles were pretreated with proteases prior to infection. Infection of trypsin- and thermolysin-treated viral particles was determined in the presence of the cathepsin L inhibitor SB412515. As expected, infection in A549* and Vero cells was completely abolished when the virus was not processed by protease prior to infection (**Figure 48C**). Conversely, thermolysin completely restored infection, as did trypsin, but to a lesser extent. Collectively, these data demonstrated that SARS-CoV-2 is no longer dependent on endosomal acidification and cathepsin L in TMPRSS2- cells when the virus was pre-activated.

3.3.9 Delta variant of SARS-CoV-2 seems to not only use TMPRSS2 in TMPRSS2+ cells for infectious entry

During the course of the pandemic, several new variants of SARS-CoV-2 emerged in 2020 and 2021. The Delta variant was first detected in India in October 2020 before spreading to Europe, where it became the dominant strain in the second half of 2021. It caused a major wave of infections in Europe in the fall of 2021, before being replaced by the Omicron variant in late 2021. To assess whether the delta variant has different entry requirements, I infected A549* cells with different levels of TMPRSS2 expression in the presence of inhibitors that block the TMPRSS2 or cathepsin-dependent pathway. As expected, inhibition of cathepsin activity in A549* cells lacking TMPRSS2 expression by SB412515 almost completely abolished infection with the original SARS-CoV-2 strain (**Figure 49, 37C, 42C**). Similarly, infection with the Delta variant was almost completely inhibited, indicating a requirement for cathepsin L activity when TMPRSS2 is not expressed (**Figure 49**). In A549* TMPRSS2+ cells, which are highly overexpressing TMPRSS2, infection with Wuhan could be blocked by more than 80% by the TMPRSS2 inhibitor camostat. Infection with the Delta variant was also reduced by camostat, but only to 50%. This suggests that the Delta variant is less dependent on TMPRSS2 activity. In A549* with a weaker expression of TMPRSS2, both protease-dependent pathways seem to play a role. Infection of the Wuhan variant was reduced by 35% and 65% by TMPRSS2 and cathepsin L inhibitor, respectively. Again, the Delta variant was less affected by the TMPRSS2 inhibitor and more hampered by the cathepsin L inhibitor compared to the Wuhan strain. Taken together, these data show that the Delta variant appears to use both the TMPRSS2 entry pathway at the cell surface and the cathepsin L-dependent entry from

endolysosomes. However, the Delta variant seems to be less dependent on TMPRSS2 cleavage than the original Wuhan strain.

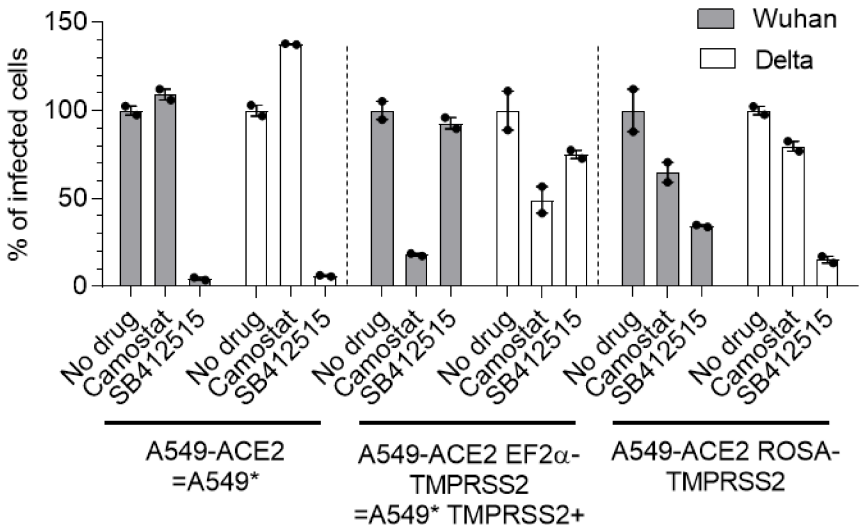

Figure 49. Delta variant of SARS-CoV-2 relies less on TMPRSS2.

A549* cells with different expression levels of TMPRSS2 were pretreated with the TMPRSS2 inhibitor camostat mesylate or the cathepsin L inhibitor SB412515. Cells were exposed to Wuhan strain (BavPat1) or Delta variant of SARS-CoV-2 at MOI 0.2 for 8 h in the continuous presence of inhibitors. Infection was analyzed by flow cytometry and normalized to samples without inhibitors. n = 1.

3.3.10 TMPRSS2 expression reduces ACE2 levels and SARS-CoV-2 binding

ACE2 was previously shown to be cleaved by TMPRSS2, which appeared to promote the entry of SARS-CoV in 293T cells (285). To evaluate the importance of the cleavage of ACE2 by TMPRSS2 in SARS-CoV-2 infection, I aimed to infect cells with different expression levels of TMPRSS2. To this end, I first assessed ACE2 expression in A549* cells expressing different levels of TMPRSS2 by western blotting. While ACE2 was highly expressed in A549* cells negative for TMPRSS2, ACE2 was barely visible in A549* cells with a weak TMPRSS2 expression (A549-ACE2 ROSA-TMPRSS2) and nearly not detectable in A549* cells overexpressing TMPRSS2 (A549-ACE2 EF2α-TMPRSS2) (**Figure 50A**). As expected, no ACE2 expression was detected in A549 cells negative for the receptor.

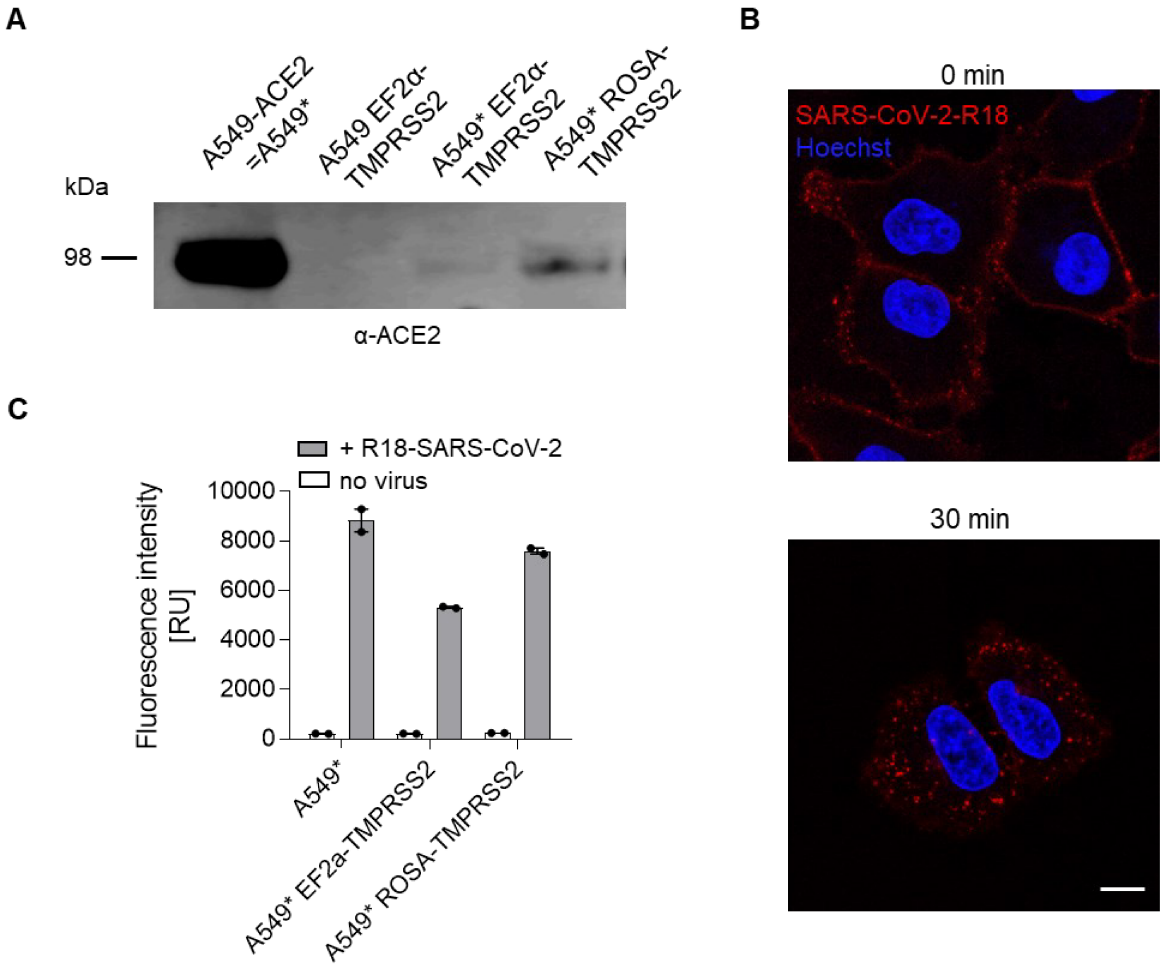

Figure 50. Reduced ACE2 expression and SARS-CoV-2 binding in TMPRSS2-expressing cells.

(A) Lysates of A549 and A549* cells with different levels of TMPRSS2 expression were separated by SDS-PAGE followed by western blotting using antibodies against ACE2. Identical protein amounts were loaded. A549 cells not overexpressing ACE2 were used as negative control. (B) The membranes of SARS-CoV-2 were fluorescently labeled with the lipophilic dye R18, and labeled viruses were purified over buffer exchange columns. Fluorescent particles were then bound to A549* cells on ice for 2 h. Cells were washed and left on ice (0 min sample) or shifted rapidly to 37°C for 30 min to allow internalization of viral particles. Cells were subsequently fixed, and nuclei were stained with Hoechst (blue). R18-fluorescently labeled SARS-CoV-2 particles (red) bound to cells were imaged by confocal microscopy. Maximum projection of three planes is shown. Scale bar, 10 µm. (C) R18-labeled SARS-CoV-2 was bound to A549*, A549* EF2α-TMPRSS2, and A549* ROSA-TMPRSS2 cells at MOI 0.03 on ice for 2 h in suspension. Cells were washed and fixed, and fluorescence associated with cells was quantified by flow cytometry. RU, relative unit. n = 1.

Next, I evaluated whether an increase in TMPRSS2 expression affects SARS-CoV-2 binding to host cells. For this purpose, I labeled the envelope of authentic SARS-CoV-2

particles with the lipophilic dye R18. I previously established that R18 labeling of TOSV at high concentrations causes autoquenching of the dye fluorescence. Here, SARS-CoV-2 membrane was labeled with lower concentrations of R18, which does not result in autoquenching. Fluorescently labeled SARS-CoV-2 had similar titers to unlabeled virus and could be detected by confocal microscopy as single fluorescent spots on the cell surface upon binding of particles to A549* cells on ice (**Figure 50B**). In addition, viral particles could be internalized upon warming the cells to 37°C for 30 min. To evaluate SARS-CoV-2 binding to cells with different levels of TMPRSS2 expression, R18-SARS-CoV-2 was bound to cells on ice for 2 h, fixed, and cell-associated fluorescence quantified by flow cytometry. The binding of fluorescent viral particles was reduced with lower ACE2 expression, which correlated with higher expression levels of TMPRSS2 (**Figure 50C**). The virus binding decreased by up to 40% in A549* cells overexpressing TMPRSS2. Taken together, these data suggested that TMPRSS2 cleaves ACE2 in addition to cleaving the SARS-CoV-2 spike protein. Increasing levels of TMPRSS2 result in decreased levels of full-length ACE2 and impaired binding of SARS-CoV-2 to host cells, while still promoting higher levels of infection. This suggests that the increase in infectivity compensated for the loss of SARS-CoV-2 binding to the cell surface.

4 Discussion

My in-depth work combined several molecular and cellular tools to elucidate early host-cell interactions of two emerging zoonotic viruses, TOSV and SARS-CoV-2. TOSV is a sand fly-transmitted virus of the family *Phenuiviridae* in the order *Bunyavirales*. It is widespread in southern Europe and northern Africa, with more than 250 million people potentially exposed. Although TOSV has not yet been detected, its vector, the phlebotomine sand fly, has been found in southern Germany. Thus, due to global warming and the expansion of arthropod vectors, more and more countries are at risk of arbovirus introduction. Although TOSV is one of the main causes of aseptic meningitis in southern Europe during the summer season, very little information is available on the cell biology of this virus. Therefore, I aimed to characterize its entry route into different human cell types. For most enveloped viruses, the entry process begins with binding to receptor(s), followed by internalization, intracellular trafficking and fusion from intracellular compartments. I then performed various quantitative and qualitative experiments to address these individual steps of the entry process of TOSV into mammalian host cells. This revealed that TOSV shares molecular and cellular features with other phenuiviruses and enters host cells by acid-activated membrane fusion from LEs. It shows remarkable pH versatility during intracellular trafficking and strong resistance to inactivation at low pH.

In addition, the COVID-19 pandemic started during my PhD studies. Therefore, I wanted to contribute to the research efforts against this virus. I therefore took the opportunity to adapt some entry protocols from the TOSV study to SARS-CoV-2. At the beginning of this project, there was a debate about whether SARS-CoV-2 requires endocytosis and vacuolar acidification for cell entry, *i.e.*, whether SARS-CoV-2 enters host cells directly from the plasma membrane or through intracellular compartments after endocytosis. Since other coronaviruses require cleavage of the transmembrane spike protein to enter cells, I selected several cell types with different expression levels of host cell proteases and analyzed the entry process of SARS-CoV-2 in all these cells. Furthermore, I was interested in the factors and cues that trigger SARS-CoV-2 membrane fusion.

4.1 TOSV is a late-penetrating virus

In this study, TOSV particles were imaged by cryo-EM for the first time. This revealed a roughly spherical shape with an average diameter of 121 nm. Spike-like protrusions with an average length of 9 nm were visualized on the viral surface formed by the viral glycoproteins Gn and Gc. Overall, these electron micrographs showed that TOSV shares

with other phenuiviruses, such as RVFV and UUKV, the same size and morphology (140, 141). Further experimental work is required to solve the X-ray structures of Gn and Gc of TOSV. This would allow the comparison with solved structures from other phenuiviruses, such as RVFV, DABV and HRTV (142–147). Tomography analysis of particles would allow to obtain details of the structural organization and to determine whether TOSV have the same atypical T = 12 symmetry as observed in UUKV and RVFV (140, 141). This in turn, could shed lights on the fusion mechanisms.

To analyze binding, internalization and intracellular trafficking of single virions, I used a labeling strategy based on reactive dyes covalently attached to free amine groups of the surface-exposed viral glycoproteins Gn and Gc. In addition, I took advantage of the lipophilic dye R18 that is autoquenched at high concentrations. This allowed the study of the acid-activated membrane fusion of TOSV. When glycoprotein-labeled fluorescent particles bound to A549 cells were imaged by confocal microscopy, I observed that the number of bound particles was approximately ten times higher than the MOI used. This indicates that every tenth bound fluorescent particle is infectious. It is tempting to speculate that most bound particles fail to fuse with a host cell membrane because glycoprotein Gc undergoes large conformational changes that might be limited by fluorophore attachment. Another explanation may be that not all virus particles contain all three segments and are therefore not infectious on their own. A recent study showed that incomplete RVFV particles can complement each other during co-infection resulting in the reconstitution of infectious virus (286). This infectious-to-fluorescent ratio of about 1:10 is still high compared to other phenuiviruses such as UUKV, where only one in 1,000 fluorescent particles is infectious, and in a similar range as for the orthobunyavirus GERV (174, 250).

From my results, it is clear that TOSV can productively infect iPSC-derived neurons. It remains to be investigated whether neurons contribute to the spread and pathogenesis of TOSV infection. Central nervous system manifestations such as meningitis and encephalitis are commonly observed in patients, but it is not clear how the virus is able to cross the blood-brain barrier and cause inflammation in the brain. *In vivo* experiments showed that only a few meningeal cells and neurons were infected after subcutaneous infection with a neuro-adapted strain of TOSV in Balb/c mice (287). After intracranial infection, TOSV replicated efficiently in the brain, causing encephalitis, and viral antigens were detected predominantly in the grey matter, especially in the deep nuclei and the hippocampus. However, it is not clear which cell types are affected by natural infection in humans and how they contribute to inflammation and pathogenesis of infection.

Many cell lines from different tissues and species were sensitive to TOSV infection suggesting a broad host and tissue tropism for TOSV. However, the full tropism in humans is not known and needs to be further investigated *in vivo*. Diverse symptoms ranging from febrile illness, central nervous system manifestations, testicular involvement, arthralgia or gastroenteritis may indicate that multiple cell types and tissues are infected *in vivo*. TOSV was also shown to have a high seroprevalence in several domestic and wild animals in endemic countries. To date, no reservoir host has been identified. Dogs and wild birds have been proposed as reservoirs because of their high seroprevalence. However, experimental infection of dogs resulted in low viral loads (61). Thus, the role of wild birds or other animals as reservoir hosts remains to be investigated in the future.

Sand fly cell lines were also sensitive to TOSV infection, but not to a high degree. It may be that TOSV requires longer periods of time to replicate and amplify in sand fly cells, as has been shown for UUKV and tick cell lines (260). Differences in TOSV infection between arthropod and mammalian cells deserve further investigation to determine whether infections are asymptomatic or not, or persistent or not, as observed for other arboviruses. Since arboviruses have a dual life cycle, it would be valuable to study differences in TOSV particles produced by arthropod and mammalian cells.

By analyzing viral entry step by step, I was able to show how TOSV enters cells and travels along the endosomal pathway to penetrate the cytosol. When single viral particles were monitored by confocal microscopy, TOSV was found to co-localize with Rab5, Rab7, and LAMP1, typical markers of endosomal vesicles. The kinetics of co-localization were consistent with the timing of other cellular cargoes that traffic to EEs, LEs and lysosomes (88). While co-localization with the EE marker Rab5a peaked at 5-10 min, co-localization with the LE and endolysosomal markers Rab7a and LAMP1 increased over time. A similar trafficking route along the endocytic pathway was previously shown for UUKV and DABV (173, 174). Thus, TOSV shares similar entry mechanisms and trafficking pathway with other phenuiviruses such as RVFV, UUKV and DABV.

From my results, it was evident that TOSV is dependent on LE maturation, which is required for the delivery of viral particles from EEs to more acidic downstream compartments. LE maturation is a complex process that involves hundreds cellular factors and is accompanied by many changes that are often interconnected and interdependent. Many monomeric GTPases are often associated with a specific intracellular compartment and shape their identity by switching between a GDP-bound inactive and a GTP-bound active state, as shown for the small GTPases Rab5 associated with EEs and Rab7 with LEs. An important step in LE maturation is the hydrolysis of Rab5-bound GTP and its

dissociation, while GTP-bound Rab7 associates in parallel. Blocking GTP hydrolysis using a constitutively active mutant of Rab5, which is maintained in its active GTP-bound state, inhibits maturation to LEs and TOSV infection. Similarly, dominant-negative mutants of Rab5 and Rab7, retained in their GDP-inactive state, block the formation of functional EEs and LEs, respectively, and were also shown to severely impair TOSV infection. This indicates that TOSV relies on functional EEs, but also on delivery to downstream organelles.

Further evidence that TOSV depends on LE maturation came from sensitivity to proteasomal inhibitors such as MG-132. MG-132 was previously shown to result in sequestration of several endocytosed viruses in EEs (288). It has been proposed that MG-132 exerts its inhibitory effect by causing a depletion of free ubiquitin in the cell, which is required for proper sorting of cargo in EEs to LEs and lysosomes (90). Thus, endocytosed virions are trapped within endosomes, unable to escape and productively infect cells. However, other roles of MG-132, such as its involvement in autophagy or inhibition of other proteases, could also explain the inhibitory cascade effects on the entry of many endocytosed viruses (289, 290).

In addition, endosome trafficking is orchestrated by the MT network and requires a temperature above 20°C. LEs undergo a net movement towards the perinuclear region, and the fusion of LEs with other LEs and with lysosomes is coordinated by MTs. Treatment with nocodazole and colcemid, both of which interfere with functional MT polymerization, hampered TOSV infection. Similar levels of inhibition were observed for UUKV and IAV, as such drugs often do not completely abolish, but rather delay, cargo transport to mature LEs and lysosomes (174, 291). At temperatures between 16°C and 20°C, endocytosis and recycling still function, albeit at reduced rates, while LE maturation and trafficking to lysosomes is completely impaired. Such low temperatures also totally block TOSV entry, suggesting that it relies on delivery to LEs. In contrast, SFV, a virus that fuses from early endosomal membranes, can still penetrate and infect cells likely because EE trafficking is not impaired at lower temperatures.

Other phenuiviruses are strictly dependent on the acidity encountered in LEs to trigger their membrane fusion. My investigations with agents that elevate endosomal pH such as lysosomotropic weak bases and vATPase inhibitors evidently showed that TOSV uses the same strategy. These agents block acidification by neutralizing the acidity or prevent pumping of protons into the endosomal lumen. A further evidence was that TOSV can fuse at the plasma membrane upon acidification at pH values typical of LEs. This low pH is similar to the fusion pH threshold reported for other phenuiviruses such as UUKV,

RVFV, and DABV with pH 5.4, 5.7, and 5.6, respectively (120, 173, 174). The pH threshold for fusion of TOSV and other phenuiviruses is slightly lower compared to other members of the order *Bunyavirales* such as the nairovirus Crimean-Congo hemorrhagic fever virus (pH 6.0) (292), the orthobunyaviruses La Crosse virus (pH 6.0 - 6.2) (293, 294) and Germiston virus (pH 6.0) (250), or the hantaviruses Andes virus (pH 5.8 – 6.0) (295, 296) and Hantaan virus (pH 6.3) (297). These higher pH thresholds of nairo- and orthobunyaviruses, may be indicative towards a penetration already from EEs, while phenuiviruses rather penetrate from LEs or downstream organelles. However, further investigations on nairo- and orthobunyaviruses are required to determine the cellular localization of fusion. Another indication that TOSV penetration occurs from LEs is the timing of the virus to pass the acid-dependent step, *i.e.*, it lasts 15 min for the surface-bound viruses to be internalized and penetrate the cytosol. Typically, cargo reach LEs in 15-25 min. The time frame of TOSV penetration was similar to that of the closely related RVFV and UUKV, the half-maximal penetration of which is 12-20 min (120, 174), but faster than DABV, which belongs to a different genus in *Phenuiviridae* and required approximately 60 min (173).

Although their penetration time span 12-60 min, phenuiviruses are evidently all L-PVs. L-PVs are a diverse group of endocytosed viruses that all share the requirement for LE maturation for penetration. Late penetration may confer various advantages to viruses such as helping to pass through the barrier formed by the cortical cytoskeleton, allowing the delivery of the viral genome nearby to the ER and Golgi often exploited by viruses for replication, or escaping host defenses. In addition, in comparison to viruses that fuse at the cell surface, endocytosed viruses do not leave traces of viral proteins at the plasma membrane and thus avoid, at least in part, immune detection. In contrast, early-penetrating viruses (E-PVs) generally enter host cells from EEs within 3-8 min (93) and fuse at pH values typical of those within EEs, *i.e.*, above 6.0, and therefore do not rely on LE maturation for infection.

Altogether my data indicated that TOSV can be confidently considered as a L-PV. TOSV shares many features with other L-PVs, such as (i) trafficking within LEs, (ii) pH for fusion below 6, (iii) penetration that lasts longer than 10 min, (iv) sensitivity to perturbants of LE trafficking and maturation, and (v) dependence on temperatures above 20°C. A comprehensive view of the TOSV entry program in mammalian cells is proposed in **Figure 51**.

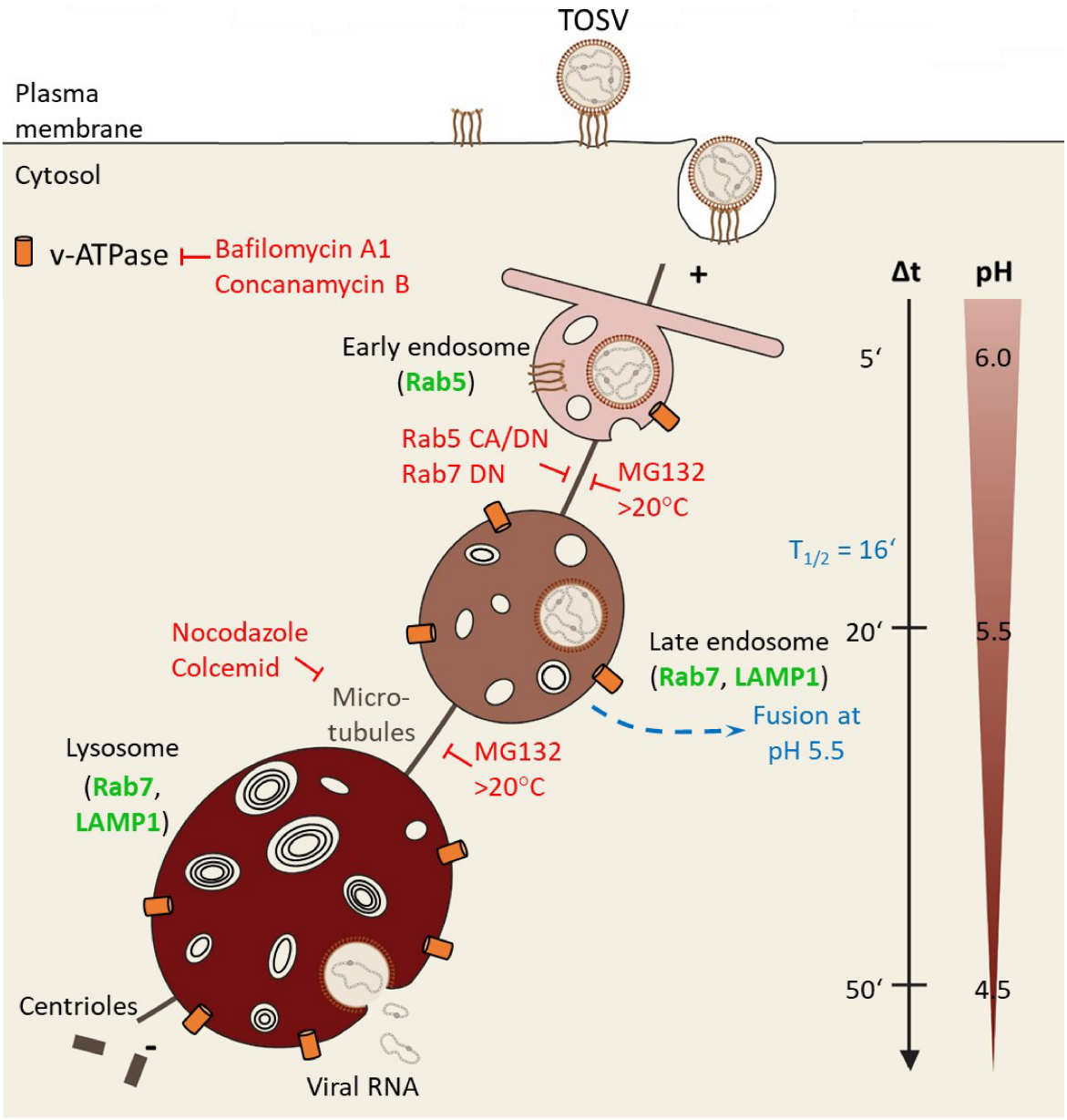

Figure 51. TOSV enters cells by acid-activated membrane fusion from late endosomes. Internalized TOSV particles traffic within Rab5a+ early, and Rab7a+ and LAMP1+ late endosomal vesicles. TOSV relied on functional late endosome maturation that could be blocked by Rab5a and Rab7a mutants, MG-132, low temperature and inhibitors of microtubule. TOSV infection was sensitive to inhibitors of vATPase, such as bafilomycin A1 or concanamycin B, and penetrated host cells from late endosomes by by acid-activated membrane fusion at pH 5.5, 16 min after warming samples to 37°C. The figure is modified from (298).

In my investigation, TOSV was produced from mammalian cells and I examined the entry process of these viruses essentially in human cells. However, TOSV is an arbovirus and as such has a dual life cycle in sand fly vectors and mammalian hosts. The mechanisms used by TOSV to enter sand fly cells could significantly differ and remain largely to be

investigated. The cell biology of arthropod cells contrasts with that of human cells and other mammalian cells in terms of growing temperature, *i.e.*, 28 °C, lipids, glycans, etc. Further studies are also needed to determine whether TOSV produced from sand fly cells enters and infects mammalian cells following the same infectious entry program that is counterpart derived from mammalian cells. Indeed, the structural organization and composition of viral particles produced from sand fly cells could significantly differ from those originating from mammalian cells in terms of lipid composition, glycans, genome editing, etc. Such differences were observed for the tick-borne UUKV depending on whether the virus was amplified in tick or mammalian cells (260).

4.2 TOSV makes an atypical use of vacuolar acidity

In the case of phenuiviruses, viral fusion is mediated by the glycoprotein Gc. The X-ray structure has been solved for the Gc proteins of several phenuiviruses, namely RVFV, DABV, and HRTV in pre- and post-fusion conformations (142–145). From these structures, Gc appeared to adopt a similar fold than that of class-II fusion proteins as the envelope glycoprotein E1 of alphaviruses or E protein of flaviviruses. Although it remains to be determined experimentally by X-ray crystallography, our prediction of TOSV Gc structure with AlphaFold models suggested that TOSV is likely a member of class-II viruses (269).

Class-II fusion proteins are classically activated upon acidification. Using complementary approaches, *i.e.*, bypass assay and R18-based fusion assay, I could show that the fusion and penetration of cell surface-bound TOSV could be achieved at the plasma membrane very quickly by artificially lowering the pH of outer medium. Evidently, acidification is necessary and sufficient to induce conformational rearrangements in TOSV Gc so that it switches from the pre- to post-fusion state that mediates fusion of the viral membrane with the plasma membrane.

At pH 5.0, the TOSV fusion step itself occurred in less than 30 sec, suggesting that fusion is a rapid process. The kinetic of acid-activated membrane fusion is slower than for UUKV that occurs within a few seconds (131) but in a similar time frame as shown for hanta- and flaviviruses (133, 299–301). Individual kinetics might be influenced by exact pH, and curvature and composition of target membrane of different studies. TOSV fusion could occur at less acidic pH when the exposure time was increased. While fusion occurs rapidly at pH <5.5, some fusion events also occurred at pH 5.8, albeit with slower kinetics.

This suggests a greater versatility in the fusion process with respect to pH, and may indicate that the virus becomes more potent for fusion as it progresses through the endocytic machinery of the host cell.

The R18-based fusion model was a good correlate with fusion, although it could be in part only hemi-fusion. Therefore, it would be interesting to address whether a pH of 5.8 would also allow complete fusion pore formation and enlargement. This could be addressed by using viral particles labeled with an autoquenched content buffer as recently shown for IAV (302). Thus, an increase in fluorescence would only occur upon fusion pore formation and dilution of the autoquenched buffer into target cells. Monitoring the fusion of single particles by microscopy would ideally complete this approach and provide further information on the cellular location from which viral fusion occurs.

The rearrangements in other class-II fusion proteins have been proposed to rely on several conserved histidines that may act as a pH switch (113, 119, 120). Upon acidification, histidines become protonated, allowing attractive or repulsive forces into the glycoprotein that can destabilize the pre-fusion or stabilize the post-fusion conformation. The role of switch histidines in the rearrangement of TOSV Gc remains to be examined.

However, a number of studies have also shown that the lipid species in the target membranes can influence the fusion of class-II fusion proteins. Fusion of UUKV was facilitated by the presence of phospholipids with negatively charged headgroups, as in BMP, which are enriched in LEs (131). A similar requirement for anionic lipids has been demonstrated for the flavivirus DENV (132). The hantavirus Andes virus and the alphavirus SFV showed a dependence on cholesterol in the target membrane (128, 130), while the alphavirus Sindbis virus required both cholesterol and sphingomyelin (303). Structural analysis of RVFV Gc revealed a glycerophospholipid-binding pocket conserved in other arboviruses of the alpha- and flavivirus families (143). Another recent report suggested a binding pocket for glycosylceramide in DABV and HRTV Gc (304). Interestingly, our group showed that TOSV is also dependent on glycosylceramide for infectious entry (305).

In addition, some class-II fusion proteins require additional factors for fusion. In recent years, an increasing number of bunyaviruses have been proposed to require elevated levels of K^+ for infection and fusion (135, 250, 306–308). The switch from Na^+ to K^+ ions in maturing endosomes was also shown to promote uncoating of IAV (309). Thus, different ion concentrations can be important for viral entry during the fusion process but also for the next step of genome release. Some studies suggest that bunyaviruses, LACV and DABV, also require serine protease activity (162), while others do not (250). In these

cases, however, it is not clear whether the serine protease activity acts directly on viral proteins or on host factors. The role of specific lipids or ion concentrations in TOSV fusion remains to be evaluated.

Previous reports suggested that the fusion process mediated by class-I and class-II fusion proteins is irreversible and fusion proteins act only once (105). Exposure of viral particles to the pH threshold for fusion in the absence of a target membrane leads to inactivation (303, 310–313). TOSV could not be inactivated by low pH treatments. In fact, acidic pretreatment of TOSV in a range of pH between 6.5 and 6.0 resulted in the increase of infection. At such pH values, TOSV binding was also enhanced. The fact that binding was enhanced although the pH of virus samples was elevated to pH 7 after low pH pretreatment suggests an irreversible conformational change in the Gn/Gc heterodimer in the glycoproteins, e.g. a lateral movement of Gn away from Gc, which favored binding. An increase in binding at lower pH was also observed for SFV, with the optimal pH depending on the cell line used (314). Low pH treatment could lead to dissociation of Gn/ Gc heterodimers and unmask epitopes with increased affinity to receptors. However, it remains to be determined whether acidic pretreatment followed by re-neutralization involves changes in phenuivirus Gn, Gc, or both. Several receptors and attachment factors have been proposed for TOSV, including the C-type lectin receptors DC-SIGN and L-SIGN, and the glucosaminoglycan heparan sulfate (160, 161, 169). Still, it is not clear whether binding occurs through Gn, Gc, or an interface shared by both, and whether different receptors share the same binding site. It is also likely that the list of receptors is not complete.

Similar to TOSV, pretreatment of other bunyaviruses at very low pH did not result in their inactivation. In contrast, infection of SFV that has a class-II fusion protein and IAV that has a class-I fusion protein was almost completely abolished by low pH pretreatment. This is consistent with previously reported studies showing that SFV and IAV particles rapidly lost their ability to fuse with target membranes when incubated at low pH in the absence of target membranes (310, 311, 315, 316). My results indicated that bunyaviruses have in common that their fusion machinery is not inactivated upon acidic exposure. The fusion mechanisms involved in the bunyavirus infectious entry are evidently more complex than those of other class-II fusion viruses. Further experimental investigations will be required to elucidate the molecular mechanisms beyond and evaluate the importance of Gn in this process. However, one can postulate that the fusion process is a multi-step mechanism involving irreversible and reversible conformational changes. Single particle kinetic studies of flavivirus fusion suggest that sequential conformational rearrangements occur in class-II fusion proteins. Dimer dissociation and fusion loop exposure appear to be rapid and

reversible, whereas trimerization and irreversible membrane binding are slower and are the rate-limiting steps during fusion (300).

When TOSV was first exposed to mildly acidic pH, fusion occurred faster, and the fusion pH threshold increased. It is tempting to speculate that such stepwise acidification, which also occurs during passage through EEs to LEs, primes the activation of TOSV fusion at lower pHs in LEs. It remains to be investigated whether acidification also induces dimer dissociation in phenuivirus Gc and what intermediate conformations are adopted by Gn and Gc during such priming by mildly acidic pH. I observed differences in the capacity of pre-activated TOSV to infect cell lines. This suggests different requirements or entry mechanisms that depend on the target cell type. Possibilities could be different expression of receptors, additional endosomal cofactors or different endosomal lipid composition that could interact with pretreated glycoproteins. Hence, the molecular and cellular mechanisms that underly why TOSV pretreated at low pH efficiently enters A549 cells but less BHK-21 and Vero cells requires further investigation.

SFV also harbors a pH-sensitive class-II fusion protein, but is otherwise unrelated to TOSV. SFV undergoes acid-activated membrane fusion at pH 6.0 (104). In contrast to TOSV, SFV lost 97% of its infectivity in BHK-21 cells when pretreated at pH 5.5. This is consistent with previously reported studies (315, 316) and similar inactivation has been reported for Sindbis virus, another alphavirus (303). This may indicate that TOSV is more resistant to pH pretreatment than alphaviruses. However, another report provided conflicting information and suggested that inactivation of SFV by low pH is reversible (317). Flaviviruses also undergo pH-dependent fusion with their class-II fusion protein. However, while West Nile virus and tick-borne encephalitis virus lost their fusogenic potential after exposure to low pH (313, 318), DENV was reported to retain its fusogenic property at low pH in the absence of anionic lipids in the target cell membrane (132). These examples of non-inactivated viruses, including bunyaviruses, suggest that the general hallmark that all class-II fusion proteins are inactivated when exposed to an acidic environment in the absence of a target membrane –in other words, these processes are irreversible– needs to be revisited. Future studies could be addressed to investigate the role of the accompanying proteins of class-II fusion proteins, namely Gn of bunyaviruses, E2 of alphaviruses, and M protein of flaviviruses, during priming and activation of fusion.

Because crystal structures only provide information about specific and stable conformations of proteins, it is difficult to capture the dynamic nature of viral fusion proteins. In addition, conformational changes in fusion proteins could be studied using cryo-electron tomography, single-molecule Förster resonance energy transfer (smFRET),

or epitope exposure. Fusion loop exposure could be tested by co-floatation studies of virus and liposomes. In addition, single-virus fusion assays with lipid mixing or transfer of a content marker and analysis by fluorescence microscopy approaches could be a next milestone in phenuivirus fusion research.

4.3 SARS-CoV-2 uses multiple distinct pathways to enter host cells

Prior to my work, several host cell proteases have been proposed to be involved in the activation of S and thus in the entry of SARS-CoV and SARS-CoV-2. These include furin, TMPRSS2, and cathepsin L. Since furin is essentially expressed in the Golgi network, its role in processing S most likely occurs during synthesis in producer cells. Therefore, I limited my study mainly to the role of TMPRSS2 and cathepsin L, which are primarily located at the plasma membrane and in lysosomes, respectively. Using several cell lines based on lung, intestinal, and kidney epithelial cells, I analyzed entry from proteolytic activation to membrane fusion.

I was able to show that entry of SARS-CoV-2 into cells could be blocked by inhibitors of TMPRSS2 even when cathepsin L was expressed, indicating that the TMPRSS2-dependent entry pathway is preferentially used by the virus. When TMPRSS2 is expressed, the proteolytic cleavage-sensitive step is mostly completed within the first 10 min. In addition, SARS-CoV-2 infection was not affected by inhibitors of either vacuolar acidification or LE maturation.

In contrast, when cells lacked TMPRSS2 expression, cathepsin L-dependent proteolytic cleavage was completed approximately 60 min after entry. This is consistent with the time required for cargo to be trafficked from the plasma membrane to endolysosomes (88). SARS-CoV-2 infection was also dependent on vacuolar acidification and LE maturation. Thus, in cells lacking TMPRSS2, SARS-CoV-2 shared several features with other late-penetrating viruses such as TOSV. Infection was sensitive to perturbants of LE maturation and relied on intact MT and proper late endosomal sorting. Similar to SARS-CoV-2, the proteasomal inhibitor MG-132 was shown to block entry of many other L-PVs. The reason may be that the drug interferes with ubiquitin-dependent sorting within LEs (90). Interestingly, the MG-132-sensitive and acidification-dependent step showed a kinetic similar to that of cathepsin L activation and occurred within approximately 40-60 min after entry. Structural and biochemical analyses indicated that MG-132 may also act directly on cathepsin L activity, thereby blocking entry via the late pathway (319). This could explain the same kinetic of inhibition by MG-132 and the cathepsin L inhibitor SB412515 and why

MG-132 has an IC_{50} value in the nanomolar range in TMPRSS2- cells while it is rather in the micromolar range for other L-PVs.

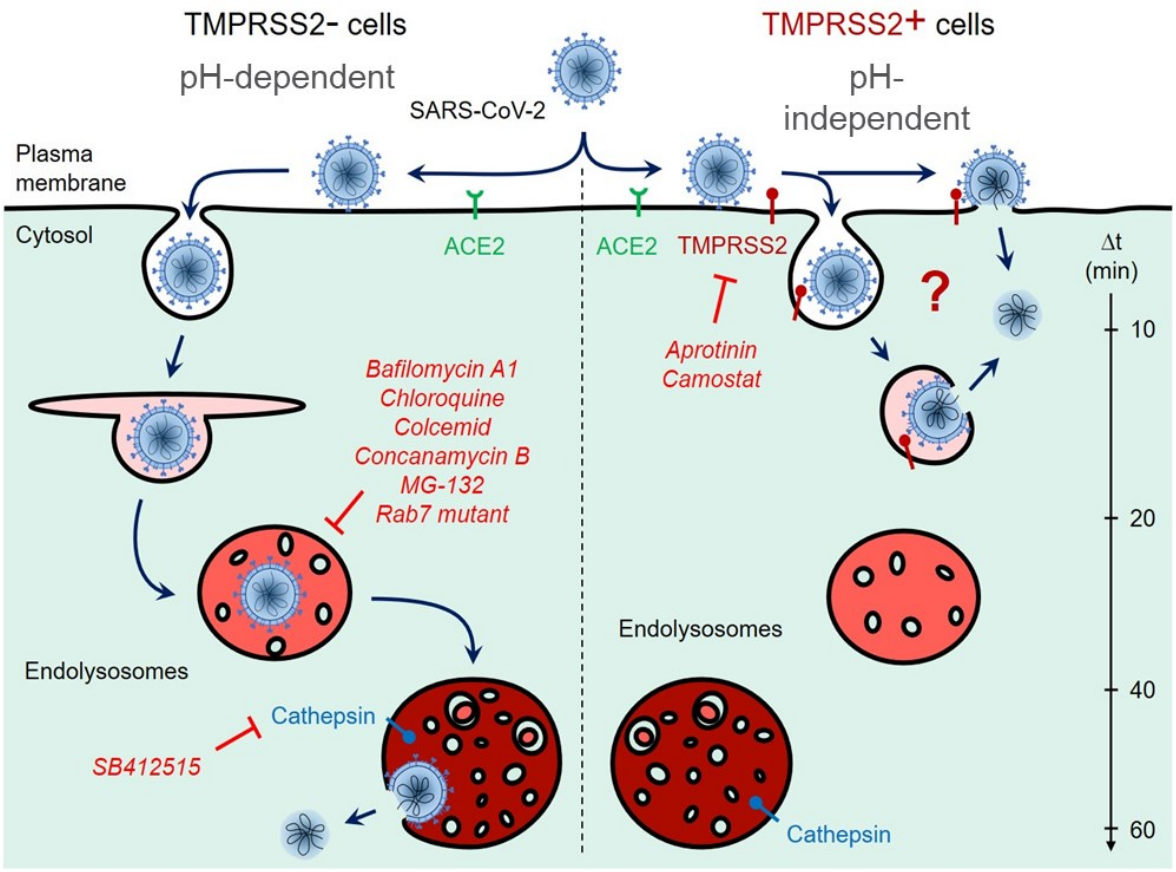

Figure 52. SARS-CoV-2 uses multiple pathways to enter host cells.
When cells expressed the serine protease TMPRSS2 on the cell surface, Spike of SARS-CoV-2 is cleaved within 5-10 min and penetration occurs in a pH-independent manner at the plasma membrane or rapidly after uptake. In cells lacking TMPRSS2, SARS-CoV-2 particles enter cells by receptor-mediated endocytosis and traffic along the endosomal route to reach endolysosomes in which the Spike protein is processed by acid-activated cathepsin L and the virus activated for fusion. Thus, entry is slower, and infection is sensitive to inhibitors of vacuolar acidification, late endosome maturation, and cathepsin L. ACE2, angiotensin-converting enzyme 2; TMPRSS2, transmembrane protease serine 2. The figure was adapted from (264).

My data, combined with other reports indicate that SARS-CoV, MERS-CoV, and SARS-CoV-2 have evolved multiple pathways to enter and infect cells (**Figure 52**) (198). This shows great flexibility in the use of host cell factors and may allow the virus to enter even when one pathway is not present in target cells, and thereby, expand tissue and species tropism. For these viruses, the entry pathway depends largely on the expression of proteases. My results show that both TMPRSS2 and cathepsin L play important roles in

SARS-CoV-2 entry, which is in agreement with other reports on SARS-CoV and SARS-CoV-2 (183, 205, 320–322). However, the TMPRSS2-dependent fast entry pathway appears to be preferred over the slower cathepsin L-dependent pathway, consistent with other reports (183, 323, 324). Interestingly, more infectious viral progeny was released from cells expressing TMPRSS2. A similar preference for the TMPRSS2 pathway and higher productivity was also shown for other human coronaviruses, such as HCoV-229E, HCoV-OC43, and HCoV-HKU1 (325, 326). Another study also reported that the TMPRSS family but not the cathepsin L pathway is linked to pathogenesis of SARS-CoV in mice (327).

Several other studies have also shown that SARS-CoV-2 is dependent on vacuolar acidification in various TMPRSS2- cell lines (183, 323, 328). While the slow entry pathway leads to fusion from endolysosomes, it is still not completely clear where fusion occurs in the early pathway. It is widely believed that fusion occurs directly at the plasma membrane. However, recent studies also suggest that fusion may occur shortly after uptake from intracellular compartments such as EEs (329). Trafficking of labeled virus particles into cells and co-localization with various endosomal markers, similar to those I developed during my PhD study, would be of great interest in future experiments to analyze from which compartment SARS-CoV-2 enters host cells regardless of the protease expression profile.

Several new variants emerged during the pandemic. Initial data suggest that the Delta variant may rely less on the TMPRSS2-dependent pathway than the original Wuhan strain. However, both entry pathways appear to be used by Delta. Other reports, mostly based on SARS-CoV-2 pseudotyped particles, failed to find differences in entry requirements between Delta and Wuhan strains (329, 330). One explanation could be that pseudotyped particles bud from the plasma membrane and may not have undergone the same proteolytic processing as authentic SARS-CoV-2, which bud from ERGIC. Recent reports also suggest that Omicron appears to be more dependent on endosomal entry than on the TMPRSS2-dependent pathway. The H655Y substitution in Omicron S was proposed to be associated with stabilization of the S trimer and a preference for the late entry pathway (330–333). In previous variants, the endosomal pathway was less favored due to endosomal restriction factors, as the interferon-induced transmembrane protein 2 (IFITM2) or lymphocyte antigen 6 complex, locus E (LY6E) (334, 335). A recent pre-print suggested that Omicron has evolved to circumvent these restrictions (336), allowing infection of a wider range of cells through a TMPRSS2-independent entry pathway, most likely the cathepsin pathway. This also led to a change in tissue tropism. Whereas the original strain and previous variants were associated with replication in the lower

respiratory tract where TMPRSS2 is predominantly expressed, Omicron appears to prefer replication in the upper respiratory tract that is linked to a higher expression of ACE2 (337) and is also associated with increased human-to-human transmission. However, also other proteases have been proposed to take over the roles of cathepsin L and TMPRSS2 in mediating the entry of the newer variants, which in turn can be exploited by the variants to extend their cellular tropism *in vivo* (will be discussed in more details below).

4.4 Fusion triggering mechanism of SARS-CoV-2

The S protein of coronaviruses has to be processed by host cell proteases in two steps at two sites, *i.e*., (i) a priming step with the cleavage at the S1/S2 interface and (ii) an activation cleavage step at S2' just upstream of the fusion peptide. SARS-CoV-2 possesses a multibasic furin cleavage site motif (RRAR) at S1/S2 that would allow cleavage of newly synthesized S by furin in producer cells prior to particle release. The RRAR motif in SARS-CoV-2 differs from the canonical furin cleavage site RX(R/K)R. Such multibasic furin cleavage motifs at the S1/S2 junction are missing in SARS-CoV and SARS-related coronaviruses that raised the question about its natural origin (338). However, several other betacoronaviruses have furin cleavage sites at the S1/S2 junction, such as MERS-CoV that carries a RSVR furin cleavage site, suggesting that furin cleavage sites occurred independently in multiple coronaviruses during the evolution of the coronavirus family (339).

Several reports have shown that the SARS-CoV-2 particles and pseudoparticles that are released in the outer medium are processed at S1/S2 (179, 205, 322, 340, 341). However, the efficiency of cleavage varies widely between different reports and different producer cell lines. Here, I could show that about one third of the S is already cleaved at S1/S2 when authentic SARS-CoV-2 particles are released from Vero cells.

Further processing of SARS-CoV-2 with exogenous furin did not increase infection or syncytia formation, indicating that furin processing was not sufficient to activate S. This is in agreement with other reports showing that although inhibition of furin abolished S processing at the S1/S2 interface (322, 342), furin did not appear to be essential for viral entry (343). It was reported that SARS-CoV-2 variants disrupted for the multi-basic cleavage site at the S1/S2 junction entered cells via the late pathway (344). This suggests that the furin cleavage site is required for the TMPRSS2-dependent early entry pathway, whereas it is dispensable for the cathepsin L-dependent late entry pathway. This is consistent with the observation that the furin cleavage site is lost after several passages of SARS-CoV-2 in TMPRSS2-deficient cells such as Vero cells (345). It has been suggested

that the furin cleavage site causes instability in S, which may lead to the shedding of the S1 domain prior to receptor engagement and thus inactivation of the virus (346). During the evolution of variants, residues adjacent to the furin cleavage site were mutated, including P681H in Alpha and Omicron or P681R in Delta, which rendered S1/S2 susceptible to additional proteases or increased processing by furin (347–349). Thus, Alpha and Delta variants show increased syncytia formation and use the TMPRSS2 entry pathway, while Omicron evolved by accumulating additional mutations such as H655Y, a mutation linked to reduced syncytia formation and TMPRSS2 usage (347, 350).

In target cells, the plasma membrane-located serine protease TMPRSS2 can cleave S at its S2' site after a single arginine residue (205). However, it is uncertain whether TMPRSS2 can also cleave at the S1/S2 site (205, 206). The observation that viruses mutated for the furin cleavage site enter only via the late TMPRSS2-independent pathway rather supports that TMPRSS2 cleaves only at S2’ site (344).

Another protease proposed to process SARS-CoV-2 S is cathepsin L. It is a cysteine protease that preferentially cleaves at peptide bonds with non-polar, aromatic residues (351). Cathepsin L has predicted cleavage sites near the polybasic site at S1/S2 and near the TMPRSS2 cleavage site at S2' (210). Thus, this protease has the ability to process both S1/S2 and S2’ sites, allowing entry of uncleaved S via the late entry pathway, independent of furin and TMPRSS2. In general, two additional cleavage sites in the S1 subunit have been shown experimentally (352). However, since cleavage by cathepsin L is rather non-specific, the exact cleavage sites remain to be determined.

In a simplified model, when S is cleaved by furin in producing cells, it could enter cells via the fast and slow pathways, although the TMPRSS2-mediated fast entry pathway seems to be preferred. In addition, it was proposed that S cleaved at S1/S2 would promote binding to ACE2, likely because S adopts the receptor accessible “up” conformation. Conversely, if S at the S1/S2 interface is not cleaved by furin, TMPRSS2 is prevented from cleaving at the activating S2’ position. Consequently, virions bind to the receptor and enter cells by endocytosis before they reach endolysosomes where S is cleaved at S1/S2 and S2' positions by cathepsin L. It has been hypothesized that the furin site in S has evolved upon the selective pressure of proteases in target cells, since TMPRSS2 may have been too inefficient in cleaving at the S1/S2 junction, or cathepsin L, that was overdigesting S due to a lower substrate specificity (346). Thus, the rate of specific processing may have been increased at the expense of decreased stability of S.

The real mechanisms are likely more complex. Other proteases may be involved in the two proteolytic S cleavages such as extracellular or cell-surface proteases that may

contribute to the cleavage at S1/S2. Besides TMPRSS2, several other members of the type-II transmembrane proteases have been proposed to promote SARS-CoV-2 entry and the cleavage of S, such as TMPRSS11D (353, 354), TMPRSS11E (354), TMPRSS11F (354), TMPRSS24 (355), or TMPRSS13 (353, 354, 356). In addition, several secreted proteases have been shown to cleave SARS-CoV-2 S, such as the secreted metalloproteases ADAM10 and ADAM17 (357) or serum coagulation factors such as factor Xa and thrombin (358, 359). However, not every protease facilitates entry, as recently shown for factor Xa-mediated cleavage of SARS-CoV-2 S, which blocks viral entry (360). It remains to be investigated at which sites S is cleaved by these proteases and how they contribute to the entry of SARS-CoV-2.

Processing of S with trypsin prior to addition to cells results in almost 100% cleavage at S1/S2 and increased entry into cells. Proteolytic pretreatment with trypsin also rendered entry into TMPRSS2-deficient cells independent of vacuolar acidification and cathepsin L activity. In addition, thermolysin, which cleaves ebolavirus GP protein similarly to cathepsin L, is functional at neutral pH (284) and thus allows the study of the cathepsin L-proteolytic processing independently of pH. Thermolysin was previously shown to cleave the S protein of SARS-CoV and to promote the cell entry of this virus (283). Here, I showed that pre-treatment of SARS-CoV-2 particles with thermolysin, like trypsin, also resulted in acidification- and cathepsin L-independent entry into cells lacking TMPRSS2 expression. Thermolysin was even more effective than trypsin in bypassing the need for vacuolar acidification. This might indicate that trypsin and thermolysin, hence also cathepsin L, do not cleave at the same site in S. Overall, further functional investigations are needed to better define the proteolytic process of the spike during the virus entry process.

A recent study showed single viral fusion events of SARS-CoV-2 pseudotyped particles. This report proposes that the SARS-CoV-2 fusion is insensitive to the exact identity of the protease and is also insensitive to whether activation occurs before or after receptor binding (361). The authors also postulate that if extracellular or cell surface proteolytic cleavage is rapid, entry tends to occur at the plasma membrane, whereas if extracellular and cell surface proteolysis is slow, entry is most likely to occur within endosomes after uptake. This is in agreement with my own results, which showed that cleavage of S by TMPRSS2 occurs within 5-10 min. As other unrelated viruses already penetrate from EEs within 3-8 min (103, 104), this kinetic might raise the question whether cleavage by TMPRSS2 and fusion rather occurs in EEs than at the plasma membrane. However, the dynamics of internalization and the exact localization of TMPRSS2 cleavage remains to be investigated.

To determine whether additional environmental cues besides proteolytic activation, such as acidification, are required for SARS-CoV-2 membrane fusion, I developed a cell-cell fusion assay. The formation of multinucleated pneumocytes has previously been observed in patients who died from COVID-19 (76, 362). In general, syncytia are large multinucleated cells in which the plasma membrane has fused and the cytoplasmic contents have been mixed. Syncytia formation as a result of viral infection *in vivo* and *in vitro* has also been reported by other viruses from a wide range of viral families such as *Herpesviridae*, *Paramyxoviridae,* or *Retroviridae* (362). Syncytia formation for these viruses contributes to pathogenesis and may facilitate viral replication and spread. In addition, it may help evade the immune system by protecting the virus from immune cells and neutralizing antibodies. To which extent the syncytia formation during SARS-CoV-2 infection contributes to the disease outcome will require further experimental investigations.

As SARS-CoV-2 particles assemble and bud from ER and Golgi compartments, the question arose how S could promote cell-cell fusion at the plasma membrane. Several studies have shown that in addition to its subcellular localization in the ER and Golgi, S can also be found on the surface of infected cells (363, 364). Analysis of the cytoplasmic tail of S then showed that the retention signals for transport to the ER and Golgi were suboptimal and might explain why S tends to leave the ER and leak to the cell surface (365). Cell surface-resident S could then interact with ACE2 and other host factors of neighboring cells, leading to cell-cell fusion. In addition, S promoted the expression of the scramblase TMEM16F, which translocated phosphatidylserine from the plasma membrane to the outer lipid layer, further promoting fusion (76). However, it remains to be investigated whether S present on the cell surface was processed proteolytically in the same way as S decorating viral particles.

Several SARS-CoV-2 variants were also associated with an altered ability to induce syncytia formation. The D614G mutation was found to increase syncytia formation compared to the Wuhan strain (348, 366). In addition, Alpha and Delta showed increased cell-cell fusion activity compared to the D614G variant, which was proposed to be related to a single mutation in S, P681H/R (347, 348, 367). On the contrary, Omicron seemed to induce less syncytia formation while surface expression of S was unaltered compared to Wuhan and Delta strain (330, 332, 368). This reduced cell-cell fusion activity was linked to another single mutation, H655Y. Interestingly, this mutation was also found to be associated with a reduced use of TMPRSS2 by the virus (331).

Here, the ability of SARS-CoV-2 to mediate cell-cell fusion was used as a surrogate to analyze the effect of acidification on the fusion process. I observed very little syncytia formation in Vero cells and A549-ACE2 cells, which both lack TMPRSS2 expression. However, expression of TMPRSS2 in A549-ACE2 cells greatly enhanced syncytia formation that could be reversed by blocking TMPRSS2. Moreover, the addition of exogenous trypsin to SARS-CoV-2 infected Vero or A549-ACE2 cells induced a large formation of syncytia with large multinucleated cells, with sometimes more than a hundred nuclei clustered together. My results showed that the addition of exogenous furin failed to promote further syncytia formation, reinforcing the view that furin cleavage alone is not sufficient to proteolytically activate S. Together, these observations are consistent with a model in which furin can only cleave at the S1/S2 site and other host cell proteases, *e.g.*, TMPRSS2, are required to cleave at the S2' site and activate S (369). Whether cell-surface proteases are necessary in donor or acceptor cells remains to be determined.

Exposure to low pH in the absence of proteases did not result in syncytia formation, suggesting that acidification alone is not sufficient to trigger S mediated fusion. Interestingly, co-treatment of low pH in combination with protease did not result in an increase in syncytia formation compared to protease treatment alone. First, this indicated that there is no additional supportive effect of low pH treatment on SARS-CoV-2 fusion. Next, this demonstrated that fusion is not dependent on acidification and that proteolytic processing is necessary and sufficient to induce fusion. The cell-cell fusion activity in A549-ACE2 cells was higher than in Vero cells. This may indicate the presence of other proteases on the cell surface of A549* cells that could process S and are absent in Vero cells.

From my results, acidification appeared to be important for the activity of cathepsin L that mediates the proteolytic activation of S, but not directly for the fusion mechanism themselves. In contrast, acidification was dispensable for fusion and infectious entry when (i) TMPRSS2+ cells were infected or (ii) SARS-CoV-2 particles are activated with exogenous proteases prior to infection. Same conclusions were reached by others (323, 343, 364). A recent study questions this model (329). The authors used VSV pseudotyped with S from SARS-CoV-2, and in their experimental settings, they observed that acidification to only pH 6.8 is required for fusion. In this investigation, the authors used particles labeled for SARS-CoV-2 S at the virion surface (ATTO565) and the VSV phosphoprotein tagged with EGFP inside virions. In this model, until particles were intact and have not fused during intracellular trafficking, they appear in yellow (result from the colocalization of both signals red and green), and then in green after fusion. This system allowed the authors to image single fusion event in cells by fluorescence confocal

microscopy. The authors claimed that the number of S-trimers at the cell-cell interface in the cell-cell fusion assay is much higher than at the virus-cell interface. Thus, the low probability of fusion events at neutral pH may be sufficient to allow fusion between adjacent cells. However, these results are not supported by the many publications showing that in TMPRSS2+ cells, continuous presence of agents neutralizing endosomal pH could not completely block infection with authentic SARS-CoV-2 particles or inhibit syncytia formation. Cell type-specific effects, expression levels of proteases, or the use of pseudotyped particles versus authentic virus could also explain the observed differences in acidification requirements.

4.5 Role of TMPRSS2 in cleaving ACE2

My preliminary results indicated that the cell surface expression of ACE2 decreased when TMPRSS2 was overexpressed, which also correlated with decreased SARS-CoV-2 binding to the cell surface. Previous reports showed that not only S of SARS-CoV-2, but also its receptor ACE2 can be cleaved at two different sites on the cell surface by TMPRSS2 and the matrix metalloproteinase ADAM17 (285, 370, 371). The cleavage results in the release of a soluble, enzymatically active form of ACE2, termed sACE2. Recently, two matrix metalloproteinases, MT1-MMP and ADAM10, have also been proposed to be involved in ACE2 shedding (372, 373). Cleavage of ACE2 by TMPRSS2, but not ADAM17, resulted in increased viral uptake of SARS-CoV (285). Together these observations indicate that SARS-CoV-2 binds more efficiently to cleaved ACE2 and thus highlight the importance of ACE2 cleavage in SARS-CoV-2. Recently, sACE2 was shown to bind SARS-CoV-2 and mediate its entry via interaction with AT1 or AVPR1B (374, 375). Still, the details mechanisms underlying this first step in SARS-CoV-2 entry must be elucidated.

For instance, it remains to be determined which version of ACE2, shed or membrane-bound, is involved in SARS-CoV-2 entry. It is tempting to speculate that the viral protein S is covered by soluble ACE2 after shedding of ACE2-SARS-CoV-2 complexes, and thus, that the viral particles are protected from neutralizing antibodies. Increased levels of sACE2 were found in COVID-19 patients and correlated with disease severity (376). In addition, shedding of ACE2 was promoted by pro-inflammatory cytokines, and it was proposed that virus-sACE2 complexes could travel across vessels to infect additional organs and tissues. Thus, a model has been proposed in which initial infection with SARS-CoV-2 leads to pro-inflammatory cytokines that promote ACE2 shedding and spread of SARS-CoV-2 to additional organs and tissues. However, it is not clear whether

ACE2 shedding has a clear physiological role or is merely correlated with disease severity. The circulation of virus-sACE2 complexes could allow entry into cell types that do not express ACE2 and provide an explanation for entry and infection of cells lacking ACE2 expression in addition to the use of alternative receptors. Finally, the interplay between pro-inflammatory cytokines, TMPRSS2, and ACE2 shedding will require further investigations.

4.6 Conclusion

The goal of my PhD project was to provide a better understanding of the entry process of two distinct zoonotic viruses. First, my work aimed to characterize the early stages of TOSV in iPSC-derived human neurons and cell lines, from virus binding and internalization to intracellular trafficking and membrane fusion. I could show that TOSV rapidly enters cells and traffics along the endosomal pathway. Infection was dependent on the transport to functional late endosomes from where TOSV penetrates host cells by acid-activated membrane fusion. In contrast to other class-II fusion proteins, the fusion machinery of TOSV and other bunyaviruses could not be inactivated upon exposure to low pH. This remarkable resistance might confer advantages to these viruses to find their way in the endocytic machinery until reaching the right place to ensure fusion and then productive infection of cells. Additionally, TOSV fusion showed a high versatility in the pH values, as fusion could also be detected upon longer exposure at higher pH values than the optimal pH. Furthermore, the progressive decrease in acidity in maturing endosomes primed particles and a faster fusion could be observed at pH values found in LEs. Thus, TOSV shares with the other phenuiviruses a similar entry route to infect host cells, *i.e.*, they penetrate the cytosol by acid-activated membrane fusion from late endosomal compartments.

My work on SARS-CoV-2 showed that the entry of the virus involves different host cell proteases, which drive the pathway used by the virus to enter cells. In cells expressing TMPRSS2, TMPRSS2 dictated the entry route. S was cleaved and activated at or nearby the cell surface, and a fast, pH-independent productive entry followed. Alternatively, in cells lacking TMPRSS2 expression, SARS-CoV-2 was endocytosed and sorted into the degradative branch of the endocytic machinery. Then SARS-CoV-2 trafficked inside the cells, likely within intracellular vesicles, until reaching endolysosomes. There, the acid-dependent cathepsin L cleaved and activated the S protein, and in turn, viral fusion occurred. The entry process was slower and relied on acidification because low pH is critical for the activity of cathepsin L. To investigate the role of proteolytic processing and

acidification directly on membrane fusion, I developed a cell-cell fusion assay. This allowed me to demonstrate that proteolytic processing of S was necessary and sufficient to induce fusion while acidification was only important for cathepsin activity. Thus, SARS-CoV-2 shares with other coronaviruses, such as SARS-CoV and MERS-CoV, to use multiple entry routes. Which of the entry routes is used by the virus largely depends on the proteases expressed in target cells.

Collectively, my comprehensive study on TOSV and SARS-CoV-2 shows that both viruses make an atypical use of vacuolar acidification. TOSV and other bunyaviruses undergo an acid-activated membrane fusion, and show a remarkable adaptability to the acidic environment in endosomal compartments. This advantage likely conferred bunyaviruses to go through trial and errors on their way until they reach the appropriate endosomes to fuse under optimal conditions. In contrast, SARS-CoV-2 fusion does not rely on pH itself, but the protease cathepsin L that proteolytically processes S does. Thereby, SARS-CoV-2 shows a high versatility to different protease species. When S is not activated directly at the cell surface, virions can enter cells and traffic to endolysosomes where the acidic environment allows cathepsin L to activate membrane fusion. Thus, in TMPRSS2- cells, SARS-CoV-2 and TOSV use a similar entry pathway, and depend on vacuolar acidification and maturation of endosomes. However, while TOSV already escapes the endocytic route from LEs by acid-activated membrane fusion, SARS-CoV-2 requires further transport to endolysosomes where processing by cathepsin L triggers the fusion process.

In sum, with this thesis, I sincerely hope I have been convincing about the biological significance and importance of studying zoonotic emerging viruses. The WHO classified twelve viruses as priority pathogens that pose the greatest public health risk due to their epidemic potential or the insufficiency of countermeasures. They include eleven known viruses and a pathogen causing disease X that represent a hypothetical, unknown pathogen that could cause a future epidemic. All eleven named pathogens are of zoonotic origin and include with SARS-CoV-2, SARS-CoV, and MERS-CoV three coronaviruses. In addition, several arboviruses with a class-II fusion machinery are listed such as the bunyaviruses RVFV and Crimean-Congo hemorrhagic fever virus, and the flavivirus Zika virus. Class-II fusion viruses also include several dozen pathogenic isolates in humans and domestic animals, most of which have no vaccines or treatments approved for human use. In this respect, the entry process is an important step in the life cycle of viruses and represents an interesting target for drug development. Hence, a deeper understanding of the cell biology of virus entry is evidently required in future works aiming to prevent

transmission, infection, and spread of zoonotic viruses, whose threats to human and veterinary public health are increasing worldwide.

5 Publications and contributions

Listings in italic show shared first authors.

First author publications

Koch, Jana; Xin, Qilin; Obr, Martin; Schäfer, Alicia; Rolfs, Nina; Anagho, Holda; Kudulyte, Aiste; Woltereck, Lea; Kummer, Susann; Campos, Joaquin; Uckeley, Zina M.; Bell-Sakyi, Lesley; Kräusslich, Hans-Georg; Schur, Florian K. M.; Acuna, Claudio; Lozach, Pierre-Yves (2023): The phenuivirus Toscana virus makes an atypical use of vacuolar acidity to enter host cells. DOI: 10.1101/2023.03.06.531240 (Research article, in revision in PLOS Pathogens).

Koch, Jana; Uckeley, *Zina M.*; Doldan, Patricio; Stanifer, Megan; Boulant, Steeve; Lozach, Pierre-Yves (2021): TMPRSS2 expression dictates the entry route used by SARS-CoV-2 to infect host cells. In *The EMBO Journal* 40 (16), e107821. DOI: 10.15252/embj.2021107821. (research article).

Koch, Jana; Uckeley, Zina M.; Lozach, Pierre-Yves (2022): [SARS-CoV-2 uses different entry routes to infect host cells]. In *Med Sci (Paris)*, pp. 419–422. DOI: 10.1051/medsci/2022048. (Review).

Koch, Jana; Uckeley, Zina M.; Lozach, Pierre-Yves (2021): SARS-CoV-2 variants as super cell fusers: cause or consequence of COVID-19 severity? In *The EMBO Journal* 40 (24), e110041. DOI: 10.15252/embj.2021110041. (News & Views)

Koch, Jana; Xin, Qilin; Tischler, Nicole D.; Lozach, Pierre-Yves (2021): Entry of Phenuiviruses into Mammalian Host Cells. In *Viruses* 13 (2). DOI: 10.3390/v13020299. (Review).

Uckeley, Zina M.; Koch, Jana; Tischler, Nicole D.; Léger, Psylvia; Lozach, Pierre-Yves (2019): Cell biology of phlebovirus entry. In *Virologie (Montrouge, France)* 23 (3), pp. 176–187. DOI: 10.1684/vir.2019.0780. (Review).

Co-author publications

Uckeley, Zina M.; Duboeuf, Maëva; Gu, Yu; Erny, Alexandra; Mazelier, Magalie; Lüchtenborg, Christian; Winter, Sophie L.; Schad, Paulina; Mathieu, Cyrille; Koch, Jana; Boulant, Steeve; Maisse, Carine; Chlanda, Petr; Brügger, Britta; Lozach, Pierre-Yves (2023): Glucosylceramide is a major structural determinant of virions essential for bunyavirus binding to host cells. (in revision in PLOS Pathogens).

Windhaber, Stefan; Xin, Qilin; Uckeley, Zina M.; Koch, Jana; Obr, Martin; Garnier, Céline; Luengo-Guyonnot, Catherine; Duboeuf, Maëva; Schur, Florian K. M.; Lozach, Pierre-Yves (2022): The Orthobunyavirus Germiston Enters Host Cells from Late Endosomes. In *Journal of Virology* 96 (5), e0214621. DOI: 10.1128/jvi.02146-21.

Léger, Psylvia; Nachman, Eliana; Richter, Karsten; Tamietti, Carole; Koch, Jana; Burk, Robin; Kummer, Susann; Xin, Qilin; Stanifer, Megan; Bouloy, Michèle; Boulant, Steeve; Kräusslich, Hans-Georg; Montagutelli, Xavier; Flamand, Marie; Nussbaum-Krammer, Carmen; Lozach, Pierre-Yves (2020): NSs amyloid formation is associated with the virulence of Rift Valley fever virus in mice. In *Nature Communications* 11 (1), p. 3281. DOI: 10.1038/s41467-020-17101-y.

Woelfl, Franziska; Léger, Psylvia; Oreshkova, Nadia; Pahmeier, Felix; Windhaber, Stefan; Koch, Jana; Stanifer, Megan; Roman Sosa, Gleyder; Uckeley, Zina M.; Rey, Felix A.; Boulant, Steeve; Kortekaas, Jeroen; Wichgers Schreur, Paul J.; Lozach, Pierre-Yves (2020): Novel Toscana Virus Reverse Genetics System Establishes NSs as an Antagonist of Type I Interferon Responses. In *Viruses* 12 (4), p. 400. DOI: 10.3390/v12040400. (Research article).

Scholarships

Bursary for the attendance of the “Bunyavirus 2022 conference” in Cambridge, UK, 2022

Conference presentations

25th annual meeting of the Club Exocytose-Endocytose – Lacanau, France, 2023. “Zoonotic viruses make a differential use of endosomal acidification for infectious entry”. (oral presentation).

Bunyavirus 2022 conference - Robinson College, University of Cambridge, UK, 2022. “Toscana virus enters human host cells by late endosomal acid-activated membrane fusion.” (oral presentation). I obtained a bursary for attendance of this conference.

19th Workshop Cell Biology of Viral Infections of the German Society for Virology (GfV) - Schöntal, Germany, 2021. “TMPRSS2 expression dictates the entry route used by SARS-CoV-2 to infect host cells” (oral presentation).

ASV 2021, 40th Annual Meeting of the American Society for Virology - virtual event, 2021. “Host Cell Proteases Drive Early or Late SARS-CoV-2 Infectious Penetration”. (oral presentation).

30th Annual Meeting of the German Society for Virology (GfV) – virtual event, 2021. “Host cell proteases drive early or late SARS-CoV-2 penetration”. (poster presentation).

18th Workshop Cell Biology of Viral Infections of the German Society for Virology (GfV) - Schöntal, Germany, 2019. “Entry of Toscana virus into Mammalian Host Cells”. (oral presentation).

Contributions to this thesis

All data shown in this thesis were acquired and analyzed by me, if not stated here otherwise.

The rotations students **Alicia Rosenberger**, **Aiste Kudulyte** and **Lea Woltereck** were directly supervised by me and assisted in generation of data. I repeated most of their experiments. Alicia Rosenberger produced of GERV and RVFVΔNSs:EGFP stock in BHK-21 and Vero cells, and assessed pH pretreatment of TOSV, GERV, and RVFVΔNSs:EGFP and infection of A549 cells. Aiste Kudulyte assessed pH pre-treatment of Influenza A virus and infection of A549 cells. Lea Woltereck assessed the fusion efficiency of R18-labeled TOSV.

The rotation student **Nina Rolfs** tested the susceptibility of different mammalian cell lines to TOSV infection and was supervised by Zina Uckeley.

Qilin Xin tested the susceptibility of the sand fly cell line PPL/LULS49 for TOSV infection.

Zina Uckeley supervised Nina Rolfs. Main part of SARS-CoV-2 project was performed in collaboration with her.

Patricio Doldan cultured and seeded Caco-2 and Calu-3 cells.

Alessandra Albertelli provided me with iPSC-derived neurons.

Vera Sonntag-Buck produced influenza A virus.

Dr. Susann Kummer performed STED imaging of fluorescently labeled TOSV particles and produced Influenza A virus.

Dr. Martin Obr performed cryo-electron microscopy of TOSV particles.

6 Acknowledgements

The present study was carried out under the supervision of Dr. Pierre-Yves Lozach in the Center of Integrative Infectious Disease Research, Virology, at the University Hospital Heidelberg and supported by DFG-ANR and the CellNetworks cluster of excellence.

First of all, I want to express my gratitude to Pierre-Yves for giving me the opportunity to perform my PhD in his group on such interesting projects. I enjoyed the very fruitful discussions, your enthusiastic and positive thinking, and the very nice working atmosphere in the lab. Thank you for taking your time for me even when it was late hours or on the weekend. Thank you for always having a door open and answer super rapidly per mail. So, even when our offices were far away in Heidelberg and Lyon, it didn't feel like any distance. It was a pleasure to be a part of your team.

My gratitude also goes to Prof. Dr. Hans-Georg Kräusslich for taking the time to accompany my project and for agreeing to be my first supervisor. The meetings and your input were always very helpful. I also want to thank Steeve Boulant for providing enormous input into our collaboration project on the entry of SARS-CoV-2 and for being a member of my TAC committee. I would also thank Prof. Dr. Freddy Frischknecht and Dr. Marco Binder for agreeing to examine my thesis.

During my PhD, I also had the opportunity to work in collaboration with several other people. Here, I would like to thank Susann Kummer and Martin Obr for providing me with such beautiful images on TOSV particles. I would also thank the whole Boulant lab, especially Steeve, Megan and Patricio. Our SARS-CoV-2 project would not have been possible without your help in and outside of the BSL3. Here, I would also like to thank the Bartenschlager lab for providing me with very nice cells.

A big thanks goes to the whole Lozach lab, to current and former members in Heidelberg and Lyon. I always enjoyed coming to the lab, or visit Lyon, and work in such a friendly environment. Here, I would especially like to thank Zina who worked jointly with me on the SARS-CoV-2 project and spent endless hours of cell harvesting and at the FACS. A thanks goes also to Stefan, who was constantly spreading positivity, Psylvia with her crazy funny mind, Anja who helped a lot at the beginning with all the entry protocols, and Colin, with whom I always had incroyable discussions. I would also thank all my rotations students Christian, Elena, Lea, Alicia and Aiste who helped moving forward with my projects. You did a great job!

Moreover, I would like to thank the people on the floor, especially Stephi, Ann-Kathrin, Charlotte and Rebecca for the nice atmosphere and productive discussions, coffee breaks, fun times (also inside cell culture). It would not have been the same without you.

Und natürlich auch ein großes Dankeschön an meine Familie, für eure bedingungslose und ständige Unterstützung , die immer sehr verständnisvoll waren, auch wenn ich nicht immer die Zeit aufwenden konnte, die ich gerne gehabt hätte. Dazu gehört natürlich auch ein riesengroßes, liebes Danke an Alex, ohne den das Ganze nicht möglich gewesen wäre. Danke für dein Verständnis, wenn ich mal wieder wenig oder keine Zeit aufbringen konnte, besonders in letzter Zeit. Danke, für die Stücke Kuchen mittags (oder die Kaltgetränke abends) und deine beruhigende Art, die schlimme Tage immer besser gemacht haben.

7 References

1. World Health Organization. WHO Health Topic Page: Zoonoses. Available from: URL: https://www.who.int/news-room/fact-sheets/detail/zoonoses.

2. Taylor LH, Latham SM, Woolhouse ME. Risk factors for human disease emergence. Philos Trans R Soc Lond B Biol Sci 2001; 356(1411):983–9.

3. World Health Organization. Prioritizing diseases for research and development in emergency contexts. Available from: URL: https://www.who.int/activities/prioritizing-diseases-for-research-and-development-in-emergency-contexts.

4. World Health Organization. Report of the WHO/FAO/OIE joint consultation on emerging zoonotic diseases. (2004). Available from: URL: https://apps.who.int/iris/bitstream/handle/10665/68899/WHO_CDS_CPE_ZFK_2004.9.pdf.

5. Rahman MT, Sobur MA, Islam MS, Ievy S, Hossain MJ, El Zowalaty ME et al. Zoonotic Diseases: Etiology, Impact, and Control. Microorganisms 2020; 8(9).

6. Young PR. Arboviruses: A Family on the Move. Adv Exp Med Biol 2018; 1062:1–10.

7. McArthur DB. Emerging Infectious Diseases. Nurs Clin North Am 2019; 54(2):297–311.

8. International committee on taxonomy of viruses (ICTV) [cited 2023 May 21]. Available from: URL: https://ictv.global/taxonomy.

9. Léger P, Lozach P-Y. Bunyaviruses: from transmission by arthropods to virus entry into the mammalian host first-target cells. Future Virology 2015; 10(7):859–81.

10. Daubney R, Hudson JR, Garnham PC. Enzootic hepatitis or rift valley fever. An undescribed virus disease of sheep cattle and man from east africa. J. Pathol. 1931; 34(4):545–79.

11. Chevalier V, Pépin M, Plée L, Lancelot R. Rift Valley fever - a threat for Europe? Eurosurveillance 2010; 15(10).

12. Wright D, Kortekaas J, Bowden TA, Warimwe GM. Rift Valley fever: biology and epidemiology. Journal of General Virology 2019; 100(8):1187–99.

13. Baba M, Masiga DK, Sang R, Villinger J. Has Rift Valley fever virus evolved with increasing severity in human populations in East Africa? Emerg Microbes Infect 2016; 5(6):e58.

14. Yu X-J, Liang M-F, Zhang S-Y, Liu Y, Li J-D, Sun Y-L et al. Fever with thrombocytopenia associated with a novel bunyavirus in China. N Engl J Med 2011; 364(16):1523–32.

15. Kim K-H, Yi J, Kim G, Choi SJ, Jun KI, Kim N-H et al. Severe fever with thrombocytopenia syndrome, South Korea, 2012. Emerging Infectious Diseases 2013; 19(11):1892–4.

16. Takahashi T, Maeda K, Suzuki T, Ishido A, Shigeoka T, Tominaga T et al. The first identification and retrospective study of Severe Fever with Thrombocytopenia Syndrome in Japan. J Infect Dis 2014; 209(6):816–27.

17. Tran XC, Yun Y, van An, Kim S-H, Thao NTP, Man PKC et al. Endemic Severe Fever with Thrombocytopenia Syndrome, Vietnam. Emerging Infectious Diseases 2019; 25(5):1029–31.

18. Casel MA, Park SJ, Choi YK. Severe fever with thrombocytopenia syndrome virus: emerging novel phlebovirus and their control strategy. Exp Mol Med 2021; 53(5):713–22.

19. Verani. Ecological and epidemiological studies of Toscana virus, an arbovirus isolated from Phlebotomus. Ann. Ist Super. Sanita. 1982; 18:397.

20. Laroche L, Jourdain F, Ayhan N, Bañuls A-L, Charrel R, Prudhomme J. Incubation Period for Neuroinvasive Toscana Virus Infections. Emerging Infectious Diseases 2021; 27(12):3147–50.

21. Bartels S, Boni L de, Kretzschmar HA, Heckmann JG. Lethal encephalitis caused by the Toscana virus in an elderly patient. J Neurol 2012; 259(1):175–7.

22. Serata D, Rapinesi C, Del Casale A, Simonetti A, Mazzarini L, Ambrosi E et al. Personality changes after Toscana virus (TOSV) encephalitis in a 49-year-old man: A case report. Int J Neurosci 2011; 121(3):165–9.

23. Oechtering J, Petzold GC. Acute hydrocephalus due to impaired CSF resorption in Toscana virus meningoencephalitis. Neurology 2012; 79(8):829–31.

24. Portolani M, Sabbatini AMT, Beretti F, Gennari W, Tamassia MG, Pecorari M. Symptomatic infections by toscana virus in the Modena province in the triennium 1999-2001. New Microbiol 2002; 25(4):485–8.

25. Baldelli F, Ciufolini MG, Francisci D, Marchi A, Venturi G, Fiorentini C et al. Unusual presentation of life-threatening Toscana virus meningoencephalitis. Clinical Infectious Diseases 2004; 38(4):515–20.

26. Tappe D, Schmidt-Chanasit J, Günther S, Ries A, Ziegler U, Müller A et al. Acute Toscana virus infection mimicked by Yersinia-induced reactive arthritis syndrome after journey to Spain. J Clin Virol 2010; 47(1):104–5.

27. Pauli C, Schwarz TF, Meyer CG, Jäger G. Neurologische Symptome nach Infektion durch Sandfliegenfieber-Virus. Dtsch Med Wochenschr 1995; 120(43):1468–72.

28. Sanbonmatsu-Gámez S, Pérez-Ruiz M, Palop-Borrás B, Navarro-Marí JM. Unusual manifestation of toscana virus infection, Spain. Emerging Infectious Diseases 2009; 15(2):347–8.

29. Marlinge M, Crespy L, Zandotti C, Piorkowski G, Kaphan E, Charrel RN et al. Afebrile meningoencephalitis with transient central facial paralysis due to Toscana virus infection, southeastern France, 2014 corrected. Eurosurveillance 2014; 19(48):20974.

30. Rota E, Morelli N, Immovilli P, Mitri P de, Guidetti D. Guillain-Barré-like axonal polyneuropathy associated with Toscana virus infection: A case report. Medicine (Baltimore) 2017; 96(38):e8081.

31. Okar SV, Bekircan-Kurt CE, Hacıoğlu S, Erdem-Özdamar S, Özkul A, Ergünay K. Toscana virus associated with Guillain-Barré syndrome: a case-control study. Acta Neurol Belg 2021; 121(3):661–8.

32. Moriconi M, Rugna G, Calzolari M, Bellini R, Albieri A, Angelini P et al. Phlebotomine sand fly-borne pathogens in the Mediterranean Basin: Human leishmaniasis and phlebovirus infections. PLOS Neglected Tropical Diseases 2017; 11(8):e0005660.

33. Charrel RN, Berenger J-M, Laroche M, Ayhan N, Bitam I, Delaunay P et al. Neglected vector-borne bacterial diseases and arboviruses in the Mediterranean area. New Microbes and New Infections 2018; 26:S31-S36.

34. Punda-Polić V, Mohar B, Duh D, Bradarić N, Korva M, Fajs L et al. Evidence of an autochthonous Toscana virus strain in Croatia. J Clin Virol 2012; 55(1):4–7.

35. Papa A, Paraforou T, Papakonstantinou I, Pagdatoglou K, Kontana A, Koukoubani T. Severe encephalitis caused by Toscana virus, Greece. Emerging Infectious Diseases 2014; 20(8):1417–9.

36. Hukić M, Salimović-Besić I. Sandfly - Pappataci fever in Bosnia and Herzegovina: the new-old disease. Bosn J Basic Med Sci 2009; 9(1):39–43.

37. Venturi G, Marchi A, Fiorentini C, Ramadani N, Quaglio G, Kalaveshi A et al. Prevalence of antibodies to phleboviruses and flaviviruses in Peja, Kosovo. Clin Microbiol Infect 2011; 17(8):1180–2.

38. Christova I, Panayotova E, Trifonova I, Taseva E, Gladnishka T, Ivanova V. Serologic evidence of widespread Toscana virus infection in Bulgaria. J Infect Public Health 2020; 13(2):164–6.

39. Popescu CP, Cotar AI, Dinu S, Zaharia M, Tardei G, Ceausu E et al. Emergence of Toscana Virus, Romania, 2017-2018. Emerging Infectious Diseases 2021; 27(5):1482–5.

40. Alkan C, Allal-Ikhlef AB, Alwassouf S, Baklouti A, Piorkowski G, Lamballerie X de et al. Virus isolation, genetic characterization and seroprevalence of Toscana virus in Algeria. Clin Microbiol Infect 2015; 21(11):1040.e1-9.

41. Saadawi WK, Abozaid FD, Almukhtar M, Annajar BB, Shaibi T. Seroprevalence study of Toscana virus in Yafran area, Libya. J Vector Borne Dis 2022; 59(2):186–9.

42. Andayi F, Charrel RN, Kieffer A, Richet H, Pastorino B, Leparc-Goffart I et al. A sero-epidemiological study of arboviral fevers in Djibouti, Horn of Africa. PLOS Neglected Tropical Diseases 2014; 8(12):e3299.

43. Dersch R, Sophocleous A, Cadar D, Emmerich P, Schmidt-Chanasit J, Rauer S. Toscana virus encephalitis in Southwest Germany: a retrospective study. BMC Neurol 2021; 21(1):495.

44. Gonen OM, Sacagiu T. Sensory polymyeloradiculopathy associated with Toscana virus infection. J Neurovirol 2013; 19(5):508–10.

45. Naucke TJ, Menn B, Massberg D, Lorentz S. Sandflies and leishmaniasis in Germany. Parasitol Res 2008; 103 Suppl 1:S65-8.

46. Oerther S, Jöst H, Heitmann A, Lühken R, Krüger A, Steinhausen I et al. Phlebotomine sand flies in Southwest Germany: an update with records in new locations. Parasit Vectors 2020; 13(1):173.

47. Es-Sette N, Nourlil J, Hamdi S, Mellouki F, Lemrani M. First detection of Toscana virus RNA from sand flies in the genus Phlebotomus (Diptera: Phlebotomidae) naturally infected in Morocco. J Med Entomol 2012; 49(6):1507–9.

48. Es-sette N, Ajaoud M, Anga L, Mellouki F, Lemrani M. Toscana virus isolated from sandflies, Morocco. Parasit Vectors 2015; 8:205.

49. Es-Sette N, Ajaoud M, Charrel RN, Lemrani M. Épidémiologie moléculaire des phlebovirus dans quatre provinces du Maroc. Bull Soc Pathol Exot 2016; 109(3):143–50.

50. Ergunay K, Kasap OE, Orsten S, Oter K, Gunay F, Yoldar AZA et al. Phlebovirus and Leishmania detection in sandflies from eastern Thrace and northern Cyprus. Parasit Vectors 2014; 7:575.

51. Ayhan N, Alten B, Ivovic V, Martinkovic F, Kasap OE, Ozbel Y et al. Cocirculation of Two Lineages of Toscana Virus in Croatia. Front Public Health 2017; 5:336.

52. Özbel Y, Oğuz G, Arserim SK, Erişöz Kasap Ö, Karaoglu B, Yilmaz A et al. The initial detection of Toscana virus in phlebotomine sandflies from Turkey. Med Vet Entomol 2020; 34(4):402–10.

53. Charrel RN, Izri A, Temmam S, Lamballerie X de, Parola P. Toscana virus RNA in Sergentomyia minuta files. Emerging Infectious Diseases 2006; 12(8):1299–300.

54. Tesh RB, Modi GB. Maintenance of Toscana virus in Phlebotomus perniciosus by vertical transmission. The American Journal of Tropical Medicine and Hygiene 1987; 36(1):189–93.

55. Maroli M, Ciufolini MG, Verani P. Vertical transmission of Toscana virus in the sandfly, Phlebotomus perniciosus, via the second gonotrophic cycle. Med Vet Entomol 1993; 7(3):283–6.

56. Ciufolini MG, Maroli M, Verani P. Growth of two phleboviruses after experimental infection of their suspected sand fly vector, Phlebotomus perniciosus (Diptera: Psychodidae). The American Journal of Tropical Medicine and Hygiene 1985; 34(1):174–9.

57. Laroche L, Ayhan N, Charrel R, Bañuls A-L, Prudhomme J. Persistence of Toscana virus in sugar and blood meals of phlebotomine sand flies: epidemiological and experimental consequences. Sci Rep 2023; 13(1):5608.

58. Tesh RB, Lubroth J, Guzman H. Simulation of arbovirus overwintering: survival of Toscana virus (Bunyaviridae:Phlebovirus) in its natural sand fly vector Phlebotomus perniciosus. The American Journal of Tropical Medicine and Hygiene 1992; 47(5):574–81.

59. Ciufolini MG, Maroli M, Guandalini E, Marchi A, Verani P. Experimental studies on the maintenance of Toscana and Arbia viruses (Bunyaviridae: Phlebovirus). The American Journal of Tropical Medicine and Hygiene 1989; 40(6):669–75.

60. Dincer E, Gargari S, Ozkul A, Ergunay K. Potential animal reservoirs of Toscana virus and coinfections with Leishmania infantum in Turkey. The American Journal of Tropical Medicine and Hygiene 2015; 92(4):690–7.

61. Muñoz C, Ayhan N, Ortuño M, Ortiz J, Gould EA, Maia C et al. Experimental Infection of Dogs with Toscana Virus and Sandfly Fever Sicilian Virus to Determine Their Potential as Possible Vertebrate Hosts. Microorganisms 2020; 8(4).

62. Ayhan N, Rodríguez-Teijeiro JD, López-Roig M, Vinyoles D, Ferreres JA, Monastiri A et al. High rates of antibodies against Toscana and Sicilian phleboviruses in common quail Coturnix coturnix birds. Front Microbiol 2022; 13:1091908.

63. Hacioglu S, Dincer E, Isler CT, Karapinar Z, Ataseven VS, Ozkul A et al. A Snapshot Avian Surveillance Reveals West Nile Virus and Evidence of Wild Birds Participating in Toscana Virus Circulation. Vector Borne Zoonotic Dis 2017; 17(10):698–708.

64. Knipe DM, Howley PM, Fields BN, editors. Emerging viruses. Seventh edition. New York, Philadelphia, Baltimore, London, Buenos Aires, Hong Kong, Sydney, Tokyo: Wolters Kluwer; 2021. (Fields virology / ed.-in-chiefVolume 1).

65. Chan-Yeung M, Xu R-H. SARS: epidemiology. Respirology 2003; 8 Suppl(Suppl 1):S9-14.

66. Shi Z, Hu Z. A review of studies on animal reservoirs of the SARS coronavirus. Virus Research 2008; 133(1):74–87.

67. Zaki AM, van Boheemen S, Bestebroer TM, Osterhaus ADME, Fouchier RAM. Isolation of a novel coronavirus from a man with pneumonia in Saudi Arabia. N Engl J Med 2012; 367(19):1814–20.

68. World Health Organization. WHO EMRO | MERS situation update. MERS-CoV | Epidemic and pandemic diseases. Available from: URL: https://www.emro.who.int/pandemic-epidemic-diseases/mers-cov/mers-situation-update-december-2019.html.

69. Zabiegala A, Kim Y, Chang K-O. Roles of host proteases in the entry of SARS-CoV-2. Anim Dis 2023; 3(1):12.

70. Wit E de, van Doremalen N, Falzarano D, Munster VJ. SARS and MERS: recent insights into emerging coronaviruses. Nature Reviews Microbiology 2016; 14(8):523–34.

71. Zhu N, Zhang D, Wang W, Li X, Yang B, Song J et al. A Novel Coronavirus from Patients with Pneumonia in China, 2019. N Engl J Med 2020; 382(8):727–33.

72. Li Q, Guan X, Wu P, Wang X, Zhou L, Tong Y et al. Early Transmission Dynamics in Wuhan, China, of Novel Coronavirus-Infected Pneumonia. N Engl J Med 2020; 382(13):1199–207.

73. Richard M, Kok A, Meulder D de, Bestebroer TM, Lamers MM, Okba NMA et al. SARS-CoV-2 is transmitted via contact and via the air between ferrets. Nature Communications 2020; 11(1):3496.

74. Huang C, Wang Y, Li X, Ren L, Zhao J, Hu Y et al. Clinical features of patients infected with 2019 novel coronavirus in Wuhan, China. Lancet 2020; 395(10223):497–506.

75. Kung Y-A, Lee K-M, Chiang H-J, Huang S-Y, Wu C-J, Shih S-R. Molecular Virology of SARS-CoV-2 and Related Coronaviruses. Microbiol Mol Biol Rev 2022; 86(2):e0002621.

76. Braga L, Ali H, Secco I, Chiavacci E, Neves G, Goldhill D et al. Drugs that inhibit TMEM16 proteins block SARS-CoV-2 spike-induced syncytia. Nature 2021; 594(7861):88–93.

77. Brazeau NF, Verity R, Jenks S, Fu H, Whittaker C, Winskill P et al. Estimating the COVID-19 infection fatality ratio accounting for seroreversion using statistical modelling. Commun Med (Lond) 2022; 2:54.

78. Ioannidis JPA. Infection fatality rate of COVID-19 inferred from seroprevalence data. Bull World Health Organ 2021; 99(1):19-33F.

79. Zhou P, Yang X-L, Wang X-G, Hu B, Zhang L, Zhang W et al. A pneumonia outbreak associated with a new coronavirus of probable bat origin. Nature 2020; 579(7798):270–3.

80. Nie J, Li Q, Zhang L, Cao Y, Zhang Y, Li T et al. Functional comparison of SARS-CoV-2 with closely related pangolin and bat coronaviruses. Cell Discov 2021; 7(1):21.

81. Voskarides K. SARS-CoV-2: tracing the origin, tracking the evolution. BMC Med Genomics 2022; 15(1):62.

82. Holmes EC, Goldstein SA, Rasmussen AL, Robertson DL, Crits-Christoph A, Wertheim JO et al. The origins of SARS-CoV-2: A critical review. Cell 2021; 184(19):4848–56.

83. Xiao X, Newman C, Buesching CD, Macdonald DW, Zhou Z-M. Animal sales from Wuhan wet markets immediately prior to the COVID-19 pandemic. Sci Rep 2021; 11(1):11898.

84. Lytras S, Xia W, Hughes J, Jiang X, Robertson DL. The animal origin of SARS-CoV-2. Science 2021; 373(6558):968–70.

85. Scovino AM, Dahab EC, Vieira GF, Freire-de-Lima L, Freire-de-Lima CG, Morrot A. SARS-CoV-2's Variants of Concern: A Brief Characterization. Front Immunol 2022; 13:834098.

86. Boulant S, Stanifer M, Lozach P-Y. Dynamics of virus-receptor interactions in virus binding, signaling, and endocytosis. Viruses 2015; 7(6):2794–815.

87. Kumar CS, Dey D, Ghosh S, Banerjee M. Breach: Host Membrane Penetration and Entry by Nonenveloped Viruses. Trends Microbiol 2018; 26(6):525–37.

88. Mercer J, Schelhaas M, Helenius A. Virus entry by endocytosis. Annu Rev Biochem 2010; 79:803–33.

89. Huotari J, Helenius A. Endosome maturation. The EMBO Journal 2011; 30(17):3481–500.

90. Piper RC, Dikic I, Lukacs GL. Ubiquitin-dependent sorting in endocytosis. Cold Spring Harb Perspect Biol 2014; 6(1).

91. Stenmark H. Rab GTPases as coordinators of vesicle traffic. Nat Rev Mol Cell Biol 2009; 10(8):513–25.

92. Guerra F, Bucci C. Multiple Roles of the Small GTPase Rab7. Cells 2016; 5(3).

93. Lozach P-Y, Huotari J, Helenius A. Late-penetrating viruses. Current Opinion in Virology 2011; 1(1):35–43.

94. Maxfield FR, Yamashiro DJ. Endosome acidification and the pathways of receptor-mediated endocytosis. Adv Exp Med Biol 1987; 225:189–98.

95. Scott CC, Gruenberg J. Ion flux and the function of endosomes and lysosomes: pH is just the start: the flux of ions across endosomal membranes influences endosome function not only through regulation of the luminal pH. BioEssays 2011; 33(2):103–10.

96. Lloyd-Evans E, Waller-Evans H. Lysosomal Ca2+ Homeostasis and Signaling in Health and Disease. Cold Spring Harb Perspect Biol 2020; 12(6).

97. Scott CC, Vacca F, Gruenberg J. Endosome maturation, transport and functions. Semin Cell Dev Biol 2014; 31:2–10.

98. Bayer N, Schober D, Prchla E, Murphy RF, Blaas D, Fuchs R. Effect of bafilomycin A1 and nocodazole on endocytic transport in HeLa cells: implications for viral uncoating and infection. Journal of Virology 1998; 72(12):9645–55.

99. Mesaki K, Tanabe K, Obayashi M, Oe N, Takei K. Fission of tubular endosomes triggers endosomal acidification and movement. PLoS One 2011; 6(5):e19764.

100. Dunn WA, Hubbard AL, Aronson NN. Low temperature selectively inhibits fusion between pinocytic vesicles and lysosomes during heterophagy of 125I-asialofetuin by the perfused rat liver. Journal of Biological Chemistry 1980; 255(12):5971–8.

101. Ellinger I, Klapper H, Courtoy PJ, Vaerman J-P, Fuchs R. Different temperature sensitivity of endosomes involved in transport to lysosomes and transcytosis in rat hepatocytes: Analysis by free-flow electrophoresis. ELECTROPHORESIS 2002; 23(13):2117.

102. Baravalle G, Schober D, Huber M, Bayer N, Murphy RF, Fuchs R. Transferrin recycling and dextran transport to lysosomes is differentially affected by bafilomycin, nocodazole, and low temperature. Cell Tissue Res 2005; 320(1):99–113.

103. Johannsdottir HK, Mancini R, Kartenbeck J, Amato L, Helenius A. Host cell factors and functions involved in vesicular stomatitis virus entry. Journal of Virology 2009; 83(1):440–53.

104. White J, Matlin K, Helenius A. Cell fusion by Semliki Forest, influenza, and vesicular stomatitis viruses. J Cell Biol 1981; 89(3):674–9.

105. Harrison SC. Viral membrane fusion. Virology 2015; 479-480:498–507.

106. White JM, Whittaker GR. Fusion of Enveloped Viruses in Endosomes. Traffic 2016; 17(6):593–614.

107. Lozada C, Barlow TMA, Gonzalez S, Lubin-Germain N, Ballet S. Identification and Characteristics of Fusion Peptides Derived From Enveloped Viruses. Front Chem 2021; 9:689006.

108. Kielian M. Mechanisms of Virus Membrane Fusion Proteins. Annu Rev Virol 2014; 1(1):171–89.

109. Guardado-Calvo P, Rey FA. The Viral Class II Membrane Fusion Machinery: Divergent Evolution from an Ancestral Heterodimer. Viruses 2021; 13(12).

110. Lobigs M, Garoff H. Fusion function of the Semliki Forest virus spike is activated by proteolytic cleavage of the envelope glycoprotein precursor p62. Journal of Virology 1990; 64(3):1233–40.

111. Guirakhoo F, Heinz FX, Mandl CW, Holzmann H, Kunz C. Fusion activity of flaviviruses: comparison of mature and immature (prM-containing) tick-borne encephalitis virions. J Gen Virol 1991; 72 (Pt 6):1323–9.

112. Guardado-Calvo P, Rey FA. The Envelope Proteins of the Bunyavirales. Adv Virus Res 2017; 98:83–118.

113. Zheng Y, Sánchez-San Martín C, Qin Z, Kielian M. The domain I-domain III linker plays an important role in the fusogenic conformational change of the alphavirus membrane fusion protein. Journal of Virology 2011; 85(13):6334–42.

114. Abou-Hamdan A, Belot L, Albertini A, Gaudin Y. Monomeric Intermediates Formed by Vesiculovirus Glycoprotein during Its Low-pH-induced Structural Transition. J Mol Biol 2018; 430(12):1685–95.

115. Connolly SA, Jardetzky TS, Longnecker R. The structural basis of herpesvirus entry. Nature Reviews Microbiology 2021; 19(2):110–21.

116. Roche S, Gaudin Y. Characterization of the equilibrium between the native and fusion-inactive conformation of rabies virus glycoprotein indicates that the fusion complex is made of several trimers. Virology 2002; 297(1):128–35.

117. Mueller DS, Kampmann T, Yennamalli R, Young PR, Kobe B, Mark AE. Histidine protonation and the activation of viral fusion proteins. Biochem Soc Trans 2008; 36(Pt 1):43–5.

118. Mair CM, Meyer T, Schneider K, Huang Q, Veit M, Herrmann A. A histidine residue of the influenza virus hemagglutinin controls the pH dependence of the conformational change mediating membrane fusion. Journal of Virology 2014; 88(22):13189–200.

119. Fritz R, Stiasny K, Heinz FX. Identification of specific histidines as pH sensors in flavivirus membrane fusion. J Cell Biol 2008; 183(2):353–61.

120. Boer SM de, Kortekaas J, Spel L, Rottier PJM, Moormann RJM, Bosch BJ. Acid-activated structural reorganization of the Rift Valley fever virus Gc fusion protein. Journal of Virology 2012; 86(24):13642–52.

121. Roche S, Bressanelli S, Rey FA, Gaudin Y. Crystal structure of the low-pH form of the vesicular stomatitis virus glycoprotein G. Science 2006; 313(5784):187–91.

122. Wallin M, Ekström M, Garoff H. Isomerization of the intersubunit disulphide-bond in Env controls retrovirus fusion. The EMBO Journal 2004; 23(1):54–65.

123. Chen B. Molecular Mechanism of HIV-1 Entry. Trends Microbiol 2019; 27(10):878–91.

124. Bose S, Jardetzky TS, Lamb RA. Timing is everything: Fine-tuned molecular machines orchestrate paramyxovirus entry. Virology 2015; 479-480:518–31.

125. Pennington HN, Lee J. Lassa virus glycoprotein complex review: insights into its unique fusion machinery. Biosci Rep 2022; 42(2).

126. Moller-Tank S, Maury W. Ebola virus entry: a curious and complex series of events. PLOS Pathogens 2015; 11(4):e1004731.

127. Das DK, Bulow U, Diehl WE, Durham ND, Senjobe F, Chandran K et al. Conformational changes in the Ebola virus membrane fusion machine induced by pH, Ca2+, and receptor binding. PLoS Biol 2020; 18(2):e3000626.

128. Kielian MC, Helenius A. Role of cholesterol in fusion of Semliki Forest virus with membranes. Journal of Virology 1984; 52(1):281–3.

129. Nieva JL, Bron R, Corver J, Wilschut J. Membrane fusion of Semliki Forest virus requires sphingolipids in the target membrane. The EMBO Journal 1994; 13(12):2797–804.

130. Kleinfelter LM, Jangra RK, Jae LT, Herbert AS, Mittler E, Stiles KM et al. Haploid Genetic Screen Reveals a Profound and Direct Dependence on Cholesterol for Hantavirus Membrane Fusion. mBio 2015; 6(4):e00801.

131. Bitto D, Halldorsson S, Caputo A, Huiskonen JT. Low pH and Anionic Lipid-dependent Fusion of Uukuniemi Phlebovirus to Liposomes. Journal of Biological Chemistry 2016; 291(12):6412–22.

132. Zaitseva E, Yang S-T, Melikov K, Pourmal S, Chernomordik LV. Dengue virus ensures its fusion in late endosomes using compartment-specific lipids. PLOS Pathogens 2010; 6(10):e1001131.

133. Espósito DLA, Nguyen JB, DeWitt DC, Rhoades E, Modis Y. Physico-chemical requirements and kinetics of membrane fusion of flavivirus-like particles. Journal of General Virology 2015; 96(Pt 7):1702–11.

134. Matos PM, Marin M, Ahn B, Lam W, Santos NC, Melikyan GB. Anionic lipids are required for vesicular stomatitis virus G protein-mediated single particle fusion with supported lipid bilayers. J Biol Chem 2013; 288(18):12416–25.

135. Punch EK, Hover S, Blest HTW, Fuller J, Hewson R, Fontana J et al. Potassium is a trigger for conformational change in the fusion spike of an enveloped RNA virus. J Biol Chem 2018; 293(26):9937–44.

136. Dubé M, Rey FA, Kielian M. Rubella virus: first calcium-requiring viral fusion protein. PLOS Pathogens 2014; 10(12):e1004530.

137. Albornoz A, Hoffmann AB, Lozach P-Y, Tischler ND. Early Bunyavirus-Host Cell Interactions. Viruses 2016; 8(5):143.

138. Wuerth JD, Weber F. Phleboviruses and the Type I Interferon Response. Viruses 2016; 8(6):174.

139. Leventhal SS, Wilson D, Feldmann H, Hawman DW. A Look into Bunyavirales Genomes: Functions of Non-Structural (NS) Proteins. Viruses 2021; 13(2).

140. Overby AK, Pettersson RF, Grünewald K, Huiskonen JT. Insights into bunyavirus architecture from electron cryotomography of Uukuniemi virus. Proc Natl Acad Sci U S A 2008; 105(7):2375–9.

141. Freiberg AN, Sherman MB, Morais MC, Holbrook MR, Watowich SJ. Three-dimensional organization of Rift Valley fever virus revealed by cryoelectron tomography. Journal of Virology 2008; 82(21):10341–8.

142. Dessau M, Modis Y. Crystal structure of glycoprotein C from Rift Valley fever virus. Proc Natl Acad Sci U S A 2013; 110(5):1696–701.

143. Guardado-Calvo P, Atkovska K, Jeffers SA, Grau N, Backovic M, Pérez-Vargas J et al. A glycerophospholipid-specific pocket in the RVFV class II fusion protein drives target membrane insertion. Science 2017; 358(6363):663–7.

144. Halldorsson S, Behrens A-J, Harlos K, Huiskonen JT, Elliott RM, Crispin M et al. Structure of a phleboviral envelope glycoprotein reveals a consolidated model of membrane fusion. Proc Natl Acad Sci U S A 2016; 113(26):7154–9.

145. Zhu Y, Wu Y, Chai Y, Qi J, Peng R, Feng W-H et al. The Postfusion Structure of the Heartland Virus Gc Glycoprotein Supports Taxonomic Separation of the Bunyaviral Families Phenuiviridae and Hantaviridae. Journal of Virology 2018; 92(1).

146. Wu Y, Zhu Y, Gao F, Jiao Y, Oladejo BO, Chai Y et al. Structures of phlebovirus glycoprotein Gn and identification of a neutralizing antibody epitope. Proc Natl Acad Sci U S A 2017; 114(36):E7564-E7573.

147. Halldorsson S, Li S, Li M, Harlos K, Bowden TA, Huiskonen JT. Shielding and activation of a viral membrane fusion protein. Nature Communications 2018; 9(1):349.

148. Wright D, Allen ER, Clark MHA, Gitonga JN, Karanja HK, Hulswit RJG et al. Naturally Acquired Rift Valley Fever Virus Neutralizing Antibodies Predominantly Target the Gn Glycoprotein. iScience 2020; 23(11):101669.

149. Koch J, Xin Q, Tischler ND, Lozach P-Y. Entry of Phenuiviruses into Mammalian Host Cells. Viruses 2021; 13(2).

150. Artika IM, Dewantari AK, Wiyatno A. Molecular biology of coronaviruses: current knowledge. Heliyon 2020; 6(8):e04743.

151. Lu S, Ye Q, Singh D, Cao Y, Diedrich JK, Yates JR et al. The SARS-CoV-2 nucleocapsid phosphoprotein forms mutually exclusive condensates with RNA and the membrane-associated M protein. Nature Communications 2021; 12(1):502.

152. Boson B, Legros V, Zhou B, Siret E, Mathieu C, Cosset F-L et al. The SARS-CoV-2 envelope and membrane proteins modulate maturation and retention of the spike protein, allowing assembly of virus-like particles. Journal of Biological Chemistry 2021; 296:100111.

153. Mandala VS, McKay MJ, Shcherbakov AA, Dregni AJ, Kolocouris A, Hong M. Structure and drug binding of the SARS-CoV-2 envelope protein transmembrane domain in lipid bilayers. Nat Struct Mol Biol 2020; 27(12):1202–8.

154. Gui M, Liu X, Guo D, Zhang Z, Yin C-C, Chen Y et al. Electron microscopy studies of the coronavirus ribonucleoprotein complex. Protein Cell 2017; 8(3):219–24.

155. Redondo N, Zaldívar-López S, Garrido JJ, Montoya M. SARS-CoV-2 Accessory Proteins in Viral Pathogenesis: Knowns and Unknowns. Front Immunol 2021; 12:708264.

156. Pizzato M, Baraldi C, Boscato Sopetto G, Finozzi D, Gentile C, Gentile MD et al. SARS-CoV-2 and the Host Cell: A Tale of Interactions. Front.Virol. 2022; 1.

157. Zhang J, Ejikemeuwa A, Gerzanich V, Nasr M, Tang Q, Simard JM et al. Understanding the Role of SARS-CoV-2 ORF3a in Viral Pathogenesis and COVID-19. Front Microbiol 2022; 13:854567.

158. Boer SM de, Kortekaas J, Haan CAM de, Rottier PJM, Moormann RJM, Bosch BJ. Heparan sulfate facilitates Rift Valley fever virus entry into the cell. Journal of Virology 2012; 86(24):13767–71.

159. Riblett AM, Blomen VA, Jae LT, Altamura LA, Doms RW, Brummelkamp TR et al. A Haploid Genetic Screen Identifies Heparan Sulfate Proteoglycans Supporting Rift Valley Fever Virus Infection. Journal of Virology 2016; 90(3):1414–23.

160. Pietrantoni A, Fortuna C, Remoli ME, Ciufolini MG, Superti F. Bovine lactoferrin inhibits Toscana virus infection by binding to heparan sulphate. Viruses 2015; 7(2):480–95.

161. Lozach P-Y, Kühbacher A, Meier R, Mancini R, Bitto D, Bouloy M et al. DC-SIGN as a receptor for phleboviruses. Cell Host & Microbe 2011; 10(1):75–88.

162. Hofmann H, Li X, Zhang X, Liu W, Kühl A, Kaup F et al. Severe fever with thrombocytopenia virus glycoproteins are targeted by neutralizing antibodies and can use DC-SIGN as a receptor for pH-dependent entry into human and animal cell lines. Journal of Virology 2013; 87(8):4384–94.

163. Tani H, Shimojima M, Fukushi S, Yoshikawa T, Fukuma A, Taniguchi S et al. Characterization of Glycoprotein-Mediated Entry of Severe Fever with Thrombocytopenia Syndrome Virus. Journal of Virology 2016; 90(11):5292–301.

164. Suzuki T, Sato Y, Sano K, Arashiro T, Katano H, Nakajima N et al. Severe fever with thrombocytopenia syndrome virus targets B cells in lethal human infections. J Clin Invest 2020; 130(2):799–812.

165. Phoenix I, Nishiyama S, Lokugamage N, Hill TE, Huante MB, Slack OAL et al. N-Glycans on the Rift Valley Fever Virus Envelope Glycoproteins Gn and Gc Redundantly Support Viral Infection via DC-SIGN. Viruses 2016; 8(5).

166. Svajger U, Anderluh M, Jeras M, Obermajer N. C-type lectin DC-SIGN: an adhesion, signalling and antigen-uptake molecule that guides dendritic cells in immunity. Cell Signal 2010; 22(10):1397–405.

167. Boukour S, Massé J-M, Bénit L, Dubart-Kupperschmitt A, Cramer EM. Lentivirus degradation and DC-SIGN expression by human platelets and megakaryocytes. J Thromb Haemost 2006; 4(2):426–35.

168. Shimojima M, Sugimoto S, Taniguchi S, Yoshikawa T, Kurosu T, Saijo M. Efficient functional screening of a cellular cDNA library to identify severe fever with thrombocytopenia syndrome virus entry factors. Sci Rep 2020; 10(1):5996.

169. Léger P, Tetard M, Youness B, Cordes N, Rouxel RN, Flamand M et al. Differential Use of the C-Type Lectins L-SIGN and DC-SIGN for Phlebovirus Endocytosis. Traffic 2016; 17(6):639–56.

170. Ganaie SS, Schwarz MM, McMillen CM, Price DA, Feng AX, Albe JR et al. Lrp1 is a host entry factor for Rift Valley fever virus. Cell 2021; 184(20):5163-5178.e24.

171. Devignot S, Sha TW, Burkard TR, Schmerer P, Hagelkruys A, Mirazimi A et al. Low-density lipoprotein receptor-related protein 1 (LRP1) as an auxiliary host factor for RNA viruses. Life Sci Alliance 2023; 6(7).

172. Sun Y, Qi Y, Liu C, Gao W, Chen P, Fu L et al. Nonmuscle myosin heavy chain IIA is a critical factor contributing to the efficiency of early infection of severe fever with thrombocytopenia syndrome virus. Journal of Virology 2014; 88(1):237–48.

173. Liu J, Xu M, Tang B, Hu L, Deng F, Wang H et al. Single-Particle Tracking Reveals the Sequential Entry Process of the Bunyavirus Severe Fever with Thrombocytopenia Syndrome Virus. Small 2019; 15(6):e1803788.

174. Lozach P-Y, Mancini R, Bitto D, Meier R, Oestereich L, Overby AK et al. Entry of bunyaviruses into mammalian cells. Cell Host & Microbe 2010; 7(6):488–99.

175. Harmon B, Schudel BR, Maar D, Kozina C, Ikegami T, Tseng C-TK et al. Rift Valley fever virus strain MP-12 enters mammalian host cells via caveola-mediated endocytosis. Journal of Virology 2012; 86(23):12954–70.

176. Filone CM, Hanna SL, Caino MC, Bambina S, Doms RW, Cherry S. Rift valley fever virus infection of human cells and insect hosts is promoted by protein kinase C epsilon. PLoS One 2010; 5(11):e15483.

177. Hackett BA, Yasunaga A, Panda D, Tartell MA, Hopkins KC, Hensley SE et al. RNASEK is required for internalization of diverse acid-dependent viruses. Proc Natl Acad Sci U S A 2015; 112(25):7797–802.

178. Wichgers Schreur PJ, Kortekaas J. Single-Molecule FISH Reveals Non-selective Packaging of Rift Valley Fever Virus Genome Segments. PLOS Pathogens 2016; 12(8):e1005800.

179. Ke Z, Oton J, Qu K, Cortese M, Zila V, McKeane L et al. Structures and distributions of SARS-CoV-2 spike proteins on intact virions. Nature 2020; 588(7838):498–502.

180. Turoňová B, Sikora M, Schürmann C, Hagen WJH, Welsch S, Blanc FEC et al. In situ structural analysis of SARS-CoV-2 spike reveals flexibility mediated by three hinges. Science 2020; 370(6513):203–8.

181. Klein S, Cortese M, Winter SL, Wachsmuth-Melm M, Neufeldt CJ, Cerikan B et al. SARS-CoV-2 structure and replication characterized by in situ cryo-electron tomography. Nature Communications 2020; 11(1):5885.

182. Shrivastava T, Singh B, Rizvi ZA, Verma R, Goswami S, Vishwakarma P et al. Comparative Immunomodulatory Evaluation of the Receptor Binding Domain of the SARS-CoV-2 Spike Protein; a Potential Vaccine Candidate Which Imparts Potent Humoral and Th1 Type Immune Response in a Mouse Model. Front Immunol 2021; 12:641447.

183. Hoffmann M, Kleine-Weber H, Schroeder S, Krüger N, Herrler T, Erichsen S et al. SARS-CoV-2 Cell Entry Depends on ACE2 and TMPRSS2 and Is Blocked by a Clinically Proven Protease Inhibitor. Cell 2020; 181(2):271-280.e8.

184. Wang L, Xiang Y. Spike Glycoprotein-Mediated Entry of SARS Coronaviruses. Viruses 2020; 12(11).

185. Clausen TM, Sandoval DR, Spliid CB, Pihl J, Perrett HR, Painter CD et al. SARS-CoV-2 Infection Depends on Cellular Heparan Sulfate and ACE2. Cell 2020; 183(4):1043-1057.e15.

186. Zhang Q, Chen CZ, Swaroop M, Xu M, Wang L, Lee J et al. Heparan sulfate assists SARS-CoV-2 in cell entry and can be targeted by approved drugs in vitro. Cell Discov 2020; 6(1):80.

187. Kearns FL, Sandoval DR, Casalino L, Clausen TM, Rosenfeld MA, Spliid CB et al. Spike-heparan sulfate interactions in SARS-CoV-2 infection. Curr Opin Struct Biol 2022; 76:102439.

188. Cantuti-Castelvetri L, Ojha R, Pedro LD, Djannatian M, Franz J, Kuivanen S et al. Neuropilin-1 facilitates SARS-CoV-2 cell entry and infectivity. Science 2020; 370(6518):856–60.

189. Daly JL, Simonetti B, Klein K, Chen K-E, Williamson MK, Antón-Plágaro C et al. Neuropilin-1 is a host factor for SARS-CoV-2 infection. Science 2020; 370(6518):861–5.

190. Mayi BS, Leibowitz JA, Woods AT, Ammon KA, Liu AE, Raja A. The role of Neuropilin-1 in COVID-19. PLOS Pathogens 2021; 17(1):e1009153.

191. Amraei R, Yin W, Napoleon MA, Suder EL, Berrigan J, Zhao Q et al. CD209L/L-SIGN and CD209/DC-SIGN Act as Receptors for SARS-CoV-2. ACS Cent Sci 2021; 7(7):1156–65.

192. Yang C, Zhang Y, Zeng X, Chen H, Chen Y, Yang D et al. Kidney injury molecule-1 is a potential receptor for SARS-CoV-2. J Mol Cell Biol 2021; 13(3):185–96.

193. Mori Y, Fink C, Ichimura T, Sako K, Mori M, Lee NN et al. KIM-1/TIM-1 is a Receptor for SARS-CoV-2 in Lung and Kidney. medRxiv 2022.

194. Wang S, Qiu Z, Hou Y, Deng X, Xu W, Zheng T et al. AXL is a candidate receptor for SARS-CoV-2 that promotes infection of pulmonary and bronchial epithelial cells. Cell Res 2021; 31(2):126–40.

195. Wang K, Chen W, Zhang Z, Deng Y, Lian J-Q, Du P et al. CD147-spike protein is a novel route for SARS-CoV-2 infection to host cells. Signal Transduct Target Ther 2020; 5(1):283.

196. Gu Y, Cao J, Zhang X, Gao H, Wang Y, Wang J et al. Receptome profiling identifies KREMEN1 and ASGR1 as alternative functional receptors of SARS-CoV-2. Cell Res 2022; 32(1):24–37.

197. Chu VC, McElroy LJ, Chu V, Bauman BE, Whittaker GR. The avian coronavirus infectious bronchitis virus undergoes direct low-pH-dependent fusion activation during entry into host cells. Journal of Virology 2006; 80(7):3180–8.

198. Tang T, Bidon M, Jaimes JA, Whittaker GR, Daniel S. Coronavirus membrane fusion mechanism offers a potential target for antiviral development. Antiviral Res 2020; 178:104792.

199. Belouzard S, Chu VC, Whittaker GR. Activation of the SARS coronavirus spike protein via sequential proteolytic cleavage at two distinct sites. Proc Natl Acad Sci U S A 2009; 106(14):5871–6.

200. Bugge TH, Antalis TM, Wu Q. Type II transmembrane serine proteases. Journal of Biological Chemistry 2009; 284(35):23177–81.

201. Donaldson SH, Hirsh A, Li DC, Holloway G, Chao J, Boucher RC et al. Regulation of the epithelial sodium channel by serine proteases in human airways. Journal of Biological Chemistry 2002; 277(10):8338–45.

202. Wilson S, Greer B, Hooper J, Zijlstra A, Walker B, Quigley J et al. The membrane-anchored serine protease, TMPRSS2, activates PAR-2 in prostate cancer cells. Biochem J 2005; 388(Pt 3):967–72.

203. Glowacka I, Bertram S, Müller MA, Allen P, Soilleux E, Pfefferle S et al. Evidence that TMPRSS2 activates the severe acute respiratory syndrome coronavirus spike protein for membrane fusion and reduces viral control by the humoral immune response. Journal of Virology 2011; 85(9):4122–34.

204. Millet JK, Whittaker GR. Host cell entry of Middle East respiratory syndrome coronavirus after two-step, furin-mediated activation of the spike protein. Proc Natl Acad Sci U S A 2014; 111(42):15214–9.

205. Bestle D, Heindl MR, Limburg H, van Lam van T, Pilgram O, Moulton H et al. TMPRSS2 and furin are both essential for proteolytic activation of SARS-CoV-2 in human airway cells. Life Sci Alliance 2020; 3(9).

206. Reinke LM, Spiegel M, Plegge T, Hartleib A, Nehlmeier I, Gierer S et al. Different residues in the SARS-CoV spike protein determine cleavage and activation by the host cell protease TMPRSS2. PLoS One 2017; 12(6):e0179177.

207. Yadati T, Houben T, Bitorina A, Shiri-Sverdlov R. The Ins and Outs of Cathepsins: Physiological Function and Role in Disease Management. Cells 2020; 9(7).

208. Bosch BJ, Bartelink W, Rottier PJM. Cathepsin L functionally cleaves the severe acute respiratory syndrome coronavirus class I fusion protein upstream of rather than adjacent to the fusion peptide. Journal of Virology 2008; 82(17):8887–90.

209. Kleine-Weber H, Elzayat MT, Hoffmann M, Pöhlmann S. Functional analysis of potential cleavage sites in the MERS-coronavirus spike protein. Sci Rep 2018; 8(1):16597.

210. Bollavaram K, Leeman TH, Lee MW, Kulkarni A, Upshaw SG, Yang J et al. Multiple sites on SARS-CoV-2 spike protein are susceptible to proteolysis by cathepsins B, K, L, S, and V. Protein Sci 2021; 30(6):1131–43.

211. Song W, Gui M, Wang X, Xiang Y. Cryo-EM structure of the SARS coronavirus spike glycoprotein in complex with its host cell receptor ACE2. PLOS Pathogens 2018; 14(8):e1007236.

212. Zhang J, Cai Y, Xiao T, Lu J, Peng H, Sterling SM et al. Structural impact on SARS-CoV-2 spike protein by D614G substitution. Science 2021; 372(6541):525–30.

213. Zhang L, Jackson CB, Mou H, Ojha A, Peng H, Quinlan BD et al. SARS-CoV-2 spike-protein D614G mutation increases virion spike density and infectivity. Nature Communications 2020; 11(1):6013.

214. Gobeil SM-C, Janowska K, McDowell S, Mansouri K, Parks R, Manne K et al. D614G Mutation Alters SARS-CoV-2 Spike Conformation and Enhances Protease Cleavage at the S1/S2 Junction. Cell Rep 2021; 34(2):108630.

215. Yurkovetskiy L, Wang X, Pascal KE, Tomkins-Tinch C, Nyalile TP, Wang Y et al. Structural and Functional Analysis of the D614G SARS-CoV-2 Spike Protein Variant. Cell 2020; 183(3):739-751.e8.

216. Benton DJ, Wrobel AG, Roustan C, Borg A, Xu P, Martin SR et al. The effect of the D614G substitution on the structure of the spike glycoprotein of SARS-CoV-2. Proc Natl Acad Sci U S A 2021; 118(9).

217. Saville JW, Berezuk AM, Srivastava SS, Subramaniam S. Three-Dimensional Visualization of Viral Structure, Entry, and Replication Underlying the Spread of SARS-CoV-2. Chem Rev 2022; 122(17):14066–84.

218. Liu H, Zhang Q, Wei P, Chen Z, Aviszus K, Yang J et al. The basis of a more contagious 501Y.V1 variant of SARS-CoV-2. Cell Res 2021; 31(6):720–2.

219. Tian F, Tong B, Sun L, Shi S, Zheng B, Wang Z et al. N501Y mutation of spike protein in SARS-CoV-2 strengthens its binding to receptor ACE2. Elife 2021; 10.

220. Carabelli AM, Peacock TP, Thorne LG, Harvey WT, Hughes J, Peacock SJ et al. SARS-CoV-2 variant biology: immune escape, transmission and fitness. Nature Reviews Microbiology 2023; 21(3):162–77.

221. V'kovski P, Kratzel A, Steiner S, Stalder H, Thiel V. Coronavirus biology and replication: implications for SARS-CoV-2. Nature Reviews Microbiology 2021; 19(3):155–70.

222. Giard DJ, Aaronson SA, Todaro GJ, Arnstein P, Kersey JH, Dosik H et al. In vitro cultivation of human tumors: establishment of cell lines derived from a series of solid tumors. J Natl Cancer Inst 1973; 51(5):1417–23.

223. Steuten K, Kim H, Widen JC, Babin BM, Onguka O, Lovell S et al. Challenges for Targeting SARS-CoV-2 Proteases as a Therapeutic Strategy for COVID-19. ACS Infect Dis 2021; 7(6):1457–68.

224. MACPHERSON I, STOKER M. Polyoma transformation of hamster cell clones--an investigation of genetic factors affecting cell competence. Virology 1962; 16:147–51.

225. Fogh J, Trempe G. New Human Tumor Cell Lines. In: Fogh J, Fogh J, editors. Human tumor cells in vitro. 1st ed. 1975. New York: Springer Science+Business Media, LLC; 1975. p. 115–59.

226. Fogh J, Wright WC, Loveless JD. Absence of HeLa cell contamination in 169 cell lines derived from human tumors. J Natl Cancer Inst 1977; 58(2):209–14.

227. Fogh J, Fogh JM, Orfeo T. One hundred and twenty-seven cultured human tumor cell lines producing tumors in nude mice. J Natl Cancer Inst 1977; 59(1):221–6.

228. Graham FL, Smiley J, Russell WC, Nairn R. Characteristics of a human cell line transformed by DNA from human adenovirus type 5. J Gen Virol 1977; 36(1):59–74.

229. Himly M, Foster DN, Bottoli I, Iacovoni JS, Vogt PK. The DF-1 chicken fibroblast cell line: transformation induced by diverse oncogenes and cell death resulting from infection by avian leukosis viruses. Virology 1998; 248(2):295–304.

230. SCHERER WF, SYVERTON JT, GEY GO. Studies on the propagation in vitro of poliomyelitis viruses. IV. Viral multiplication in a stable strain of human malignant epithelial cells (strain HeLa) derived from an epidermoid carcinoma of the cervix. J Exp Med 1953; 97(5):695–710.

231. Nakabayashi H, Taketa K, Miyano K, Yamane T, Sato J. Growth of human hepatoma cells lines with differentiated functions in chemically defined medium. Cancer Res 1982; 42(9):3858–63.

232. Zhang Y, Pak C, Han Y, Ahlenius H, Zhang Z, Chanda S et al. Rapid single-step induction of functional neurons from human pluripotent stem cells. Neuron 2013; 78(5):785–98.

233. Schneider U, Schwenk HU, Bornkamm G. Characterization of EBV-genome negative "null" and "T" cell lines derived from children with acute lymphoblastic leukemia and leukemic transformed non-Hodgkin lymphoma. Int J Cancer 1977; 19(5):621–6.

234. Earl WR. Production of Malignancy in Vitro. IV. The Mouse Fibroblast Cultures and Changes Seen in the Living Cells. JNCI: Journal of the National Cancer Institute 1943.

235. Sanford KK, Earle WR, Likely GD. The Growth in Vitro of Single Isolated Tissue Cells. J Natl Cancer Inst 1948; 9(3):229–46.

236. Bell-Sakyi L, Darby A, Baylis M, Makepeace BL. The Tick Cell Biobank: A global resource for in vitro research on ticks, other arthropods and the pathogens they transmit. Ticks Tick Borne Dis 2018; 9(5):1364–71.

237. Bell-Sakyi L, Beliavskaia A, Hartley CS, Jones L, Luu L, Haines LR et al. Isolation in Natural Host Cell Lines of Wolbachia Strains wPip from the Mosquito Culex pipiens and wPap from the Sand Fly Phlebotomus papatasi. Insects 2021; 12(10).

238. GREEN IJ. Serial propagation of influenza B (Lee) virus in a transmissible line of canine kidney cells. Science 1962; 138(3536):42–3.

239. Gaush CR, Hard WL, Smith TF. Characterization of an established line of canine kidney cells (MDCK). Proc Soc Exp Biol Med 1966; 122(3):931–5.

240. PULVERTAFT JV. CYTOLOGY OF BURKITT'S TUMOUR (AFRICAN LYMPHOMA). Lancet 1964; 1(7327):238–40.

241. Smith SD, Morgan R, Link MP, McFall P, Hecht F. Cytogenetic and immunophenotypic analysis of cell lines established from patients with T cell leukemia/lymphoma. Blood 1986; 67(3):650–6.

242. Means RE, Matthews T, Hoxie JA, Malim MH, Kodama T, Desrosiers RC. Ability of the V3 loop of simian immunodeficiency virus to serve as a target for antibody-mediated neutralization: correlation of neutralization sensitivity, growth in macrophages, and decreased dependence on CD4. Journal of Virology 2001; 75(8):3903–15.

243. Biedler JL, Helson L, Spengler BA. Morphology and growth, tumorigenicity, and cytogenetics of human neuroblastoma cells in continuous culture. Cancer Res 1973; 33(11):2643–52.

244. Ross RA, Spengler BA, Biedler JL. Coordinate morphological and biochemical interconversion of human neuroblastoma cells. J Natl Cancer Inst 1983; 71(4):741–7.

245. Tsuchiya S, Yamabe M, Yamaguchi Y, Kobayashi Y, Konno T, Tada K. Establishment and characterization of a human acute monocytic leukemia cell line (THP-1). Int J Cancer 1980; 26(2):171–6.

246. Pontén J, Macintyre EH. Long term culture of normal and neoplastic human glia. Acta Pathol Microbiol Scand 1968; 74(4):465–86.

247. Björndal A, Deng H, Jansson M, Fiore JR, Colognesi C, Karlsson A et al. Coreceptor usage of primary human immunodeficiency virus type 1 isolates varies according to biological phenotype. Journal of Virology 1997; 71(10):7478–87.

248. Price PJ, Gregory EA. Relationship between in vitro growth promotion and biophysical and biochemical properties of the serum supplement. In Vitro 1982; 18(6):576–84.

249. Earley, E., K. M. Johnson. The lineage of the Vero, Vero 76 and its clone C1008 in the United States; 1988. Available from: URL: https://scholar.google.com/citations?user=3r5tj20aaaaj&hl=de&oi=sra.

250. Windhaber S, Xin Q, Uckeley ZM, Koch J, Obr M, Garnier C et al. The Orthobunyavirus Germiston Enters Host Cells from Late Endosomes. Journal of Virology 2022; 96(5):e0214621.

251. Francis T. TRANSMISSION OF INFLUENZA BY A FILTERABLE VIRUS. Science 1934; 80(2081):457–9.

252. Francis T, Magill TP. IMMUNOLOGICAL STUDIES WITH THE VIRUS OF INFLUENZA. J Exp Med 1935; 62(4):505–16.

253. Billecocq A, Gauliard N, Le May N, Elliott RM, Flick R, Bouloy M. RNA polymerase I-mediated expression of viral RNA for the rescue of infectious virulent and avirulent Rift Valley fever viruses. Virology 2008; 378(2):377–84.

254. Krähling V, Halwe S, Rohde C, Becker D, Berghöfer S, Dahlke C et al. Development and characterization of an indirect ELISA to detect SARS-CoV-2 spike protein-specific antibodies. J Immunol Methods 2021; 490:112958.

255. Benning L, Morath C, Bartenschlager M, Reineke M, Töllner M, Nusshag C et al. Neutralizing antibody activity against the B.1.617.2 (delta) variant 8 months after two-dose vaccination with BNT162b2 in health care workers. Clin Microbiol Infect 2022; 28(7):1024.e7-1024.e12.

256. Helenius A, Kartenbeck J, Simons K, Fries E. On the entry of Semliki forest virus into BHK-21 cells. Journal of Cell Biology 1980; 84(2):404–20.

257. Giorgi C, Accardi L, Nicoletti L, Gro MC, Takehara K, Hilditch C et al. Sequences and coding strategies of the S RNAs of Toscana and Rift Valley fever viruses compared to those of Punta Toro, Sicilian Sandfly fever, and Uukuniemi viruses. Virology 1991; 180(2):738–53.

258. Woelfl F, Léger P, Oreshkova N, Pahmeier F, Windhaber S, Koch J et al. Novel Toscana Virus Reverse Genetics System Establishes NSs as an Antagonist of Type I Interferon Responses. Viruses 2020; 12(4):400.

259. Pettersson R, Kääriäinen L, Bonsdorff CH von, Oker-Blom N. Structural components of Uukuniemi virus, a noncubical tick-borne arbovirus. Virology 1971; 46(3):721–9.

260. Mazelier M, Rouxel RN, Zumstein M, Mancini R, Bell-Sakyi L, Lozach P-Y. Uukuniemi Virus as a Tick-Borne Virus Model. Journal of Virology 2016; 90(15):6784–98.

261. Kielian M, Jungerwirth S, Sayad KU, DeCandido S. Biosynthesis, maturation, and acid activation of the Semliki Forest virus fusion protein. Journal of Virology 1990; 64(10):4614–24.

262. Persson R, Pettersson RF. Formation and intracellular transport of a heterodimeric viral spike protein complex. Journal of Cell Biology 1991; 112(2):257–66.

263. Patzke C, Brockmann MM, Dai J, Gan KJ, Grauel MK, Fenske P et al. Neuromodulator Signaling Bidirectionally Controls Vesicle Numbers in Human Synapses. Cell 2019; 179(2):498-513.e22.

264. Koch J, Uckeley ZM, Doldan P, Stanifer M, Boulant S, Lozach P-Y. TMPRSS2 expression dictates the entry route used by SARS-CoV-2 to infect host cells. The EMBO Journal 2021; 40(16):e107821.

265. Martínez-Sobrido L, García-Sastre A. Generation of recombinant influenza virus from plasmid DNA. J Vis Exp 2010; (42).

266. Hierholzer JC, Killington RA. Virus isolation and quantitation. In: Virology Methods Manual. Elsevier; 1996. p. 25–46.

267. Hoffmann AB, Mazelier M, Léger P, Lozach P-Y. Deciphering Virus Entry with Fluorescently Labeled Viral Particles: Springer New York. Methods Mol Biol; 2018. (Methods in Molecular Biology; vol 1836).

268. Kummer S, Avinoam O, Kräusslich H-G. IFITM3 Clusters on Virus Containing Endosomes and Lysosomes Early in the Influenza A Infection of Human Airway Epithelial Cells. Viruses 2019; 11(6).

269. Koch J, Xin Q, Obr M, Schäfer A, Rolfs N, Anagho H et al. The phenuivirus Toscana virus makes an atypical use of vacuolar acidity to enter host cells; 2023.

270. Navarro-Marí JM, Palop-Borrás B, Pérez-Ruiz M, Sanbonmatsu-Gámez S. Serosurvey study of Toscana virus in domestic animals, Granada, Spain. Vector Borne Zoonotic Dis 2011; 11(5):583–7.

271. Alwassouf S, Christodoulou V, Bichaud L, Ntais P, Mazeris A, Antoniou M et al. Seroprevalence of Sandfly-Borne Phleboviruses Belonging to Three Serocomplexes (Sandfly fever Naples, Sandfly fever Sicilian and Salehabad) in Dogs from Greece and Cyprus Using Neutralization Test. PLOS Neglected Tropical Diseases 2016; 10(10):e0005063.

272. Alwassouf S, Maia C, Ayhan N, Coimbra M, Cristovao JM, Richet H et al. Neutralization-based seroprevalence of Toscana virus and sandfly fever Sicilian virus in dogs and cats from Portugal. Journal of General Virology 2016; 97(11):2816–23.

273. Lelli D, Scanferla V, Moreno A, Sozzi E, Ravaioli V, Renzi M et al. Serological Evidence of Phleboviruses in Domestic Animals on the Pre-Apennine Hills (Northern Italy). Viruses 2021; 13(8).

274. Ayhan N, Sherifi K, Taraku A, Bërxholi K, Charrel RN. High Rates of Neutralizing Antibodies to Toscana and Sandfly Fever Sicilian Viruses in Livestock, Kosovo. Emerging Infectious Diseases 2017; 23(6):989–92.

275. Stenmark H, Parton RG, Steele-Mortimer O, Lütcke A, Gruenberg J, Zerial M. Inhibition of rab5 GTPase activity stimulates membrane fusion in endocytosis. The EMBO Journal 1994; 13(6):1287–96.

276. Zhang M, Chen L, Wang S, Wang T. Rab7: roles in membrane trafficking and disease. Biosci Rep 2009; 29(3):193–209.

277. Ohkuma S, Poole B. Fluorescence probe measurement of the intralysosomal pH in living cells and the perturbation of pH by various agents. Proc Natl Acad Sci U S A 1978; 75(7):3327–31.

278. Winckler B, Faundez V, Maday S, Cai Q, Guimas Almeida C, Zhang H. The Endolysosomal System and Proteostasis: From Development to Degeneration. J Neurosci 2018; 38(44):9364–74.

279. Marsh M, Bolzau E, Helenius A. Penetration of Semliki Forest virus from acidic prelysosomal vacuoles. Cell 1983; 32(3):931–40.

280. Düzgüneş N, Pedroso de Lima MC, Stamatatos L, Flasher D, Alford D, Friend DS et al. Fusion activity and inactivation of influenza virus: kinetics of low pH-induced fusion with cultured cells. J Gen Virol 1992; 73 (Pt 1):27–37.

281. Monteiro JT, Lepenies B. Myeloid C-Type Lectin Receptors in Viral Recognition and Antiviral Immunity. Viruses 2017; 9(3).

282. Chen Y-W, Lee M-S, Lucht A, Chou F-P, Huang W, Havighurst TC et al. TMPRSS2, a serine protease expressed in the prostate on the apical surface of luminal epithelial cells and released into semen in prostasomes, is misregulated in prostate cancer cells. Am J Pathol 2010; 176(6):2986–96.

283. Matsuyama S, Ujike M, Morikawa S, Tashiro M, Taguchi F. Protease-mediated enhancement of severe acute respiratory syndrome coronavirus infection. Proc Natl Acad Sci U S A 2005; 102(35):12543–7.

284. Schornberg K, Matsuyama S, Kabsch K, Delos S, Bouton A, White J. Role of endosomal cathepsins in entry mediated by the Ebola virus glycoprotein. Journal of Virology 2006; 80(8):4174–8.

285. Heurich A, Hofmann-Winkler H, Gierer S, Liepold T, Jahn O, Pöhlmann S. TMPRSS2 and ADAM17 cleave ACE2 differentially and only proteolysis by TMPRSS2 augments entry driven by the severe acute respiratory syndrome coronavirus spike protein. Journal of Virology 2014; 88(2):1293–307.

286. Bermúdez-Méndez E, Bronsvoort KF, Zwart MP, van de Water S, Cárdenas-Rey I, Vloet RPM et al. Incomplete bunyavirus particles can cooperatively support virus infection and spread. PLoS Biol 2022; 20(11):e3001870.

287. Cusi MG, Gori Savellini G, Terrosi C, Di Genova G, Valassina M, Valentini M et al. Development of a mouse model for the study of Toscana virus pathogenesis. Virology 2005; 333(1):66–73.

288. Schneider SM, Lee BH, Nicola AV. Viral entry and the ubiquitin-proteasome system. Cell Microbiol 2021; 23(2):e13276.

289. Pandey UB, Nie Z, Batlevi Y, McCray BA, Ritson GP, Nedelsky NB et al. HDAC6 rescues neurodegeneration and provides an essential link between autophagy and the UPS. Nature 2007; 447(7146):859–63.

290. Tsubuki S, Saito Y, Tomioka M, Ito H, Kawashima S. Differential inhibition of calpain and proteasome activities by peptidyl aldehydes of di-leucine and tri-leucine. J Biochem 1996; 119(3):572–6.

291. Khor R, McElroy LJ, Whittaker GR. The ubiquitin-vacuolar protein sorting system is selectively required during entry of influenza virus into host cells. Traffic 2003; 4(12):857–68.

292. Garrison AR, Radoshitzky SR, Kota KP, Pegoraro G, Ruthel G, Kuhn JH et al. Crimean-Congo hemorrhagic fever virus utilizes a clathrin- and early endosome-dependent entry pathway. Virology 2013; 444(1-2):45–54.

293. Pobjecky N, Smith J, Gonzalez-Scarano F. Biological studies of the fusion function of California serogroup Bunyaviruses. Microb Pathog 1986; 1(5):491–501.

294. Hacker JK, Hardy JL. Adsorptive endocytosis of California encephalitis virus into mosquito and mammalian cells: a role for G1. Virology 1997; 235(1):40–7.

295. Cifuentes-Muñoz N, Barriga GP, Valenzuela PDT, Tischler ND. Aromatic and polar residues spanning the candidate fusion peptide of the Andes virus Gc protein are essential for membrane fusion and infection. Journal of General Virology 2011; 92(Pt 3):552–63.

296. Bignon EA, Albornoz A, Guardado-Calvo P, Rey FA, Tischler ND. Molecular organization and dynamics of the fusion protein Gc at the hantavirus surface. Elife 2019; 8.

297. Arikawa J, Takashima I, Hashimoto N. Cell fusion by haemorrhagic fever with renal syndrome (HFRS) viruses and its application for titration of virus infectivity and neutralizing antibody. Archives of Virology 1985; 86(3-4):303–13.

298. Uckeley ZM, Koch J, Tischler ND, Léger P, Lozach P-Y. Entrée cellulaire des phlébovirus chez l'hôte mammifère. Virologie (Montrouge) 2019; 23(3):176–87.

299. Guardado-Calvo P, Bignon EA, Stettner E, Jeffers SA, Pérez-Vargas J, Pehau-Arnaudet G et al. Mechanistic Insight into Bunyavirus-Induced Membrane Fusion from Structure-Function Analyses of the Hantavirus Envelope Glycoprotein Gc. PLOS Pathogens 2016; 12(10):e1005813.

300. Chao LH, Klein DE, Schmidt AG, Peña JM, Harrison SC. Sequential conformational rearrangements in flavivirus membrane fusion. Elife 2014; 3:e04389.

301. Rawle RJ, Webster ER, Jelen M, Kasson PM, Boxer SG. pH Dependence of Zika Membrane Fusion Kinetics Reveals an Off-Pathway State. ACS Cent Sci 2018; 4(11):1503–10.

302. Liu KN, Boxer SG. Single-virus content-mixing assay reveals cholesterol-enhanced influenza membrane fusion efficiency. Biophys J 2021; 120(21):4832–41.

303. Smit JM, Bittman R, Wilschut J. Low-pH-dependent fusion of Sindbis virus with receptor-free cholesterol- and sphingolipid-containing liposomes. Journal of Virology 1999; 73(10):8476–84.

304. Xia T, Wu X, Hong E, Jung K, Lai C-J, Kwak M-J et al. Glucosylceramide is essential for Heartland and Dabie bandavirus glycoprotein-induced membrane fusion. PLOS Pathogens 2023; 19(3):e1011232.

305. Uckeley ZM, Mazelier M, Lüchtenborg C, Winter SL, Schad P, Chlanda P et al. The glycolipid GlcCer is recruited into the viral envelope to promote phenuivirus binding to host cells; 2022.

306. Hover S, King B, Hall B, Loundras E-A, Taqi H, Daly J et al. Modulation of Potassium Channels Inhibits Bunyavirus Infection. J Biol Chem 2016; 291(7):3411–22.

307. Hover S, Foster B, Fontana J, Kohl A, Goldstein SAN, Barr JN et al. Bunyavirus requirement for endosomal K+ reveals new roles of cellular ion channels during infection. PLOS Pathogens 2018; 14(1):e1006845.

308. Sandler ZJ, Firpo MR, Omoba OS, Vu MN, Menachery VD, Mounce BC. Novel Ionophores Active against La Crosse Virus Identified through Rapid Antiviral Screening. Antimicrobial Agents and Chemotherapy 2020; 64(6).

309. Stauffer S, Feng Y, Nebioglu F, Heilig R, Picotti P, Helenius A. Stepwise priming by acidic pH and a high K+ concentration is required for efficient uncoating of influenza A virus cores after penetration. Journal of Virology 2014; 88(22):13029–46.

310. White J, Kartenbeck J, Helenius A. Membrane fusion activity of influenza virus. The EMBO Journal 1982; 1(2):217–22.

311. Sato SB, Kawasaki K, Ohnishi S. Hemolytic activity of influenza virus hemagglutinin glycoproteins activated in mildly acidic environments. Proc Natl Acad Sci U S A 1983; 80(11):3153–7.

312. Carr CM, Kim PS. A spring-loaded mechanism for the conformational change of influenza hemagglutinin. Cell 1993; 73(4):823–32.

313. Gollins SW, Porterfield JS. The uncoating and infectivity of the flavivirus West Nile on interaction with cells: effects of pH and ammonium chloride. J Gen Virol 1986; 67 (Pt 9):1941–50.

314. Fries E, Helenius A. Binding of Semliki Forest virus and its spike glycoproteins to cells. Eur J Biochem 1979; 97(1):213–20.

315. Wahlberg JM, Bron R, Wilschut J, Garoff H. Membrane fusion of Semliki Forest virus involves homotrimers of the fusion protein. Journal of Virology 1992; 66(12):7309–18.

316. Bron R, Wahlberg JM, Garoff H, Wilschut J. Membrane fusion of Semliki Forest virus in a model system: correlation between fusion kinetics and structural changes in the envelope glycoprotein. The EMBO Journal 1993; 12(2):693–701.

317. Waarts B-L, Smit JM, Aneke OJC, McInerney GM, Liljeström P, Bittman R et al. Reversible acid-induced inactivation of the membrane fusion protein of Semliki Forest virus. Journal of Virology 2005; 79(12):7942–8.

318. Stiasny K, Allison SL, Schalich J, Heinz FX. Membrane interactions of the tick-borne encephalitis virus fusion protein E at low pH. Journal of Virology 2002; 76(8):3784–90.

319. Costanzi E, Kuzikov M, Esposito F, Albani S, Demitri N, Giabbai B et al. Structural and Biochemical Analysis of the Dual Inhibition of MG-132 against SARS-CoV-2 Main Protease (Mpro/3CLpro) and Human Cathepsin-L. Int J Mol Sci 2021; 22(21).

320. Liu T, Luo S, Libby P, Shi G-P. Cathepsin L-selective inhibitors: A potentially promising treatment for COVID-19 patients. Pharmacol Ther 2020; 213:107587.

321. Matsuyama S, Nao N, Shirato K, Kawase M, Saito S, Takayama I et al. Enhanced isolation of SARS-CoV-2 by TMPRSS2-expressing cells. Proc Natl Acad Sci U S A 2020; 117(13):7001–3.

322. Shang J, Wan Y, Luo C, Ye G, Geng Q, Auerbach A et al. Cell entry mechanisms of SARS-CoV-2. Proc Natl Acad Sci U S A 2020; 117(21):11727–34.

323. Ou T, Mou H, Zhang L, Ojha A, Choe H, Farzan M. Hydroxychloroquine-mediated inhibition of SARS-CoV-2 entry is attenuated by TMPRSS2. PLOS Pathogens 2021; 17(1):e1009212.

324. Peacock TP, Goldhill DH, Zhou J, Baillon L, Frise R, Swann OC et al. The furin cleavage site in the SARS-CoV-2 spike protein is required for transmission in ferrets. Nat Microbiol 2021; 6(7):899–909.

325. Shirato K, Kanou K, Kawase M, Matsuyama S. Clinical Isolates of Human Coronavirus 229E Bypass the Endosome for Cell Entry. Journal of Virology 2017; 91(1).

326. Shirato K, Kawase M, Matsuyama S. Wild-type human coronaviruses prefer cell-surface TMPRSS2 to endosomal cathepsins for cell entry. Virology 2018; 517:9–15.

327. Zhou Y, Vedantham P, Lu K, Agudelo J, Carrion R, Nunneley JW et al. Protease inhibitors targeting coronavirus and filovirus entry. Antiviral Res 2015; 116:76–84.

328. Wang M, Cao R, Zhang L, Yang X, Liu J, Xu M et al. Remdesivir and chloroquine effectively inhibit the recently emerged novel coronavirus (2019-nCoV) in vitro. Cell Res 2020; 30(3):269–71.

329. Kreutzberger AJB, Sanyal A, Saminathan A, Bloyet L-M, Stumpf S, Liu Z et al. SARS-CoV-2 requires acidic pH to infect cells. Proc Natl Acad Sci U S A 2022; 119(38):e2209514119.

330. Willett BJ, Grove J, MacLean OA, Wilkie C, Lorenzo G de, Furnon W et al. SARS-CoV-2 Omicron is an immune escape variant with an altered cell entry pathway. Nat Microbiol 2022; 7(8):1161–79. Available from: URL: https://www.nature.com/articles/s41564-022-01143-7.

331. Hu B, Chan JF-W, Liu H, Liu Y, Chai Y, Shi J et al. Spike mutations contributing to the altered entry preference of SARS-CoV-2 omicron BA.1 and BA.2. Emerg Microbes Infect 2022; 11(1):2275–87.

332. Meng B, Abdullahi A, Ferreira IATM, Goonawardane N, Saito A, Kimura I et al. Altered TMPRSS2 usage by SARS-CoV-2 Omicron impacts infectivity and fusogenicity. Nature 2022; 603(7902):706–14.

333. Qu P, Evans JP, Kurhade C, Zeng C, Zheng Y-M, Xu K et al. Determinants and Mechanisms of the Low Fusogenicity and High Dependence on Endosomal Entry of Omicron Subvariants. mBio 2023; 14(1):e0317622.

334. Winstone H, Lista MJ, Reid AC, Bouton C, Pickering S, Galao RP et al. The Polybasic Cleavage Site in SARS-CoV-2 Spike Modulates Viral Sensitivity to Type I Interferon and IFITM2. Journal of Virology 2021; 95(9).

335. Pfaender S, Mar KB, Michailidis E, Kratzel A, Boys IN, V'kovski P et al. LY6E impairs coronavirus fusion and confers immune control of viral disease. Nat Microbiol 2020; 5(11):1330–9.

336. Peacock TP, Brown JC, Zhou J, Thakur N, Sukhova K, Newman J et al. The altered entry pathway and antigenic distance of the SARS-CoV-2 Omicron variant map to separate domains of spike protein; 2022.

337. Ortiz ME, Thurman A, Pezzulo AA, Leidinger MR, Klesney-Tait JA, Karp PH et al. Heterogeneous expression of the SARS-Coronavirus-2 receptor ACE2 in the human respiratory tract. EBioMedicine 2020; 60:102976.

338. Chan YA, Zhan SH. The Emergence of the Spike Furin Cleavage Site in SARS-CoV-2. Mol Biol Evol 2022; 39(1).

339. Wu Y, Zhao S. Furin cleavage sites naturally occur in coronaviruses. Stem Cell Res 2020; 50:102115.

340. Walls AC, Park Y-J, Tortorici MA, Wall A, McGuire AT, Veesler D. Structure, Function, and Antigenicity of the SARS-CoV-2 Spike Glycoprotein. Cell 2020; 181(2):281-292.e6.

341. Wrobel AG, Benton DJ, Xu P, Roustan C, Martin SR, Rosenthal PB et al. SARS-CoV-2 and bat RaTG13 spike glycoprotein structures inform on virus evolution and furin-cleavage effects. Nat Struct Mol Biol 2020; 27(8):763–7.

342. Cheng Y-W, Chao T-L, Li C-L, Chiu M-F, Kao H-C, Wang S-H et al. Furin Inhibitors Block SARS-CoV-2 Spike Protein Cleavage to Suppress Virus Production and Cytopathic Effects. Cell Rep 2020; 33(2):108254.

343. Papa G, Mallery DL, Albecka A, Welch LG, Cattin-Ortolá J, Luptak J et al. Furin cleavage of SARS-CoV-2 Spike promotes but is not essential for infection and cell-cell fusion. PLOS Pathogens 2021; 17(1):e1009246.

344. Zhu Y, Feng F, Hu G, Wang Y, Yu Y, Zhu Y et al. A genome-wide CRISPR screen identifies host factors that regulate SARS-CoV-2 entry. Nature Communications 2021; 12(1):961.

345. Sasaki M, Uemura K, Sato A, Toba S, Sanaki T, Maenaka K et al. SARS-CoV-2 variants with mutations at the S1/S2 cleavage site are generated in vitro during propagation in TMPRSS2-deficient cells. PLOS Pathogens 2021; 17(1):e1009233.

346. Jackson CB, Farzan M, Chen B, Choe H. Mechanisms of SARS-CoV-2 entry into cells. Nat Rev Mol Cell Biol 2022; 23(1):3–20.

347. Mlcochova P, Kemp SA, Dhar MS, Papa G, Meng B, Ferreira IATM et al. SARS-CoV-2 B.1.617.2 Delta variant replication and immune evasion. Nature 2021; 599(7883):114–9.

348. Rajah MM, Hubert M, Bishop E, Saunders N, Robinot R, Grzelak L et al. SARS-CoV-2 Alpha, Beta, and Delta variants display enhanced Spike-mediated syncytia formation. The EMBO Journal 2021; 40(24):e108944.

349. Jaimes JA, Millet JK, Whittaker GR. Proteolytic Cleavage of the SARS-CoV-2 Spike Protein and the Role of the Novel S1/S2 Site. iScience 2020; 23(6):101212.

350. Strobelt R, Broennimann K, Adler J, Shaul Y. SARS-CoV-2 Omicron Specific Mutations Affecting Infectivity, Fusogenicity, and Partial TMPRSS2-Independency. Viruses 2023; 15(5):1129.

351. Biniossek ML, Nägler DK, Becker-Pauly C, Schilling O. Proteomic identification of protease cleavage sites characterizes prime and non-prime specificity of cysteine cathepsins B, L, and S. J Proteome Res 2011; 10(12):5363–73.

352. Zhao M-M, Zhu Y, Zhang L, Zhong G, Tai L, Liu S et al. Novel cleavage sites identified in SARS-CoV-2 spike protein reveal mechanism for cathepsin L-facilitated viral infection and treatment strategies. Cell Discov 2022; 8(1):53.

353. Kishimoto M, Uemura K, Sanaki T, Sato A, Hall WW, Kariwa H et al. TMPRSS11D and TMPRSS13 Activate the SARS-CoV-2 Spike Protein. Viruses 2021; 13(3).

354. Chan JF-W, Huang X, Hu B, Chai Y, Shi H, Zhu T et al. Altered host protease determinants for SARS-CoV-2 Omicron. Sci Adv 2023; 9(3):eadd3867.

355. Zang R, Gomez Castro MF, McCune BT, Zeng Q, Rothlauf PW, Sonnek NM et al. TMPRSS2 and TMPRSS4 promote SARS-CoV-2 infection of human small intestinal enterocytes. Sci Immunol 2020; 5(47).

356. Stevaert A, van Berwaer R, Mestdagh C, Vandeput J, Vanstreels E, Raeymaekers V et al. Impact of SARS-CoV-2 Spike Mutations on Its Activation by TMPRSS2 and the Alternative TMPRSS13 Protease. mBio 2022; 13(4):e0137622.

357. Jocher G, Grass V, Tschirner SK, Riepler L, Breimann S, Kaya T et al. ADAM10 and ADAM17 promote SARS-CoV-2 cell entry and spike protein-mediated lung cell fusion. EMBO Rep 2022; 23(6):e54305.

358. Kastenhuber ER, Mercadante M, Nilsson-Payant B, Johnson JL, Jaimes JA, Muecksch F et al. Coagulation factors directly cleave SARS-CoV-2 spike and enhance viral entry. Elife 2022; 11.

359. Wettstein L, Immenschuh P, Weil T, Conzelmann C, Almeida-Hernández Y, Hoffmann M et al. Native and activated antithrombin inhibits TMPRSS2 activity and SARS-CoV-2 infection. J Med Virol 2023; 95(1):e28124.

360. Dong W, Wang J, Tian L, Zhang J, Settles EW, Qin C et al. Factor Xa cleaves SARS-CoV-2 spike protein to block viral entry and infection. Nature Communications 2023; 14(1):1936.

361. Sengar A, Cervantes M, Bondalapati ST, Hess T, Kasson PM. Single-Virus Fusion Measurements Reveal Multiple Mechanistically Equivalent Pathways for SARS-CoV-2 Entry. Journal of Virology 2023:e0199222.

362. Rajah MM, Bernier A, Buchrieser J, Schwartz O. The Mechanism and Consequences of SARS-CoV-2 Spike-Mediated Fusion and Syncytia Formation. J Mol Biol 2022; 434(6):167280.

363. Zhang Z, Zheng Y, Niu Z, Zhang B, Wang C, Yao X et al. SARS-CoV-2 spike protein dictates syncytium-mediated lymphocyte elimination. Cell Death Differ 2021; 28(9):2765–77.

364. Buchrieser J, Dufloo J, Hubert M, Monel B, Planas D, Rajah MM et al. Syncytia formation by SARS-CoV-2-infected cells. The EMBO Journal 2020; 39(23).

365. Cattin-Ortolá J, Welch LG, Maslen SL, Papa G, James LC, Munro S. Sequences in the cytoplasmic tail of SARS-CoV-2 Spike facilitate expression at the cell surface and syncytia formation. Nature Communications 2021; 12(1):5333.

366. Jiang X, Zhang Z, Wang C, Ren H, Gao L, Peng H et al. Bimodular effects of D614G mutation on the spike glycoprotein of SARS-CoV-2 enhance protein processing, membrane fusion, and viral infectivity. Signal Transduct Target Ther 2020; 5(1):268.

367. Saito A, Irie T, Suzuki R, Maemura T, Nasser H, Uriu K et al. Enhanced fusogenicity and pathogenicity of SARS-CoV-2 Delta P681R mutation. Nature 2022; 602(7896):300–6.

368. Bowen JE, Addetia A, Dang HV, Stewart C, Brown JT, Sharkey WK et al. Omicron spike function and neutralizing activity elicited by a comprehensive panel of vaccines. Science 2022; 377(6608):890–4.

369. Takeda M. Proteolytic activation of SARS-CoV-2 spike protein. Microbiology and Immunology 2022; 66(1):15–23.

370. Lambert DW, Yarski M, Warner FJ, Thornhill P, Parkin ET, Smith AI et al. Tumor necrosis factor-alpha convertase (ADAM17) mediates regulated ectodomain shedding of the severe-acute respiratory syndrome-coronavirus (SARS-CoV) receptor, angiotensin-converting enzyme-2 (ACE2). Journal of Biological Chemistry 2005; 280(34):30113–9.

371. Shulla A, Heald-Sargent T, Subramanya G, Zhao J, Perlman S, Gallagher T. A transmembrane serine protease is linked to the severe acute respiratory syndrome coronavirus receptor and activates virus entry. Journal of Virology 2011; 85(2):873–82.

372. Guo X, Cao J, Cai J-P, Wu J, Huang J, Asthana P et al. Control of SARS-CoV-2 infection by MT1-MMP-mediated shedding of ACE2. Nature Communications 2022; 13(1):7907.

373. Niehues RV, Wozniak J, Wiersch F, Lilienthal E, Tacken N, Schumertl T et al. The collectrin-like part of the SARS-CoV-1 and -2 receptor ACE2 is shed by the metalloproteinases ADAM10 and ADAM17. FASEB J 2022; 36(3):e22234.

374. Karthika T, Joseph J, Das VRA, Nair N, Charulekha P, Roji MD et al. SARS-CoV-2 Cellular Entry Is Independent of the ACE2 Cytoplasmic Domain Signaling. Cells 2021; 10(7).

375. Yeung ML, Teng JLL, Jia L, Zhang C, Huang C, Cai J-P et al. Soluble ACE2-mediated cell entry of SARS-CoV-2 via interaction with proteins related to the renin-angiotensin system. Cell 2021; 184(8):2212-2228.e12.

376. Wang J, Zhao H, An Y. ACE2 Shedding and the Role in COVID-19. Front Cell Infect Microbiol 2021; 11:789180.